Low-lying magnetic excitations, Magnetic anisotropy, Electrical transport, Magnetotransport and Resonant microwave absorption in Nanocrystalline Nickel

A Thesis submitted in partial fulfillment
of the award of the degree of
Doctor of Philosophy

By
Pavan Venu Prakash Madduri

School of Physics
University of Hyderabad
Hyderabad - 500 046, India
June 2017

D E C L A R A T I O N

I, **Pavan Venu Prakash Madduri**, hereby declare that the matter embodied in the thesis- **"Low-lying magnetic excitations, magnetic anisotropy, electrical transport, magnetotransport and resonant microwave absorption in nanocrystalline Ni"**, is the result of the investigations carried out by me in the School of Physics, University of Hyderabad, Hyderabad, India, under the supervision of **Prof. Sharika Nandan Kaul** and **Prof. S. Srinath**. This thesis is free from plagiarism. I hereby declare that it has not been submitted previously in part or in full to this University or any other University or Institution for award of any degree or diploma.

(Pavan Venu Prakash Madduri)
Reg. No: 10PHPH20

Date:
Place: Hyderabad

C E R T I F I C A T E

This is to certify that the thesis entitled "***Low-lying magnetic excitations, magnetic anisotropy, electrical transport, magnetotransport and resonant microwave absorption in nanocrystalline Ni***", submitted by Mr. Pavan Venu Prakash Madduri, bearing registration number 10PHPH20, in partial fulfillment of the requirements for award of Doctor of Philosophy in the School of Physics is a bonafide work carried out by him under my direct supervision and co-supervision of Prof. S. Srinath.

This thesis is free from plagiarism and has not been submitted previously in part or in full to this or any other University or Institution for award any degree or diploma.

Further, the student has the following publications (1-4) and conference proceedings (5 and 6) before the submission of the thesis for adjudication.

1. Magnon-induced interband spin-flip scattering contribution to resistivity and magnetoresistance in a nanocrystalline itinerant-electron ferromagnet: effect of crystallite size
   P. V. Prakash Madduri and S. N. Kaul
   Phys. Rev. B **95**, 184402 (2017), **Chapter-5**.

2. Diorder-induced non-Fermi liquid behavior of electrical resisitivity in nanocrystalline Ni
   P. V. Prakash Madduri and S. N. Kaul
   Physica B **448**, 147 (2014), **Chapter-5**.

3. Thermal demagnetization due to spin waves in nanocrystalline Ni
   P. V. Prakash Madduri and S. N. Kaul
   J. Magn. Magn. Mater. **418**, 143 (2016), **Chapter-4**.

4. Core and surface/interface magnetic anisotropies in nanocrystalline nickel
   P. V. Prakash Madduri and S. N. Kaul
   J. Alloys Compd. **689**, 533 (2016), **Chapter-3**.

5. Magnetic irreversibility and magnetocrystalline anisotropy in nanocrystalline nickel
   P. V. Prakash Madduri, S. Srinath and S. N. Kaul
   AIP Conf. Proc. **1665**, 130049 (2015), **Chapter-3**.

6. Low-lying magnetic excitations, magnetic irreversibility and approach-to-saturation in nanocrystalline Ni
   P. V. Prakash Madduri, S. P. Mathew and S. N. Kaul
   AIP Conf. Proc. **1536**, 89 (2013), **Chapter-4**.

Further, the student has passed the following courses towards the fulfillment of coursework required for PhD.

Course Code	**Name**	**Credits**	**Pass/Fail**
PY801	Advanced Quantum Mechanics	4	Pass
PY803	Advanced Statistical Mechanics	4	Pass
PY804	Advanced Electromagnetic Theory	4	Pass
PY821	Research Methodology	4	Pass

(Thesis Supervisor)

(Thesis Co-supervisor)

Dean
School of Physics
University of Hyderabad.

To

My Family
and
All my Teachers

Acknowledgements

I would like to express my sincere gratitude to many people who stood with me during the entire tenure of my PhD studies at the University of Hyderabad.

Obviously, my thesis supervisor, Prof. Sharika Nandan Kaul, stands first in the row. I am extremely grateful to have Prof. S. N. Kaul as my guide for PhD. With his great knowledge, experience, patience and rigorous scientific attitude towards research, I benefited a lot. I always feel a positive energy in his presence. Mrs. Manju Kaul (W/o Prof. Kaul), showed motherly affection. Thanks to her for her care and suggestions about my personal life.

I thank my co-supervisor, Prof. S. Srinath, for his valuable discussions, comments and encouragement towards my thesis work. His ideas and suggestions greatly improved my presentations at the department as well as at Conferences.

I would like to thank my Doctoral Committee members: Prof. Ashok Chatterjee, Dr. G. Venkataiah for their valuable discussions and advice.

Further, I am grateful to the present Dean, Prof. Bindu Bambah, and former Deans, School of Physics, for making available all the necessary facilities for research. I would like to thank Prof. S. N. Kaul once again, as a coordinator of Centre for Nanotechnology and Chairman of the University Cryogenic Facility. Because of his all out efforts to ensure smooth running of the physical and magnetic property measurement systems, I could perform sufficient measurements for my PhD thesis.

I acknowledge the help rendered by Mr. Mantoo Kumar and Mr. Giri in producing and transferring Liquid Helium and Nitrogen for low temperature and high magnetic field measurements.

I am also thankful to all non-teaching staff, particularly Mr. K. Srinivas, Mr. Abraham, Mrs. Sailaja, Ms. Deepika and Mrs. Grace for their cooperation in dealing with official works. Thanks to my cousin, Venkat, for providing a peaceful environment during my hostel stay.

I thank my lab mates Umasankar (deceased) and Ravikumar for their assistance and support in carrying out the experiments, subject discussions and for the memorable time, we shared in the lab. I can never forget their support in my personal life in some critical situations.

I should also thank my senior lab mates Dr. Shinto, Dr. Yugandhar and Dr. Basheed for their support during my research work. My sincere thanks to Dr. Sai Kiran, Dr. Koteswara Rao, Dr. Sunderayya for giving valuable guidance and support in my research trajectory. I thank my friends Ramesh, Pavankumar, Umalavanya. My best wishes to Binoy and Leela Sree. I should acknowledge my friend Satyanarayana for his help in qualifying the CSIR exam.

I am grateful to UoH for BBL Scholarship and financial support by CSIR through JRF and SRF.

I am very much grateful to my parents for giving freedom and helping me to fulfill all my desires. My heartfelt gratitude to my brother, Sastry, and my wife, Himabindu. I share my lab incidents with them. Thanks to them for listening with patience and giving righteous suggestions whenever I sought them. Finally, I thank my cute daughter, Lalitha Sri Vagdhevi, for playing with me and relaxing my mind.

Beyond everything, I am grateful to God, the Omnipresent, for blessing me in all situations throughout my life.

Contents

Chapter 1

Introduction

After giving a brief introduction to the nanocrystalline magnetic materials, this chapter outlines a critical assessment of the literature that existed on the magnetic properties of nanocrystalline transition metal ferromagnets before the work embodied in this thesis was initiated. Critical evaluation is followed by the aim and scope of the thesis.

1.1 Introduction

Nanocrystalline materials are polycrystals in which the size of the individual crystallites is of the order of several nanometers. In such materials, considerable fraction of the atoms/molecules lie at the surface or interface region between the adjacent grains/crystallites. Structural disorder at the surface/interface and broken translational symmetry arising from the small grain size and relatively high volume fraction of the grain boundary regions (internal interfaces) in which the atoms have to accommodate to the different alignment of neighboring grains results in making any structure-sensitive physical properties of nanocrystalline materials to differ from their bulk counterparts.

In nanocrystalline magnetic materials, as the characteristic length scale of microstructure (e.g., grain size or crystallite size (d) in three-dimentional (3D) bulk materials; thickness (t) in two-dimentional (2D) systems in thin film form; length (l) in case of one-dimentional (1D) quantum wires) in the nanometer range becomes comparable to the fundamental magnetic characteristic lengths such as critical single-domain size (D_{cr}), superparamagnetic critical diameter (D_{cr}^{spm}), domain wall thickness (δ_0), exchange correlation length (L_{ex}), spin diffusion length (l_{sd}), electron mean free path (λ_{mfp}) etc., magnetic and magnetotransport properties are expected to undergo profound fundamental changes. An apt example for this length scale trade off is nanocrystalline soft magnetic alloys of the NANOPERM or VITROPERM type, which exhibit an unusually low coercivity and high permeability whenever the structural correlation length (average particle size in this particular case) is smaller than the magnetic exchange correlation length [1–3]. In addition, magnetic properties in nanomaterials are strongly influenced by other microstructural parameters such as grain size distribution, grain shape anisotropy, internal stress, crystallographic texture, etc.

Ever-growing scientific interest in the study of magnetic nanomaterials is driven not only by the fundamental physics considerations but also by the envisaged potential for technical applications that include high-density magnetic recording media [4,5], magnetic logic [6–9], spin-torque oscillators [10–12], magnon spintronics [13–16], spin caloritronics [17], magnetic field sensing [18, 19], spintronic devices [20, 21], ceramics [22], bio medial applications such as magnetic biocatalysts [23, 24], drug delivery systems [25, 26], ferrofluids [27] and medical diagnostics [28].

1.2 Nanocrystalline Elemental Ferromagnets: Literature Review

Even though there exist a wide variety of nanomagnetic systems for numerous technological applications, main focus is on studying nanocrystalline single-phase ferromagnets such as elemental band ferromagnets Fe [29–33], Co [30,34–37], Ni [30,38–44] and the localized-spin ferromagnet Gd [45–52], for the following reasons. (i) They are the simplest model systems for understanding magnetic microstructure dependent physical properties at the nanoscale. (ii) These elements are the basic building blocks for numerous nanomagnetic compounds as well as nanocrystalline composite ferromagnets. (iii) In the bulk (single crystalline/polycrystalline) form, these elemental ferromagnets have been well studied and various theories enjoy considerable success so far as their magnetic, electrical transport and magnetotransport properties are concerned. Thus, studying these systems in the nanometric form should facilitate understanding fundamental changes brought about by crystallite size, spatial dimensionality and atomic structure.

Gleiter [29] was first to observe that a 40% decrease in saturation magnetization (M_s) in nanocrystalline (nc-) Fe with an average grain size of 6 nm, prepared by the inert gas condensation technique (IGC), when compared to bulk Iron. This reduction in M_s was attributed to the differences in the magnetic microstructure between nanocrystalline and conventional polycrystalline Fe. Wagner *et al.* [31] used small-angle neutron scattering (SANS) technique to probe magnetic microstructure of the nanocrystalline Fe sample. The SANS results suggest a microstructural model involving ferromagnetic grains and nonmagnetic (or weakly magnetic) interfaces. The average atomic density in the grain-grain interfaces was found to be about 40% of the atomic density of the crystallite core. Different magnetic contributions to the scattering contrast suggested that the interfaces have significantly lower average

magnetic moment than the core of the grains/crystallites.

In the case of ultrafine particles of Fe, Co and Ni (of crystallite sizes in the range 10 nm - 80 nm), prepared by gas evaporation method, Gong *et al.* [30] observed a rapid decrease in saturation magnetization, M_s, with decreasing grain size, d ($\approxeq$ 33 % in the case of Ni when d reduces from 50 nm to 10 nm; $\approxeq$ 69 % in Co when d decreases from 55 nm to 10 nm; $\approxeq$ 45 % in Fe when d falls from 80 nm to 10 nm). Reduction in M_s was ascribed to the oxidation of surface layer which is antiferromagnetic in nature. They also pointed out a peculiar particle size effect on coercive field (H_c). The coercivity initially increased with the decrease in particle size and reached a maximum value at the critical single-domain size and with further decrease in particle size, H_c declined very fast. In 1991, Du *et al.* [53] observed a drastic decrease in the saturation magnetization (M_s) in spherical Ni ultra-fine particles with grain sizes (d) in the range 9 nm to 85 nm when compared to bulk Ni. In this particular case, coercive field (H_c) approached zero at $d = 15$ nm. Drastic decline in M_s and H_c was explained in terms of superparamagnetism. Larger effective anisotropy (5.8 $\times 10^5$ erg/cc) in these ultra-fine particles than in bulk Ni (4.5 $\times 10^4$ erg/cc) was attributed to the surface anisotropy prevalent in nanocrystalline materials. Another important observation is that ferromagnetic Curie temperature, T_c, was found to reduce from 631 K (reported for bulk Ni) to 573 K for nanocrystalline Ni when $d = 9$ nm.

Schaefer *et al.* [38] reported a decrease in saturation magnetization in consolidated nanocrystalline Ni with average crystallite size (d) of 10 nm, prepared by the inert gas condensation technique. In this case, the atomic density of nanocrystalline Ni (ρ_{nc}) was found to be $\approx$ 80 % of the bulk density ($\rho_B = 8.9$ g/cc). Spontaneous magnetization (M_{spon}) was found to decrease as T^2 with increasing temperature (T) form 4 K to 350 K. T^2- power law thermal decline in M_{spon} implies that the Stoner single-particle excitations, prevalent in band ferromagnets, are responsible for the thermal demagnetization in nanocrystalline Ni. Moreover, a ferromanetic-to-paramagnetic

phase transition at T = 545 K was reported for the interfacial component (interface between grains/crystallites). To explain the results, it was assumed that an interfacial Ni atom carries a magnetic moment of 0.34 μ_B in comparison to 0.61 μ_B in bulk Ni, and 33 % of atoms reside at the interfaces. Smaller values of magnetic moment and Curie temperature of the interfaces in nanocrystalline Ni was explained by assuming that the structural disorder at the interfaces reduces the density of states, $N(E_F)$, at the Fermi level, E_F. According to the Stoner criterion of ferromagnetism ($IN(E_F) > 1$), for a given intra-atomic Coulomb interaction, I, a reduction in $N(E_F)$ weakens the ferromagnetic behavior and causes the decline in magnetization. Temperature variation of coercive field is governed by both crystalline anisotropy and shape anisotropy. While the crystalline anisotropy dominates at temperatures below 45 K and the magnetization reversal process proceeds via homogeneous rotation of magnetic moments, shape anisotropy plays a decisive role at temperatures above 45 K. Coercive field at 5 K, is higher by 9 % than that in bulk Ni.

Nanoparticles of metallic Fe have been studied by Bϕdker *et al.* [54] employing the Mössbauer effect spectroscopy. The main findings are : (1) metallic iron particles with diameters as small as 2 nm have properties similar to bulk α-Fe, (2) the magnetic anisotropy energy constant increases with decreasing particle size, presumably because of the infiuence of surface effects, and (3) spin polarized photoemission revealed that the chemisorption of oxygen results in the formation of a surface layer, which is ferromagnetically coupled to the core of the particles.

Kisker *et al.* [42] produced high purity nanocrystalline Ni by means of inert gas condensation (IGC) technique. No significant change in saturation magnetization (M_s) of bulk nickel was observed in nanocrystalline Ni. When these nanocrystalline Ni samples were exposed to air, M_s reduced to 80 % of the bulk value because of the oxygen contamination. In 'as-prepared' nanocrystalline Ni powders, magnetization reversal proceeds through homogeneous rotation of single domain particles but when

the powder specimens were compacted using high pressures ($\approx$ 2 GPa), magnetization process evolved through domain wall movement. Upon annealing at 373 K, diffused domain structure (resulting from the highly disordered crystallite interfaces and hence by small effective anisotropy) changed to elongated domains which can be ascribed to dominating magnetoelastic anisotropy. This was later experimentally observed by magneto-optic Kerr microscopy.

Small angle neutron scattering (SANS) investigation [56] of magnetic microstructure in nanocrystalline Fe ($d = 20$ nm) and nanocrystalline Ni ($d = 20$ nm) prepared by inert gas condensation revealed the existence of inter-crystallite magnetic correlations across the individual cystallites via their interfaces. In case of nanocrystalline Fe, few tens of individual grains are correlated magnetically whereas in nanocrystalline nickel this magnetic correlation extends over a distance of 200 nm. This exchange correlation works against the magnetic anisotropy energy of individual crystallites and prevents the magnetization from following the random crystallographic orientation of crystallites.

Investigations on ball-milled Ni and Fe nanocrystalline powders by Daróczi [55] revealed that the saturation magnetization is independent of crystallite size. Coercivity (H_c) followed the predictions of the random anisotropy model, originally proposed for amorphous ferromagnets. In case of Ni, they found an exchange correlation length, $L_{ex} = 28$ nm. When the average crystallite size, d is less than L_{ex}, H_c falls as $\backsim d^6$. According to the random anisotropy model, when $d \lesssim L_{ex}$, the ferromagnetic exchange interaction between small grains works against the random anisotropy (which causes the easy direction of intra-grain magnetization to change randomly from grain to grain) and forces the parallel alignment of spins of the adjacent grains. Consequently, effective anisotropy drastically decreases which causes H_c to mimic the same trend. This was the first experimental verification of the random anisotropy model in nanomagnetic materials produced by ball milling.

Furthermore, Yao *et al.* [41] carried out the thermal and magnetic charecterisation on ultra-fine Ni particles with d in the range 10 nm to 100 nm, prepared by the evaporation technique. They observed higher specific heat in nanocrystalline Ni compared to bulk Ni. An endothermic peak near the temperature $T \approx 560$ K in differential scanning calorimetry data was related to magnetic phase transition of the interface component. When the grain size is below 50 nm, they observed asymmetric $M - H$ hysteresis loops for temperatures $T \leq 50$ K. Arguing that high surface area for small particle sizes resulted in the oxidation of surface layer and formation of NiO shell, they assert that a coupling between Ni core and NiO shell gives rise to the exchange anisotropy. Similar observations were made in the case of ultrafine Co particles at $T \leq 150$ K [34].

In contrast to the results reported for ultrafine particles [30, 34, 53], Aus *et al.* [39] reported that the saturation magnetization (M_s) of nanocrystalline Ni was not strongly dependent on the grain size (d) down to about 10 nm. The observed M_s for nanocrystalline Ni with $d = 10$ nm was only 10% less than that for polycrystalline Ni. The finding that the reduction in M_S is only 10% is in agreement with the results of the theoretical calculations based on the local-spin-density functional theory that uses the TB-LMTO-ASA (tight binding-linear muffin-tin orbital and atomic-sphere) approach. These calculations account for the effect of structural disorder introduced by grain boundaries on the magnetic properties of nanocrystalline metals [58]. Even when all the volume belongs to the structurally disordered interfaces, the magnetic moment is reduced by only about 15% compared to bulk Ni. These results were obtained on bulk nanocrystalline Ni produced by electroplating. It was concluded that electroplated pure nanocrystalline nickel has a higher saturation magnetization than nanocrystalline Ni, prepared by the Inert gas condensation technique, due to the presence of clean grain boundaries, low porosity and the absence of nickel oxide phase.

The magnetic properties of the graphite encapsulated ferromagnetic metallic nanocrystals of Fe, Co, Ni prepared by tungsten-arc-discharge method [57], were characterized [59] with regard to the nano-scale nature of the particles and the influence of graphite coating, which prevents the possible rapid environmental contamination (e.g., oxidation), owing to a very high surface area to volume ratio and high reactivity. The saturation magnetization of encapsulated Ni nanocrystals with an average size of about 18.2 nm is suppressed, 21% in magnitude, compared to that of the microcrystalline Ni. This was attributed to superparamgnetic nature of the encapsulated particles. Compared to microcrystalline nickel particles, a significant decrease in M_r and H_c at 300 K in case of graphite encapsulated Ni nanocrystals was observed. Considering that the graphite encapsulation tends to protect the nanocrystals from any environmental degradation, and that the nanocrystals are pure Ni metal, discounting carbon solid solution, the reduction of H_c appears to be intrinsic to the nanocrystals of small size and the contribution from high density of surface atoms with respect to the bulk.

Magnetic properties of nanostructured elemental ferromagnets Fe, Co, Ni, with grain sizes ranging between 10 nm - 100 nm, prepared by inert gas condensation, were studided by Löffler *et al.,* using small-angle nuetron scattering [60] and bulk magnetic measurements [61,62]. Density of the samples was measured by the Archimedes immersion method. The density of the nanocrystalline samples was found to be approximately 81 - 86 % of that of their corresponding bulk materials. Influence of both grain size and oxidation effects were observed on the magnetic properties. Specimens, prepared by inert gas condensation technique, invariably suffer from oxidation at the interfaces because of the residual oxygen present in the evaporation chamber. This oxygen contamination is more effective at lower grain sizes. While the random orientation of the grains and hence of magnetization vectors was concluded from isotropic SANS. Anisotropic SANS data confirmed interaction between the fer-

romagnetic grains and anti-ferromagnetic or ferrimagnetic interfacial oxide phase. In nanocrystalline Fe, coercive field showed an increasing trend with decreasing grain size from 100 nm to 30 nm, and then a steep decrease as the grain size decreased further. This behavior is discussed in terms of the random-anisotropy model [63], which predicts that the effective anisotropy constant responsible for magnetization reversal is reduced by averaging over magnetically coupled grains. A decrease in coercive field with increasing temperature observed for nanocrystalline Fe and nanocrystalline Ni is also in agreement with the predictions of random anisotropy model. According to the random anisotropy model, the ferromagnetic correlation length increases with increasing temperature with the consequence that the anisotropy constant is reduced by averaging over more correlated grains. Hysteresis measurements at low temperatures ($\approx$ 5 K) after field-cooling (in a field of 20 kOe) showed a shift and broadening of the hysteresis loops for both Fe and Ni. This loop shift was attributed to an exchange coupling between the ferromagnetic grains and antiferromagnetic oxide (NiO in case of Ni) or ferrimagnetic oxide (Fe_3O_4 in case of Fe) interfacial phases. The hysteresis loop-shift decreases and finally vanishes with increasing grain size. In all the samples, saturation magnetization (M_S) decreased with diminishing average grain size. This reduction in M_S was explained in terms of the grain size and oxidation effects. Reduction in the grain size brings reduction in the atomic density in the grain-boundary region and hence lowest saturation magnetization occurs in the samples with the highest volume fraction of grain boundaries. Similarly, oxygen atoms in oxide layers at the interfaces/surfaces reduces the contribution of ferromagnetism more efficiently at lower grain sizes.

Low temperature magnetic behavior of ball-milled nanocrystalline Fe with an average grain size of 12 nm (prepared by mechanical energy transfer technique through ball milling) was investigated [33] by measuring ac susceptibility, time-dependent magnetization and the thermoremanent magnetization. A transition from a high-

temperature ferromagnetic state to a low-temperature disordered frozen magnetic state, observed at a characteristic temperature $\sim 70\ K$ in nanocrystalline Fe, was attributed to the competition between the interfacial anisotropy brought about by the structural disorder at the grain boundary and magneto-crystalline anisotropy. As the temperature is reduced, the anisotropy at the grain boundaries swamps the ferromagnetic exchange across the interfaces. The inter-grain exchange interaction tries to hold the boundary spins aligned in the direction of magnetization vectors of the surrounding grains. As a result of the overwhelming grain boundary anisotropy, short-range exchange interactions cannot be transmitted across grain-grain interfaces. However, the long-range dipole-dipole interactions still persist. All these competing interactions are responsible for the freezing of the magnetic moments of grains in random orientations at low temperatures. Consequently, a cluster spin glass state is established.

Muon spin rotation (μSR) measurements on nanocrystalline Ni and Co indicated magnetically ordered regions (crystallite core) surrounded by disordered surface layers [65]. Similar results were obtained with perturbed $\gamma - \gamma$ angular correlation spectroscopy (PAC) [66] on pulse electrodeposited nanocrystalline Ni doped with a radioactive Indium isotope (In^{111}). These measurements showed that in nanocrystalline Ni with average crystallite size of 40 nm, 37 % of the total atoms reside in a perturbed local magnetic environment (surfaces/interfaces) in contrast to the crystallite cores.

Irreversible magnetization in Ni nanoparticles of size 10 nm, prepared by magnetron sputtering, were reported by Zhang *et al.* [67]. Magnetization as a function of field and temperature showed that the nanoparticle system behaves like a random magnet with a large field-dependent irreversibility temperature, T_{irr}. The nanoparticle system behaves like a superparamagnet at temperatures below T_{irr} and exhibits a spin glass state above T_{irr}. With increasing strength of external magnetic field, the

irreversibility temperature decreases. Magnetic relaxation studies show a clear logarithmic time dependence and a strongly field- and temperature-dependent effective anisotropy energy barrier.

A detailed crystalline and magnetic microstructure study [68] in pulse electrodeposited nanocrystalline Ni and Co samples, with average crystallite sizes in the range 10 - 60 nm, was carried out by means of small-angle neutron scattering, small-angle x-ray scattering and magnetization. Porosity of the samples was measured to be 0.5 to 3 %. The zero-field small-angle neutron scattering contributions indicate that both nanocrystalline Ni and nanocrystalline Co have magnetic domains of size around 150 nm. Samples prepared by pulse electrodeposited have higher atomic density than the inert gas condensed samples. Higher atomic density in pulse electrodeposited samples could be responsible for strong magnetic interaction across the grain boundaries that leads to domains accommodating several crystallites. It is argued that the random anisotropy model is applicable in this case also. In nanocrystalline Ni with grain size 20 nm, the saturation magnetization is reduced by 6 % with respect to the polycrystalline Ni.

Weissmüller and Michels *et al.* [36] were first to measure exhange stifness constant, A (an important material parameter in the theory of micromagnetics used to tailor macroscopic magnetic properties such as magnetization reversal in nanocrystalline soft and hard magnetic materials) of nanocrystalline transition metal ferromagnets - Co and Ni from the *magnetic contribution of the small-angle neutron scattering (SANS)*. Exchange stiffness constant for pulse electrodeposited nanocrystalline Ni has the value $9.2(2) \times 10^{-7}$ erg/cm at $T = 5$ K and $7.6(3) \times 10^{-7}$ erg/cm at $T = 295$ K. Similarly, for pulse electrodeposited nanocrystalline Co, they obtained the value, 'A' $= 28(1) \times 10^{-7}$ erg/cm at $T = 295$ K. Weissmüller *et al.* [37] analyzed the small-angle neutron scattering data of nanocrystalline Ni and Co in terms of a micromagnetic theory [64] developed for nanocrystalline ferromagnets with non-

uniform magnetic anisotropy in which differential scattering cross-section depends on magnetic field as well as on the scattering wave vector. This analysis provided information about the magnetic microstructure, exchange stiffness and magnitude of magnetic anisotropy. From the magnetic small-angle neutron scattering cross-section, they obtained spin misalignment correlation length (l_C) [69], which is a characteristic dimension of the regions wherein the magnetic moments are coherently misaligned in the same direction relative to the direction of mean magnetization, $\langle \mathbf{M} \rangle$. At room temperature and low applied magnetic fields, $l_C = 94$ nm (45 nm) for nanocrystalline Co (nanocrystalline Ni) with $d = 10$ nm (49 nm). The results for l_C suggested that in nanocrystalline Co the main source of non-uniformity in the spin system is the anisotropy field of each individual crystallite that differs from crystallite to crystallite. By contrast, in nanocrystalline Ni, spin disorder originates from the twin faults and/or from the disordered grain boundaries.

Manetization reversal dynamics in chemically synthesized clusters of single domain Ni nanoparticles was investigated by Rana *et al.* [70]. Assuming a finite overlap between the nanoparticles (as opposed to isolated randomly oriented nanoparticles), theoretical simulations reproduced well the observed $M - H$ loops. A finite overlap between the magnetic nanoparticles signals the presence of both long-range magnetostatic and short-range exchange interactions between the particles. The magnetization reversal of the entire cluster of nanoparticles occurs through the appearance of various domain states including C-state, vortex-like state, and flower-like state, although the individual particles in the cluster maintain primarily single domain state. Various domain structures occur in the cluster due to the incoherence of the magnetization reversal between the constituent particles in the cluster.

Magnetic properties of single-phase spherial Ni nanoparticles (23 to 114 nm in diameter), prepared by thermal decomposition, were studied by He *et al.* [71]. The Curie temperature (T_C) of the 23, 45, 80, and 114 nm Ni particles was found to

be 335 °C, 346 °C, 351 °C, and 354 °C, respectively, from the differential thermal analysis. Considering the size- and shape- dependent cohesive energy, a theoretical model was proposed to explain the finite-size effects on T_C. From the magnetic hysteresis loops, it was observed that the saturation magnetization (M_s) and remanent magnetization (M_r) both increase while the coercivity (H_c) decreases monotonously with increasing particle size. By adopting a magnetically dead-layer theory, the saturation magnetization of the nanoparticles, M_{np} was observed to follow the relation $M_{np} = M_{bulk}(1-6t/D)$, where M_{bulk} is the saturation magnetization of corresponding bulk materials, t is the thickness of magnetically inactive layer and D is the diameter of nanoparticles. Furthermore, it was concluded that the thickness of magnetically inactive layer increases with the reduction in Ni particle size.

Contribution of the Néel surface anisotropy [76] to the effective anisotropy of the spherical magnetic nanopartiles was considered by Garanin and Kachkachi [74]. Evidence of surface anisotropy in magnetic CoFe thin films was provided by Schmool [75] through the ferromagnetic resonance technique. Films with lower thickness exhibit enhancement in the FMR linewidth. Surface effects are expected to cause line broadening, which is proportional to the amount of surface present per unit volume. A detailed theoretical framework to understand effective anisotropies and energy barriers of small particles within the Néel surface anisotropy was proposed by Yanes *et al.* [77]. It was assumed that the energy of many-spin nanoparticles, cut from cubic lattices, could be well represented by an effective one-spin potential containing uniaxial and cubic anisotropies. With the aid of numerical modelling, the magnitude and signs of anisotropy constants were shown to strongly depend on the surface spin arrangement of the particle, crystal structure of the core of the particle and the shape of the particles. They also found that (i) in elongated particles, surface effects can change the sign of the effective uniaxial anisotropy, (ii) in symmetric particles (spherical and truncated octahedral) with cubic core anisotropy, surface

effects can change the sign of uniaxial surface anisotropy. They also showed that the competition between the core and surface anisotropies leads to an additional energy that contributes to both the second- and fourth-order effective anisotropies. Studies on the strength of energy barriers ($\Delta E = K_{eff} \times V$) as a function of surface anisotropy and particle size proved that the consistency of the widely-used formula $K_{eff} = K_V + 6K_s/D$ (where K_V is the core anisotropy constant, K_s is a phenomenological constant related to surface anisotropy, and D is the particle size) is applicable only for elongated particles. In a further work, the same authors evaluated the temperature dependence of the effective anisotropies in spherical Co nanoparticles, cut from simple cubic crystal structure (with diameters of the order 3 - 8 nm), assuming Néel surface anisotropy [78]. To model the magnetic behavior, they used a classical atomistic spin model that takes into account Heisenberg exchange interactions. An additional cubic anisotropy, due to the spin nonlinearities produced by the surface anisotropy, is not only present at 0 K but also persistant at finite temperatures. They obtained a scaling behavior of the effective anisotropy (K) on the nanoparticle magnetization (M) as $K(T) \propto M(T)^{\gamma}$. For microcrystalline/bulk samples, the scaling exponent, γ, was found to be 3 and 10 for uniaxial and cubic anisotropies [79], respectively. γ has the values 2.81 and 5.61 for uniaxial and cubic core anisotropies in the case of nanocrystalline systems showing that the scaling exponent strongly depends on the surface anisotropy. Lower values of γ for nanocrystalline systems when compared to bulk specimens suggests strong magnetization fluctuations at the surface.

A quantitative comparison of the observed $M(H)$ loop at $T = 2$ K in pulse electrodeposited nanocrystalline Ni with average crystallite size 23 nm was made with the result of the numerical simulations, based on the modified Landau-Lifshitz-Gilbert (LLG) equation of motion, that incorporate the intrinsic fields arising from the intra-grain core, grain boundary anisotropies and the interacting fields resulting from the dipolar and exchange couplings between the neighboring grains. Such a

comparison indicated that the grain boundary anisotropy in nanocrystalline Ni at low temperatures ($T = 2$ K) can be represented by an uniaxial anisotropy with the anisotropy constant, $K_1^s = -6.0 \times 10^5$ erg/cc. An inter-grain exchange coupling constant, $A_p = 2.16 \times 10^{-7}$ erg/cm, nearly equal to the exchange stiffness constant of bulk-Ni, asserts strong inter-grain exchange interactions mediate by surface spins.

Electrical resistivity (ρ) and temperature coefficient of resistivity (α) have been studied for electrodeposited nanocrystalline Ni with average crystallite size 50 nm by Bakonyi [80]. It was observed that ρ increased while α decreased when compared to polycrystalline Ni. Near room temperature, α has the value 25×10^{-4} K^{-1}. Analysis of the temperature dependence of resistivity from 4.2 K to 300 K showed that, besides crystalline boundaries there exist a large amount of other types of lattice imperfections, created during the processing of nanocrystalline materials, that account for the large residual resistivity.

The effect of grain boundaries on the electrical resistivity of pulse electrodeposited nanocrystalline Ni with grain sizes 11 nm, 15 nm, 34 nm, 500 nm was investigated by Aus *et al.* [81]. Resistivity was found to increase with decreasing grain size. This enhancement was attributed to the increased volume fraction of interfaces at smaller grain sizes and the associated electron scattering events at the grain boundaries. A temperature coefficient of resistivity $= 28.5 \times 10^{-4}$ K^{-1} was observed for nanocrystalline Ni with 11 nm average grain size in comparison to 40×10^{-4} K^{-1} observed for polycrystsalline Ni. The temperature coefficient of resistivity was found to decrease with decreasing grain size. At room temperature, the resistivity of the material with a grain size of 11 nm is enhanced by a factor of 3 over the resistivity value observed for a polycrystalline nickel.

The electrical resistivity was measured for nanocrystalline high purity Cu, Ni and Fe (with mean grain sizes in the range 100 - 200 nm), prepared by severe torsional deformation at a quasi- hydrostatic pressure of 6 GPa. The absolute resistivities at

250 K are about 2, 10 and 16 $\mu\Omega$ cm for Cu, Ni and Fe, respectively. These values are roughly 15, 35 and 55 % higher than the electrical resistivity of their polycrystalline counterparts. The increased resistivity of the nanocrystalline metals studied was attributed to the additional electron scattering on the increased number of grain boundaries as the nanoparticle size shrinks.

Raquet *et al.* [82] performed the longitudinal magnetoresistance (MR) measurements on epitaxial Fe, Co, and Ni thin films under a 4×10^5 Oe pulsed magnetic field, well above the technical saturation of magnetization over a temperature range 4 K to 500 K. Both the nature of the spin disorder, collective spin excitations and their contribution to magnetoresistance arising from spin-flip electron scattering were determined. They reported an almost linear and non-saturating negative magnetoresistance of around 0.01 - 0.03 $\times 10^{-4} \mu\Omega$ cm Oe^{-1} at 300 K, for the three 3d metals and ascribed the linear relation between magnetoresistance and field to the electron-magnon scattering and the spin-wave damping at high fields. A theoretical model was proposed to calculate magnetoresistance, which takes into account the spin-flip intraband $s-s$, $d-d$ and interband $s-d$ transitions induced by the scattering of conduction electrons off magnons. This model makes provision for the high-field effect on the magnon spectrum and the magnon mass renormalization. A good consistency was found between the predictions of the proposed model and experimentally measured high-field magnetoresistance. The main finding was that, at room temperature, the spin-flip scattering induced by magnons accounts for 15 %, 18 %, and 30 % of the total resistivity in Fe, Co, and Ni, respectively.

Electrical transport properties in the temperature range of 3 K - 300 K on the arrays of nickel nanowires with diameters ranging from 55 to 13 nm (fabricated by electrodeposition into the cylindrical pores of anodic alumina membrane) were investigated by Kamalakar and Raychaudhari [83]. This work revealed intrinsic differences in the transport mechanisms taking place in these wires when the diameter of the

wires is brought down from bulk to nanometer regime. The resistivity data were analyzed using the Bloch-Wilson function for the electron-phonon contribution to resistivity, ignoring the electron-magnon scattering contribution, for temperatures above 15 K. The Debye temperature showed a systematic decrease with the reduction in the diameter of the nanowires. An increase in the residual resistivity due to surface scattering was observed as the diameter of wire decreases. A strong suppression in the magnon contribution to the resistivity of the magnetic nanowires was observed at temperatures $T \leq 15$ K as the diameter is decreased.

1.3 Critical evaluation of the literature

Magnetic properties of nanocrystalline 3d transition metal ferromagnets, Fe, Co, Ni and their alloys have been extensively studied both experimentally and theoretically with a view to understand magnetization reversal, magnetic exchange coupling at the interfaces and spin misalignment correlation length across the grains. Much of the earlier work focused on the non-interacting spin systems, in which crystallites/grains are well separated. By comparison, highly dense nanocrystalline magnetic systems with a finite overlap between the crystallite surfaces/interfaces resulting in inter-particle interactions (both short-range exchange and long-range dipolar interactions) have received less attention. Inter-particle interactions have profound influence on the magnetic and transport properties. For example, in nanocrystalline Ni with an average crystallite size of 10 nm, prepared by inert gas condensation technique, the spontaneous magnetization declines with increase in temperature (T) as T^2 [38]. In this case, the nanocrystalline Ni has an atomic density (ρ_n) that is $\approx$ 80 % of the bulk density (ρ_B). The T^2 power law decline in magnetization was taken to imply that the Stoner single-particle excitations are responsible for thermal demagnetization. In contradiction to this, small-angle neutron scattering experiments on pulse

electrodeposited nanocrystalline Ni, with an average crystallite size of 55 nm and $\rho_n = \rho_B$, revealed the existence of well-defined spin waves [37]. It is not clear from these conflicting reports if the drastic change in density and hence in the atomic structure in the grain boundary regions is at the root of this discrepancy or if the reduction in average crystallite size (d) changes the nature of low-lying magnetic excitations or if below a certain value of d, it is harder to excite spin waves at low and intermediate temperatures. There are no other studies concerning the magnetic excitations in nanocrystalline ferromagnets. Similarly, the magnetization reversal and relaxation shows marked differences in the case of interacting and non-interacting nanoparticle assemblies. So far as the transport properties of nanocrystalline- Fe, Co, Ni, are concerned, the main focus has been on the surface/interface and grain boundary scattering effects in thin films, nanowires and nanoparticle systems. No sincere attempts have been made to understand the basic scattering mechanisms responsible for electrical- and magneto-transport in nanocrystalline ferromagnets. From a critical appraisal of the literature, several issues that include the nature of low-lying magnetic excitations, surface/ interface magnetic anisotropies, electrical-, magneto-transport and spin dynamics in interacting nanoparticle systems, need to be addressed in great detail.

1.4 Aim and scope of the Thesis

In view of a critical evaluation of the literature existing prior to the present study, a careful and detailed investigation of the magnetic, electrical transport, magnetotransport and ferromagnetic resonance behavior in nanocrystalline Ni has been undertaken with the following objectives in mind.

- To investigate the effect of finite crystallite size on the magnetization processes and 'approach-to-magnetic saturation' in nanocrystalline nickel.
- To have a basic understanding of how the inter-grain interactions, intra-grain/core magnetic anisotropy, surface/interface magnetic anisotropy and shape anisotropy affect the magnetization reversal processes in nanocrystalline ferromagnets.
- To study the effect of average crystallite size on the nature of low-lying magnetic excitations in nanocrystalline Ni.
- To thoroughly study the effect of the size-reduction on the electrical transport and magnetotransport properties of nanocrystalline Ni, which are extremely sensitive to the charge and spin scattering of conduction electrons from the particle surfaces/interfaces and to estimate the effect of the finite crystallite size in the nanometer range on various scattering contributions to the intrinsic resistivity and magnetoresistance of bulk nanocrystalline Ni.
- To probe the spin dynamics, relaxation phenomena, and magnetic anisotropy in nanocrystalline Ni using the ferromagnetic resonance technique.

References

1. G Herzer, *Handbook of Magnetic Materials* Vol **10**, edited by K H J Buschow (Amsterdam: Elsevier) pp 415-62 (1997).

2. K Suzuki and G Herzer, *Advanced Magnetic Nanostructures* edited by D Sellmayer and R skomski (New York : Springer) pp 365-401 (2006).

3. G. A. Bhaseed and S. N. Kaul, *Solid State Physics* (India), **49**, 265-266 (2004).

4. W J Gallangher and S S P Parkin, *IBM J. Res. Dev.* **50**, 5 (2006).

5. Z Z Bandić and R H Victora, *Proc. IEEE* **96**, 1749 (2008).

6. Semiconductor Industry Associations, *The International Technology Roadmap for Semiconductors: Emerging Research Devices* (2011) *www.itrs.net*

7. G. Csaba, A. Imre, G. H. Bernstein, W. Porod, and V. Metlushko, *IEEE Trans. Nanotechnol.* **1**, 209 (2002).

8. M. Becherer, G. Csaba, R. Emling, W. Porod, P. Lugli, D. Schmitt-Landsiedel, *IEEE Int. Solid-State Circuits Conf.,* ISSCC (San Francisco, CA) pp 474-5 (2009).

9. M. Niemier, G. Csaba, A. Dingler, X. S. Hu, W. Porod, X. Ju, M. Becherer, D. Schmitt-Landsiedel, P. Lugli, *Proc. 13th Int. Workshop on Cellular Nanoscale Networks and their Applications (Turin, Italy)* pp 59-64 (2012).

10. J. V. Kim, *Solid State Phys.* **63**, 21760 (2012).

11. J. C. Slonczewski *J. Magn. Magn. Mater.* **159**, L1 (1991).

12. L. Berger *Phys. Rev. B* **54**, 9353 (1996).

13. T. Schneider, A. A. Serga, B. Leven, B. Hillebrands, R. L. Stamps and M. P. Kostylev, *Appl. Phys. Lett.* **92**, 022505 (2008)

14. V. V. Kruglyak, S. O. Demokritov, and D. Grundler, *J. Phys. D: Appl. Phys.* **43**, 264001 (2010)

15. A. A. Serga, A. V. Chumak and B. Hillebrands, *J. Phys. D: Appl. Phys.* **43**, 264002 (2010)

16. B. Lenk, H. Ulrichs and M. Münzenberg, *Phys. Rep.* **507**, 107 (2011).

17. G. E. W. Bauer, E. Saitoh and B. J. V. Wees, *Nature Mater.* **11**, 391 (2012).

18. P. Kalita, J. Singh, M. K. Singh, P. R. Solanki, G. Sumana and B. D. Malhotra, *Appl. Phys. Lett.* **100**, 093702 (2012).

19. S H Chung, A Hoffmann, S D Bader, C Liu, B Kay, L Makowski and L Chen, *Appl. Phys. Lett.* **85**, 2971 (2004).

20. S.D. Bader and S.S.P. Parkin, *Annu. Rev. Condens. Matter Phys.* **1**, 71-88 (2010).

21. I. Zutic, J. Fabian, S. D. Sarma, *Rev. Mod. Phys.* **76**, 323 (2004).

22. M. D. Kaminski, H. Chen, X. Liu, D. Rempfer and A. J. Rosengart, *Magnetic Nanoparticles. From Fabrication to Clinical Applications* edited by N. T. K. Thanh (Boca Raton, FL: CRC Press) pp 195-214 (2012).

23. A H Lu, W Schmidt, N Matoussevitch, H Bönnemann, B Spliethoff, B Tesche, E Bill, W Kiefer and F Schüth, *Angew. Chem.* **116**, 4403 (2004).

24. R Bussamara, D Eberhardt, A F Feil, P Migowski, H Wender, D P de Moraes, G Machado, R M Papaléo, S R Teixeira and J Dupont, *Chem. Commun.* **49**, 1273 (2013).

25. M Arruebo, R Fernández-Pachcco, M R Ibarra and Santamaría, *Nanotoday* **2**, 22 (2007).

26. C. Alexious, R. Jurgons, in *Magnetic Drug Targetting* edited by W. Andră, H. Nowak. *Magnetism in Medicine: A Handbook 2nd edn.*, (Wiley, Weinheim) pp. 596-605 (2007).

27. S. Odenbach, *Ferrofluids* edited by K. H. J. Buschow, *Handbook of Magnetic materials*, vol 16 (Elsevier, Amsterdam), pp. *127-208* (2006).

28. A K Gupta and M Gupta, *Biomaterials* **26**, 3995 (2005).

29. H. Gleiter, *Progr. Mater. Sci.* **33**, 223 (1989).

30. W. Gong, H. Li, Z. Zhao and J. Chen, *J. Appl. Phys.* **69**, 5119 (1991).

31. W. Wagner, A. Wiedenmann, W. Petry, A. Geibel and H. Gleiter, *J. Mater. Res.* **6**, 2305 (1991).

32. L. D. Bianco, A. Hernando, E. Bonetti and E. Navarro, *Phys. Rev. B* **56**, 8894 (1997).

33. E. Bonetti, L. D. Bianco, D. Fiorani, D. Rinaldi, R. Caciuffo and A. Hernando, *Phys. Rev. Lett.* **83**, 2829 (1999).

34. S. Gangopadhyay, G. C. Hadjipanayis, C. M. Sorensen, and K. J. Klabunde, *Nanostr. Mater.* **1**, 449 (1992).

35. M. J. Aus, C. Cheung, B. Szpunar, U. Erb and J. Szpunar, *J. Mater. Sci. Lett.* **17**, 1949 (1998).

36. A. Michels, J. Weissmüller, A. Wiedenmann, J. G. Barker, *Phil. Mag. Lett.* **80**, 785 (2000).

37. J. Weissmüller, A. Michels, J. G. Barker, A. Wiedenmann, U. Erb, R. D. Shull, *Phys. Rev. B* **63**, 214414 (2001).

38. H. E. Schaefer, H. Kisker, H. Kronmüller and R. Wurschum, *Nanostr. Mater.* **1**, 77 (1992).

39. M. J. Aus, B. Szpunar, A. M. El-Sherik, U. Erb, G. Palumbo and K. T. Aust, *Scripta. Metal. Mater.* **27**, 1639 (1992).

40. L. Daroczi, D. L. Beke, G. Posgay, G. F. Zhou and H. Bakker, *Nanostr. Mater.* **2**, 512 (1993).

41. Y. D. Yao, Y. Y. Chen, C. M. Hsu, H. M. Lin, C. Y. Tung, M. F. Tai, D. H. Wang, K. T. Wu and C. T. Suo, *Nanostr. Mater.* **6**, 993 (1995).

42. H. Kisker, T. Gessmann, R. Wurschum, H. Kronmüller and H. E. Schaefer, *Nanostr. Mater.* **6**, 925 (1995).

43. I. Bakonyi, E. Toth-Kadar, J. Toth, T. Tarnoczi and A. Cziraki, *Processing and properties of nanocrystalline materials*, edited by C. Suryanarayana, J. Singh F. H. Froes (The Minerals, Metals and Materials Society) (1996).

44. J. Weissmüller, R. D. McMicheal, J. Barker, H. J. Brown, U. Erb and R. D. Shull, *Mater. Res. Soc. Symp. Proc.* **457**, 231 (1997).

45. D. Michels, C. E. Krill III and R. Birringer, *J. Magn. Magn. Mater.* **250**, 203 (2002).

46. R. Kruk, M. Ghafari, H. Hahn, D. Michels, R. Birringer, C. E. Krill III, R. Kmiec and M. Marszalek, *Phys. Rev. B* **73**, 054420 (2006).

47. A. Michels, F. Dbrich, M. Elmas, A. Ferdinand, J. Markmann, M. Sharp, H. Eckerlebe, J. Kohlbrecher and R. Birringer, *Europhys. Lett.* **81**, 66003 (2008).

48. P. M. Shand, J. G. Bohnet, J. Goertzen, J. E. Shield, D. Schmitter, G. Shelburne and D. L. Leslie-Pelecky, *Phys. Rev. B* **77**, 184415 (2008).

49. S. N. Kaul and S. P. Mathew, *Phys. Rev. Lett.* **106**, 247204 (2011).

50. S. N. Kaul and S. P. Mathew, *Nanosci. Nanotechnol. Lett.* **3**, 556 (2011).

51. S P Mathew and S N Kaul *J. Phys.: Condens. Matter* **24**, 256008 (2012).

52. S P Mathew and S N Kaul *J. Phys.: Condens. Matter* **27**, 056003 (2015).

53. Y. Du, M. Xu, J. Wu, Y. Shi, H. Lu and R. Xue, *J. Appl. Phys.* **70**, 5903 (1991).

54. F. Bϕdker, S. Mϕrup, and S. Linderoth *Phys. Rev. Lett.* **72**, 282 (1994).

55. I. Daroczi, D. L. Beke, G. Posgay and M. Kisvarga, *Nanostr. Mater.* **6**, 981 (1995).

56. W. Wagner, H. Van Swygenhoven, H.J. Hiifler and A. Wiedenmann, *Nanostr. Mater.* **6**, 929 (1995).

57. V. P. Dravid, J. J. Host, M. H. Teng, B. R. Elliott, J.-H. Hwang, D. L. Johnson, T. O. Mason, and J. R. Weertman, *Nature* (London) **374**, 602 (1995).

58. B. Szpunar, U. Erb, G. Palumbo, K. T. Aust and L. J. Lewis, *Phys. Rev. B* **53**, 5547 (1996).

59. J. -H. Hwang et al., *J. Mater. Res.* **12**, 1076 (1997).

60. J. Löffler, W. Wagner, H. Van Swygenhoven and A. Wiedenmann, *Nanostr. Mater.* **9**, 331 (1997).

61. J. Löffler, H. Van Swygenhoven, W. Wagner, J. Meier, B. Doudin and J.-Ph Ansermet, *Nanostr. Mater.* **9**, 523 (1997).

62. J. Löffler, J. P. Meier, B. Doudin, J.-Ph Ansermet, and W. Wagner, *Phys. Rev. B* **57**, 2915 (1997).

63. Eugene M. Chudnovsky, in Chapter 3 *The Magnetism of Amorphous Metals and Alloys* edited by J. A. Fernandez-Baca and Wai-Yim Ching (World Scientific, Singapore) (1995).

64. J. Weissmüller, R. D. McMichael, A. Michels and R. D. Shull, *J. Res. Natl. Inst. Stand. technol.* **104**, 261 (1999).

65. O. Hartmann, R. Wäppling, M. Ekström, B. Heisel, M. Schmelzer, H. Natter, and R. Hempelmann, *Nanostruct. Mater.* **12**, 943 (1999).

66. St. Lauer, Z. Guan, H. Wolf, H. Natter, M. Schmelzer, R. Hempelmann, and Th. Wichert, *Nanostruct. Mater.* **12**, 955 (1999).

67. P. Zhang, F. Zuo, F.K. Urban III, A. Khabari, P. Griffiths, A. Hosseini-Tehrani, *J. Magn. Magn. Mater.* **225**, 337 (2001).

68. R. Przenioslo, R. Winter, H. Natter, M. Schmelzer, and R. Hempelmann and W. Wagner, *Phys. Rev. B* **63**, 054408 (2001).

69. A. Michels, R. N. Viswanath, J. G. Barker, R. Birringer and J. Weissmüller, *Phys. Rev. Lett.* **91**, 267204 (2003).

70. Bivas Rana, Milan Agarwal, Semanti Pal and Anjan Barman *J. Appl. Phys.* **107**, 09B513 (2010).

71. Xuemin He, Wei Zhong, Chak-Tong Au and Youwei Du, *Nanoscale Research Letters* **8**, 446 (2013).

72. J. Weissmüller, A. Michels, D. Michels, A. Wiedenmann, C. E. Krill III, H. M. Sauer and R. Birringer, *Phys. Rev. B* **69**, 054402 (2004).

73. R. Skomski, *J. Phys.: Condens. Matter* **15**, R841 (2003).

74. D.A. Garanin, H. Kachkachi, *Phys. Rev. Lett.* **90**, 065504 (2003).

75. D.S. Schmool, R. Rocha, J.B. Sousa, J.A.M. Santos and G. Kakazei *J. Magn. Magn. Mater.* **300**, e331 (2006).

76. L. Néel, *J. Phys. Radium* **15**, 225 (1954)

77. R. Yanes, O. Chubykalo-Fesenko, H. Kachkachi, D. A. Garanin, R. Evans and R. W. Chantrell, *Phys. Rev. B* **76**, 064416 (2007).

78. R. Yanes, O. Chubykalo-Fesenko, R. F. L. Evans and R. W. Chantrell, *J. Phys. D: Appl. Phys.* **43**, 474009 (2010).

79. H. B. Callen and E. Callen, *J. Phys. Chem. Solids* **27**, 1271 (1966).

80. I. Bakonyi, E. Tóth-Kádár, J. Tóth, A Cziráki, B. Fogarassy, *Nanophase materilas* **260**, 423 (1994).

81. M. J. Aus, B. Szpunar, U. Erb, and A. M. El-Sherik, G. Palumbo and K.T.Aust, *J. Appl. Phys.* **75**, 3632 (1994).

82. B. Raquet, M. Viret, E. Sondergard, O. Cespedes, and R. Mamy, *Phys. Rev. B* **66**, 024433 (2002).

83. M. Venkata Kamalakar and A. K. Raychaudhuri *Phys. Rev. B* **79**, 205417 (2009).

Chapter 2

Experimental Techniques

This chapter describes the synthesis and characterization of the nanocrystalline Ni samples used in the present work. The experimental techniques used for measuring the temperature- and field-dependent magnetization, electrical transport, magneto-transport and spin dynamics are also presented.

2.1 Sample Preparation

2.1.1 Pulse Electrodeposition

Pulse electrodeposition (PED) is one of the novel techniques for producing pore-free and high-density consolidated nanocrystalline materials. Nanocrystalline Ni samples were synthesized by pulse electrodeposition technique. Pulse electrodeposition is a bottom up approach in preparing nanocrystalline materials and is based on electro-chemical reactions. In contrast to conventional (DC) electroplating, the pulsed-current electrodeposition does not use constant electric current but (as the name suggests) the electric power is turned on and off periodically during the electrodeposition process. The electro-chemical deposition of nanostructured metals is

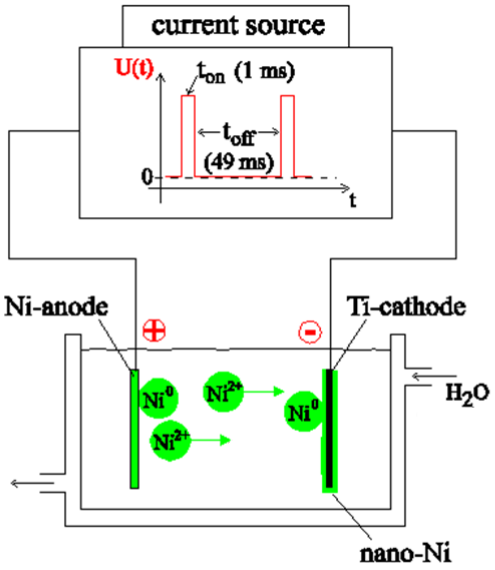

Figure 2.1: *Schematic diagram of pulse electrodeposition setup.*

possible if (i) a large number of grain nuclei is created on the electrode surface and (ii) if the growth of the nuclei and crystallites is impeded. The first requirement can be realized by the use of high current densities (1-2 A/cm^2). Such high currents and high voltages are not conceivable in direct current (DC) plating because of electrolyte decomposition and limitations in materials transport. In pulse electrodeposition, the peak current density is very high but a very short on-time (T_{ON}) of the order of milliseconds requires a voltage which is comparable to that used in DC plating. As a result of high current density, grain nucleation is favored over grain growth. Immediately after a strong current pulse, the electrolyte in the vicinity of the electrode is depleted of cations but materials supply occurs during the break between two pulses. A schematic diagram of the pulse electrodeposition [1,2] setup is shown in figure 2.1.

We have adopted similar pulse plating conditions as mentioned in Ref. [3] for electrodepositing nanocrystalline Ni samples with diffferent average crystallite sizes.

The electrodeposition was carried out using a Nickel sacrificial anode and an inert Titanium cathode. In order to ensure that the electrodeposition is done continuously at a constant rate, the concentration of the metal ion in the solution must be kept constant. $NiSO_4$ solution was used as electrolyte for nanocrystalline Ni deposition. Metal ions from the electrolyte solution are reduced and deposited as a metal onto the cathode. The electrolyte solution also contains Na-K tartarate (120 g/l), Boric acid (45 g/l), $NiCl_2$ (45 g/l) and Na saccharin (0.5-10 g/l) as grain growth refiners. As a result, surface mobility of deposited atoms on the cathode is greatly reduced and surface diffusion is minimized. The modulated currents were generated by a signal generator that contains a bipolar operation source combined with a galvanostatic unit in order to keep the current constant at a given value during the pulse. The bath temperature was kept constant at 340 K, during each electrodeposition. pH of the electrolyte bath was mainted at 2.0 using 7:1 ratio H_2SO_4:HC1 acid mixture. The current was applied in rectangular pulses with an on-time (T_{ON}) duration of 2.5 ms interrupted by time-periods (T_{OFF}) of 50 ms. Crystallite size of the deposit was manipulated by changing the saccharin content in the plating bath as (a) 0.0 g/l (for sample S_1), (b) 0.5 g/l (for sample S_2), (c) 2.5 g/l (for sample S_3), (d) 5 g/l (for sample S_4) and (e) 10 g/l (for sample S_5). It is observed that greater the saccharin content, smaller the average crystallite size. The resulting nanocrystalline deposits S_1, S_2, S_3, S_4, S_5 in the form of 300 μm thick sheets were mechanically removed from the cathode by a sharp knife. The nanocrystalline Ni samples, so synthesized, are ductile but the ductility is greatly reduced [3] compared to the bulk. The atomic density of the nanorystalline Ni samples, $\rho_{nc} \simeq 99.6(3)$ % of bulk density, ρ_B, regardless of the average crystallite size, d. 10 mm $\times$ 10 mm square pieces, circular discs with 3 mm diameter and rectangular stripes of 2.5 mm width and 10 mm length were spark-cut from the nanocrystalline sheets for characterization and physical property measurements.

2.2 Characterization

2.2.1 X-ray diffraction (XRD)

X-ray diffraction patterns of nanocrystalline Ni samples with different average crystallite sizes, were measured using Bruker D8 Discover diffractometer which uses x-rays of the Cu K_α line (with wavelength, $\lambda = 1.5406\ \mathring{A}$), produced by impinging an 40 mA electron beam on a Cu target. The x-ray detector could be moved through the scattering angle, 2θ, between 10 ° to 120 ° with a step of 0.02 ° at a counting time of 2 s per step using a software package.

Fig. 2.2 displays the x-ray diffraction (XRD) patterns taken on the pulse electrodeposited nanocrystalline Ni samples at room temperature. Fundamental Bragg reflections (111), (200), (220), (311) and (222), characteristic of the fcc structure, were observed in all the samples. To facilitate a direct comparison between the XRD data taken on samples of different crystallite size, the scattered x-ray intensity for each sample is normalized to its corresponding peak intensity of (111) Bragg reflection. The Rietveld refinement [4–6] of the XRD patterns, shown in figure 2.3, confirms that all the samples are single phase (with space group, Fm-3m, same as that in the bulk) by ruling out the presence of other phases such as NiO, Ni_2O_3, etc. Average size-strain (ASS) plots [7], based on the Rietveld refinement of the XRD patterns, were constructed using the Halder-Wagner (HW) approximation [8] and are shown in Fig. 2.4.

XRD peaks are broadened by small crystallite size and lattice distortion caused by lattice dislocations. However, effect of strain and imperfection on the line broadening differs from the effect of crystalline size. Assuming that total broadening of hkl planes (β_{hkl}) is the sum of size- (β_D) and strain-broadening (β_S), we will have

$$\beta_{hkl} = \beta_D + \beta_S = \frac{K\lambda}{D\ cos\theta} + 4\epsilon_{str}\ tan\theta \tag{2.1}$$

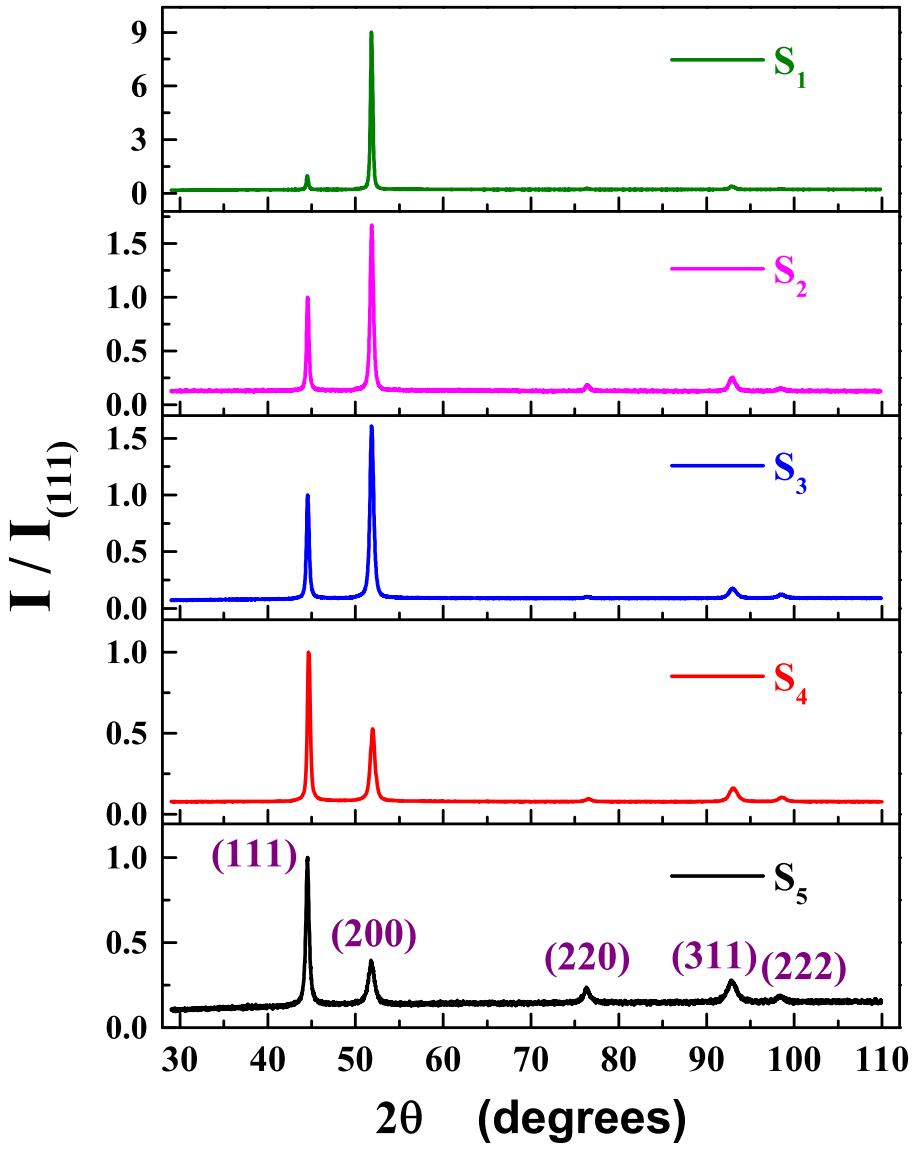

Figure 2.2: *Room temperature x-ray diffraction patterns for the nanocrystalline Ni samples S_1, S_2, S_3, S_4, S_5 with different average crystallite sizes (d). Note that the scattered x-ray intensity in each XRD pattern is normalized to the peak intensity of (111) Bragg reflection.*

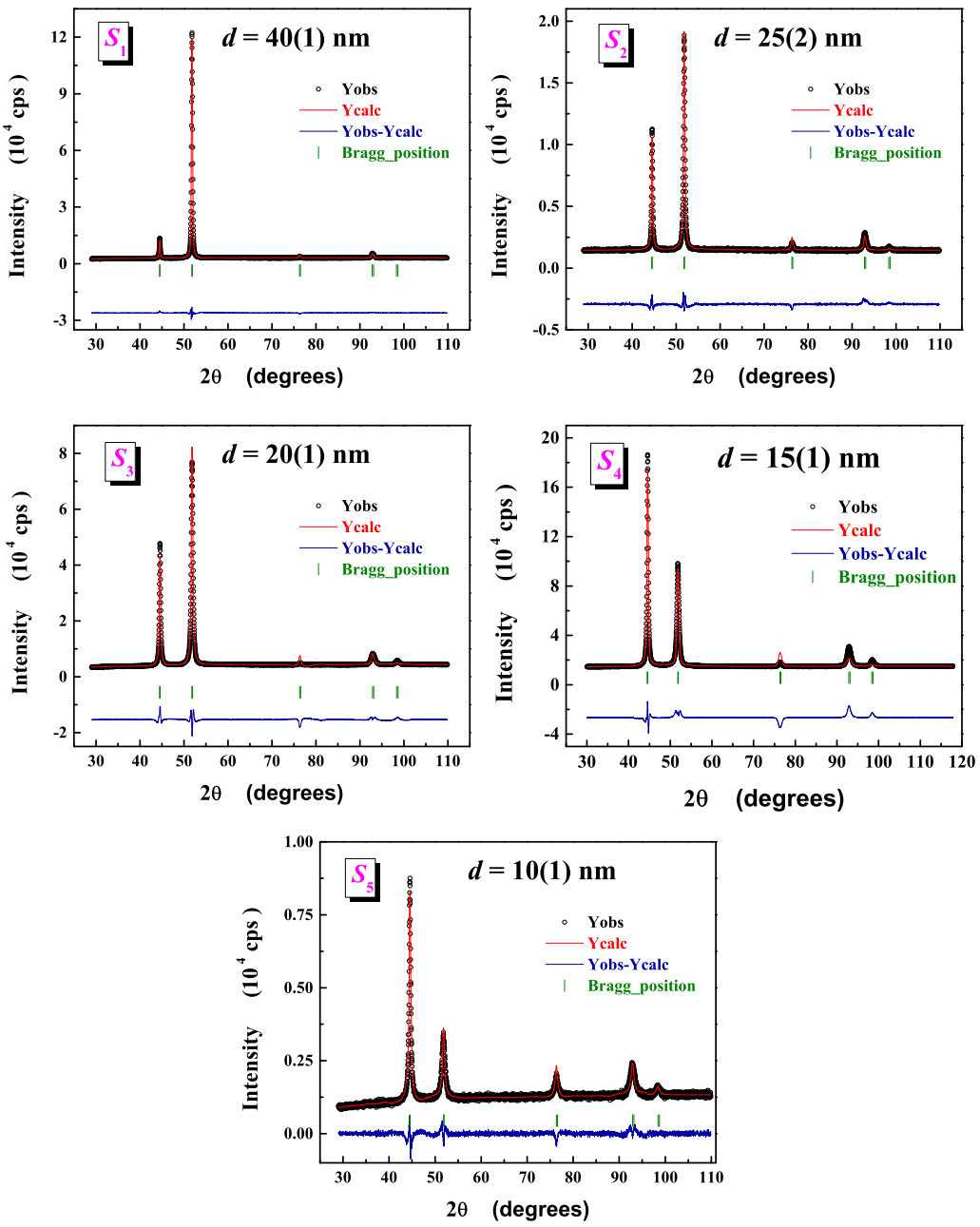

Figure 2.3: *Rietveld refinement for the XRD spectra for the nanocrystalline Ni samples $S_1(d = 40\ nm)$, $S_2(d = 25\ nm)$, $S_3(d = 20\ nm)$, $S_4(d = 15\ nm)$ and $S_5(d = 10\ nm)$.*

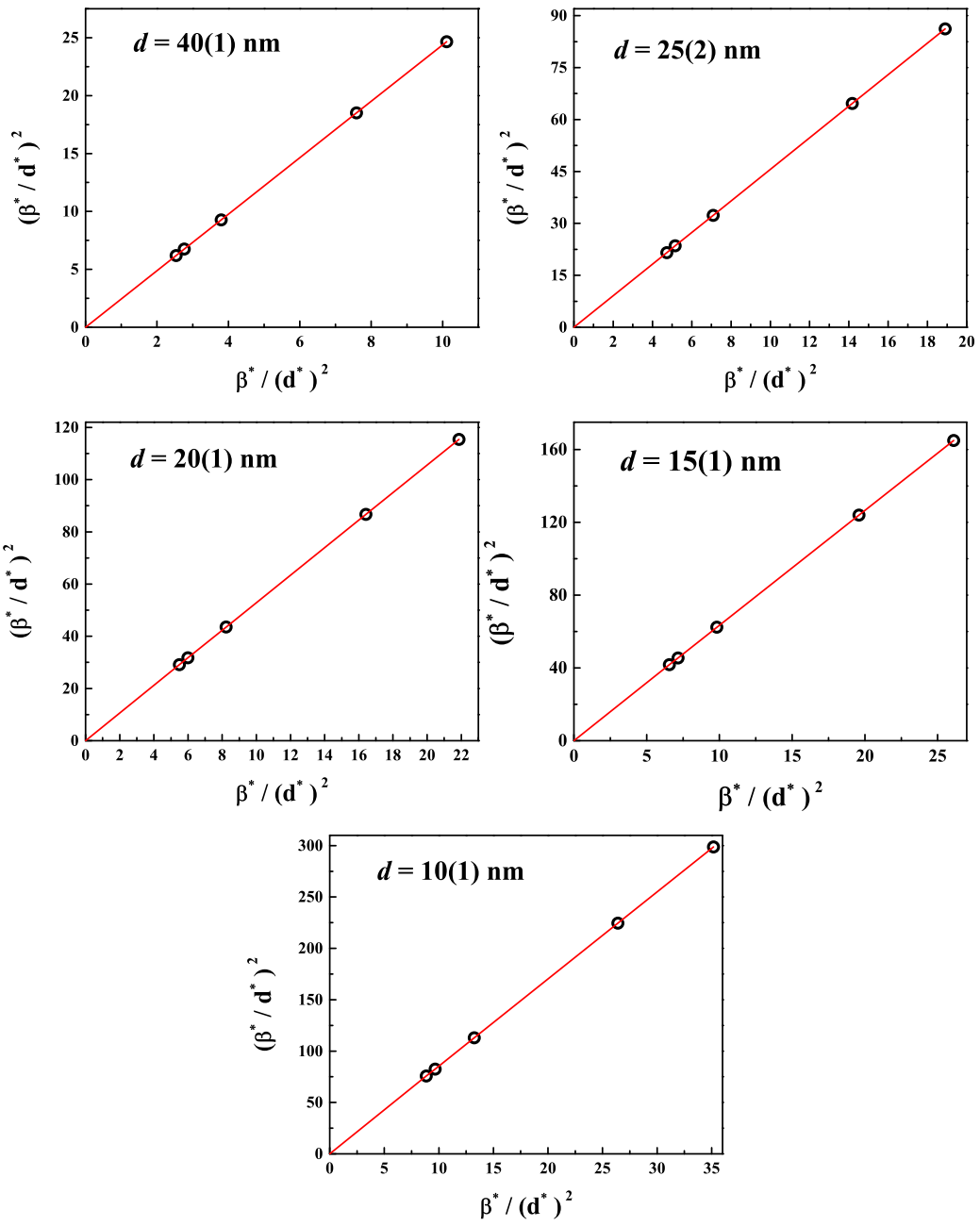

Figure 2.4: *Average size-strain Halder-Wagner plot for diffferent nanocrystalline Ni samples.*

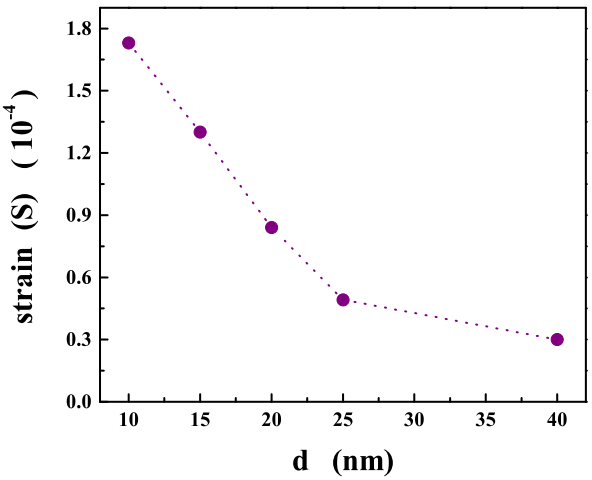

Figure 2.5: *Strain values obtained from Halder-Wagner plots as a function of average crystallite size in the nanocrystaalline Ni samples.*

By rewriting the above equation as

$$\beta_{hkl}\ cos\theta = \frac{K\lambda}{D} + 4\epsilon_{str} sin\theta \tag{2.2}$$

the term $\beta_{hkl}\ \ cos\theta$, when plotted vs 4 $sin\theta$ for each reflection gives a straight line. The crystallite size and strain can be determined from the slope and y-intercept of the straight line. Above equation considers the isotropic nature of crystal and assumes size and strain to be uniform in all crystallographic directions.

Halder-Wagner approximation considers the anisotropic nature (deviation from the spherical shape) of size broadening of different diffracting domains. The volume of the elongated crystallites is approximated by that of equivalent spheres and the volume-weighted mean crystallite size (d) is obtained using the log-normal distribution of the crystallite diameter (D_c). Halder and Wagner [8] have given an approximation to the integral breadth of a Voigt function as:

$$\beta_{hkl}^2 = \beta_L\ \beta_{hkl} + \beta_G^2 \tag{2.3}$$

where β_L and β_G are the Lorentzian and Gaussian components, respectively. In HalderWagner method, the crystallite size and strain profiles are described by the Lorentzian and Gaussian functions, respectively. Thus,

$$\left(\frac{\beta^*_{hkl}}{d^*_{hkl}}\right)^2 = \frac{1}{D}\left(\frac{\beta^*_{hkl}}{(d^*_{hkl})^2}\right) + \left(\frac{\varepsilon}{2}\right)^2 \tag{2.4}$$

where $\beta^*_{hkl} = \beta_{hkl}\ cos\theta/\lambda$ and $d^*_{hkl} = 2d_{hkl}\ sin\theta/\lambda$. From the linear fits to the $\left(\frac{\beta^*_{hkl}}{d^*_{hkl}}\right)^2$ Vs. $\left(\frac{\beta^*_{hkl}}{(d^*_{hkl})^2}\right)$ data, the average strain and the average crystallite size are obtained from the intercept on the ordinate and the slope of the fitted straight line, respectively.

The slope of the Halder-Wagner ASS plots, thus, yielded the volume-weighted average crystallite size [9] (in a direction normal to the reflecting parallel planes) d = 40 $\pm$ 1 nm for the sample S_1, 25 $\pm$ 1 nm for the sample S_2, 20 $\pm$ 1 nm for the sample S_3, 15 $\pm$ 2 nm for the sample S_4 and 10 $\pm$ 1 nm for the sample S_5. It is evident from Fig. 2.2 that Bragg peaks broaden upon reduction in average crystallite size, d, and a sizable (200) texture develops as d increases. The evolution of (200) texture with increasing d in PED nanocrystalline Ni has been reported [10] earlier. Rietveld refinement of the XRD data reveals that the lattice parameter retains its bulk value a = 3.526 $\pm$ 0.001 $\mathring{A}$ for samples of all d (within the uncertainty limits) while the strain, deduced from the Halder-Wagner ASS plots (intercept on the ordinate scale), increases from 3.0 $\times 10^{-5}$ for d = 40 nm to 1.7$\times 10^{-4}$ for d = 10 nm (see figure 2.5). Considerably enhanced strain at small crystallite size (d) can be understood in terms of increase in inter-crystallite volume fraction (grain boundaries and triple junctions) with decreasing grain size. The growth of (200) texture with increasing average crystallite size, d, could be an outcome of the strain relief process.

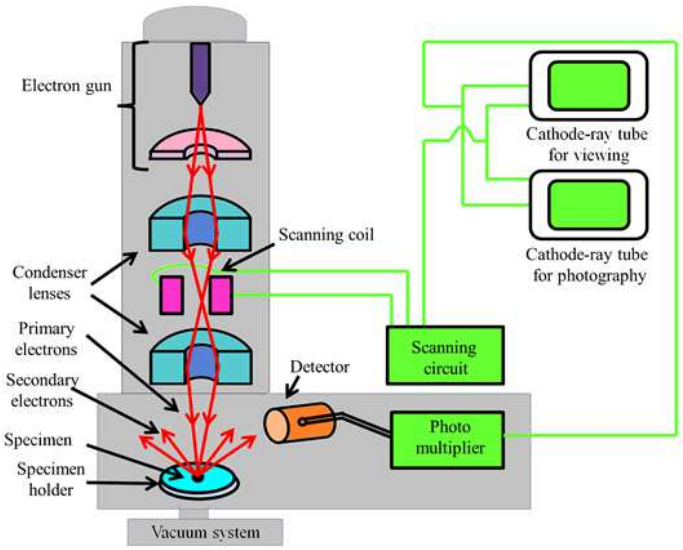

Figure 2.6: *Schematic diagram illustrating the working of a field emission scanning electron microscope.*

2.2.2 Field Emission Scanning Electron Microscopy (FE-SEM)

Zeiss Ultra-55 high-resolution field emission scanning electron microscope (FESEM) was used to investigate the morphology and microstructure of the nanocrystalline samples synthesized by pulse electrodeposition. Electrons are liberated by a filament (single crystal tungsten acts as a field emission source) by applying a huge electrical potential gradient ($\sim 10^7$ V/cm) and accelerated in a high electrical field gradient. Within the high vacuum column these primary electrons are focused and deflected by magnetic lenses to produce a narrow scan beam that bombards the object/specimen. As a result, secondary electrons are emitted from each spot on the object. The angle and velocity of these secondary electrons relates to the surface structure of the object. A detector catches the secondary electrons and produces an electronic signal. This signal is amplified and transformed to a digital image that can be seen on a monitor and can be saved for further processing. A schematic picture describing the working

of a FESEM is shown in Fig. 2.6.

The field-emission scanning electron microscope (FESEM) images are obtained at a working distance of typically 3 mm, using an accelerating voltage of 3-5 kV, and at a very high magnification. Such FESEM images for the nanocrystalline Ni samples of different d are shown in Fig. 2.7. These images show largely the agglomerates and/or assemblies of nanoparticles but not well-separated individual nanoparticles because the samples have nearly the same atomic density as that in the bulk.

2.3 Physical Property Measurement

2.3.1 Magnetic Property Measurement System SQUID VSM

Magnetic Property Measurement System with Vibrating Sample Magnetometer (MPMS-VSM) using Super Conducting Quantum Interference Device (SQUID)- is a SQUID magnetometer, based on the 2ω detection, that combines the SQUID and VSM. It can measure dc and ac magnetic moment (down to $\sim 10^{-9}$ emu) in the temperature range 1.8 K to 400 K with a maximum temperature sweep rate of 50 K/min and fields up to $\pm$ 70 kOe with a maximum field ramp rate of 700 Oe/sec [11].

The MPMS SQUID VSM uses a superconducting magnet (a solenoid of superconducting wire) to subject samples to magnetic fields up to 7 Tesla (70 kOe). The SQUID and magnet must both be cooled to liquid helium temperatures. Liquid helium is also used to cool the sample chamber, providing temperature control of samples from 400 K down to 1.8 K. To minimize liquid helium consumption, the system is designed to use less-costly liquid nitrogen to precool the helium tank and thereby arrest the heat flow to the helium tank. The SQUID VSM operates properly only when both the cryogens, liquid helium and liquid nitrogen, are used. The

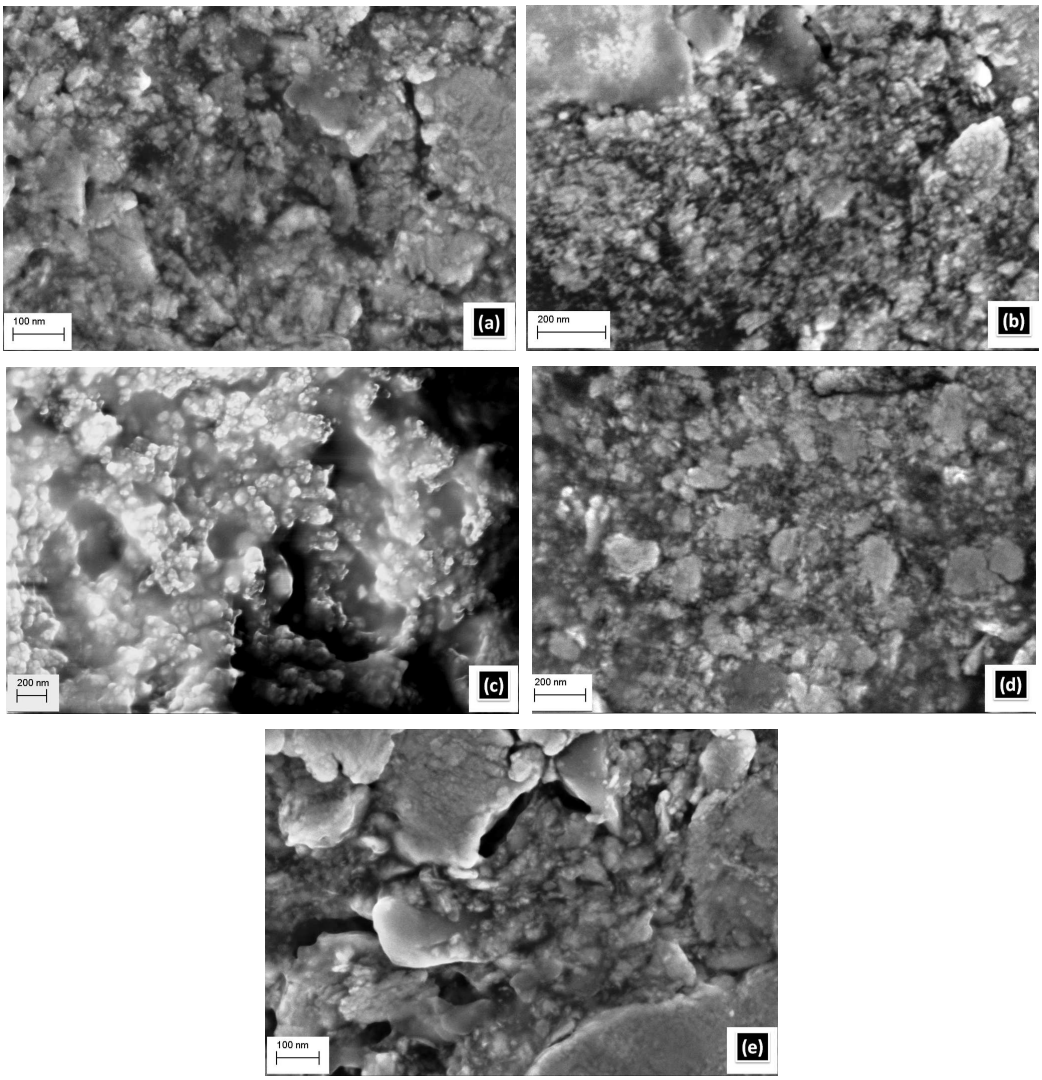

Figure 2.7: *FESEM Images for the nc-Ni samples with (a) d = 10 nm, (b) d = 15 nm, (c) d = 20 nm, (d) d = 25 nm, (e) d = 40 nm.*

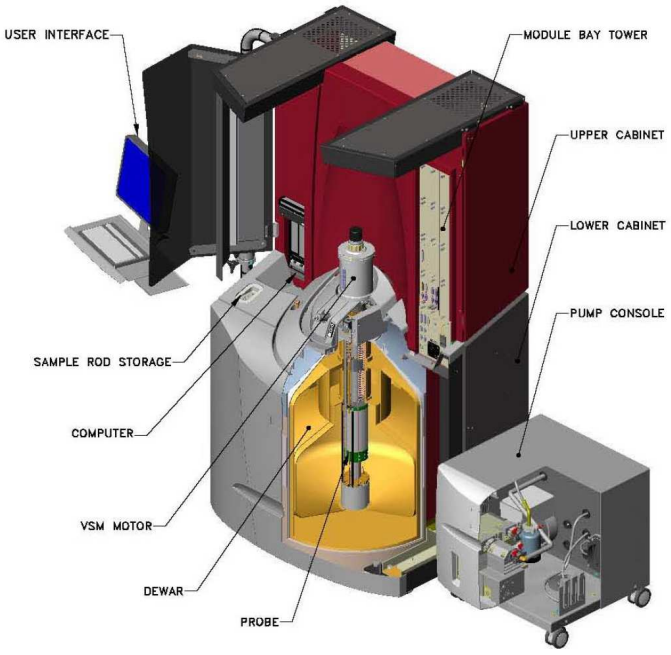

Figure 2.8: *System setup for Magnetic Property Measurement System - Vibrating Sample Magnetometer (MPMS-VSM) with Superconducting Quantum Interference Device (SQUID).*

SQUID VSM hardware is primarily contained in a two-part metal cabinet (see figure 2.8). The upper half of the cabinet contains a computer running the MultiVu software and the instruments modular electronics. The lower half of the cabinet contains a cryostat: liquid helium and liquid nitrogen tanks and a cryogenic insert that hangs into the helium tank. The VSM head, or motor, is mounted on top of the cryogenic insert. The lower end of the insert contains the shielded SQUID, superconducting magnet, and associated hardware. The cryostat is mounted on vibration isolation springs and magnetically shielded to confine magnetic fields greater than 5 Gauss to the interior of the cabinet.

Superconducting Quantum Interference Device (SQUID) is an extremely sensitive flux-to-voltage transducer that converts a change in magnetic flux to change

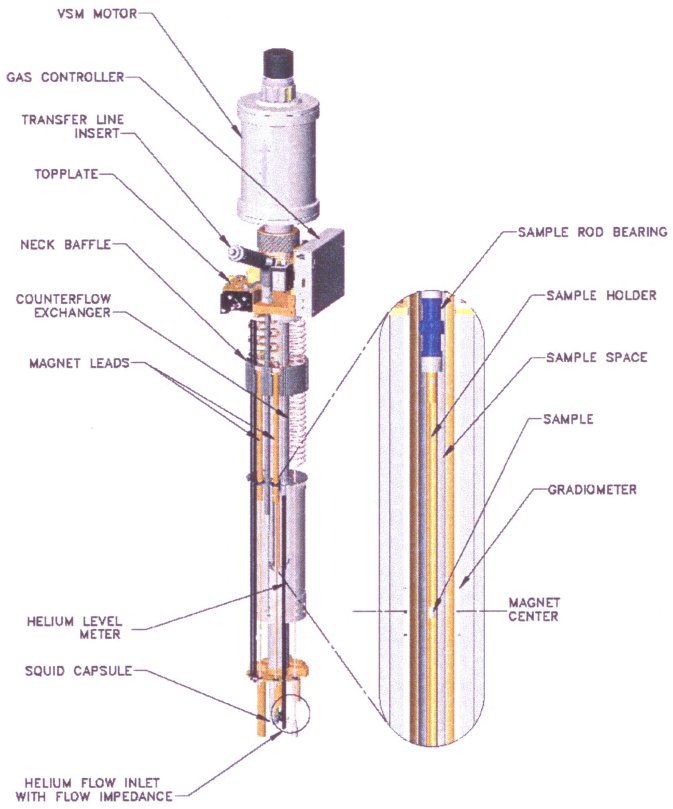

Figure 2.9: *VSM head, sample rod assembly and magnet for MPMS VSM SQUID.*

in voltage, which is readily detectable with conventional electronics. It is a device which makes use of flux quantization and Josephson tunneling and can operate at temperatures as low as few Kelvin. The sensitivity of a Josephson junction to applied magnetic field increases with the area of the junction, which justifies making the devices large so that the control currents can be reduced to a minimum. The switching speed of the junction, however, decreases as the area increases. In recent devices, the conflicting demands of speed and sensitivity are met by replacing a single junction with two or more junctions connected by a continuous superconducting loop. Such a multi-junction device is called a Josephson interferometer or a Superconducting Quantum Interference Device (SQUID). In the case of two Josephson

junctions connected in parallel, as the magnetic flux Φ threading a superconducting loop is changed, the critical current of two junctions oscillates with a period equal to the flux quantum Φ_0. These oscillations arise due to the interference of macroscopic wave functions at two junctions. This phenomenon of superconductiing quantum interference forms the basis of a SQUID.

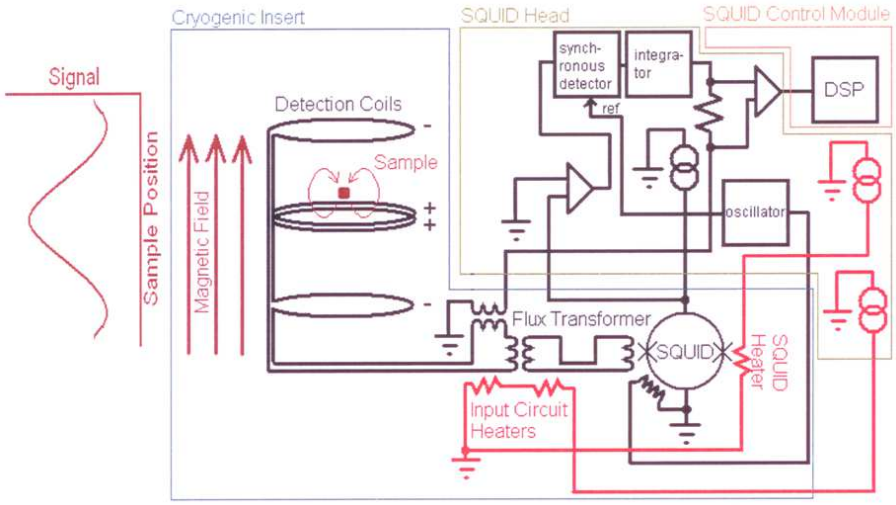

Figure 2.10: *SQUID detection system in a simplified diagram.*

The superconducting detection coils are configured as a second-order gradiomater, with counterwound outer loops which make the set of coils non-responsive to uniform magnetic fields and linear magnetic field gradients. The detection coils only generate a current in response to local magnetic field disturbances. The current in the detection coils is a function of sample position (see Fig. 2.10) and it is inductively coupled to the instrument's SQUID. The SQUID feedback nulls the current in the detection coils and this nulling current yields the actual SQUID voltage for analysis. The sample is set to vibrate at a frequency, ω, about the center of the detection coils, where the signal peaks as a function of sample position, z. $V(z) = Az^2$ for small vibration amplitude, B and $z(t) = Bsin(\omega t)$, it generates a SQUID signal, V, as a

function of time, t

$$V(t) = AB^2 sin^2(\omega t)$$

$$= \frac{AB^2}{2}(1 - cos(2\omega t)) \tag{2.5}$$

where 'A' is a scaling factor related to the magnetic moment of the sample. The lock-in technique is used to isolate and quantify the signal occurring at frequency 2ω, which is caused extensively by the sample. Briefly, this is achieved by multiplying the measured signal with a phase corrected reference signal at 2ω and then extracting the DC component, which is proportional to the 2ω component of the measured signal. This technique quickly and precisely isolates the sample signal from other noise sources, including drifting SQUID signal and mechanical noise sources synchronized to the sample. To locate the sample position in the detection coil, sample signal for various vertical sample positions are obtained and compared with the response of a point dipole in a uniform magnetic field.

The VSM head or motor, is a long-throw linear motor mounted on springs within its casing for vibration isolation. The VSM head receives a DC signal that controls the sample position and an AC signal that determines the vibration amplitude and frequency from the motor control module. A precision optical encoder in the VSM head reads the position of the motor armature to within 0.01 mm. This signal is fed to the motor control module and used in a feed back loop to obtain precise sample positioning and vibration. The default vibration frequency is 14 Hz and amplitude is 2 mm. This can be varied, within the prescribed limit, to get better accuracy depending on the sample magnetic moment and weight. Samples were mounted securely on quartz sample holder (to attain highest instrument sensitivity and accuracy). The sample holder was then connected to sample rod of nearly 140 cm and inserted into the sample chamber. Whenever a sample was installed in the sample chamber, it was centered within the detection coils for accurate magnetic

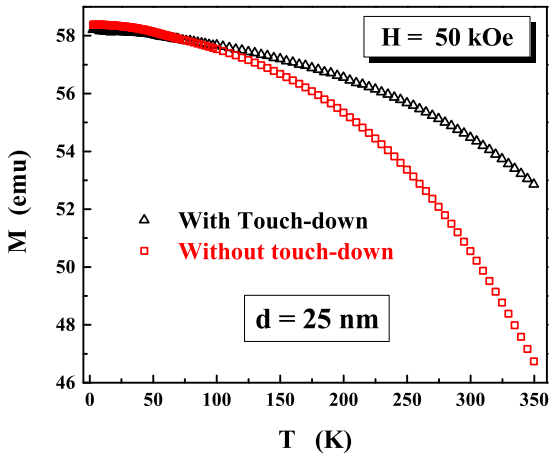

Figure 2.11: *Comparison of the thermal demagnetization data taken with and without touch-down operation.*

measurements. The mounting is such that, the samples plane is parallel to the applied magnetic field and hence demagnetization effects are negligible. Magnetization (M) as a function of temperature (T) was measured on pulse electrodeposited (PED) nanocrystalline Ni samples with average crystallite size, d, varying from 10 nm to 40 nm, at fixed applied static magnetic fields (H) ranging from 10 kOe to 70 kOe over the temperature range 2 K $\leq T \leq$ 124 K at 1 K intervals, 125 K $\leq T \leq$ 150 K at 2 K steps and 155 K $\leq T \leq$ 350 K at 5 K intervals. To eliminate errors in the reported magnetic moment in the temperature dependent magnetization measurements, arising from the relative length changes in the VSM sample rod length with respect to the SQUID sample chamber over different ranges of temperature, 'touch-down' operation of sample rod was performed. During each touch-down operation, the sample is re-centered with respect to the pick-up coils. Fig. 2.11 gives a comparison between the measurements taken with and without 'touch-down' at a constant magnetic field of 50 kOe on the nanocrystalline Ni sample with d = 25 nm. This comparison clearly demonstrates that the thermal demagnetization rate

is overestimated if the 'touch-down' method is not used. This artifact leads to erroneous results. Note that when magnetization is measured without 'touch-down', a constantly changing sample position in the heating or cooling cycle leads to an apparently large thermal variation in magnetization.

2.3.2 Physical Property Measurement System (PPMS)

The Physical Property Measurement System (PPMS) [12] provides a flexible, automated workstation that can perform a variety of experiments requiring precise thermal control. PPMS can be used to perform magnetic, electrical- or magneto-transport, specific heat or thermo-electric power measurements, or can be modified to perform the user-select experiment. The unique open architecture of the PPMS allows to fully configure the basic PPMS platform or to use the PPMS with different measurements options, such as AC susceptibility, DC magnetization, heat capacity, resistivity or ultra-low field. The PPMS has extremely good temperature control over the entire range of 1.8 K $\leq T \leq$ 350 K. This system possesses a superconducting magnet which can generate fields up to $\pm$ 90 kOe, with a high field-homogeneity (0.01%) within the measuring region. The software also provides options for sweeping the magnetic field in several modes, the most important of which are *linear* and *no-overshoot*. In the linear mode, the field is ramped linearly to the set-point, while in the *no-overshoot* mode, the field is quickly ramped to $\sim$ 70 % of the desired value, then slowly increased to avoid overshooting the set-point. The PPMS platform can apply a constant field during both AC and DC measurements.

2.3.2.1 VSM option

VSM option for PPMS is a fast and sensitive DC magnetometer consisting of a VSM linear motor transport head (same as that used in the MPMS VSM SQUID, except

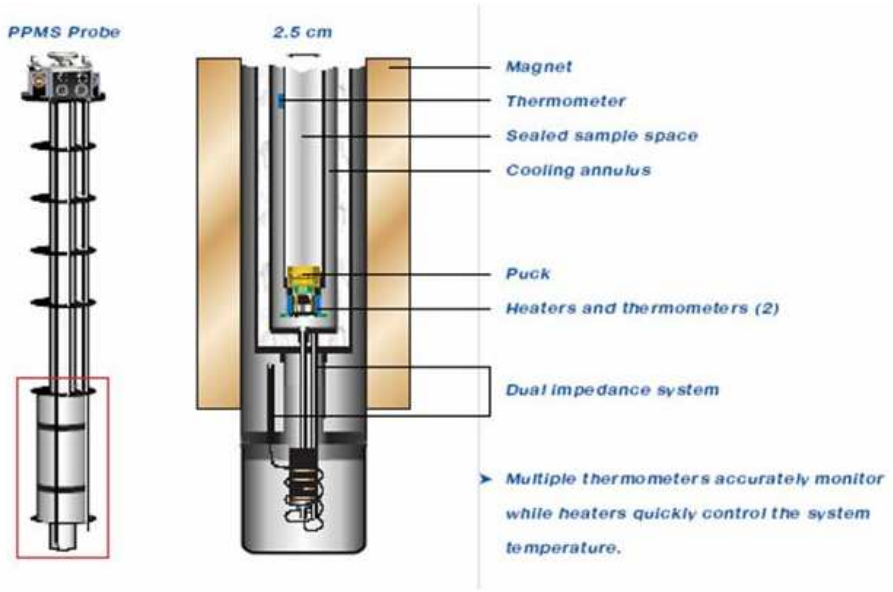

Figure 2.12: *Sample rod assemble for Physical Property Measurement System.*

for the working amplitude and frequency of oscillation). To locate the sample and for vibrating it, a compact gradiometer pickup coil for detection and the electronics for driving the linear motor transport and detecting the response from the pick up coils are used. With relatively large oscillation amplitude (1-3 mm peak) and a frequency of 40 Hz, the system can resolve magnetization changes of less than 10^{-6} emu at a data sampling rate of 1 Hz. When the sample is set to vibrate sinusoidally, the changing magnetic flux induces a time-dependent voltage in the pickup coil,

$$V_{coil} = \frac{d\Phi}{dt} = \left(\frac{d\Phi}{dz}\right)\left(\frac{dz}{dt}\right)$$

$$= 2\pi f C m A \; sin(2\pi f t) \tag{2.6}$$

where Φ is the flux enclosed by the pickup coil, z is the vertical position of the sample with respect to the coil, t is time, C is the coupling constant, m is the

DC magnetic moment of the sample, A is the amplitude and f is the frequency of oscillation. The response from the pickup coil is calibrated with a standard sample. After obtaining the signal profile in the pickup coil, the system identifies the sample position with respect to the pickup coil and locates the sample at the center of the coil after the touch-down process. If the measurement is a temperature dependent one, the sample position may change due to the thermal expansion/contraction of the sample rod. Hence the sample position in the pickup coil has to be monitored by touching the sample rod down and relocate it to the actual position, if it has changed.

Using the VSM option for PPMS system, magnetization (M) versus magnetic field (H) isotherms in fields up to $H = 90$ kOe were recorded in the temperature range 2 K $\leq T \leq$ 300 K.

2.3.2.2 Resistivity option

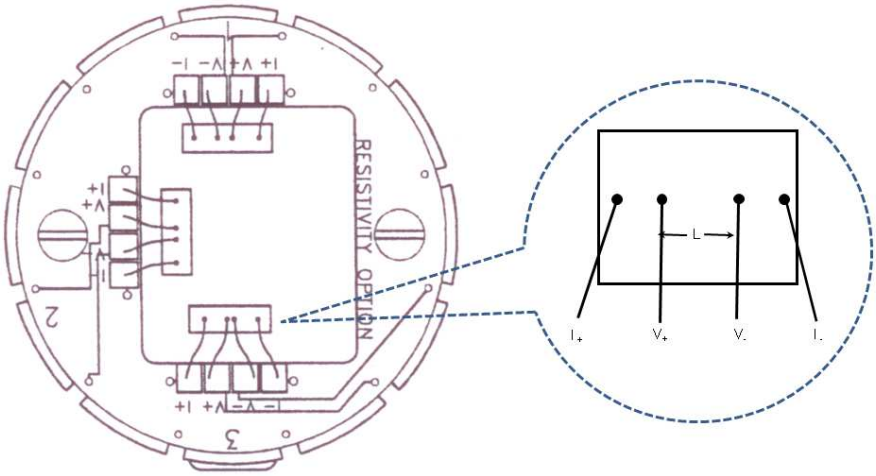

Figure 2.13: *The resistivity sample puck with three samples mounted for four-wire resistance measurements.*

Resistivity option is a configurable resistance bridge board. It can simultaneously

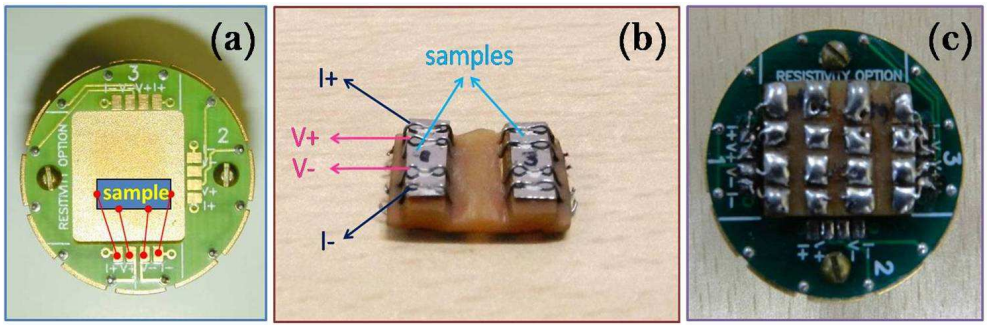

Figure 2.14: *(a) Example of fourwire resistance measurement with sample mounted on standard PPMS sample puck supplied by Quantum Design. (b) Four-probe pressure contacts to the samples. (c) Copper PCB along with the four-probe connections fixed and connected to the resistivity sample puck.*

measure electrical resistance/resistivity of 3 samples using four probe method with current reversal option. A resistivity puck with three samples mounted for four probe measurement is shown in figure 2.13. The user bridge board automatically adjusts the excitation current of its active channels, but the maximum allowable current, power and voltage can be specified. The current, power and voltage limits are ± 0.01-5 mA, 0.001-1 mW and 1-95 mV, respectively. The nominal resolution in the most sensitive range is 3.8 nV/5 mA=0.76 $\mu\Omega$.

Rectangular strips of dimensions 10 × 2.5 × 0.3 mm^3 were spark-cut from the pulse electrodeposited nanocrystalline Ni sheets with different average crystallite sizes ranging from 10 nm to 40 nm. Electrical resistivity, $\rho(T)$ and transverse magnetoresistance (MR(T, H)) measurements were performed on the Quantum Design make Physical Property Measurement System using standard four-probe method. 32/34 SWG copper wire was used as current/ voltage leads. Very tiny drops of silver paste were sandwiched between the pressure-contacts and the sample to improve the electrical contact with the samples. The four-probe arrangement was made using a rectangular sample holder made of 1 mm thick single side Copper clad PCB. The sample holder was fixed to the resistivity-puck provided by Quantum Design and

compatible with PPMS transport option (see figure 2.14). To ensure a good thermal contact of the sample with the thermometers, a thin layer of Apiezon-N grease was applied to the resistivity-puck platform before mounting the sample on the puck. Since the puck platform is a conducting base, to prevent short circuit, a thin mica sheet for complete electrical insulation and good thermal conduction is sandwiched between the sample with measuring leads and transport-puck platform. Typically, a dc current of 5 mA in the AC drive mode was used to measure the voltage drop across the sample. In the AC mode, the user bridge board applies a DC excitation to the sample and reads the potential drop across the sample. Then the user bridge board reverses the current and reads the potential drop again. The final voltage reading is the mean of the absolute values of the positive and negative voltage readings. The AC excitation, which is a square-wave excitation, is synchronized to the AC line frequency of 50 Hz in order to reject AC line noise. Operation in AC mode eliminates errors from DC offset voltages and produces the most accurate readings.

Electrical resistivity, ρ, was measured as a function of temperature at 1 K intervals in the range 2 K $\leq T \leq$ 50 K and at 2 K intervals in the range 50 K $\leq T \leq$ 300 K in 'zero-field' and at various fixed external magnetic fields (H) up to 90 kOe, with the direction of H perpendicular to the sample plane and the electrical current along the length in the sample plane (Transverse magnetoresistance) on the nanocrystalline Ni samples under investigation. Magnetoresistance (MR) was measured as a function of external magnetic field from $H = 0$ to $H = 90$ kOe in 10 kOe intervals at fixed temperatures covering the range 1.8 K - 300 K.

2.3.3 Ferromagnetic Resonance (FMR)

2.3.3.1 FMR experimental set-up

To record the FMR spectra for a given sample, a commercial JEOL - FA200 Electron Spin Resonance (ESR) spectrometer, which operates in the X-band of the microwave frequencies, has been used. The block diagram of the spectrometer is given in Fig. 2.15. Besides the electromagnet, the instrument is equipped with a pair of secondary coils and a sweep generator to give a wide field scan. The coils are usually required to supply an *oscillating* magnetic field of maximum amplitude 5 kOe and frequency of 110 kHz. The arrangement serves two main purposes. First, it provides a modulator or chopper frequency to which the detector amplifier system may be tuned in order to improve the signal-to-noise ratio. Second, use of this arrangement allows the spectrum to be displayed in the derivative mode, which, in turn, facilitates accurate determination of the linewidth and resonance center.

A cavity resonator [13] is placed between the pole pieces of an electromagnet, which produces a steady and uniform magnetic field. This field can be swept by sweep generator at a constant rate and is modulated at 110 kHz. The instrument also consists of the microwave unit, Automatic Frequency Control (AFC) circuit, preamplifier, and gunn oscillator power supply which are all housed in a single unit. A klystron tube, which is tunable over a narrow range with frequency stabilization system is used to generate the microwave radiation which passes as a linearly polarised beam through a wave guide. After traversing through a ferrite isolator, which prevents back reflections, the beam is divided at a magnetic tee or hybrid tee. One part of which is fed into a phase shifter and another part into the cavity resonator through a circulator. The sample in a cavity is subjected to the microwave field applied perpendicular to the applied field. At resonance, the sample absorbs energy from microwave field, which results in the change of Q-value of the cavity resonator.

This Q-value variation is detected, amplified and recorded when the magnetic field is varied while the microwave frequency is kept constant. An absorption signal having a discernible width is observed. In addition, if an ac magnetic field having the same direction as H and with an amplitude smaller than the absorption signal width is applied to magnetic field H, and when the field is varied, the detected output at each point on the absorption signal will form a sinusoidal wave having the same period as alternating field and an amplitude in proportion to the gradient of the absorption line.

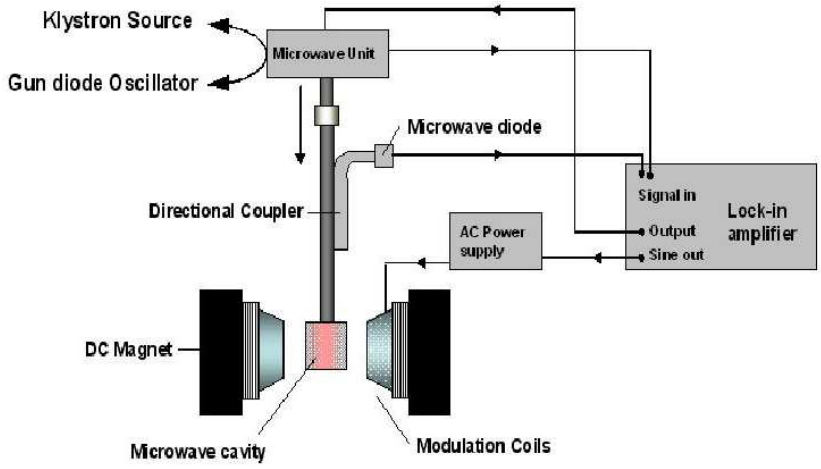

Figure 2.15: *Block diagram of the Electron Spin Resonance spectrometer*

A selective amplifier amplifies this sinusoidal wave and the phase is detected throughout the absorption signal width. The amplifier employs a narrow bandwidth which reduces noise and therefore facilitates the observation and recording of extremely weak absorption signals. Since the crystal noise output is inversely proportional to modulation frequency, the application of a high frequency magnetic field modulation enables high-precision electron spin resonance measurements to be carried out. At resonance, the imbalance of the bridge occurs and the reflected microwave energy from the cavity and the reference wave, whose phase is adjusted, are

fed into the 4th arm of the direction coupler. The balancing of bridge is achieved by making the reference wave equal in amplitude and opposite in phase, to the reflected wave from the cavity.

2.3.3.2 Sample mounting and procedure for recording FMR signals

An appropriate sample mounting technique [14], which ensures high reproducibility in the data by getting rid of specious stress-induced effects, was used for measurements. The sample (a circular disc of diameter 3 mm and thickness 0.3 mm) was mounted on the flat surface and sandwiched with a small flat quartz piece on top and fixed with nonmagnetic tape. The quartz rod was then inserted into the cavity. The cavity is provided with a goniometer arrangement which enables rotation of the sample plane at specific angles with respect to the external field during the angular measurement of resonance field. Ferromagnetic resonance measurements were performed at the operating frequency 9.23 GHz of the spectrometer. The FMR measurements consist of recording the microwave power absorption derivative with respect to the static field H, i.e., $dP_{\parallel}/dH$ versus H curves, were recorded on disk-shaped (3 mm in diameter) nanocrystalline Ni samples with different average crystallite sizes, 'd' = 10(1) nm, 15(1) nm, 20(1) nm, 25(2) nm and 40(1) nm, at fixed microwave field frequency of 9.23 GHz and fixed temperatures in the range 110 K $\lesssim T \lesssim$ 325 K in the parallel ($\parallel$) sample configuration (i.e., when the applied static field lies within the sample plane). The angular variation of FMR spectra in the 'in-plane' (dP_{IP}/dH versus H) and 'out-of-plane' (dP_{OP}/dH versus H) configurations, at a few selected temperatures in the range 127 K $\leq T \leq$ 321 K, were also recorded as a function of the angle 'Ψ' or 'α'. The angles 'Ψ' and 'α' subtended by the static magnetic field in the 'in-plane', IP, and 'out-of-plane', OP, sample configurations are defined as shown in figure 2.17.

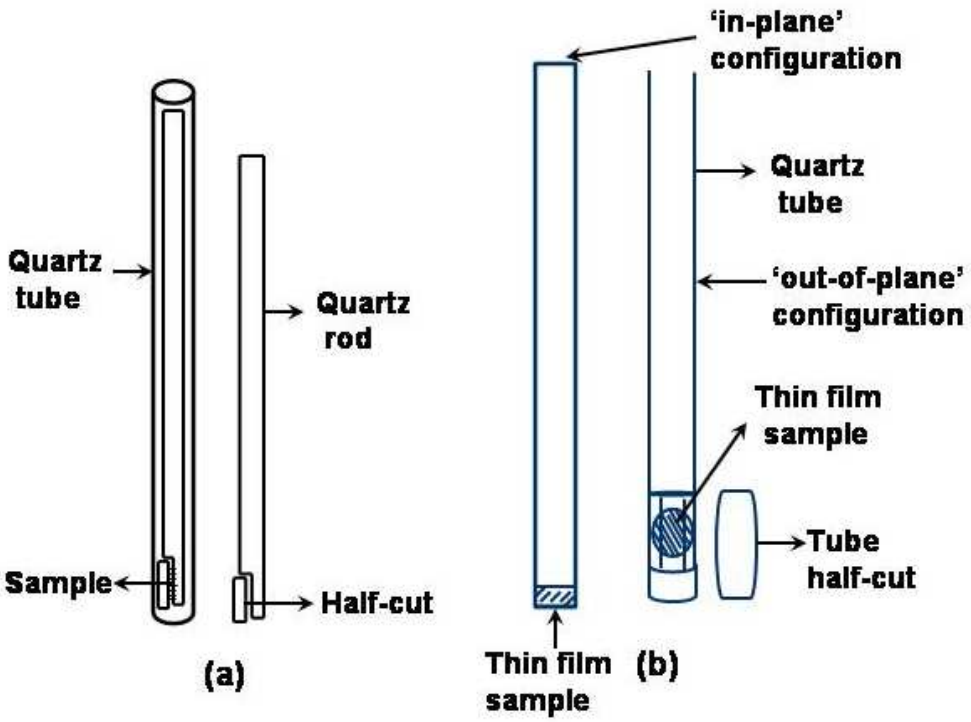

Figure 2.16: *Sample mounting with Quartz tube and quartz rod combination (a) for Metallic ribbons (b) for Thin film samples / bulk samples (disk shaped).*

2.3.3.3 Advantage of ferromagnetic resonance

The g factor, damping parameter and anisotropy constants can be accurately determined by using the ferromagnetic resonance technique.

2.3.3.4 Experimental Accuracy and Sources of Error

Sample mounting plays an important role in the measurement of ferromagnetic resonance. Incorrect sample mounting leads to errors in the FMR data. The magnetic properties of the sample, which are very sensitive to stress, may be affected by certain types of mounting, so much so that they yield distorted lineshapes and irreproducible results. Slight misorientation of the sample from the required sample geometry pro-

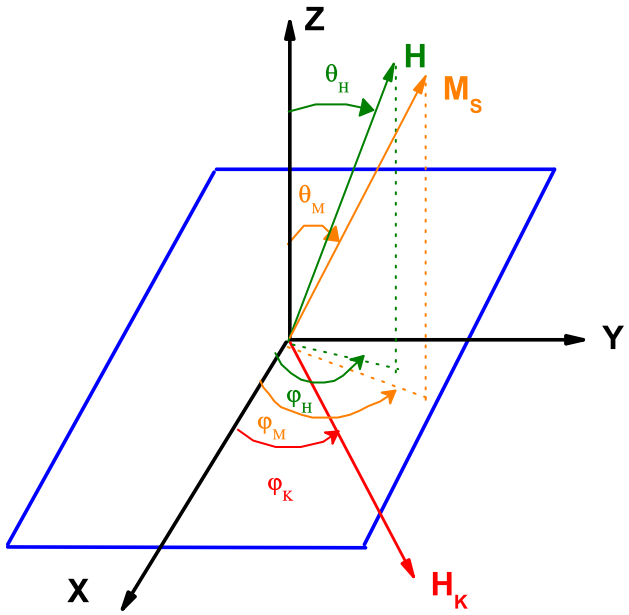

Figure 2.17: *The coordinate system used for specifying the orientations of magnetic field and magnetization in the 'in-plane'(IP) and 'out-of-plane'(OP) sample configurations.*

duces tremendous changes in the values of linewidth and resonance, etc. To minimize or to completely eliminate these errors, the samples should be mounted in a stress-free manner and in the correct orientation for reproducible results. The sample and sample rod should be thoroughly cleaned with '*ethanol*' before mounting to eliminate the contamination effects, if any, on the FMR results.

Resolution in the measurements of the external field is an important factor in measuring power absorption derivative spectra accurately since the resolution of the field is 0.01 Oe when the sweep width is high, the upper bound on the error in the measurement of the resonance field is given by above resolution limit and the error in the peak-to-peak line width measured is twice this value.

References

1. A. M El-Sheric and U. Erb, *J. Mater. Sci.*, **30**, 5743-5749 (1995).
2. H. Natter, M. Schmelzer, and R. Hempelmanna, *J. Mater. Res.*, **13** 1186-1197 (1997).
3. U. Erb, *Nanostr. Mater* **6**, 533 (1995) and references cited therein.
4. H.M. Rietveld, *Line Profiles of Neutron Powder-diffraction Peaks for Structure Refinement*, Acta Cryst., **22**, 151 (1967).
5. H.M. Rietveld, *A Profile Refinement Method for Nuclear and Magnetic Structures*, J. Appl. Cryst., **2**, 65 (1969).
6. R.A. Young, *The Rietveld Method*; Oxford University Press: Oxford, 1995.
7. L. Motevalizadeh, Z. Heidary and M. Ebrahimizadeh Abrishami, *Bull. Mater. Sci.,* **37**, 397 (2014).
8. N. C. Halder and C. N. J. Wagner, *Acta Cryst.* **20**, 312 (1966).
9. C. E. Krill and R. Birringer, *Phil. Mag. A* **77**, 621 (1998).
10. B. Szpunar, U. Erb and G. Palumbo, *Phys. Rev. B* **53**, 5547 (1996).
11. Magnetic Property Measurements System (MPMS), SQUID VSM User's Manual, Thirteenth ed., Quantum Design, San Diego, CA, USA, **1500-100, E0**, (2010).
12. Physical Property Measurements System (PPMS), User's Manual, Quantum Design, San Diego, CA, USA, **1084-100A**, (2009).
13. C. P. Poole Jr., Electron Spin Resonance, second ed. John Wiley & Sons, Inc. (1983).

14. S. N. Kaul and T. V. S. M. Mohan Babu , *J. Phys.: Cond. Matter.* **1**, 8509 (1989).

Chapter 3

Irreversibility in Magnetization and Magnetic Anisotropy

This chapter discusses the magnetization processes that come into play when external magnetic fields (H) up to 90 kOe are applied at fixed temperatures (T) in the range 2 K - 300 K and temperature evolution of magnetization at low magnetic fields in the range 10 Oe $\leq H \leq$ 5 kOe. By making use of the micromagnetic theory for the 'approach-to-saturation' in magnetization, the effective magnetic anisotropy (MA) constant (MA energy density), K_{eff}, as a function of temperature in the range 2 K $\leq T \leq$ 300 K, is deduced from the magnetization versus magnetic field isotherms ($M_T(H)$) taken on nanocrystalline Ni samples with average crystallite size, d, ranging from 10 nm to 40 nm. For a fixed d and at any given temperature, the contributions to $K_{eff}(T)$ arising from the volume (core) magnetocrystalline anisotropy, $K_1^c(T)$, the surface/interface anisotropy, $K_s(T)$, and shape anisotropy, $K_{shape}(T)$, are assumed to be additive. The result that a linear relationship exists between '$K_{eff} \times d$' and 'd' not only validates this assumption in the present case but also permits an accurate

This chapter is based on the following articles:
1. P. V. Prakash Madduri and S. N. Kaul, *J. Alloys. Compd.*, **689**, 533 (2016).
2. P. V. Prakash Madduri, S. Srinath, S. N. Kaul, *AIP Conf. Proc.*, **1665**, 130049 (2015).
3. P. V. Prakash Madduri and S. N. Kaul, *AIP Conf. Proc.*, **1536**, 89 (2013).

determination of $K_1^c(T)$, $K_s(T)$ and $K_{shape}(T)$. Thermal activation over an effective anisotropy energy barrier (which separates two local energy minima and depends on both temperature and magnetic field), as the mechanism for magnetization reversal, is shown to account for the observed temperature dependence of the coercive field. Another important finding is that the magnetic moment per Ni atom, μ_{Ni}, deduced from the saturation magnetization at 2 K, increases with d in accordance with the relation $\mu_{Ni}(d) = \mu_{Ni}(d = \infty)$ [1 - $b \times d^{-3/2}$], with the magnetic moment per Ni atom in the bulk at $T = 2$ K, $\mu_{Ni}(d = \infty) = 0.616\ \mu_B$, and $b = 0.50(5)$. Magnetization as a function of temperature ($M_H(T)$) at static applied magnetic fields (H) in the range 0 kOe $\leq H \leq$ 5 kOe, measured in 'zero-field-cooled' and 'field-cooled' modes, reveals irrevesibility in magnetization below a characteristic field (H_S = Switching field) in nanocrystalline Ni. This irreversibility is explained in terms of the trapping of sizable fraction of magnetization in the metastable states below the switching field. These metastable states are separated in energy from the stable states by the energy barriers caused by effective anisotropy that is a resultant of intragrain crystalline and inter-grain interfacial and/or surface anisotropies.

3.1 Introduction

Ever-growing scientific interest in the study of magnetic nanomaterials has been fueled by their novel and diverse magnetic properties that make them well-suited for many exotic applications. There are basically two categories of nanomaterials: (I) free-standing nanoparticles with passivated surfaces or nanoparticles dispersed/embedded in different non-magnetic media, and (II) single- or multi-phase polycrystalline materials with crystallites/grains of nanometre size. In materials of type I, long-range dipole-dipole (LRD) interactions give rise to a weak coupling between magnetic nanoparticles and such nanoparticles find applications in bio-

catalysis, biomedicine, magnetic resonance imaging and magnetic field sensing [1–6], to name a few. By comparison, in addition to the inter-grain LRD interactions, the presence of grain boundaries or interfaces in type-II nanomaterials, enables the short-range exchange (SRE) interactions (mediated by the spins in the grain boundary/interfacial regions) to directly couple adjacent grains. These interactions in nanocrystalline ferromagnetic materials lead to a substantial variation of the magnetic properties in contrast with the non-interacting magnetic nanoparticle systems. Type II materials hold great promise for applications in spintronics and data storage [7, 8] because the interactions between single domain magnetic particles ensure that the stored information is not lost by the flipping of domain magnetizations between easy directions (separated by anisotropic energy barriers) caused by thermal energy at finite temperatures.

In order to arrive at a magnetic nanomaterial that is best suited as the particulate medium for high-density magnetic recording, a basic understanding of the individual roles of inter-grain interactions, intra-grain/core magnetic anisotropy and surface/interface magnetic anisotropy in affecting the magnetization reversal processes in nanocrystalline ferromagnets is required. To this end, a detailed but systematic magnetic study of the crystallite size (d) dependence of the magnetic properties of nanocrystalline (nc-) elemental 3d transition metal ferromagnet Ni has been undertaken.

3.2 Theoretical Considerations

3.2.1 Approach-to-saturation

The change in magnetization with the applied magnetic field involves the process which depend on the state (bulk / polycrystalline / amorphous) of materials as well

as the types of defects/non-magnetic impurities and anisotropies present in a material. An understanding of the magnetization process can be facilitated by a quantitative comparison between the experimental results and the predictions made by the theoretical models, proposed in the literature to describe the process of 'approach-to-saturation' in magnetization.

3.2.1.1 Brown - Néel Model

The change in magnetization of ferromagnets near saturation proceeds via the rotation of magnetization vector under the combined influence of the applied magnetic field and crystalline anisotropy torques. The effect of this mechanism for polycrystalline specimens was first theoretically calculated by Akulov [9] and Gans [10].

$$M(H) = M_S \left(1 - \frac{c}{H^2}\right) \tag{3.1}$$

where M_s is the saturation magnetization, H is the applied external magnetic field and c is a constant related to the square of crystalline anisotropy constant. The drawback of this theory is that it considers only the effect of crystalline anisotropy on the saturation process of magnetization. It completely ignores the influence of lattice vacancies, distortions, crystalline defects and local concentration fluctuations that impede the motion of domain walls. Later, Brown Jr., [11, 12], formulated a micomagnetic theory, that considers (i) the structural inhomogeneity due to imperfections (dislocations and/or defects) which causes fluctuations in the local internal stress field via magneto-elastic coupling, (ii) effect of magnetic anisotropy responsible for the significant deviations from saturation in ferromagnetic crystals. Barring the last term involving the high-field susceptibility, χ_{hf}, Brown Jr. [11, 12] derived the following law of approach-to-saturation,

$$M(T, H) = M_s(T) \left[1 - \frac{a(T)}{H} - \frac{b(T)}{H^2}\right] + \chi_{hf}(T)\ H \tag{3.2}$$

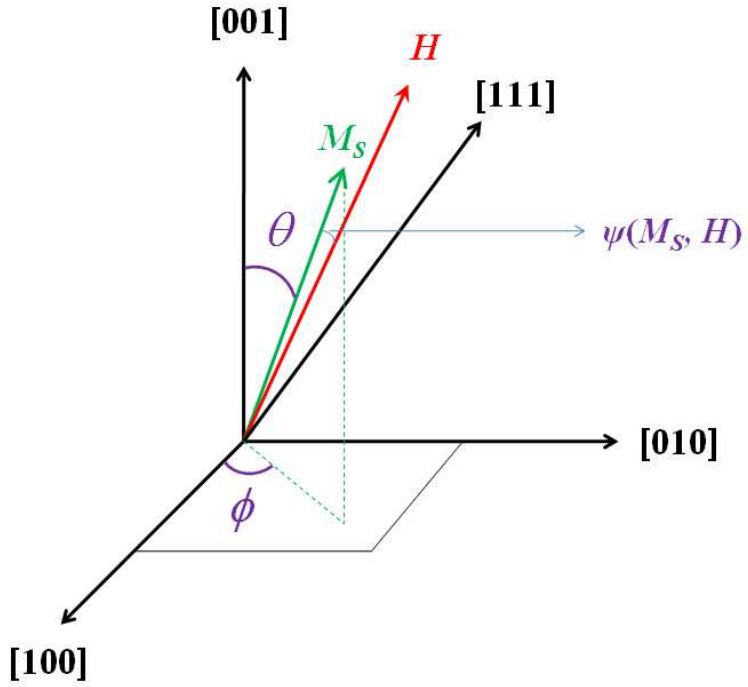

Figure 3.1: *Coordinate system used in deriving the relationship between the coeffficient of* $1/H^2$ *term in the Eq.(3.2) and magnetic anisotropy constant (K).*

In this relation, M_s is the saturation ("spontaneous") magnetization. The term $(a(T)/H)$ is due to the plastic strain caused by defects/grain boundaries. Néel [13] showed that non-magnetic inclusions and/or voids, also contribute to this term. The term $(b(T)/H^2)$ is a direct measure of magnetic anisotropy and $\chi_{hf}H$ term accounts for the paraprocess. For a polycrystalline (bulk) ferromagnetic material with cubic magnetocrystalline anisotropy (MCA) (in which grains have random crystallographic orientations), the coefficient $b(T)$ of the $1/H^2$ term in Eq.(3.2) is related to the cubic MCA (*energy density*) constant, $K_1^b(T)$, by the relation [14]

$$K_1^b(T) = \pm\ [(105/8)\ b(T)]^{1/2}\ M_s(T) \tag{3.3}$$

In the following, the steps that lead to Eq.(3.3) are outlined. Under moderately strong magnetic fields, all the domain wall displacements are essentially finished and hence the magnetization points almost parallel to the magnetic field. The component of magnetization along the magnetic field is

$$\begin{aligned} M &= M_S \, cos\psi \\ &= M_S \left(1 - \frac{\psi^2}{2} + \cdots\right) \end{aligned} \tag{3.4}$$

where 'ψ', the angle between the magnetization and magnetic field vectors, is assumed to be small. The torque exerted by the magnetic field equals and counter balances, the torque caused by the magnetic anisotropy energy (E_a), i.e.,

$$M_S H sin\psi = -\frac{\partial E_a}{\partial \psi} \tag{3.5}$$

Since ψ is very small (as magnetization vector nearly points in the direction of field at high fields),

$$M_S H sin\psi \approx M_S H\psi = -\frac{\partial E_a}{\partial \psi} \Rightarrow \psi = \frac{1}{H}\frac{c}{M_S} \tag{3.6}$$

where

$$c = -\left(\frac{\partial E_a}{\partial \psi}\right)_{\psi \sim 0} \tag{3.7}$$

Substituting Eq.(3.6) in Eq.(3.4), we obtain

$$M = M_S \left(1 - \frac{b}{H^2} - \cdot\cdot\right) \tag{3.8}$$

where

$$b = \frac{1}{2}\frac{c^2}{M_S^2} \tag{3.9}$$

Evaluation of the coefficient 'b' for the case of cubic anisotropy: The magnetization rotates along the maximum gradient of anisotropy energy in the neighborhood of H. Using spherical polar coordinates to describe the orientation of the

magnetization vector and writing anisotropy energy also in polar coordinates, we obtain,

$$\nabla E_a = \frac{\partial E_a}{\partial r}\ \hat{r} + \frac{1}{r}\ \frac{\partial E_a}{\partial \theta}\ \hat{\theta} + \frac{1}{r\ sin\theta}\ \frac{\partial E_a}{\partial \phi}\ \hat{\phi} \tag{3.10}$$

Assuming that the ∇E_a is pointing already in the radial direction, the component of magnetization in the radial direction experiences a constant force from E_a and hence the first term in the Eq.(3.10) becomes zero, with the result

$$\begin{aligned} c^2 &= |\nabla E_a|^2 \\ &= \left(\frac{\partial E_a}{\partial \theta}\right)^2 + \frac{1}{sin^2\theta}\left(\frac{\partial E_a}{\partial \phi}\right)^2 \end{aligned} \tag{3.11}$$

and hence,

$$b = \frac{1}{2{M_S}^2}\left[\left(\frac{\partial E_a}{\partial \theta}\right)^2 + \frac{1}{sin^2\theta}\left(\frac{\partial E_a}{\partial \phi}\right)^2\right] \tag{3.12}$$

Rewriting, $\frac{\partial E_a}{\partial \theta}$ and $\frac{\partial E_a}{\partial \phi}$ in terms of direction cosines ($\alpha_1 = sin\theta\ cos\phi$, $\alpha_2 = sin\theta\ sin\phi$, $\alpha_3 = cos\theta$) of magnetization with respect to the chosen coordinate system,

$$\frac{\partial E_a}{\partial \theta} = \frac{\partial E_a}{\partial \alpha_1}\ \frac{\partial \alpha_1}{\partial \theta} + \frac{\partial E_a}{\partial \alpha_2}\ \frac{\partial \alpha_2}{\partial \theta} + \frac{\partial E_a}{\partial \alpha_3}\ \frac{\partial \alpha_3}{\partial \theta} \tag{3.13}$$

similarly,

$$\frac{\partial E_a}{\partial \phi} = \frac{\partial E_a}{\partial \alpha_1}\ \frac{\partial \alpha_1}{\partial \phi} + \frac{\partial E_a}{\partial \alpha_2}\ \frac{\partial \alpha_2}{\partial \phi} + \frac{\partial E_a}{\partial \alpha_3}\ \frac{\partial \alpha_3}{\partial \phi} \tag{3.14}$$

and solving the above expressions, we can obtain

$$b = \frac{1}{2{M_S}^2}\left[\sum_{i=1}^{3}\left(\frac{\partial E_a}{\partial \alpha_i}\right)^2 - \left(\sum_{i=1}^{3}\left(\frac{\partial E_a}{\partial \alpha_i}\right)\alpha_i\right)^2\right] \tag{3.15}$$

For the cubic case, E_a is related to the anisotropy constants K_1 and K_2 as

$$E_a = K_1(\alpha_1^2\alpha_2^2 + \alpha_2^2\alpha_3^2 + \alpha_3^2\alpha_1^2) + K_2(\alpha_1^2\alpha_2^2\alpha_3^2) + ... \tag{3.16}$$

Considering only the first term in Eq.(3.16), we get

$\frac{\partial E_a}{\partial \alpha_1} = 2K_1\alpha_1(1-\alpha_1^2)$, $\frac{\partial E_a}{\partial \alpha_2} = 2K_1\alpha_2(1-\alpha_2^2)$, $\frac{\partial E_a}{\partial \alpha_3} = 2K_1\alpha_3(1-\alpha_3^2)$.

Then, Eq.(3.15) becomes,

$$b = \frac{4}{2}\frac{K_1^2}{M_s^2}\left[(\alpha_1^6+\alpha_2^6+\alpha_3^6) - (\alpha_1^8+\alpha_2^8+\alpha_3^8) - 2(\alpha_1^4\alpha_2^4+\alpha_2^4\alpha_3^4+\alpha_3^4\alpha_1^4)\right]. \quad (3.17)$$

Assuming random orientation of crystallites/grains for a polycrystalline material, averaging of 'b' over all possible directions (by considering the average values of direction cosines over a solid sphere where 'θ' ranges from angle 0° to 180° and 'ϕ' takes on values 0° to 360°), we obtain

$$\langle b\rangle_{avg} = \frac{4}{2}\frac{K_1^2}{M_s^2}\left\{\frac{3}{7} - \frac{3}{9} - \frac{6}{105}\right\} = \frac{8}{105}\frac{K_1^2}{M_s^2} \quad (3.18)$$

Note: Eq.(3.2) is strictly valid only for $H \gtrsim 4\pi M_s$, when the sample is nearly in a single domain state and the magnetic field has to work against the anisotropy energy barriers to rotate the domain magnetization towards its own direction. In other words, a precise estimate of the parameter 'b' and hence of the magnetic anisotropy constant, K_1, can be obtained when sufficiently large magnetic fields ($H \gg 4\pi M_s$) are applied to saturate magnetization in materials so as to arrive at a single domain configuration and magnetization points in the direction of the applied external magnetic field.

3.2.1.2 Random Anisotropy Model

In nanocrystalline magnetic materials, the magnetic order at the grain boundary regions, where the atomic spins at the surfaces/interfaces experience inter-grain exchange interaction and anisotropy effects, can be understood in terms of the amor-

phous models of magnetism [15, 16]. Originally proposed for the amorphous ferromagents by Chudnovsky [16, 17], random anisotropy model assumes either random space distribution of exchange [18] or random distribution of anisotropy axis [19]. Since the saturation magnetization in nanocrystalline magnetic materials is reduced by about $3-8\%$ compared to their bulk counterparts and the easy axis of magnetization varies randomly from grain to grain, the anisotropy energy is weaker than the exchange energy. The large exchange favours uniform magnetization while the magnetization experiences random local anisotropy field in the grain boundary region and across the grains.

In the macroscopic approach to the description of amorphous magnetism with random anisotropy field $\overrightarrow{n}(x)$ ($\overrightarrow{n}^2(x)=1$) and $\lambda \ll 1$ (λ is the ratio of anisotropy energy to exchange energy), the easy axes of magnetization are correlated over a length R_a of several atomic spacing a while the directions of local magnetization $\overrightarrow{M}(x)$ are correlated over a length scale R_m. The local magnetization is assumed to rotate smoothly over the volume so that $M^2(x) = const.$ However, $R_a \gg a$ and $R_m \gg R_a$ for the random anisotropy associated with polycrystallite system. In three-dimensions, the system prefers to be in the spin-glass state when $R_m \sim R_a$. The amorphous magnetic state of the polycrystallite system in the presence of external magnetic field, $\overrightarrow{H}$, can be described by the macroscopic energy density [16, 17]

$$\epsilon = \frac{1}{2}\,\alpha\left(\frac{\partial \overrightarrow{M}}{\partial x_i}\right)^2 - \frac{1}{2}\,\beta\left(\overrightarrow{M}.\overrightarrow{n}\right)^2 - \overrightarrow{M}\cdot\overrightarrow{H} \tag{3.19}$$

The condition $\lambda \ll 1$ corresponds to $\beta a^2/\alpha \ll 1$, $\alpha \propto Ja^2$, where J is the microscopic exchange constant. The characteristic fields associated with random anisotropy and exchange are defined as $H_{ex} \equiv \alpha M_0/R_a^2$, called the exchange field and $H_r \equiv \beta M_0$, called the anisotropy field.

For ferromagnets with *weak random anisotropy*, depending on the strength of the applied magnetic field, H, the random anisotropy model [17] predicts a correlated

spin glass state [20] (with a finite ferromagnetic correlation length) at low fields, $H < H_s$, a ferromagnet with wandering axis [20] at intermediate fields, $H_s < H < H_{ex}$, and a ferromagnetic state, in which all the spins are virtually aligned with the field albeit a slight tipping angle due to the local random anisotropy, at high fields $H > H_{ex}$. The strength of H is measured relative to a parameter H_s, defined as

$$H_s = \frac{H_r^4}{H_{ex}^3} \tag{3.20}$$

where H_r and H_{ex} are the random anisotropy field and the exchange field, respectively. In the intermediate-field regime, the magnetization approaches saturation in accordance with the relation

$$M = M_{sat}\left[1 - \frac{1}{15}\left(\frac{H_s}{H}\right)^{1/2}\right] + \chi_{hf}H \tag{3.21}$$

whereas in the high-field regime, M is predicted to approach its saturation value, M_{sat}, as

$$M(T,H) = M_{sat}(T)\left[1 - \frac{1}{15}\left(\frac{H_r}{H + H_{ex}}\right)^2\right] + \chi_{hf}(T)\ H \tag{3.22}$$

3.2.1.3 Micromagnetic Model

This model was proposed by the Kronmüller [15] for amorphous ferromagnets. Contrasted with the crystalline ferromagnets, where the $1/H$ term in the law of approach-to-saturation, Eq.(3.2), arises from lattice imperfections, ΔM_{imp}, additional contribution to the total deviation ΔM $(= M_S - M(H))$ of magnetization from its saturation value in nanocrystalline ferromagnets comes from the intrinsic fluctuations of the material parameters, ΔM_{intr} due to the magnetostatic stray fields arising from the volume charges. As a result, the orientation of magnetization becomes inhomogeneous. In particular, when there are interactions (dipolar and/or exchange) between the crystallites of nanometer size, the interparticle exchange and anisotropy

energies play a decisive role in controlling the intrinsic fluctuations of magnetization. As in the case of crystalline ferromagnets at finite temperatures, there is yet another contribution to ΔM in nanocrystalline ferromagnets due to the suppression of spin waves by external magnetic field, ΔM_{para}, the so-called *Holstein-Primakoff* spin-wave para-process. Thus, the total deviation ΔM from saturation is the sum of three terms

$$\delta M = \delta M_{imp} + \delta M_{intr} + \delta M_{para} \tag{3.23}$$

For a ferromagnet with a position-dependent spontaneous magnetization, $M(r)$, in an external magnetic field, H, applied parallel to the x_2-axis, is defined as [15]

$$M(r) = g\mu_B S(r)/\Omega(r) \tag{3.24}$$

where $S(r)$ is the spin quantum number and $\Omega(r)$ is the atomic volume per magnetic atom at position r (x_1, x_2, x_3). For sufficiently large fields, the transverse components M_i ($i = 1, 3$) of $M(r)$

$$\frac{M_{1,3}(r)}{M_S} \to 0 \quad while \quad \frac{M_2(r)}{M_S} \to 1 \tag{3.25}$$

where M_S is the volume average $\langle M(r)\rangle$. The volume average $\langle M_2\rangle$ can be written as [15]

$$\langle M_2\rangle = M_S \left\{1 - \frac{1}{2M_S^2}\left[\langle M_1^2(r)\rangle + \langle M_3^2(r)\rangle\right]\right\} \tag{3.26}$$

where $\langle M_i^2(r)\rangle_{i=1,3}$ is the volume averages of the squares of the transverse components of $M(r)$. The components $M_i(r)$ can be determined from the micromagnetic equations, which are obtained by minimizing the Gibbs free energy, $\wp$, of the ferromagnet [15],

$$\begin{aligned}\wp = \int \Bigg\{ & \frac{1}{2}\sum_{i,m,n} C_{mn}(r)[\nabla_m M_i(r)][\nabla_n M_i(r)] - \frac{1}{2}\sum_i H_{S,i}(r)M_i(r) \\ & + \sum k_{ij}(r)M_i(r)M_j(r) - \sum_i H_i(r)\cdot M_i(r)\Bigg\} d^3r\end{aligned} \tag{3.27}$$

where i refers to the i^{th} components of the field variables M, H_S and H. $C_{mn}(r)$ and $k_{ij}(r)$ are the position-dependent tensors for the exchange energy and for the local magnetocrystalline energy, respectively. The magnetostatic stray field $\overrightarrow{H}_S = -\overrightarrow{\nabla}U(r)$, where $U(r)$, the magnetostatic potential, obeys Poisson's equation

$$\triangle U(r) = 4\pi \overrightarrow{\nabla} \cdot \overrightarrow{M}(r) \tag{3.28}$$

The micromagnetic equations so obtained may be written as [15]

$$\begin{aligned} &\sum_{m,n=1}^{3} M(r)C_{mn}(r)\nabla_m\nabla_n M_i(r) + \sum_{n=1}^{3} M(r)B_n(r)\nabla_n M_i(r) \\ &- 2(k_{ii}(r) - k_{22}(r))M_i(r)M(r) - 2\sum_{j\neq 1} k_{ij}(r)M_j(r)\cdot M(r) \\ &2k_{i2}M^2(r) + H_{S,i}(r)M(r) - HM_i(r) = 0 \end{aligned} \tag{3.29}$$

with $i = 1,3$, $j \neq 1,3$ and $B_n(r) = \sum_i \dfrac{\partial C_{in}(r)}{\partial X_i}$, which takes into account the position dependence of the exchange parameter $C_{mn}(r)$. Eq.(3.29) describes four types of fluctuations denoted as *intrinsic* and *magnetoelastic* fluctuations. *Intrinsic fluctuations* are due to the *short-range* variations of the material parameters such as i) *magnetostatic fluctuations*, $\delta M(r)$, ii) magnetocrystalline fluctuations, $\delta k_{ij}(r)$ and iii) exchange fluctuations, $\delta C_{mn}(r)$, $\delta B_n(r)$. Magnetoelastic fluctuations are due to modification of $k_{ij}(r)$ by *long-range internal stresses*, σ. Regardless of the origin of the fluctuations in magnetization ($\delta M(r)$), $M(r)$ can be written as

$$M(r) = \langle M(r)\rangle + \delta M(r) \tag{3.30}$$

One source of intrinsic magnetization fluctuations could be the magnetostatic stray fields resulting from volume charges, $\nabla \cdot (\delta M(r))$, that make the orientation of the spontaneous magnetization inhomogeneous. The other source could be the fluctuations of the magnetocrystalline energy, which can be written as

$$k_{i2}(r) = \langle k_{i2}(r)\rangle + \delta k_{i2}(r) \tag{3.31}$$

For perfectly random orientations of the nanocrystallite axes, the volume average $\langle k_{i2}(r)\rangle$ vanishes. The transverse components, $M_{1,3}$, are linear functions of fluctuations δM and δk. Since the fluctuations are uncorrelated, the volume averages $\langle \delta k \delta M_i\rangle$ vanish and hence the effect of fluctuations δM and δk can be treated separately.

3.2.1.4 Magnetostatic fluctuations

Replacing the terms $C_{mn}(r)M(r)$, $B_n(r)M(r)$ and $\langle k_{ij}M^2(r)\rangle$ in the micromagnetic equation (3.29) with their volume averages, yields [15]

$$\left(\frac{2A}{M_S}\right)\sum_{m=1}^{3}\nabla_m^2 M_i(r) + \langle M(r)\rangle H_{S,i}(r) - H\cdot M_i(r) = 0 \tag{3.32}$$

By solving the coupled system of differential equations, Eqs.(3.32) and (3.28), the deviation from saturation, $\triangle M = M_S - \langle M_2(r)\rangle$, for $H >> 4\pi M_S$, is given by [15]

$$\Delta M_{intr} = M_S\ \Omega_0\ \frac{(2A/M_S)^{1/2}}{120\ \pi}\ \kappa_S^4\ \left(\frac{1}{H^{1/2}} - \frac{1}{2}\frac{4\pi M_S}{H^{3/2}} + \cdot\cdot\right) \tag{3.33}$$

3.2.1.5 Magnetocrystalline fluctuations

Neglecting the magnetostatic fluctuations in Eq.(3.29) one obtains [15]

$$\left(\frac{2A}{M_S}\right)\sum_{m=1}^{3}\nabla_m^2 M_i(r) - 2k_{i2}\langle M^2(r)\rangle - H\cdot M_i(r) = 0 \tag{3.34}$$

Solving the micromagnetic equation, Eq.(3.33), with the fluctuation $\delta k_{i2}(r)$ for a vanishing volume average $\langle k_{i2}\rangle = 0$, the deviation from saturation, ΔM, is given by [15]

$$\Delta M_{intr} = \frac{1}{4}\ M_S\ \Omega_0\ \frac{1}{(2\pi)^4}\ \kappa_S^4\ (\langle k_{12}^2\rangle + \langle k_{32}^2\rangle)\ \frac{(2A/M_S)^{1/2}}{H^{1/2}} \tag{3.35}$$

Disregarding the magnetoelastic fluctuations, at a constant temperature, T, all the material-dependent physical parameters in equations (3.33) and (3.35) remain constant and the magnetization within the framework of the micromagnetic model can be written as

$$M(T,H) = M_S(T,H)\left[1 - \frac{a(T)}{H^{1/2}} + \frac{b(T)}{H^{3/2}}\right] + \chi_{hf}(T)H \tag{3.36}$$

The last term in Eq.(3.36) accounts for the increase in magnetization caused by the external magnetic field over and above the spontaneous magnetization at that temperature.

3.2.2 Magnetization Reversal and Coercivity

According to Néel model [21], the magnetization reversal takes place via thermal activation over a temperature-dependent and magnetic field-dependent anisotropy energy barrier, $E(T,H)$, which separates two local energy minima. At a given temperature ($T \ll T_c$), for external magnetic fields (H) below the switching field at $T = 0$, H_0, there are two local energy minima, whereas for $H \geq H_0$, only one energy minimum exists and the energy barrier vanishes. The energy barrier, that tends to impede the magnetization reversal, has the functional dependence on H of the form [21]

$$E(T,H) = E_0(T)\ \left[1 - \frac{H(T)}{H_0}\right]^2 \tag{3.37}$$

$E_0(T)$ is the energy barrier at $H = 0$ for a given temperature, and H_0 is the minimum value of H at $T = 0$ (the switching field) at which the energy barrier $E(T = 0, H)$ vanishes. This relation holds when H is applied along the easy direction of magnetization, common to both uniaxial anisotropy and shape anisotropy. Eq.(3.37) can be rewritten as

$$H(T) = H_0\ \left[1 - \left(\frac{E(T,H)}{E_0(T)}\right)^{1/2}\right] \tag{3.38}$$

If the contributions due to core anisotropy, surface/interface anisotropy and shape anisotropy are of comparable magnitude and H may not necessarily point along the easy direction of magnetization, dictated by the resultant (K_{eff}) of these anisotropies, Eq.(3.38) can be generalized to

$$H_c(T) = H_0 \left[1 - \left(\frac{E(T,H)}{E_0(T)}\right)^{\beta}\right] \tag{3.39}$$

In Eq.(3.39), $E(T,H) = k_B T\ ln[t(T,H)/\tau]$ (if the thermal activation [22] over the anisotropy energy barriers is responsible for the temperature dependence of coercivity), $E_0(T) = \mid K_{eff}(T) \mid \times V$ and V is the volume of a crystallite in units of cm^3. The exponent 'β' depends on the angle, 'ψ', between the applied field direction and the easy direction of magnetization. The final expression for the temperature dependence of coercivity in terms of the effective anisotropy is, thus, given by

$$H_c(T) = H_0 \left[1 - \left(C \times \frac{T}{\mid K_{eff}(T) \mid}\right)^{\beta}\right] \tag{3.40}$$

where $C = k_B\ ln[t/\tau]/V$.

3.3 Data Analysis, Results and Discussion

Magnetization (M) versus magnetic field (H) isotherms in fields up to $H = 90$ kOe were recorded in the temperature range 2 K $\leq T \leq$ 300 K. These measurements were performed on the Quantum Design PPMS VSM system.

3.3.1 Core and surface/interface magnetic anisotropies

With a view to ascertain the type of magnetic anisotropies prevalent in nanocrystalline Ni and quantify their relative magnitudes and to understand the finite size effets on the magnetization process, magnetization versus magnetic field (M-H)

isotherms in the temperature range 2 K $\leq T \leq$ 300 K are analyzed in terms of the well known (i) Random Anisotropy (RA) [17], (ii) Micromagnetic (MM) [15] and (iii) Brown-Néel (BN) [11] models proposed in the literature for the approach-to-saturation of magnetization in ferromagnets. Assuming that the surfaces/interfaces of the nanosized crystallites have amorphous order and position-dependent magnetostatic and magnetocrystalline fluctuations are prevalent in nanocrystalline magnetic materials, fits to the $M-H$ isotherms are attempted using the expressions Eq.(3.36) and Eq.(3.22) of the micromagnetic [15] and random anisotropy [17] models. Both these models failed to reproduce the observed functional dependence of M on H at any temperature. In particular, the RA model completely fails to fit the magnetization data. By comparison, the MM model fits the observed magnetization as a function of field at low temperatures better, but the fit parameters are unphysical.

An attempt is made to find out if the relation described by Eq.(3.2) of the Brown-Néel (BN) [11] model fits the experimentally observed $M-H$ isotherms. Note that in this relation, M_s is the saturation ("spontaneous") magnetization, $(a(T)/H)$ term arises due to the plastic strain caused by defects/grain boundaries and/or non-magnetic inclusions, $(b(T)/H^2)$ term is a direct measure of magnetic anisotropy and $\chi_{hf}H$ term accounts for the paraprocess. This model accurately reproduces the observed magnetization as a function of applied magnetic filed at fixed temperatures, $M_T(H)$. Fig. 3.2 shows the comparison of the reduced sum of deviation squares (χ^2_{Red}) for different nanocrystalline Ni samples, obtained when the experimentally obtained $M_T(H)$ are fitted using the expressions given by the three models discussed above. It is clear that the deviations between the fits and the data and hence the χ^2_r is minimum only in the case of Brown-Néel model.

Figure 3.3 demonstrates that the theoretical fits (continuous curves), based on the Brown-Néel model (Eq.(3.2)), accurately describe the approach-to-saturation of magnetization in the nanocrystalline Ni samples under study. The best theoretical

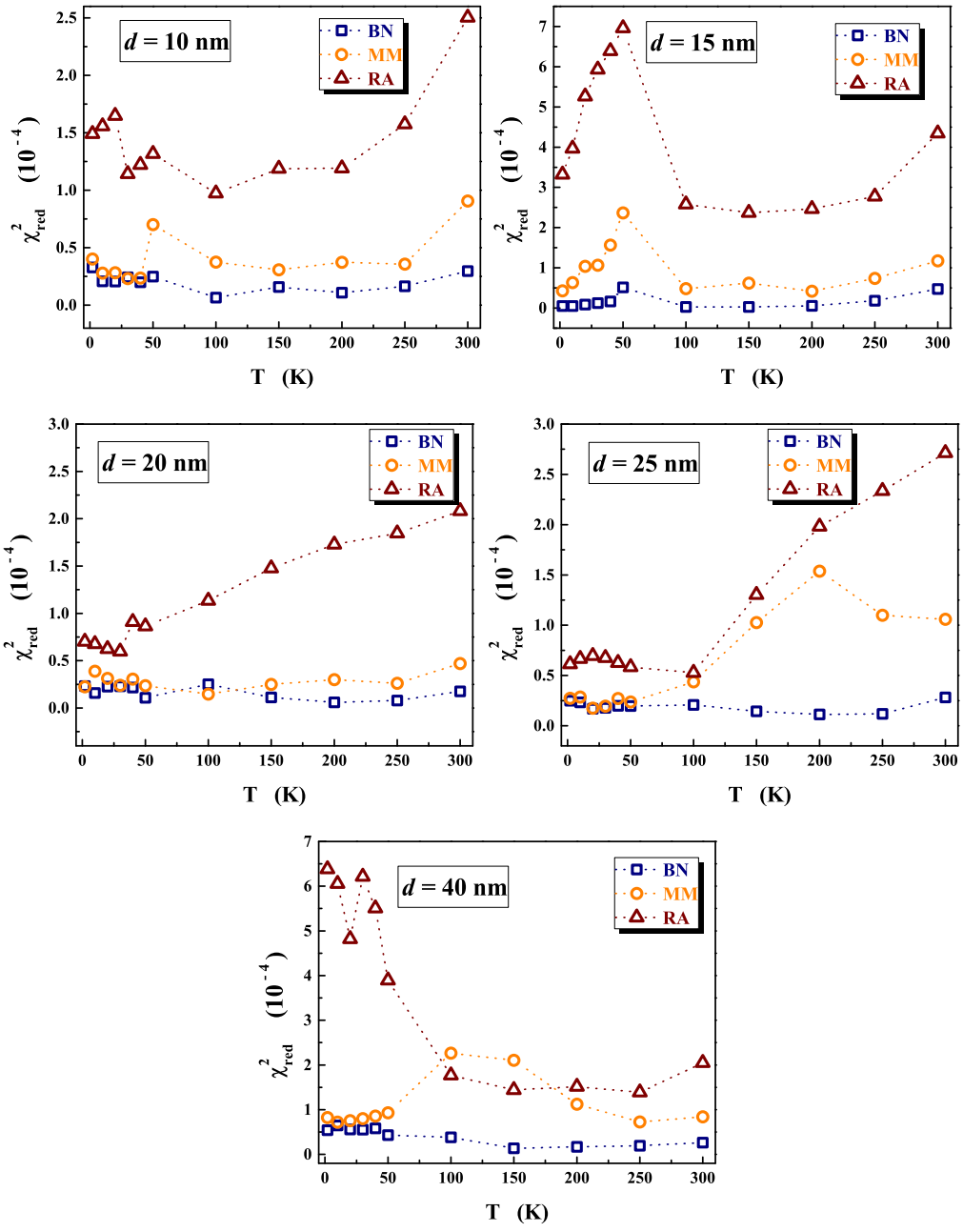

Figure 3.2: *The reduced sum of deviation squares (χ^2_{red}) for the fits based on the BN model ([11]), MM model ([15]), RA model ([17]) for the $M_T(H)$ data at temperatures in the range 2 K $\leq T \leq$ 300 K for nanocrystalline Ni samples with average crystallite size(d) in the range 10 nm $\leq d \leq$ 40 nm.*

fits to the $M_T(H)$ data, shown in Fig. 3.3, are obtained as follows. The parameters M_s, a, b and χ_{hf} at different temperatures have been accurately determined by employing the 'range-of-fit' analysis. In this analysis, the change in the values of these free parameters is constantly monitored as the field range, defined as $H_{min} \leq H \leq H_{max}$, is varied by keeping H_{max} fixed at 90 kOe and lowering H_{min} to smaller values. The optimum field range (typically 3.5 kOe $\leq H \leq$ 90 kOe) is the widest range over which the fit parameters approach constant (within the uncertainty limits) values and when H_{min} is lowered further, drastic changes in the parameter values occur. The coefficient 'a' of the $1/H$ term in Eq.(3.2) is found to make a significant contribution to $M_T(H)$ in the above-mentioned optimum field range. This is also borne out by the fact that, at any temperature, the $M_T(H)$ versus $1/H^2$ plot is not linear over any reasonably wide field range.

It is observed that spin-wave excitations completely account for the observed temperature variation of magnetization at fixed magnetic fields ranging from 10 kOe to 70 kOe in the nanocrystalline Ni samples in question [23] (shown in chaper 4). The spin-wave description also holds true for the temperature dependence of saturation magnetization, $M_s(T)$, as is evident from an excellent agreement between the spin-wave fits (continuous curves) and the observed $M_s(T)$ (symbols) in figure 3.4(a). At any given temperature, saturation magnetization, M_s, increases with cryatallite size, d, and so does the magnetic moment per Ni atom, μ_{Ni}, obtained from the expression, $\mu_{Ni} = M_s/N\mu_B$, where N is the number of Ni atoms per cm^3 and μ_B is the Bohr magneton. We find that μ_{Ni} (open circles), deduced from M_s at 2 K, increases with 'd' in accordance with the empirical relation $\mu_{Ni}(d) = \mu_{Ni}(d = \infty)$ [1 - $b \times d^{-n}$], with $\mu_{Ni}(d = \infty) = 0.616\ \mu_B$ (magnetic moment per Ni atom in the bulk at $T = 0$ K), $b = 0.55(10)$ and $n = 1.53(7)$. Inset of Fig. 3.4 highlights the $d^{-3/2}$ power law dependence of μ_{Ni} on the average crystallite size, d. By predicting that $\mu_{Ni} \sim d^{-1}$, the magnetic dead-layer theory [24] obviously does not account for the observed

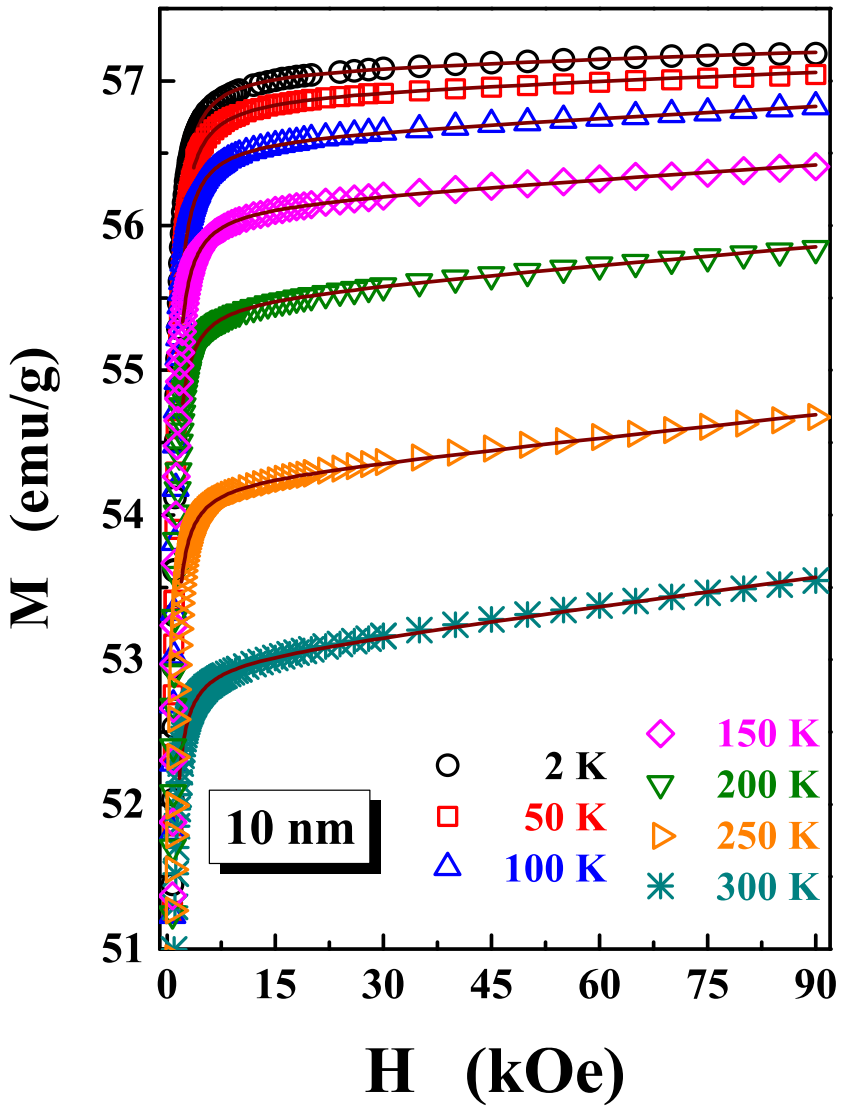

Figure 3.3: *M-H isotherms (symbols) in the temperature range 2 K $\leq T \leq$ 300 K, along with the best fits based on the Brown-Néel model [11] (continuous curves), i.e., Eq.(3.2) in case of nanocrystalline Ni with an average crystallite size of 10 nm.*

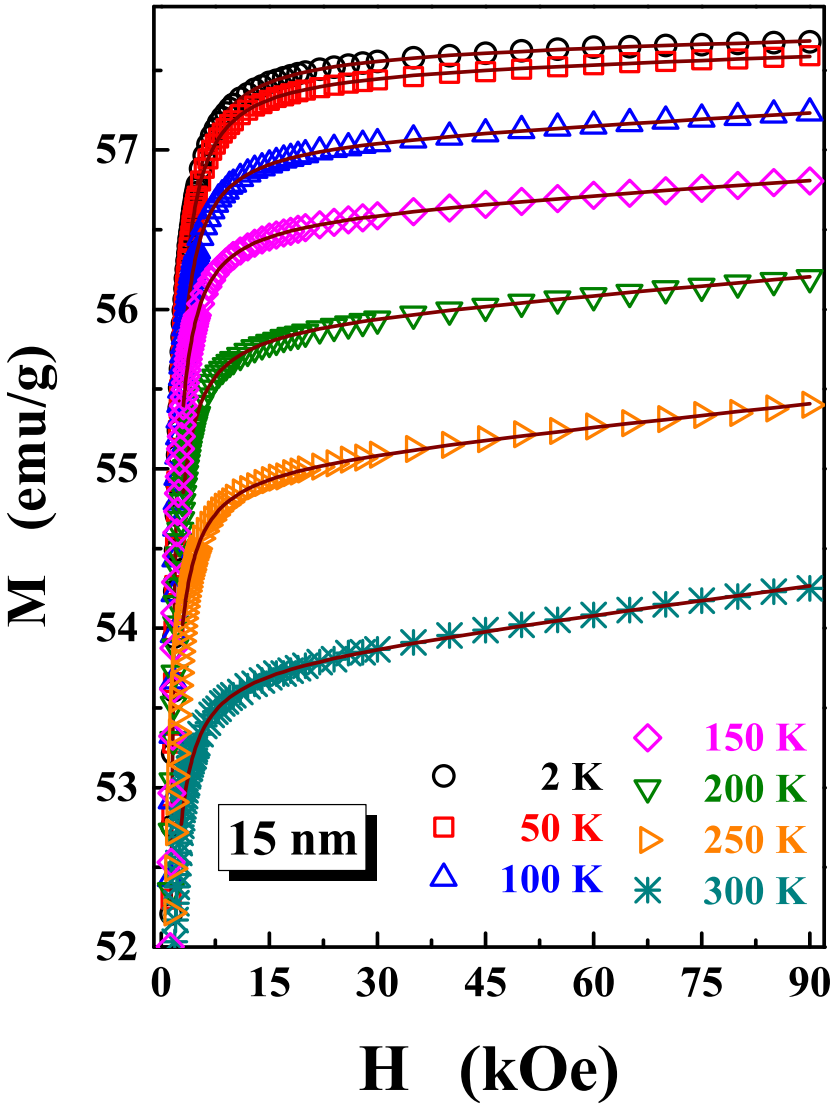

Figure 3.3 (Continued): *M-H isotherms (symbols) in the temperature range 2 K $\leq T \leq$ 300 K, along with the best fits based on the Brown-Néel model [11] (continuous curves), i.e., Eq.(3.2) in case of nanocrystalline Ni with an average crystallite size of 15 nm.*

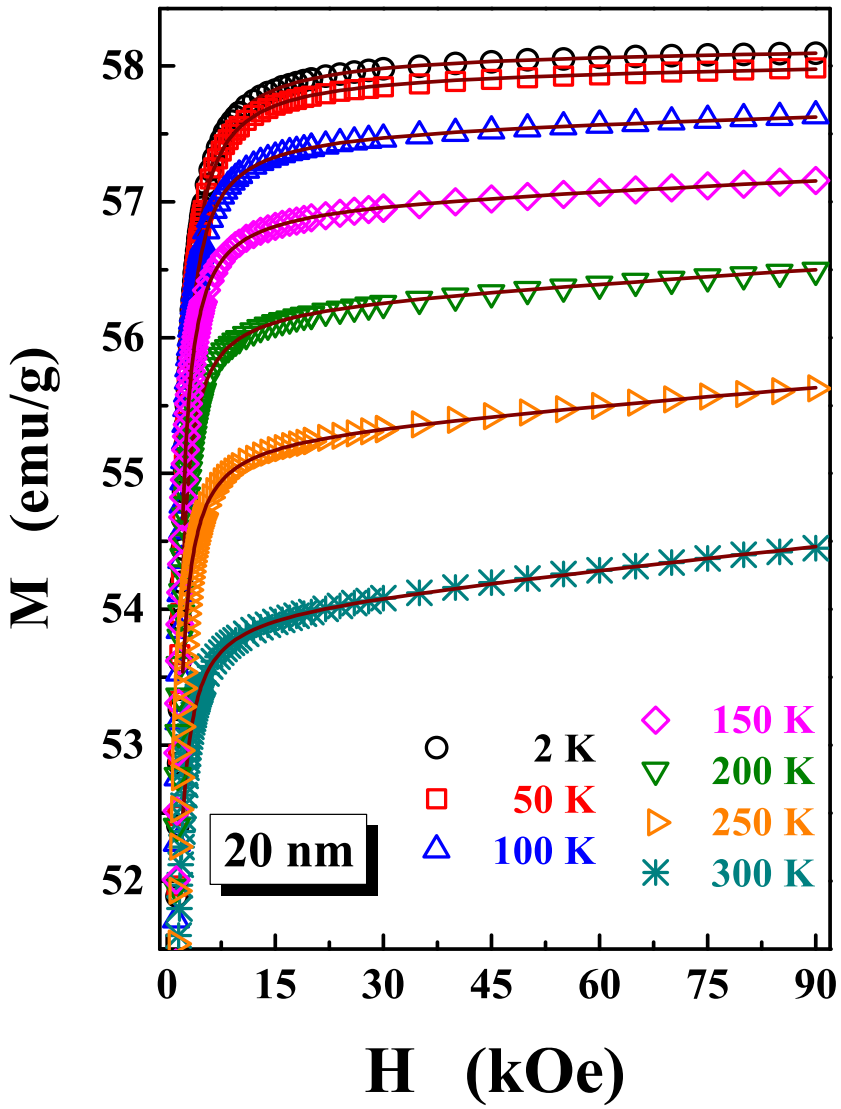

Figure 3.3 (Continued): *M-H isotherms (symbols) in the temperature range 2 K $\leq T \leq$ 300 K, along with the best fits based on the Brown-Néel model [11] (continuous curves), i.e., Eq.(3.2) in case of nanocrystalline Ni with an average crystallite size of 20 nm.*

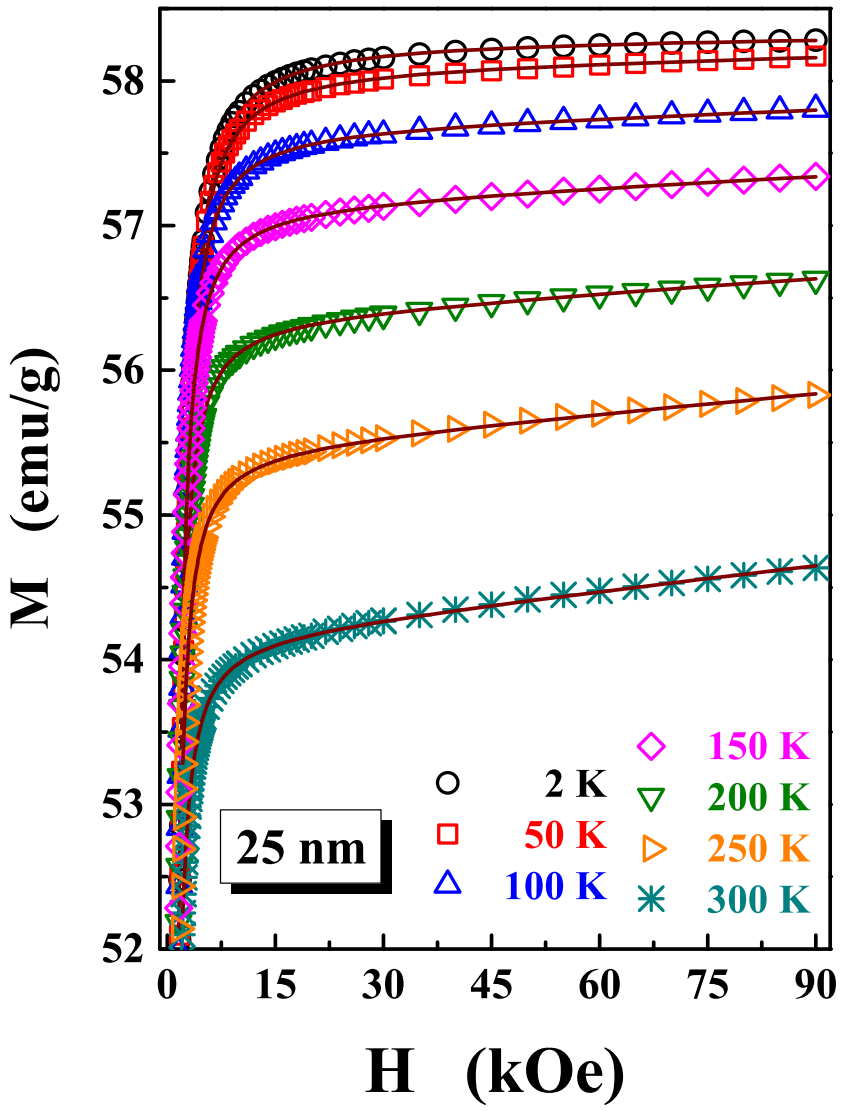

Figure 3.3 (Continued): *M-H isotherms (symbols) in the temperature range 2 K $\leq T \leq$ 300 K, along with the best fits based on the Brown-Néel model [11] (continuous curves), i.e., Eq.(3.2) in case of nanocrystalline Ni with an average crystallite size of 25 nm.*

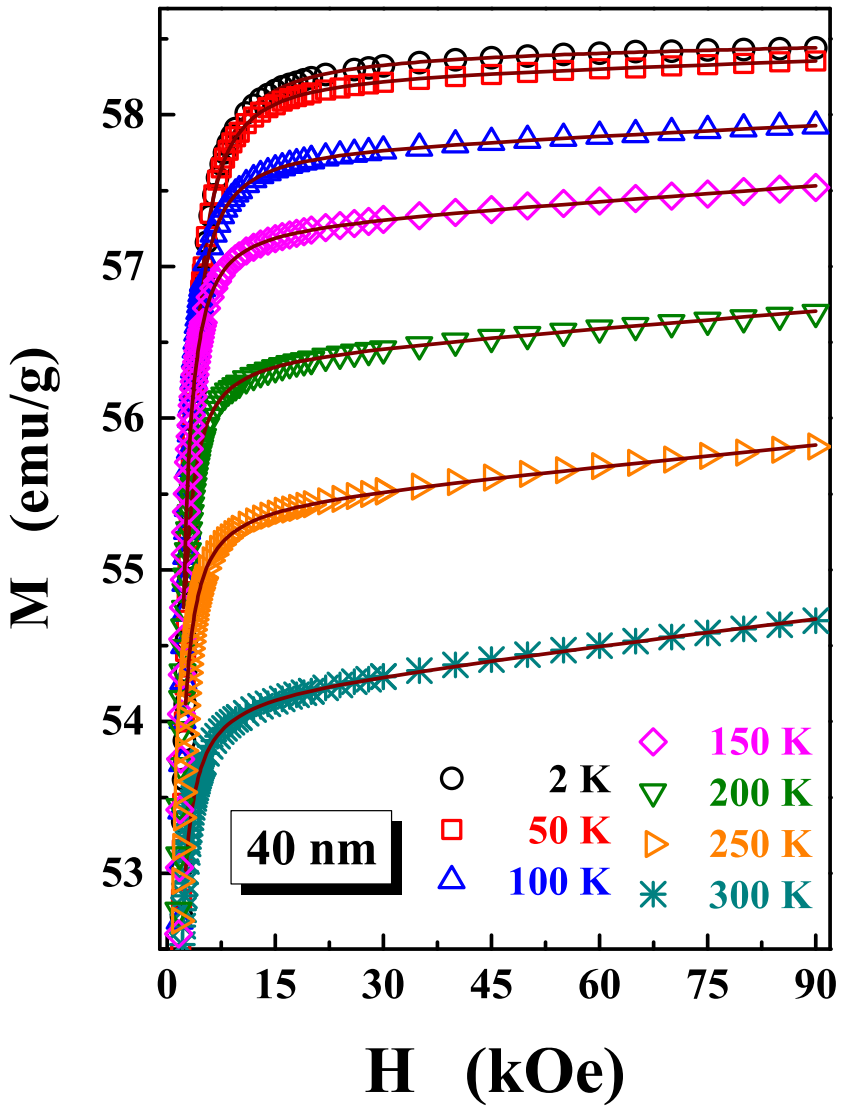

Figure 3.3 (Continued): *M-H isotherms (symbols) in the temperature range 2 K $\leq T \leq$ 300 K, along with the best fits based on the Brown-Néel model [11] (continuous curves), i.e., Eq.(3.2) in case of nanocrystalline Ni with an average crystallite size of 40 nm.*

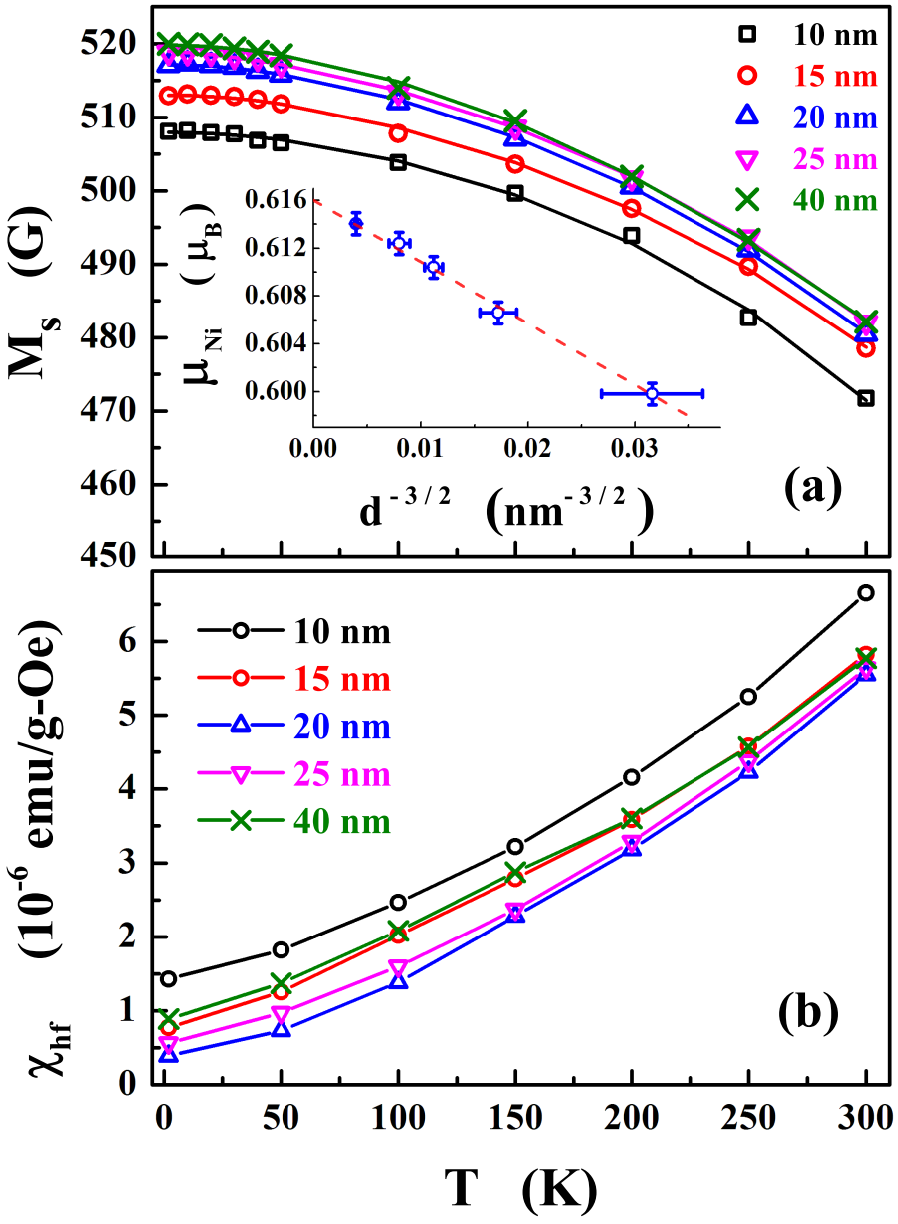

Figure 3.4: *Temperature variations of the parameters (a) saturation magnetization, M_s and (b) high-field suseptibility, χ_{hf}, for nanocrystalline Ni samples with different crystallite size, d in question. The inset of panel (a) highlights the $d^{-3/2}$ power law variation of magnetic moment per Ni atom, μ_{Ni} with d.*

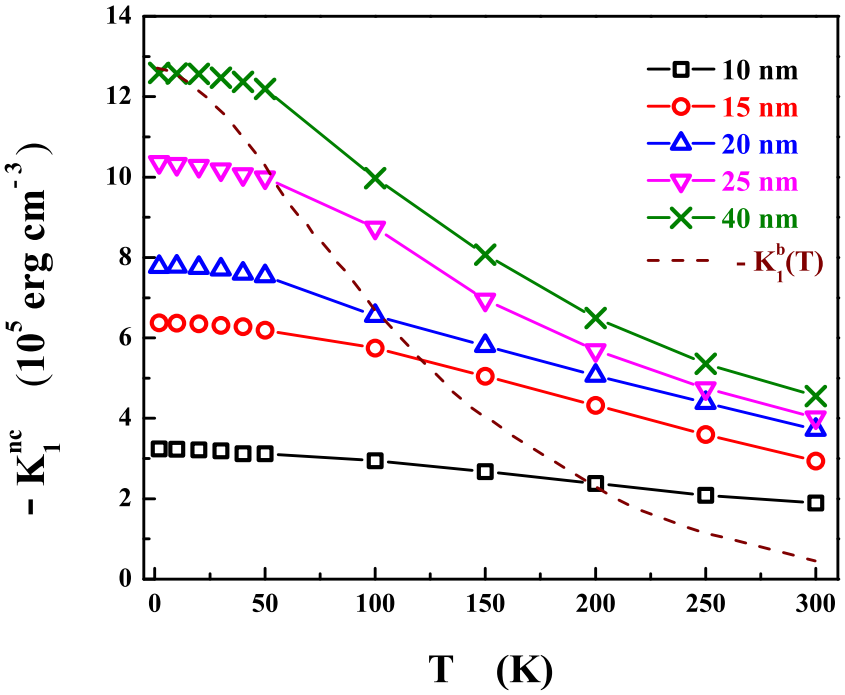

Figure 3.5: *The anisotropy constant, $-K_1^{nc}$, as a function of temperature in nanocrystalline Ni. The dashed curve highlights the temperature variation of the cubic magnetocrystalline anisotropy constant, $-K_1^b$, for bulk Ni.*

$\mu_{Ni}(d)$ in the present case. The percentage change of saturation magnetization, M_s, relative to that of bulk/polycrystalline Ni [25], i.e., [M_s(bulk)-$M_s(d)$]/M_s(bulk), ranges from 2.4 % for d = 10(1) nm to 0.3 % for d = 40(1) nm. The reduction in M_s with decreasing d could stem from the disorder in the spin orientation at the surface caused by surface magnetic anisotropy which increases with shrinking grain size. Hence, as the particle size increases, lower and lower applied magnetic fields are required to saturate magnetization with the result that the effective magnetic moment per Ni atom approaches the bulk value at large particle size, d. As expected, the high-field suseptibility, χ_{hf} increases with temperature (Fig. 3.4(b)) regardless of the value of crystallite size, d.

For a polycrystalline (bulk) ferromagnetic material with cubic magnetocrystalline anisotropy (MCA) (in which grains have random crystallographic orientations), the coefficient $b(T)$ of the $1/H^2$ term in Eq.(3.2) is related to the cubic MCA (*energy density*) constant, $K_1^b(T)$, by the relation Eq.(3.3) [14] , i.e.,

$$K_1^b(T) = \pm\ [(105/8)\ b(T)]^{1/2}\ M_s(T)$$

Consistent with the fact that the easy direction of magnetization in bulk Ni is [111], negative sign for K_1^b in Eq.(3.3) is chosen. The anisotropy constant $K_1^{nc} < 0$ as a function of temperature, so obtained, for the nanocrystalline (nc-) Ni samples of different average crystallite size, d, is shown in figure 3.5 and compared with the cubic MCA constant, $K_1^b(T)$, (dashed curve) previously reported [26,27] for crystalline Ni. From this comparison, the following obvious inferences can be drawn.

(a) If the cubic MCA alone were present in the nanocrystalline Ni samples, the $K_1^{nc}(T)$ curves for nanocrystalline Ni with different crystallite size, d, would exactly coincide with $K_1^b(T)$ at all temperatures because the nanocrystalline samples in the present case have the same crystallographic symmetry and lattice parameter as that of the crystalline (bulk) Ni. Since this is clearly not the case, it immediately follows that magnetic anisotropies, other than cubic MCA, are concomitantly present.

(b) At any given temperature, K_1^{nc} *increases* as average crystallite size, d decreases, e.g., at 2 K, K_1^{nc} increases from - 12.6 $\times$ 10^5 erg cm^{-3} at d = 40 nm to - 3.2 $\times$ 10^5 erg cm^{-3} at d = 10 nm. Considering that the surface effects become increasingly pronounced as the particle size reduces, the increase in K_1^{nc} as the average particle size, d decreases basically reflects the size-induced enhancement in the surface magnetic anisotropy.

(c) That K_1^{nc} in the sample with d = 40 nm approaches the bulk value of K_1^b (i.e., $K_1^{nc} \simeq K_1^b$) at $T \leq$ 10 K, asserts that the surface magnetic anisotropy

in this sample is weak. Thus, the growing discrepancy between K_1^b and K_1^{nc} with increasing temperature in the case of $d = 40$ nm must originate from yet another form of anisotropy (presumably the shape anisotropy).

In nanocrystalline Ni, K_1^{nc} should, thus, be the net result (K_{eff}) of the contributions due to different types of magnetic anisotropy as demonstrated below.

(I) Cubic magnetocrystalline anisotropy of the crystallite core, K_1^c, that has the same origin as that in the bulk; i.e., this anisotropy arises from the indirect coupling between the spins and the lattice, in that the spin couples to the orbit via spin-orbit coupling and the orbit, in turn, couples to the lattice via the interaction between orbital angular momentum and crystal field, which entails the symmetry of the lattice.

(II) Néel surface/interface magnetic anisotropy, K_s, [28] resulting from the broken local crystallographic symmetry at the surface/interface, leading to non-collinear spin structure at the surface/interface.

(III) Magnetic self-energy (shape anisotropy, K_{shape}), arising from the magnetostatic (dipole-dipole) interaction of the magnetization with the magnetic field (which depends on the sample shape) that magnetization itself creates.

(IV) Magnetoelastic anisotropy, K_{me}, arising from the crystallographic axis-dependent interaction between the magnetization and the internal strain, whose microscopic origin lies in the spin-orbit interaction.

Assuming that the above contributions to the anisotropy energy density are additive and the particles are spherical in shape, K_{eff} is given by the expression,

$$K_{eff} = K_1^c - \frac{2\pi}{3} M_s^2 + K_{me} + \frac{6}{d} K_s. \tag{3.41}$$

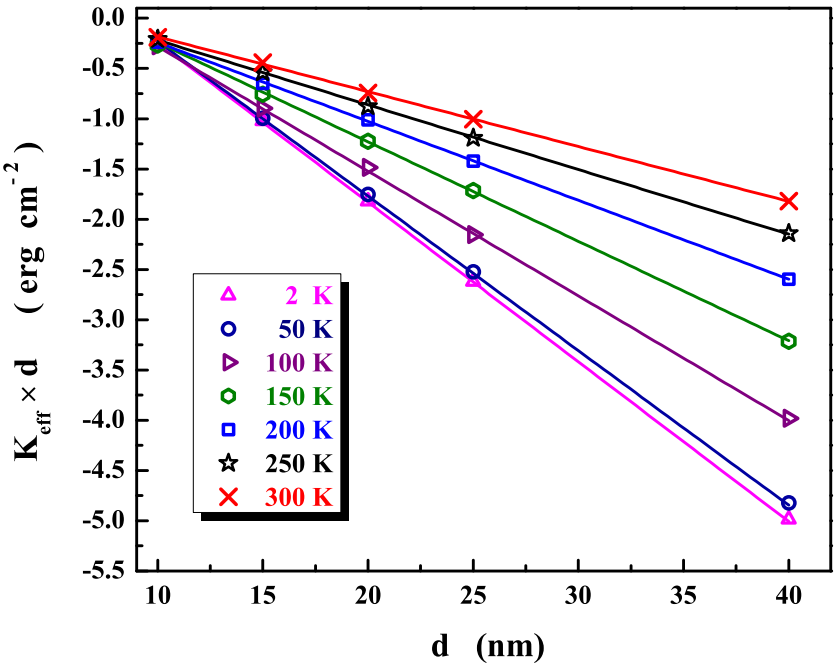

Figure 3.6: *Linear plots of '$K_{eff} \times d$' versus 'd' at different temperatures within the range 2 K $\leq T \leq$ 300 K.*

where the second term stands for the magnetic self-energy density, K_{shape}. Eq.(3.41), if valid, permits determination of K_1^c and K_s when the product '$K_{eff} \times d$' is plotted against 'd' at different temperatures, as shown in figure 3.6. The linear $K_{eff} \times d$ versus d plot isotherms with slopes $[K_1^c(T)$ - $\frac{2\pi}{3}M_s^2(T) + K_{me}(T)]$, when extrapolated to $d = 0$, yield intercepts on the ordinate equal to 6 $K_s(T)$.

Using $M_s(T)$ (obtained from the analysis based on Eq.(3.2)) and $K_s(T)$ (from the intercepts) and assuming that $K_{me}(T) \approx 0$, $K_1^c(T)$ is computed from the slopes at different temperatures. Panel (a) in figure 3.7 demonstrates that, within the uncertainty limits (which increase with temperature from 2.5% at 2 K to 11% at 300 K), $K_1^c(T)$ is *independent* of the crystallite size (as should be the case if the core anisotropy is indeed the bulk cubic MCA) and agrees quite well with the magnetocrystalline anisotropy constant $K_1^b(T)$, reported earlier [26,27] for Ni single crystal, particularly

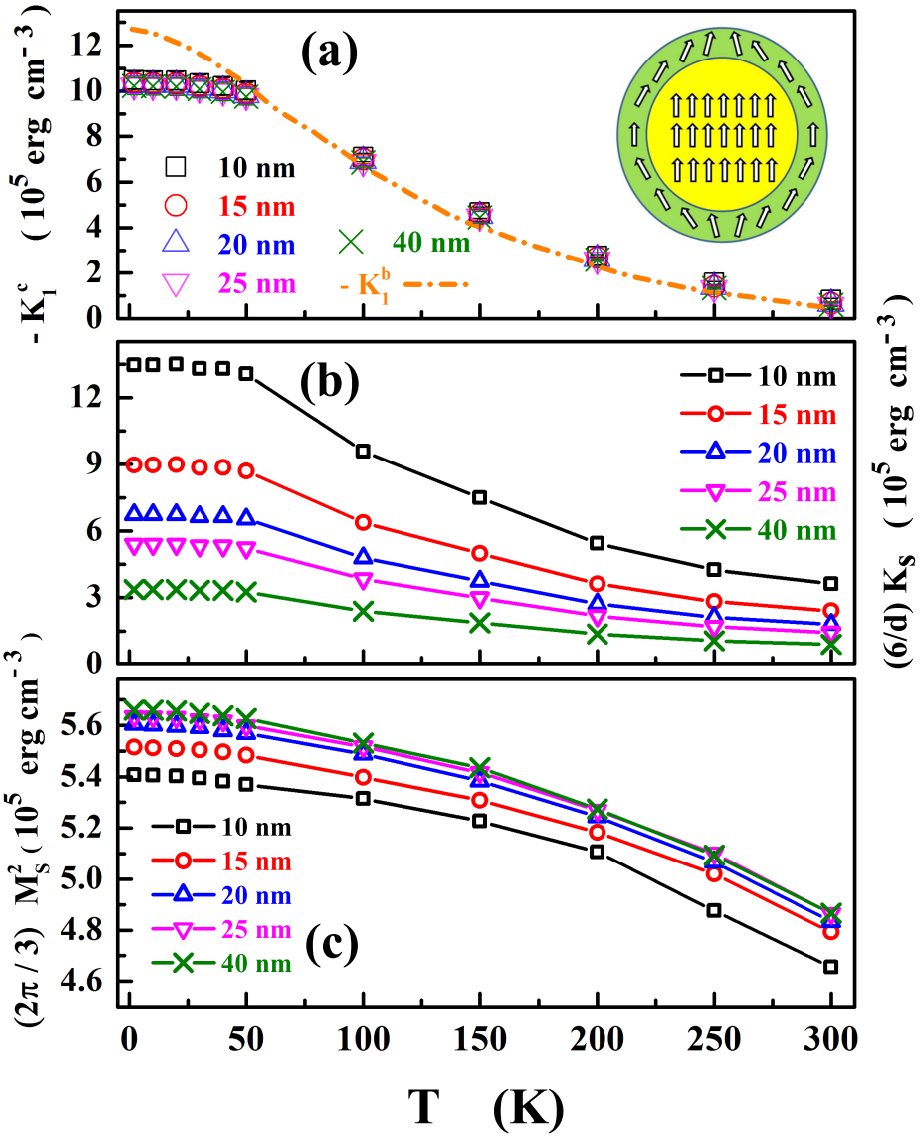

Figure 3.7: *Variations with temperature of the contributions to the effective anisotropy constant, K_{eff} for nanocrystalline Ni, arising from the (a) core anisotropy (b) surface/interface anisotropy and (c) shape anisotropy. A schematic sketch of the spin arrangement within an individual nanoparticle is shown in the inset of Fig. 3.7(a).*

for temperatures $T \geq 50$ K. Strong deviations of K_1^c from K_1^b at temperatures $T < 50$ K presumably signal the importance of K_{me} at low temperatures. The panels (b) and (c) of Fig. 3.7 respectively plot the contributions made by surface/interface anisotropy and shape anisotropy to K_{eff} (Eq.(3.41)), as functions of temperature. As expected, the surface anisotropy increases with the reduction in the average crystallite size. The surface anisotropy, $K_s(T)$ is *positive* for all d (Fig. 3.7(b)) in the present case. The sign of K_s decides the local easy directions at the surface/interface, e.g., $K_s > 0$ ($K_s < 0$) gives rise to the *tangential* (*radial*) spin structure [29] at the particle surface. At this stage, it is important to note that, at an individual nanoparticle level, the total energy (cf. Eq.(3.41)) attains its minimum value when the easy direction of magnetization, dictated by the core cubic MCA (i.e., [111] direction), is more or less preserved by the shape and surface/interface anisotropies, as schematically sketched in Fig. 3.7(a). This easy direction of magnetization varies randomly from particle to particle. Thus, K_1^{nc}, deduced from Eq.(3.2) when the measured value of the coefficient 'b' at a given temperature is used, is nothing but effective magnetic anisotropy, K_{eff}.

Note that the *percentage error* in K_1^{nc} or K_{eff} increases from 2.5 to 5.0 at 2 K and from 3.0 to 8.0 at 300 K as the average crystallite size decreases from $d = 40$ nm to $d = 10$ nm and that K_1^{nc} is enhanced a little bit (< 3 %) compared to the completely random case when the texture fraction, prevalent in the samples with average crystallite size, d ranging from 15 nm to 40 nm, is taken into account. Even in the sample with $d = 40$ nm, which has the highest texture fraction of $\simeq 45\%$, the enhanced value of K_1^{nc}, at a given temperature, falls well within the error bars of the corresponding value in the perfectly random case.

The presently determined values for the surface/interface anisotropy constant, $(6/d)\ K_s$, at 2 K for the nanoccrystalline Ni samples with crystallite size, $d = 20$ nm and 25 nm tally quite well in magnitude (but not in sign) with the estimate ($(6/d)$

K_s = - 6.0 $\times 10^5$ erg/cm^3) at 2 K for the (200)-textured nanocrystalline Ni sample (as is the case with our samples too) with d = 22.5 nm yielded by the theoretical model [30], which takes into account the intra-crystallite (core) cubic magnetocrystalline and surface/interface anisotropies as well as the exchange and dipolar interactions between the neighboring crystallites. Implicit in a close agreement between the theoretical and experimental magnitudes of $((6/d)\ K_s$ in nanocrystalline Ni is the exchange and dipolar coupling between nanograins. Our observation that Eq.(3.41) holds, is consistent with the theoretical result [31] that Eq.(3.41) is valid only in the case of elongated particles. However, there are other theoretical models [32,33], that assert that the surface/interface and core anisotropies are inextricably intertwined and hence Eq.(3.41) is merely an oversimplification. In view of the latter theoretical result, our experimental observations suggest that the interplay between the surface/interface and core anisotropies is either negligibly small, or even absent, in the present case.

3.3.2 Coercivity

Figure 3.8 depicts the M-H hysteresis loops taken over the magnetic field range - 90 kOe to +90 kOe at the end temperatures 2 K and 300 K (which are also representative of those taken at intervening temperatures). Insets show an enlarged view of the loops in the field range - 1.0 kOe to + 1.0 kOe. A complete absence of the exchange-bias effect, indicated by the perfectly symmetric hysteresis loops at all temperatures, lends firm support to our observation, based on the Rietveld refinement of the observed XRD patterns and compositional analysis, that NiO is not present in our PED nanocrystalline Ni samples. Coercive field, H_c, decreases at different rates with increasing temperature in different nanocrystalline Ni samples (figure 3.9). Instead of a monotonous thermal decline in H_c in the PED nanocrystalline Ni samples (Fig. 3.9), $H_c(T)$ peaks at $T \approx 30$ K in the nanocrystalline Ni sample with d = 15

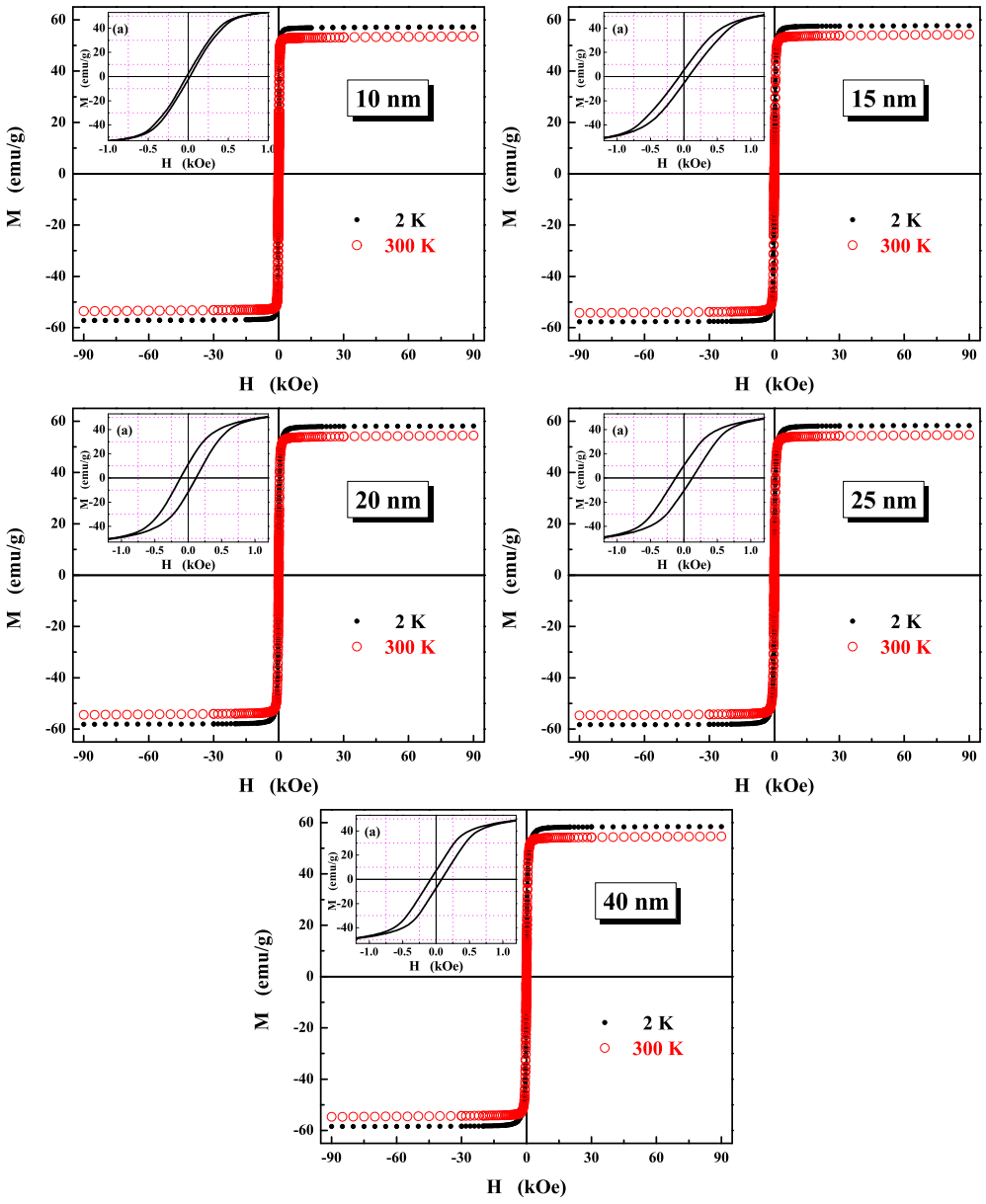

Figure 3.8: *$M-H$ hysteresis loops at temperatures 2 K and 300 K in the field range -90 kOe $\leq H \leq$ +90 kOe for the nanocrystalline Ni samples with 10 nm $\leq d \leq$ 40 nm. Insets (a) show a magnified view of the low-field portions of the hysteresis curves taken at 2 K.*

nm (prepared by the inert gas condensation (IGC) technique) and this peak broadens and shifts to lower temperatures as the crystallite size increases [34]. This peak in $H_c(T)$ has been attributed to [34] the formation of NiO at the grain boundaries. Absence of such a peak in our PED samples is consistent with the fact that due to the higher density of these samples, they are less prone to oxidation than the IGC samples. At any given temperature, H_c is smaller in IGC-nanocrystalline Ni when compared to the PED counterparts.

A decreasing $H_c(T)$ is generally understood in terms of the Néel model [21] in which the magnetization reversal takes place via thermal activation over a temperature-dependent and magnetic field-dependent anisotropy energy barrier, $E(T, H)$, which separates two local energy minima (as described in the section **3.2.2**). Fig. 3.9 bears out that, regardless of the value of crystallite size, d, the observed coercivity, $H_c(T)$ (symbols) for different nanocrystalline Ni samples are well described by the optimum fits (continuous curves), obtained by inserting the $\mid K_{eff}(T) \mid \equiv \mid K_1^{nc}(T) \mid$ data from Fig. 3.5 into Eq.(3.40) shown below and treating H_0, C and β as free parameters.

$$H_c(T) = H_0 \left[1 - \left(C \times \frac{T}{\mid K_{eff}(T) \mid}\right)^{\beta}\right]$$

These parameters are plotted as functions of average crystallite size, d, in figure 3.10. Fig. 3.10(a) includes H_c ($T = 2$ K) for comparison and serves to highlight that $H_0 \simeq H_c$ ($T = 2$ K) for all crystallite sizes, d. Barring the nanocrystalline Ni sample with $d = 20$ nm, the parameter C decreases monotonously with increasing d (Fig. 3.10(b)). If $ln[t/\tau]$ is a constant independent of d, one expects that $C \sim d^{-3}$. Obviously, this expectation is not borne out by the experiment. It follows that the quantity $ln[t/\tau]$ sensitively depends not only on average crystallite size, d, but also on the crystallite-size distribution for a given d. Fig. 3.10(c) shows that the exponent 'β' increases from $\simeq 1/2$ for $d = 10$ and 15 nm to $\simeq 2/3$ for $d = 25$ and 40 nm. If the

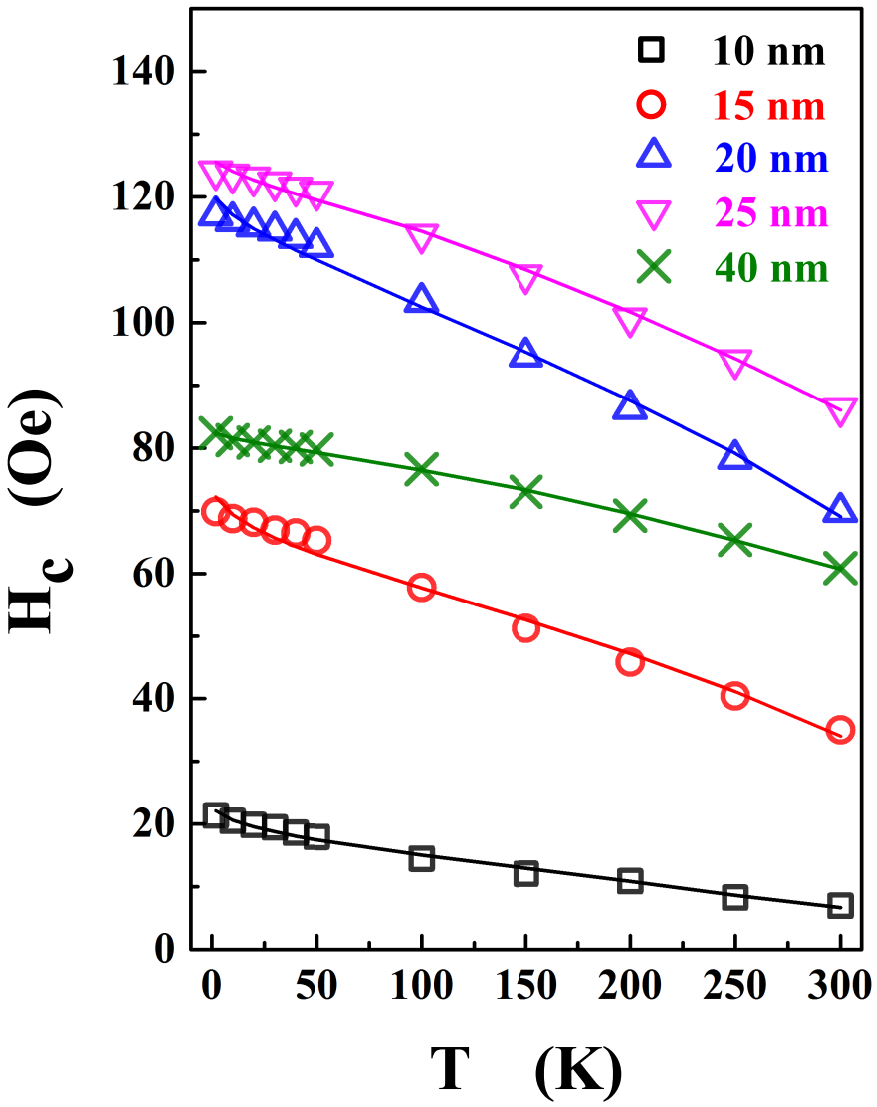

Figure 3.9: *Observed (symbols) and the theoretically predicted (continuous curves, based on Eq.(3.40)) temperature variations of H_c for nanocrystalline Ni with different average crystallite size, d. Note that the size of the symbols indicate the uncertainty in the ordinate values.*

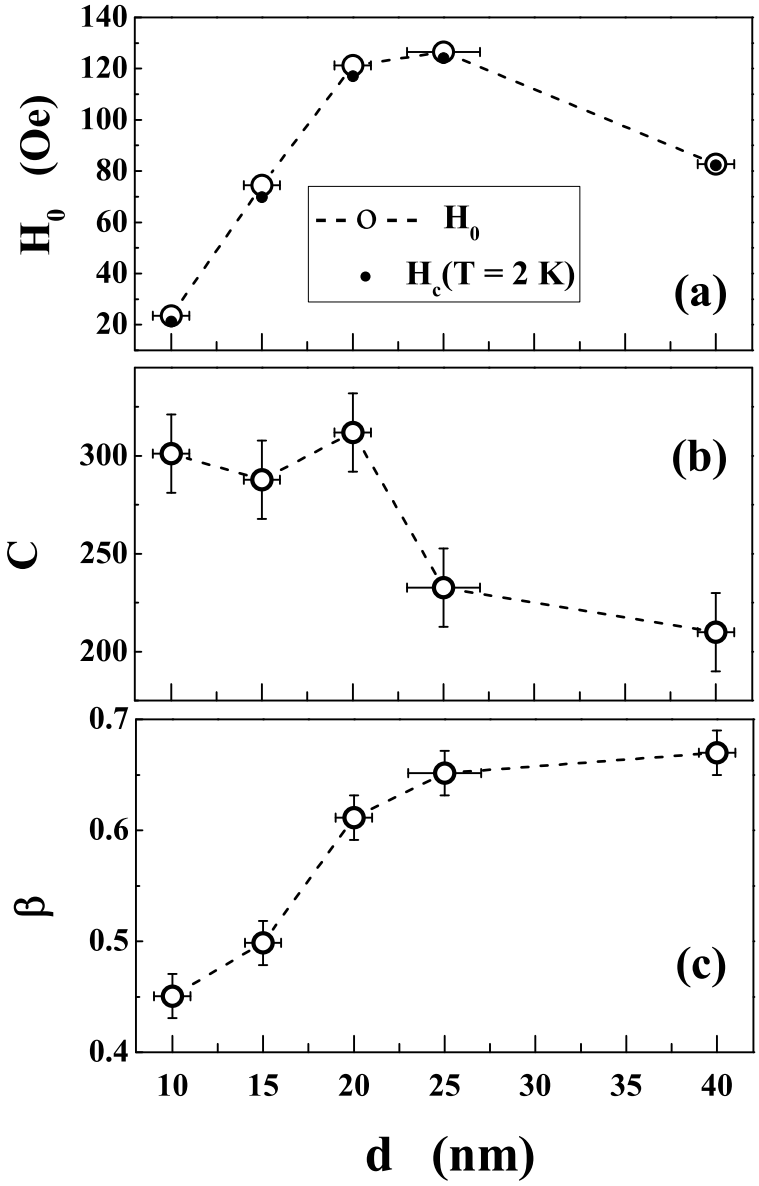

Figure 3.10: *Fit parameters: (a) H_0, (b) C and (c) β, appearing in Eq.(3.40), as functions of average grain size (d). The panel (a) includes $H_c(T = 2K)$ for comparison and demonstrates that $H_0 \simeq H_c(T = 2K)$ for all d.*

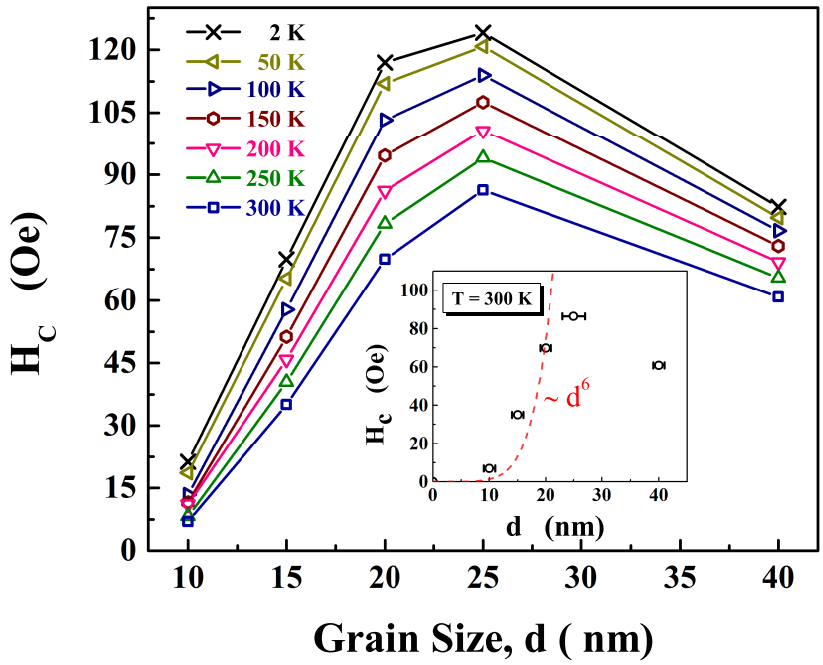

Figure 3.11: *Observed variations of H_c as a function of average crystallite size, for different temperatures, T in the range 2 K to 300 K. The inset plot compares $H_c(d)$ at T = 300 K with the d^6 power law variation (dashed curve) of H_c, predicted by the random anisotropy model, for $d \leq 20$ nm.*

angle 'ψ' is within a few degrees of the easy direction of magnetization, Victora [35] demonstrated that the exponent ($\beta = 1/2$) in Eq.(3.38) changes to $\beta \simeq 2/3$. In view of this result, the presently determined values of β indicate that H points in a direction which is not far from the easy direction of magnetization.

For fixed temperatures, as a function of the average crystallite size, H_c goes through a maximum at $d_{max} \simeq 25$ nm, as is evident from the Fig. 3.11. d_{max} has nearly the same value, 25(2) nm, as that of the single-domain critical diameter, D_{cr}, in bulk nickel, calculated from the expression [36,37] $D_{cr} = 9\ (AK)^{1/2}/\pi M_s^2$. A peak in $H_c(d)$ is generally understood in terms of the random anisotropy (RA) model [38]. According to this model, the ferromagnetic exchange interaction between *small* grains works against the random anisotropy (which causes the easy direction of intra-grain magnetization to change randomly from grain to grain) to align the spins of the

adjacent grains parallel. Consequently, the decrease in H_c for $d \lesssim D_{cr}$ results from the averaging out of the crystalline anisotropy of $(L_{ex}/d)^3$ number of grains/crystallites falling within the volume L_{ex}^3, defined by the exchange ferromagnetic length

$$L_{ex} = (A/ < K >)^{1/2} \tag{3.42}$$

where A is the exchange stiffness and $< K >$ is the average anisotropy. The random anisotropy model [38] predicts that $H_c \sim d^6$ when $L_{ex} \gg d$ and $H_c \sim d^{-1}$ when the average crystallite size exceeds the domain wall width, i.e., when $d > \pi L_{ex}$. In an attempt to find out whether this model explains the observed decline in $H_c(d)$ on either side of $d_{max} \simeq 25$ nm, the values for various relevant parameters/lengths, listed in table 3.1, are calculated as follows. While $< K > (T) \equiv K_{eff}(T)$, the exchange stiffness is computed from the spin wave stiffness, D, using the relation $A = M_s D/2g\mu_B$. 'Zero-field' $D(T)$ for the PED nanocrystalline Ni samples, same as those used in the present investigation, has been accurately determined [23] by an elaborate analysis [39–50] of the thermomagnetic data taken in the field range 10 kOe $\leq H \leq$ 70 kOe. The values of spin-wave stiffness, D at 0 K and 300 K, so obtained, are included in table 3.1. The inset of Fig. 3.11 compares the $H_c(d)$ data at a temperature of 300 K for $d \lesssim d_{max}$ with the d^6 variation (dashed curve) of coercive field, H_c, with the average crystallite size, d, predicted by the RA model when $L_{ex} \gg d$. At the first sight, a meaningful comparison between theory and experiment may not seem possible since the values of L_{ex}(300 K), listed in table 3.1, assert that the condition $L_{ex} \gg d$ is not met in the present case. However, a log-normal particle size distribution [51] ensures that a sufficient number of particles of size $\ll d$ do exist, particularly in the samples with small grain sizes (d), which significantly contribute to the reduction in H_c. Similarly, H_c decreases when crystallite size, d, increases beyond d_{max} since the RA condition $d > \pi L_{ex}$ is satisfied for the particles with size larger than d within the size distribution. Thus, the discussion of $H_c(d)$ in terms of the RA model is relevant. A drop in H_c when crystallite size, d exceeds $d_{max} \simeq D_{cr}$

(i.e., in the nanocrystalline Ni samples with multi-domain structure), also observed earlier in coarse-grain polycrystalline Ni samples, is due to the pinning of domain walls at the grain boundaries [37].

3.3.3 Irreversibility in Magnetization

Magnetization (M), was measured as a function of temperature (T), over the temperature range 2 K $\leq T \leq$ 350 K at fixed magnetic fields in the range 10 Oe $\leq H \leq$ 70 kOe under 'zero-field-cooled' (ZFC) and 'field-cooled' (FC) conditions on Quantum Design SQUID magnetometer. The measurement protocol for the ZFC and FC magnetizations is as follows. For the ZFC thermomagnetic data, the sample is first cooled in zero-field from high temperatures (350 K in the present case), down to the lowest possible temperature (2 K). A static magnetic field (H) is applied and the magnetization as a function of temperature is measured in the warming cycle from 2 K to 350 K with desired temperature steps. The FC magnetization data are obtained by measuring the magnetization while cooling the sample to low temperatures (i.e., from 350 K down to 2 K) in the same field.

The 'zero-field-cooled' magnetization ($M_{ZFC}(T)$) and 'field-cooled' magnetization ($M_{FC}(T)$) at magnetic fields (H) in the range 10 Oe $\leq H \leq$ 5 kOe are shown in figure 3.12 for samples with d = 10 nm, 15 nm, 20 nm, 25 nm and 40 nm. It is observed that the temperature, T_{irr}, at which the bifurcation between the $M_{ZFC}(T)$ and $M_{FC}(T)$ curves occurs shifts to lower temperatures with increasing applied magnetic field, particularly when applied magnetic field, $H \geq$ 500 Oe, so much so that the irreversibility in magnetization is completely suppressed for $H \backsim$ 5 kOe irrespective of average crystallite size $d \lesssim 40\ nm$ in nanocrystalline Ni.

Table 3.1: *Spontaneous magnetization (M_s), magnetic anisotropy constant (K_{eff}), spin-wave stiffness (D), exchange stiffness constant (A) and exchange ferromagnetic length (L_{ex}). The numbers within the parentheses denote the errors in the least significant figure.*

Specimen	M_s(2 K) (emu g^{-1})	-K_{eff}(2 K) (10^6 erg cm^{-3})	-K_{eff}(300 K) (10^6 erg cm^{-3})	D(0 K) (meV$\AA^2$)	D(300 K) (meV$\AA^2$)	A (0 K) (10^{-7}erg cm^{-1})	A (300 K) (10^{-7}erg cm^{-1})	L_{ex} (2 K) (nm)	L_{ex} (300 K) (nm)
Bulk-Ni	58.57(3)[a]	1.27(1)[b]	0.057(5)[c]	550(5)[d]	450(10)[d]	11.32(2)	8.60(1)	9.44(3)	38.8(17)
nc-Ni 55 nm	58.0(1)[e]	–	–	450(10)[e]	370(20)[e]	9.2(2)[e]	7.6(3)[e]	–	–
nc-Ni 40 nm	58.420(8)[g]	1.259(32)[g]	0.455(13)[g]	432(1)[f]	416(2)[f]	8.87(2)[g]	7.92(4)[g]	8.4(1)[g]	13.2(2)[g]
nc-Ni 25 nm	58.290(7)[g]	1.037(35)[g]	0.402(11)[g]	410(2)[f]	374(5)[f]	8.40(4)[g]	7.12(9)[g]	9.0(2)[g]	13.3(1)[g]
nc-Ni 20 nm	58.098(2)[g]	0.777(30)[g]	0.372(11)[g]	404(1)[f]	357(1)[f]	8.25(2)[g]	6.77(2)[g]	10.3(3)[g]	13.5(2)[g]
nc-Ni 15 nm	57.633(1)[g]	0.638(30)[g]	0.294(20)[g]	398(2)[f]	339(3)[f]	8.06(4)[g]	6.40(6)[g]	11.2(4)[g]	14.8(11)[g]
nc-Ni 10 nm	57.085(1)[g]	0.324(15)[g]	0.190(15)[g]	393(2)[f]	313(2)[f]	7.89(4)[g]	5.83(4)[g]	15.6(3)[g]	17.5(14)[g]

[a]Ref [25]; [b]Ref [26, 27]; [c]Ref [14]; [d]Ref [52]; [e]Ref [53] ; [f] Ref [23]; [g] Present work.

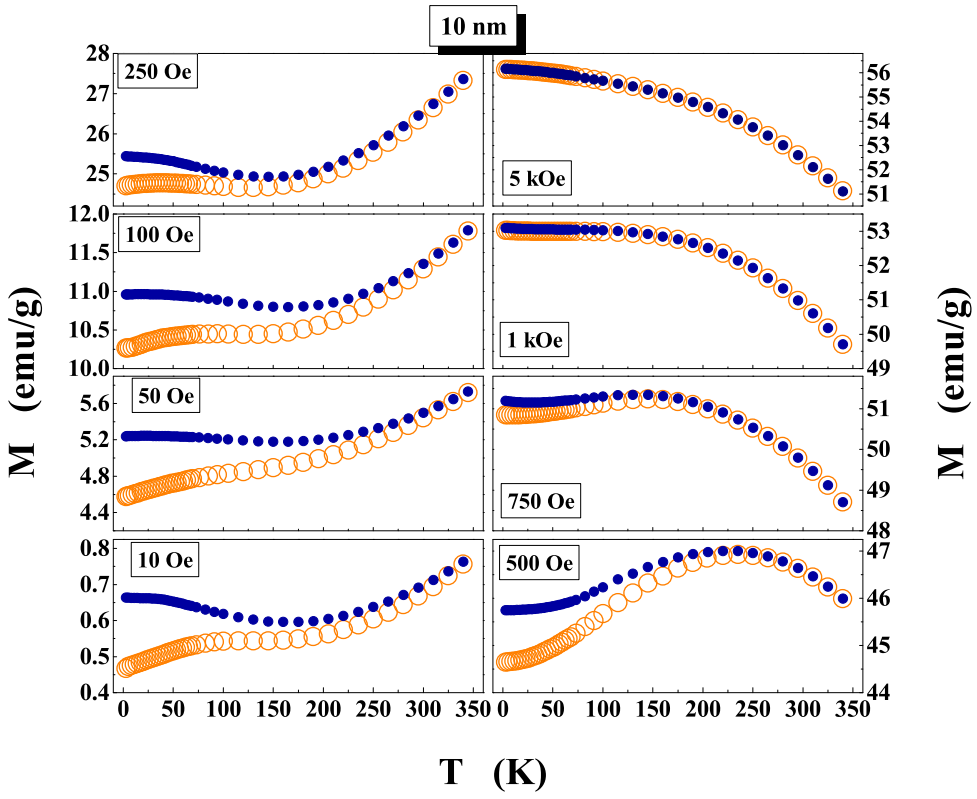

Figure 3.12: *The 'field-cooled' (FC) (•) and 'zero-field-cooled' (ZFC) (○) magnetizations as functions of temperature, T, at fixed fields in the range, 10 Oe ≤ H ≤ 5 kOe for nc Ni with d = 10(1) nm.*

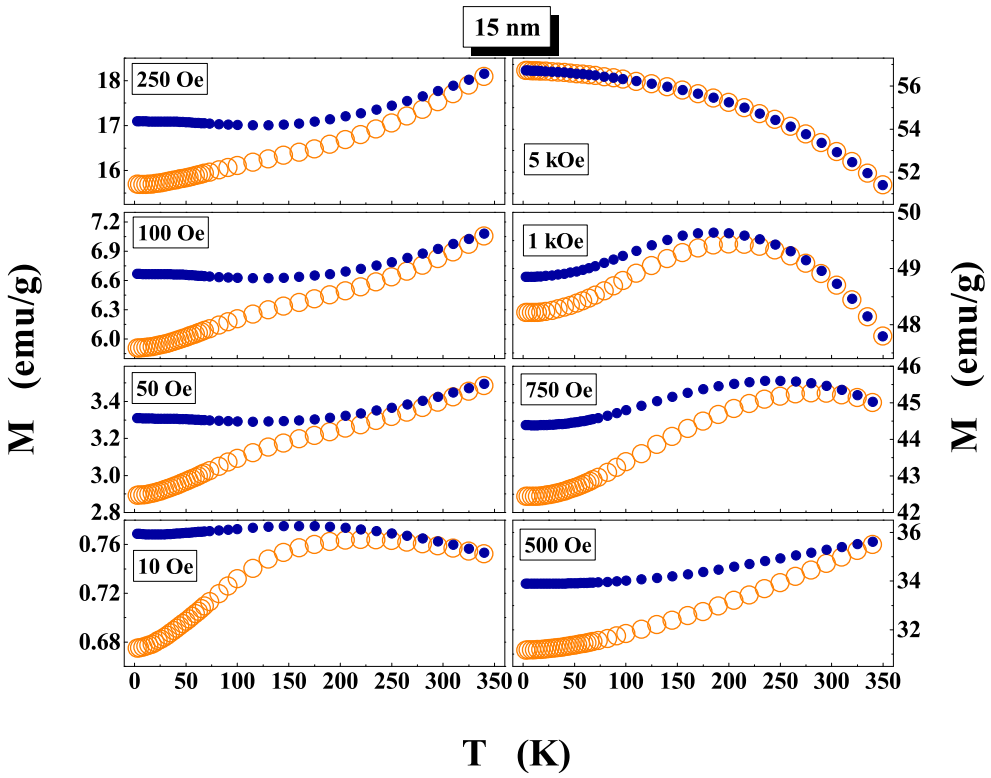

Figure 3.12 (Continued): *The 'field-cooled' (FC) (•) and 'zero-field-cooled' (ZFC) (○) magnetizations as functions of temperature, T, at fixed fields in the range, 10 Oe ≤ H ≤ 5 kOe for nc Ni with d = 15(1) nm.*

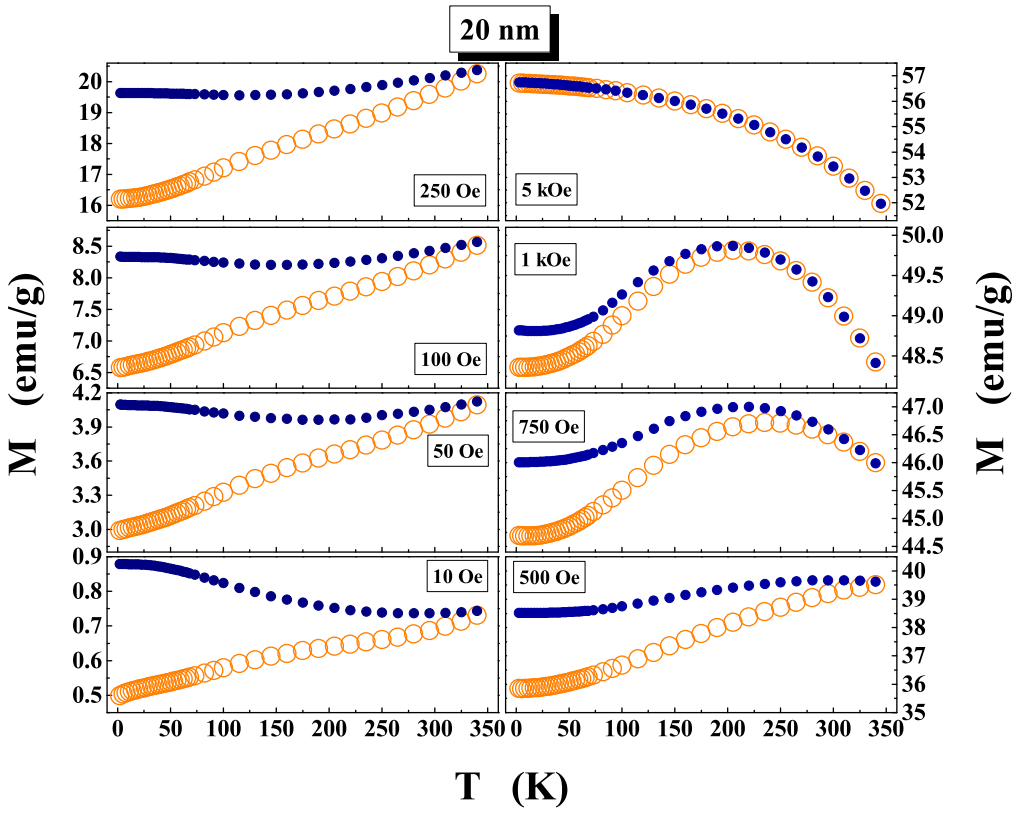

Figure 3.12 (Continued): *The 'field-cooled' (FC) (•) and 'zero-field-cooled' (ZFC) (○) magnetizations as functions of temperature, T, at fixed fields in the range, 10 Oe ≤ H ≤ 5 kOe for nc Ni with d = 20(1) nm.*

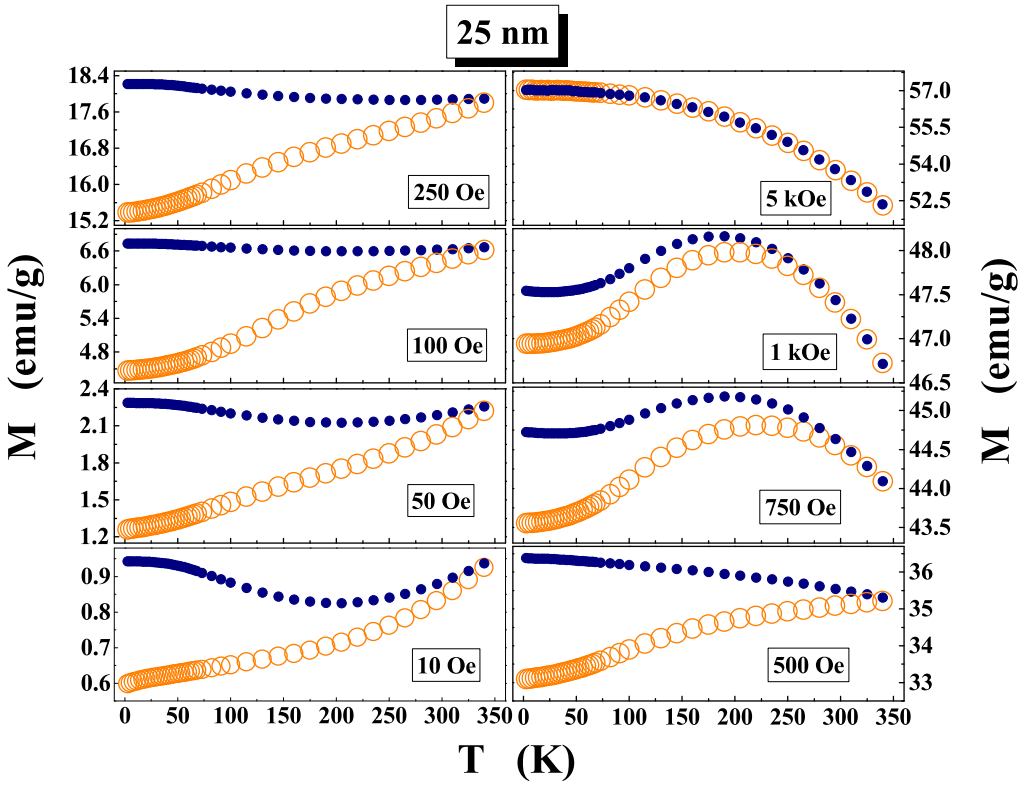

Figure 3.12 (Continued): *The 'field-cooled' (FC) (•) and 'zero-field-cooled' (ZFC) (○) magnetizations as functions of temperature, T, at fixed fields in the range, 10 Oe ≤ H ≤ 5 kOe for nc Ni with d = 25(2) nm.*

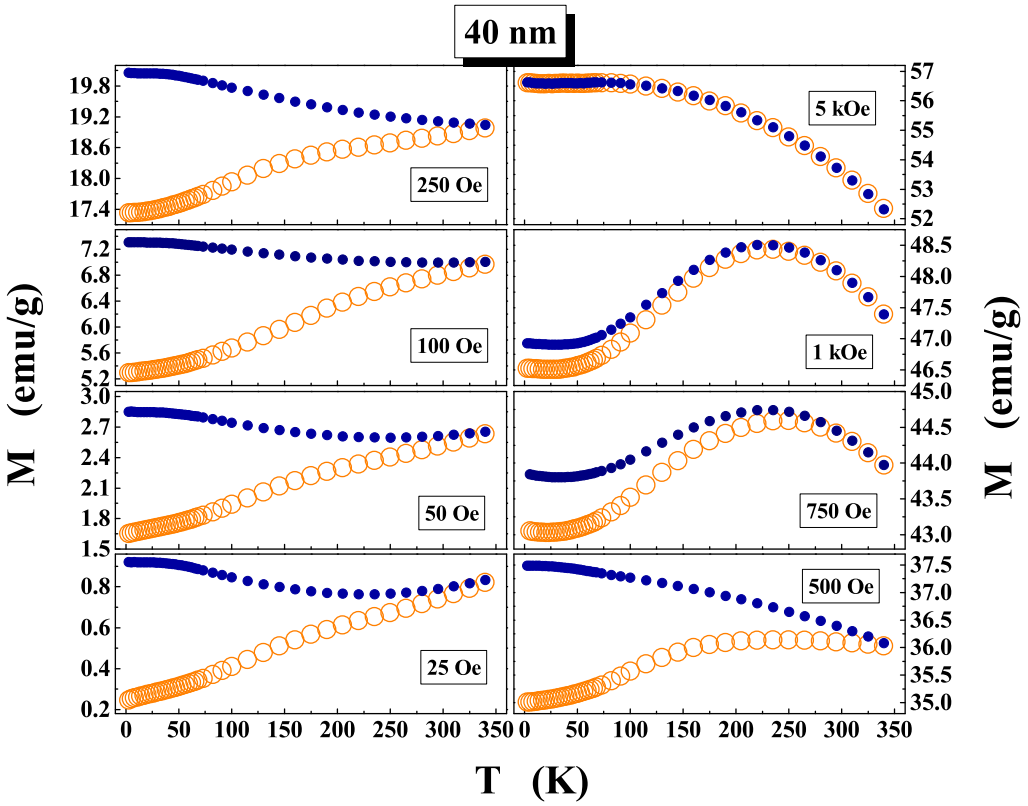

Figure 3.12 (Continued): *The 'field-cooled' (FC) (•) and 'zero-field-cooled' (ZFC) (○) magnetizations as functions of temperature, T, at fixed fields in the range, 10 Oe ≤ H ≤ 5 kOe for nc Ni with d = 40(1) nm.*

Figure 3.13 displays the difference between the FC magnetization, and ZFC magnetization, $\triangle$M(T) $\equiv$ [$M_{FC}(T)$ - $M_{ZFC}(T)$], normalized to field-cooled magnetization, i.e., $\triangle$M(T) / $M_{FC}(T)$, at fields in the range 10 Oe $\leq H \leq$ 5 kOe, for the nanocrystalline Ni samples under study. The difference between the FC and ZFC magnetizations at a given temperature $T \lesssim T_{irr}$, $\triangle$M(T), is a direct measure of the irreversibility in magnetization and arises when the intra-grain magnetizations of a sizable fraction of the total number of grains/crystallites are trapped in the high-energy metastable 'zero-field-cooled' magnetization state, which is separated from the stable minimum energy 'field-cooled' magnetization state by the energy barriers caused by the effective magnetocrystalline (intra-grain and grain boundary / interfacial) anisotropy [22]. When the applied magnetic field is sufficient to make the spins to overcome these effective anisotropy energy barriers, there is only one stable minimum energy configuration which is 'field-cooled' state, and the difference between $M_{FC}(T)$ and $M_{ZFC}(T)$ vanishes.

In an attempt to qualitatively understand as to how the trapping of the spin system in a metastable or a stable state depends on the thermal/field pre-history of the system and how this process gives rise to a large irreversibility in magnetization, we put forward an intuitive picture of the magnetization state of a single-domain grain in terms of its free energy, E, as a function of the angle between magnetization and the easy direction of magnetization, θ, for a uniaxial system, as given in figure 3.14. When the nanocrystalline ferromagnetic system is cooled in 'zero-field' from a temperature above its ordering temperature, T_C, where the long-range magnetic order sets in, magnetization vector in each grain is frozen along the easy direction of magnetization - either in the M_0 state or M_{180} state, which are equally probable (Fig. 3.14(b)). Hence, when the ensemble of grain magnetizations is considered, M_0 and M_{180} states will be equally populated. Since the crystallographic directions of each grain is oriented at random, the magnetization vector in each grain is also oriented

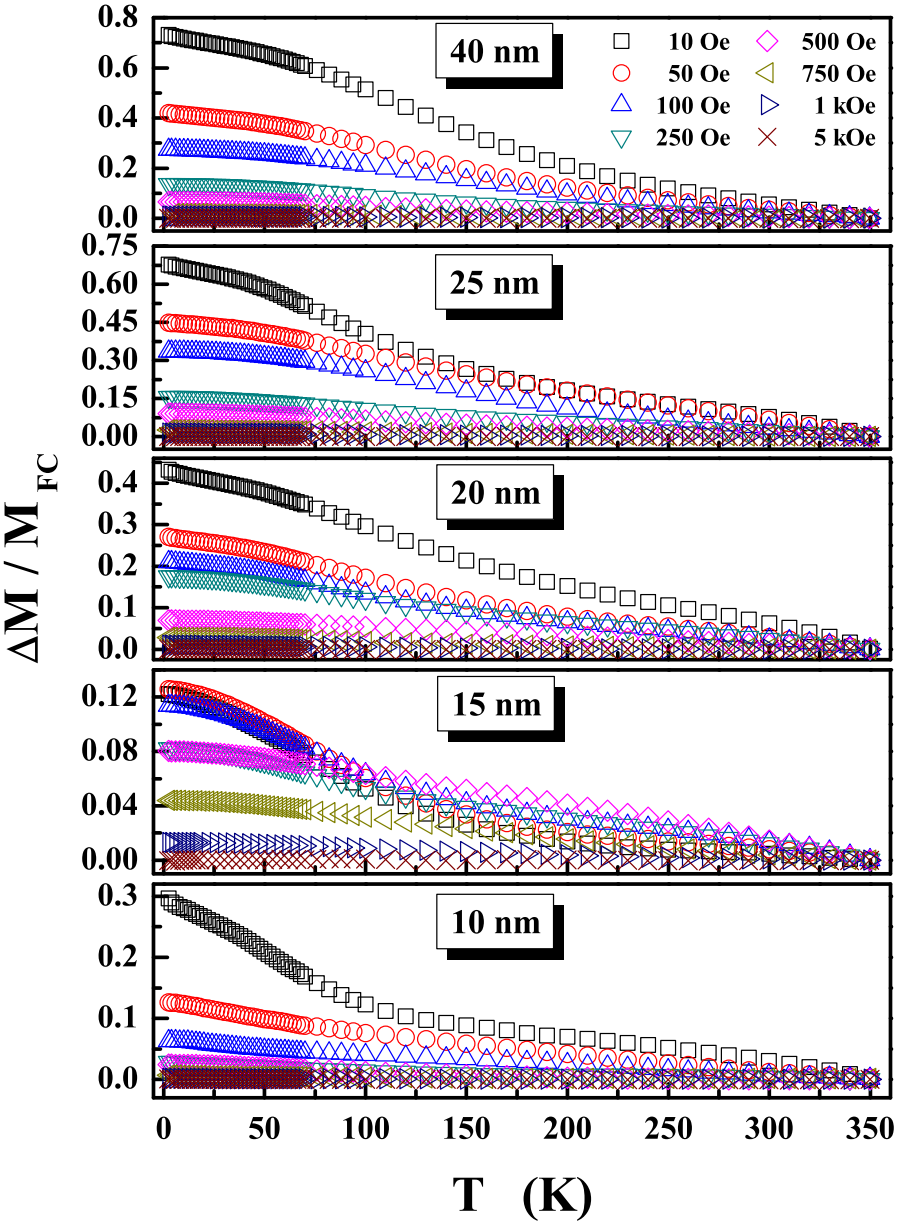

Figure 3.13: *Irreversibility in magnetization, $\triangle M(T)$, normalized to the field-cooled magnetization, $M_{FC}(T)$, over a temperature range $2K \leq T \leq 350$ K at fixed magnetic fields, 10 Oe $\leq H \leq$ 5 kOe.*

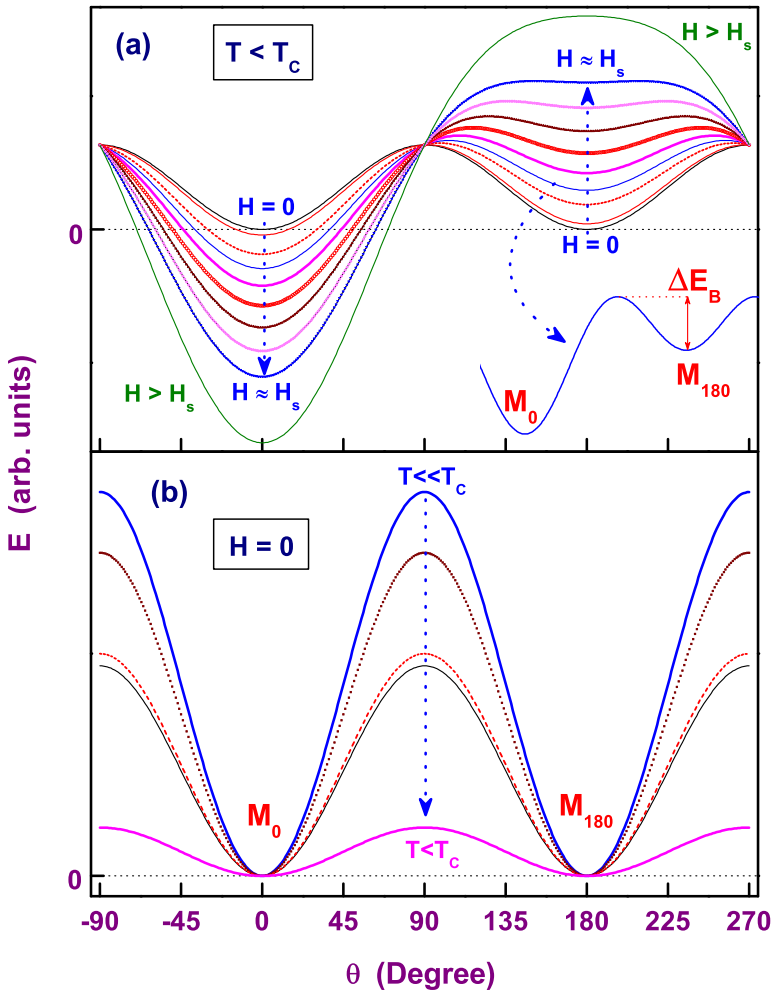

Figure 3.14: *A schematic representation of the free energy, E, versus the angle between magnetization and the easy direction of magnetization, θ, for a uniaxial system. M_0 (M_{180}) is the energy state of a single grain when the magnetization is pointing along (opposite to) the easy direction of magnetization $\theta = 0$ ($\theta = 180$). At zero-field, both the M_0 and M_{180} states are equally probable. ΔE_B is the effective energy barrier height seen by the spins in the M_{180} state, which varies with the effective field and temperature. (a) The E versus θ curves at a temperature, $T < T_C$, for various fields starting from $H = 0$ to $H > H_s$ and (b) at various temperatures starting from $T \ll T_C$ to $T < T_C$ in zero field, $H = 0$.*

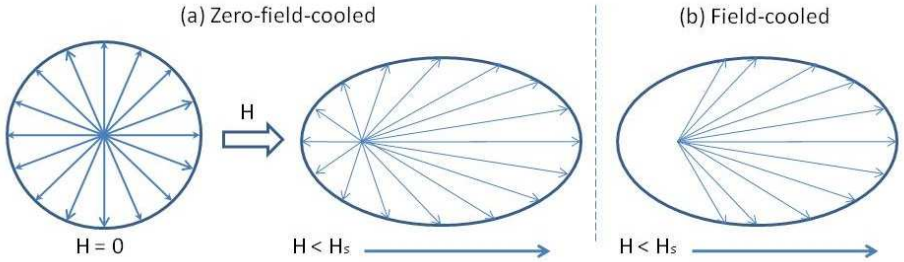

Figure 3.15: *A representative picture describing the orientation of magnetization vector in different grains before and after the application of field in the 'zero-field-cooled' state and in the 'field-cooled' state.*

at random, giving rise to zero net magnetization as represented by the $H = 0$ case in figure 3.15(a). At finite positive field ($H < H_s$, the switching field), applied parallel to the easy direction of magnetization, the energy, E, versus θ curves get biased such that the stable minimum is at $\theta = 0$ (Fig. 3.15(a)). In this condition, the population in the M_0 state, the stable minimum state, will be more than that in the M_{180} state, the metastable minimum state, so that the net magnetization along the field direction is positive. At a finite temperature and field, the spins in the metastable state see an effective energy barrier, ΔE_B, due to the intragranular and interfacial magnetic anisotropies and the external magnetic field. ΔE_B decreases with increasing field but the temperature dependence of ΔE_B arises from the temperature dependence of the effective anisotropy field. With decreasing ΔE_B, the population of spins in the stable state increases at the expense of that in the metastable state.

When the magnetic field is applied at the lowest temperature after cooling the system in 'zero-field', the net magnetization along the field direction will be the ensemble average of the magnetizations of the grains, more of them in the stable minimum energy state, M_0, than in the metastable state, M_{180}. The metastable state corresponds to the low-magnetization state, M_{ZFC}. In this state, the temperature dependence of the component of magnetization along the field direction at fixed fields, $H < H_s$, is governed by three factors, i) the usual decrease in the domain

magnetization due to the thermal effect, ii) the population of spins in the metastable state changes depending on how the $\Delta E_B(T)$ compares with thermal energy, k_BT, and iii) the average component of magnetization along the field direction is decided by the relative strength of the temperature-dependent effective anisotropy field and the external magnetic field. The spin system attains high-magnetization stable state when the system is cooled 'in-field' from a temperature above T_C and the domain formation takes place in presence of external magnetic field, the magnetization in most of the grains corresponds to the stable minimum, M_0, at $\theta = 0$ (Fig. 3.14(a)). Therefore, the magnetizations of the grains will be pointing in a hemisphere along the field direction and the population of spins in the metastable state goes on reducing with increasing field (Fig. 3.15(b)). Consequently, magnetization enters into the high-magnetization stable state, M_{FC}.

The $M_{ZFC}(T)$ at low fields is a clear depiction of the temperature dependence of the effective anisotropy field. With increasing field, the effective energy barrier height seen by the spins in the metastable state decreases and the thermal energy suffices to activate magnetization across the energy barrier. As a result, the overall magnetization prefers to be in M_{FC} state and this, in turn, reduces the irreversibility in magnetization. When a threshold (switching) field, H_s, is reached, only a single global minimum, corresponding to the high-magnetization stable state, M_{FC}, exists. Thus, the magnetic irreversibility vanishes for $H \geq H_s$. Obviously, H_s depends on temperature; H_s will have its maximum value at $T = 0$ and $H_s = 0$ at $T \geq T_C$ where only the global minimum survives and the critical fluctuations of magnetization ensure that the spontaneous magnetization goes to zero.

3.4 Summary and Conclusion

By making use of the micromagnetic treatment of the 'approach-to-saturation' in magnetization, based on the Brown-Néel model, the effective magnetic anisotropy (MA) constant (MA energy density), K_{eff}, as a function of temperature in the range 2 K $\leq T \leq$ 300 K, is deduced from the magnetization (M) versus magnetic field (H) isotherms taken on nanocrystalline Ni samples with average crystallite size, d, ranging from 10 to 40 nm.

- For a fixed d and at any given temperature, the contributions to $K_{eff}(T)$ arising from the volume (core) magnetocrystalline anisotropy, $K_1^c(T)$, the surface/interface anisotropy, $K_s(T)$, and shape anisotropy, $K_{shape}(T)$, are assumed to be additive.

- The result that a linear relationship exists between '$K_{eff} \times d$' and 'd' not only validates this assumption in the present case but also permits an accurate determination of $K_1^c(T)$, $K_s(T)$ and $K_{shape}(T)$.

- Thermal activation over an effective anisotropy energy barrier (which separates two local energy minima and depends on both temperature and magnetic field), as the mechanism for magnetization reversal, is shown to account for the observed temperature dependence of the coercive field.

- Another important finding is that the magnetic moment per Ni atom, μ_{Ni}, deduced from the saturation magnetization at 2 K, increases with d in accordance with the relation $\mu_{Ni}(d) = \mu_{Ni}(d = \infty)$ [1 - $b \times d^{-3/2}$], with the magnetic moment per Ni atom in the bulk at $T = 2$ K, $\mu_{Ni}(d = \infty) = 0.616\ \mu_B$, and $b = 0.50(5)$.

- High-precision magnetization, $M(T, H)$, measured in 'zero-field-cooled', ZFC

and 'field-cooled', FC modes reveals irrevesibility in magnetization below a characteristic field (H_S = Switching field) in nanocrystalline Ni.

- Irreversibility in magnetization is completely suppressed for $H \backsim 5$ kOe irrespective of average crystallite size $d \lesssim 40$ nm in nanocrystalline Ni. This irreversibility is addressed in terms of the trapping of sizable fraction of magnetization in the metastable (high-energy) states separated from the stable (low-energy) states below the switching field, due to the energy barriers caused by effective anisotropy that is a resultant of intragrain crystalline and intergrain interfacial and/or surface magnetic anisotropies.

References

1. A. H. Lu, W. Schmidt, N. Matoussevitch, H. Bönnemann, B. Spliethoff, B. Tesche, E. Bill, W. Kiefer and F. Schüth, *Angew. Chem.* **116**, 4403 (2004).

2. M. Arruebo, R. Fernández-Pachcco, M. R. Ibarra and Santamaría, *Nanotoday* **2**, 22 (2007).

3. A. K. Gupta and M. Gupta, *Biomaterials* **26**, 3995 (2005).

4. R. Bussamara, D. Eberhardt, A. F. Feil, P. Migowski, H. Wender, D. P. de Moraes, G. Machado, R. M. Papaléo, S. R. Teixeira and J. Dupont, *Chem. Commun.* **49**, 1273 (2013).

5. P. Kalita, J. Singh, M. K. Singh, P. R. Solanki, G. Sumana and B. D. Malhotra, *Appl. Phys. Lett.* **100**, 093702 (2012).

6. S. H. Chung, A. Hoffmann, S. D. Bader, C. Liu, B. Kay, L. Makowski and L. Chen, *Appl. Phys. Lett.* **85**, 2971 (2004).

7. W. J. Gallangher and S. S. P. Parkin, *IBM J. Res. Dev.* **50**, 5 (2006).

8. Z. Z. Bandić and R. H. Victora, *Proc. IEEE* **96**, 1749 (2008).

9. N. S.Akulov, *Zeits. f. Physik* **69**, 822 (1931).

10. R. Gans, *Ann. d. Physik* **15**, 28 (1932).

11. W. F. Brown, Jr., *Phys. Rev.* **58**, 736 (1940).

12. W. F. Brown, Jr., *Phys. Rev.* **60**, 139 (1941).

13. L Néel, *J. Phys. Rad.* **9**, 184 (1948); L Néel, *J. Phys. Rad.* **9**, 193 (1948).

14. S. Chikazumi, *Physics of Ferromagnetism*, Oxford University Press (Oxford, UK), p **506, 251**, 1997.

15. H. Kronmüller, *IEEE. Trans. Magn.* **MAG-15**, 1218 (1979).

16. E. M. Chudnovsky and R. A. Serota, *Phys. Rev. B* **26**, 2697 (1982).

17. E. M. Chudnovsky, V. M. Saslow and R. A. Serota, *Phys. Rev. B* **33**, 251 (1986).

18. S. F. Edwards and P. W. Anderson, *J. Phys. F* **5**, 965 (1975).

19. R. Harris, M. Plischke and M. J. Zuckermann, *Phys. Rev. Lett.* **31**, 160 (1973).

20. S. N. Kaul, *Current Science* **88**, 78 (2005).

21. L. Néel, *Ann. Geophys.* **5**, 99 (1949).

22. S. P. Mathew and S. N. Kaul, *J. Phys.: Condens. Matter.* **24**, 256008 (2012).

23. P. V. Prakash Madduri and S. N. Kaul, *J. Mag. Mag. Mater.* **418**, 143 (2016).

24. Xuemin He, Wei Zhong, Chak-Tong Au and Youwei Du, *Nanoscale Research Letters* **8**, 446 (2013).

25. H. Danan, A. Herr and A. J. P. Mayer, *J. Appl. Phys.* **39**, 669 (1968).

26. G. Aubert, *J. Appl. Phys.* **39**, 504 (1968).

27. P. Escudier, *Ann. Phys., Paris* **9**, 125 (1975).

28. L. Néel, *J. Phys. Rad.* **15**, 225 (1954).

29. X. Batlle and A. Labarta, *J. Phys. D: Appl. Phys.* **35**, R 15 (2002).

30. Q. Bian and M. Niewczas, *J. Appl. Phys.* **116**, 033921 (2014).

31. R. Yanes, O. Chubykalo-Fesenko, H. Kachkachi, D. A. Garanin, R. Evans and R. W. Chantrell, *Phys. Rev. B* **76**, 064416 (2007).

32. D. A. Garanin and H. Kachkachi, *Phys. Rev. Lett.* **90**, 065504 (2003) ; H. Kachkachi and E. Bonet, *Phys. Rev. B* **73**, 224402 (2006).

33. R. Yanes, O. Chubykalo-Fesenko, R. F. L. Evans and R. W. Chantrell, *J. Phys. D: Appl. Phys.* **43**, 474009 (2010).

34. J. F. Löffler, J. P. Meier, B. Doudin, J-P. Ansermet and W. Wagner, *Phys. Rev. B* **57**, 2915 (1998).

35. R. H. Victora, *Phys. Rev. Lett.* **63**, 457 (1989).

36. C. Kittel, *Rev. Mod. Phys.* **21**, 541 (1949).

37. A. Mager, *Ann. Phys. (Leipzig)* **11**, 15 (1952).

38. G. Herzer, *J. Mag. Mag. Mater.* **122**, 258 (1992).

39. S. N. Kaul and M. Rosenberg, *Phys. Rev.* B **25**, 5863 (1982).

40. S. N. Kaul and M. Rosenberg, *Phys. Rev.* B **27**, 5698 (1983).

41. S. N. Kaul, *Phys. Rev.* B **27**, 5761 (1983); S. N. Kaul, *Phys. Rev.* B **27**, 6923 (1983).

42. S. N. Kaul, *J. Phys.: Condens. Matter* **3**, 4027 (1991).

43. S. N. Kaul, V. Siruguri and G. Chandra, *Phys. Rev.* B **45**, 12343 (1992).

44. S. N. Kaul and P. D. Babu, *Phys. Rev.* B **45**, 295 (1992).

45. S. N. Kaul and P. D. Babu, *Phys. Rev.* B **50**, 9308 (1994).

46. S. N. Kaul and P. D. Babu, *J. Phys.: Condens. Matter* **10**, 1563 (1998).

47. S. N. Kaul, *J. Phys.: Condens. Matter* **11**, 7597 (1999).

48. A. Semwal and S. N. Kaul, *Phys. Rev.* B **60**, 12799 (1999).

49. S. N. Kaul, A. Semwal and H. E. Schaefer, *Phys. Rev.* B **62**, 13892 (2000).

50. S. N. Kaul, *J. Phys.: Condens. Matter* **17**, 5595 (2005).

51. A. M. El-sheric and U. Erb, *J. Mater. Sci.* **30**, 5743 (1995).

52. A. T. Aldred, *Phys. Rev. B* **11**, 2597 (1975).

53. J. Weissmüller, A. Michels, J. G. Barker, A. Widenmann, U. Erb and R. D. Shull, *Phys. Rev. B* **63**, 214414 (2001).

Chapter 4

Low-lying Magnetic Excitations

This chapter deals with the nature of low-lying (in energy) magnetic excitations in nanocrystalline itinerant-electron ferromagnet such as Ni. An elaborate analysis of the decline of magnetization with increasing temperature, observed in nanocrystalline (nc-) Ni samples with average crystallite size, d, varying from d = 10 nm to 40 nm, permits us to (i) completely rule out a possible Stoner single-particle contribution to the thermal demagnetization, $M(T)$, at external magnetic fields 10 kOe $\leq H \leq$ 70 kOe and temperatures $T \leq$ 350 K, (ii) demonstrate that spin-wave (SW) excitations alone account for the observed $M_H(T)$ and (iii) the thermal renormalization of spin-wave stiffness is primarily due to the magnon-magnon interactions. For fields H $\geq$ 20 kOe, the spin-wave stiffness at 0 K, $D(T = 0, H)$, is found to decrease with field as $D(T = 0, H) \sim H^{1/2}$ for all the nanocrystalline samples. Extrapolation of the $D(T = 0, H)$ - $H^{1/2}$ straight line to $H = 0$ yields $D_0 \equiv D(T = 0, H = 0)$ for a sample of given d. D_0 varies with average crystallite size, d, as $d^{4/3}$. This power law behavior of D_0 asserts that the crystallite size is the relevant length scale for spin waves. Strong departures from the spin-wave behavior are observed at low

This chapter is based on the following articles:
1. P. V. Prakash Madduri and S. N. Kaul, *J. Mag. Mag. Mater.*, **418**, 143 (2016).
2. P. V. Prakash Madduri and S. N. Kaul, *AIP Conf. Proc.*, **1536**, 89 (2013).

temperatures $T \leq T^{\dagger}(H)$ in nanocrystalline Ni with average crystallite size, $d = 10$ nm. Such departures, marked by the $T^{4/3}$ power law behavior of $[M_H(T)]^2$, are a manifestation of damped spin waves, which act as non-propagating spin fluctuations and get suppressed by magnetic field in accordance with the $H^{1/2}$ power law.

4.1 Introduction

Despite intense efforts to ascertain the average crystallite size (d) dependence of magnetic properties of nanocrystalline (nc-) elemental 3d transition metal ferromagnets, Fe, Co, Ni, many aspects of magnetic behavior still remain obscure. One such issue, which is of primary concern in the present investigation, pertains to the nature of low-lying magnetic excitations. To elucidate this point further, strong departures from the spin-wave $T^{3/2}$ variation of magnetization for $T \leq 350$ K were reported [1] in nanocrystalline Ni with $d = 10$ nm. This sample was prepared by the inert gas condensation (IGC) technique and had an atomic mass density (ρ_n) that is ~ 80 % of the bulk density (ρ_B). The T^2 power law decline in magnetization with increasing temperature observed in the $d = 10$ nm IGC nanocrystalline Ni was taken to imply that the Stoner single-particle excitations are responsible [1] for the thermal demagnetization. In sharp contrast, small-angle neutron scattering (SANS) experiments [2] on nanocrystalline Ni with $d \simeq 55$ nm and $\rho_n \cong \rho_B$, synthesized by the pulsed electrodeposition (PED), revealed the existence of well-defined spin waves. It is not clear from these conflicting reports if the drastic change in density and hence in the atomic structure in the grain boundary regions is at the root of this discrepancy or if the reduction in d changes the nature of low-lying magnetic excitations or if below a certain value of d, it is harder to excite spin waves at low and intermediate temperatures. Thus, a systematic study of the effect of crystallite size on magnetic excitations, particularly in the PED nanocrystalline samples (which, unlike

their IGC counterparts, are not prone to oxidation), is called for.

4.2 Theoretical Considerations

4.2.1 Low-lying Magnetic Excitations in Itinerant-electron Ferromagnes

Unlike localized-spin ferromagnets in which spin waves are the only magnetic excitations that fill the entire Brillouin zone, in itinerant-electron ferromagnets, apart from propagating transverse spin fluctuations (spin waves), there exist non-propagating longitudinal and transverse spin fluctuations, and Stoner single-particle excitations.

4.2.2 Spin waves

In a wide variety of spin systems regardless of whether they are crystalline or amorphous, insulating (localized-spin) or metallic (itinerant-spin), ferromagnetic or antiferromagnetic, or even ferrimagnetic, spin waves exist as well-defined low-lying (in energy) collective magnetic excitations from the ground state. Spin wave excitations, involving energy transfer typically of the order of ($\sim$) 100 meV, are amenable to direct detection in the inelastic neutron scattering experiments on bulk samples [3]. The transfer of an electron-hole pair excitation, which results from a spin-flip on an atom, from atom to atom gives rise to spin-wave excitations (Schematic representation is shown in figure 4.1). The typical spin wave energy is about $\sim$ 100 meV, nearly two orders of magnitude smaller than the 3d-band width and hence the time scale associated with this energy is $t_{SW} \approx h/W \approx 10^{-13}s$ [3]. In itinerant-electron ferromagnets, spin waves exist as well-defined collective excitations only in the small momentum transfer, q and small $E_q = \hbar\omega_q$ region in the Brillouin zone (see figure 4.3).

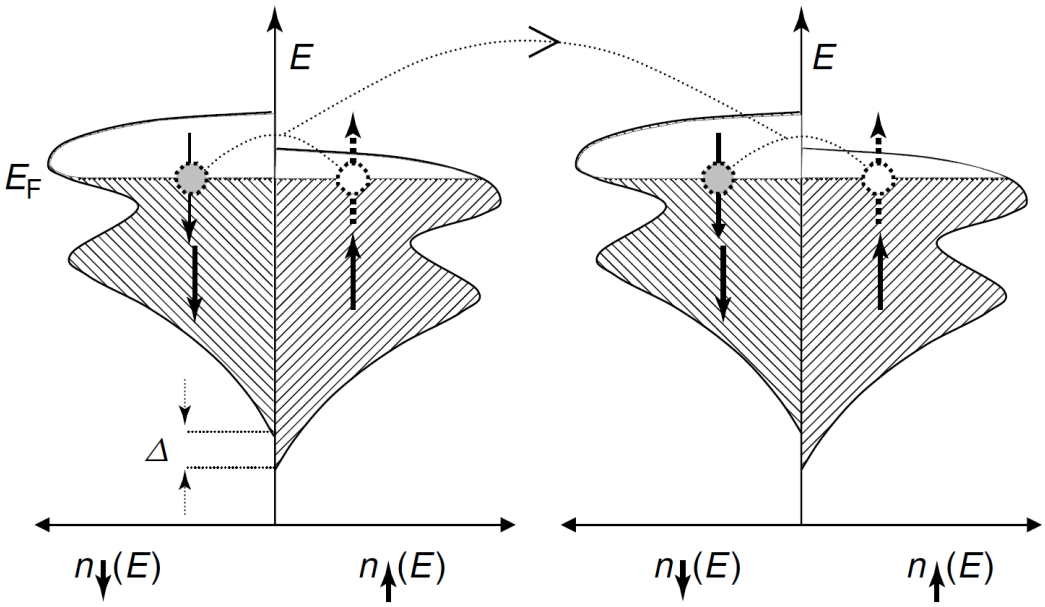

Figure 4.1: *Schematic representation of spin-wave excitation in weak itinerant-electron ferromagnet [3].*

4.2.3 Stoner single-particle excitations

At low temperatures, the spin-flip excitation spectrum consists of single-particle excitations and collective excitations. Spin-up holes and spin-down electrons are created by intra-atomic spin-flip transitions of electrons (as sketched in figure 4.2 for weak itinerant(WI) and strong itinerant(SI)-electron ferromagnets). These spin-up holes and spin-down electrons move independent of one another in a common mean (exchange) field and constitute the single-particle excitations. Such excitations form the Stoner continuum, which, at finite momentum transfer q, extends from $E_q = 0$ in figure 4.2(a) ($E_q = \Delta' = E_F(Fermi\ energy) - E_{\uparrow}^{top}$ in Fig 4.2(b)) to high

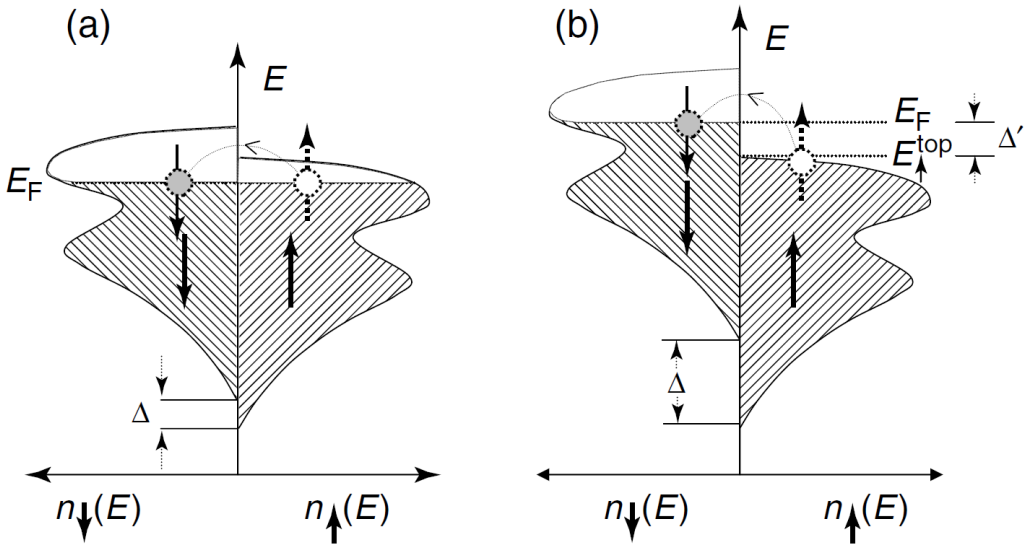

Figure 4.2: *Schematic representation of spin-flip Stoner single particle excitation in (a) weak itinerant electron ferromagnet and (b) strong itinerant electron ferromagnet [3].*

energies, as schematically depicted in Fig 4.2(a) (4.2(b)) for weak (strong) itinerant-electron ferromagnets. Single-particle excitations with zero momentum transfer ($q = 0$) cost an energy equal to the exchange splitting (figure 4.3). Stoner single-particle excitations require high energies of the order of intra-atomic exchange splitting $\Delta = U\,(n_\uparrow - n_\downarrow)$; U is the intra-atomic exchange interaction and $n_\uparrow(n_\downarrow)$ is the population of the spin-up (spin-down) band (figures 4.2 and 4.3).

4.2.4 Spin fluctuations

As the momentum transfer q increases from zero, the energy gap between the Stoner continuum and spin-wave spectrum reduces rapidly so much so that beyond a certain threshold value of $q = q_{SB}$, where SB is Stoner Boundary of the single particle excitations, the spin wave dispersion curve enters the Stoner continuum. For $q > q_{SB}$, the spin waves get damped with the result that the collective magnetic excitations

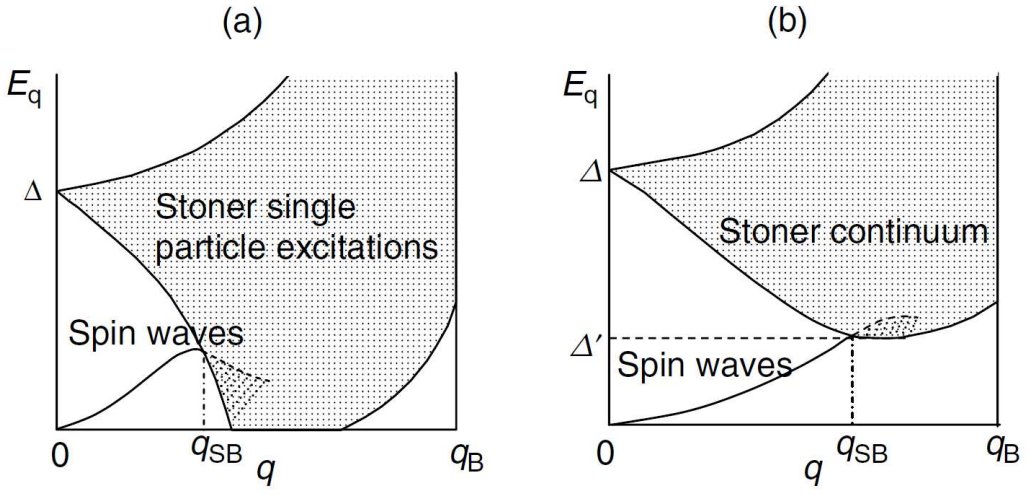

Figure 4.3: *Schematic representation of magnetic dispersion and magnetic excitations in a (a) weak itinerant-electron ferromagnet and (b) strong itinerant-electron ferromagnet [3].*

in the Stoner continuum are the overdamped (non-propagating) modes of exchange-enhanced longitudinal and transverse spin-density fluctuations. For spin fluctuations of given q, in the longitudinal mode, the magnetic moments point in the same direction but their amplitude fluctuates from one lattice site to the other whereas in the transverse mode, amplitude of the magnetic moments remains nearly constant while their direction varies from site to site. Since spin wave modes of larger and larger q are excited as the temperature is raised from $T = 0$, the transition at $q = q_{SB}$, from well-defined spin waves to non-propagating exchange-enhanced transverse spin fluctuations should be observed at a certain finite value of temperature. By contrast, the thermally-excited non-propagating exchange-enhanced longitudinal spin-density fluctuations persist down to $q = 0$ and coexist with, but are swamped by, spin waves for $q \leq q_{SB}$ [4, 5].

In itinerant-electron ferromagnets such as Fe, Co, Ni, spin waves (SW) and Stoner single-particle (SP) excitations independently contribute to the fractional decrease in

magnetization with increasing temperature at a given field, defined as $\Delta m(T,H) \equiv [M(0,H) - M(T,H)]/M(0,H)$. Thus, $\Delta m(T,H)$ is the sum [3–17] of the SW and SP contributions, $\Delta m_{SW}(T,H)$ and $\Delta m_{SP}(T,H)$, i.e.,

$$\Delta m(T,H) = \Delta m_{SW}(T,H) + \Delta m_{SP}(T,H) \tag{4.1}$$

with $\Delta m_{SW}(T,H)$ and $\Delta m_{SP}(T,H)$ given by

$$\Delta m_{SW}(T,H) = \frac{g\mu_B}{M(0,H)} \left[Z(3/2,t_H) \left(\frac{k_B T}{4\pi D(T)} \right)^{3/2} + 15\pi\ \beta\ Z(5/2,t_H) \left(\frac{k_B T}{4\pi D(T)} \right)^{5/2} \right] \tag{4.2}$$

$$\Delta m_{SP}(T,H) = A'(H)\ T^{3/2}\ exp(-\Delta_{SP}/k_B T) \tag{4.3}$$

for a strong itinerant-electron (SI) ferromagnet and

$$\Delta m_{SP}(T,H) = A(H)\ T^2 \tag{4.4}$$

for a weak itinerant-electron (WI) ferromagnet.

In Eq.(4.2), the Bose-Einstein integral functions $Z(s,t_H) = \Sigma\ n^{-s}$ exp(- $n\ t_H$) and $t_H = g\ \mu_B\ H_{eff}\ /\ k_B T$ (with H_{eff} standing for the external magnetic field corrected for the shape and other magnetic anisotropies) allows for the extra energy gap $g\ \mu_B\ H_{eff} = \Delta_{SW} = k_B T_{gap}$ in the SW spectrum arising from the effective field, H_{eff}, that the spins within the sample experience and the parameter β is a direct measure of the mean-square range of the exchange interaction, $\langle r^2 \rangle$, since $\langle r^2 \rangle = 20\ \beta$. The $T^{3/2}$ and $T^{5/2}$ terms in Eq.(4.2) originate from the terms quadratic and quartic in q (momentum transfer) in the spin-wave dispersion relation

$$\hbar\omega_q(T) = \Delta_{SW} + D(T)\ q^2\ (1 - \beta\ q^2). \tag{4.5}$$

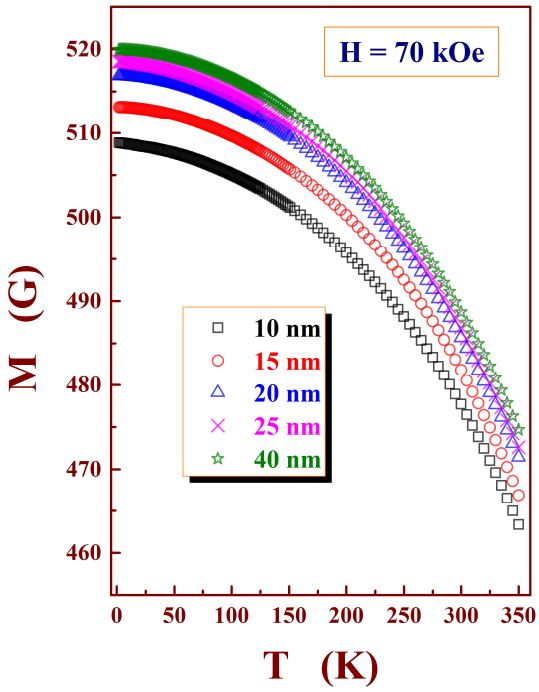

Figure 4.4: *The observed decline in magnetization with temperature in nanocrystalline nickel with different average crystallite size in the range 10 nm to 40 nm at a fixed magnetic field of 70 kOe.*

The spin-wave stiffness, D, renormalizes with temperature according to the relation

$$D(T) = D(0)\ [1 - D_2\ T^2 - D_{5/2}\ T^{5/2}] \tag{4.6}$$

In the itinerant-electron case, which is of interest in this work, the T^2 term in Eq.(6) results from the interaction between spin waves and SP excitations while the $T^{5/2}$ term arises from the magnon-magnon interactions.

4.3 Data Analysis, Results and Discussion

Magnetization (M) as a function of temperature (T) was measured on pulse electrodeposited (PED) nanocrystalline (nc-) Ni samples with different average crystallite size d, varing from 10 nm to 40 nm, at fixed applied static magnetic fields (H) ranging from 10 kOe to 70 kOe over the temperature range 2 K $\leq T \leq$ 124 K at 1 K intervals, 125 K $\leq T \leq$ 150 K at 2 K steps and 155 K $\leq T \leq$ 350 K at 5 K intervals. Fig.(4.4) shows typical magnetization versus temperature plot for different nanocrystalline samples in question at a magnetic field of 70 kOe.

The thermomagnetic, $M_H(T)$, data taken over the temperature range 2 K $\leq T \leq$ 350 K at fixed fields in the range 10 kOe $\leq H \leq$ 70 kOe, are analyzed in terms of the expressions (4.1) - (4.4) by considering the following possibilities.

(i) When the Stoner single-particle excitation contribution is absent, i.e., $\Delta m_{SP} = 0$ in Eq.(4.1), and only the $T^{3/2}$ term in Δm_{SW} (i.e., only the first term in Eq.(4.2)) contributes.

(ii) When the Stoner single-particle excitation contribution is absent, i.e., $\Delta m_{SP} = 0$ in Eq.(4.1) and both the $T^{3/2}$ and $T^{5/2}$ terms in Δm_{SW} are taken into account.

(iii) Along with $\Delta m_{SW} \sim T^{3/2}$ or $\Delta m_{SW} \sim T^{3/2} + T^{5/2}$, Δm_{SP} of the form of Eq.(4.3) or Eq.(4.4) is considered.

To determine the *leading* thermal renormalization term in Eq.(4.6), in each of the above cases (i) - (iii), $D(T)$ in Eq.(4.2) is given by either $D(T) = D(0)$ [1 - D_2 T^2] or $D(T) = D(0)$ [1 - $D_{5/2}$ $T^{5/2}$]. For each case, optimum fits to the $M_H(T)$ data have been attempted over different temperature ranges, $T_{min} \leq T \leq T_{max}$, by keeping T_{min} fixed at a certain value (2 K for all the samples except for the one with $d = 10$ nm which exhibits strong departures from the SW behavior of either $T^{3/2}$ or $T^{3/2} + T^{5/2}$ below a characteristic temperature $T^{\dagger}$, which is field-dependent, as elucidated later in this chapter) and varying T_{max}, and the values of the fit parameters are monitored as functions of T_{max}. This method of data analysis is henceforth referred to as the 'range-of-fit' (ROF) analysis. This ROF analysis is illustrated in figure 4.5 for the nanocrystalline nickel samples with $d = 10$ nm, 20 nm and 40 nm on the thermomagnetic data at a field of 70 kOe and it is a representative of other nickel samples and at all the applied magnetic fields $H \geq 10$ kOe as well.

Fig. 4.5 compares the reduced sum of deviation squares, defined as $\chi_r^2 = \Sigma_i\{(Y_{expt}^i - Y_{fit}^i)^2/(Y_{expt}^i)^2\}$, as a function of the upper bound, T_{max}, of the temperature range, $T_{min} = 2$ K $\leq T \leq T_{max}$ for nanocrystalline Ni with $d = 20$ nm and 40 nm ($T_{min} = 33$ K $\leq T \leq T_{max}$ for nanocrystalline Ni with $d = 10$ nm at $H = 70$ kOe), over which the theoretical fits are attempted for the above-stated cases (i) - (iii). From this comparison, the following conclusions can be drawn.

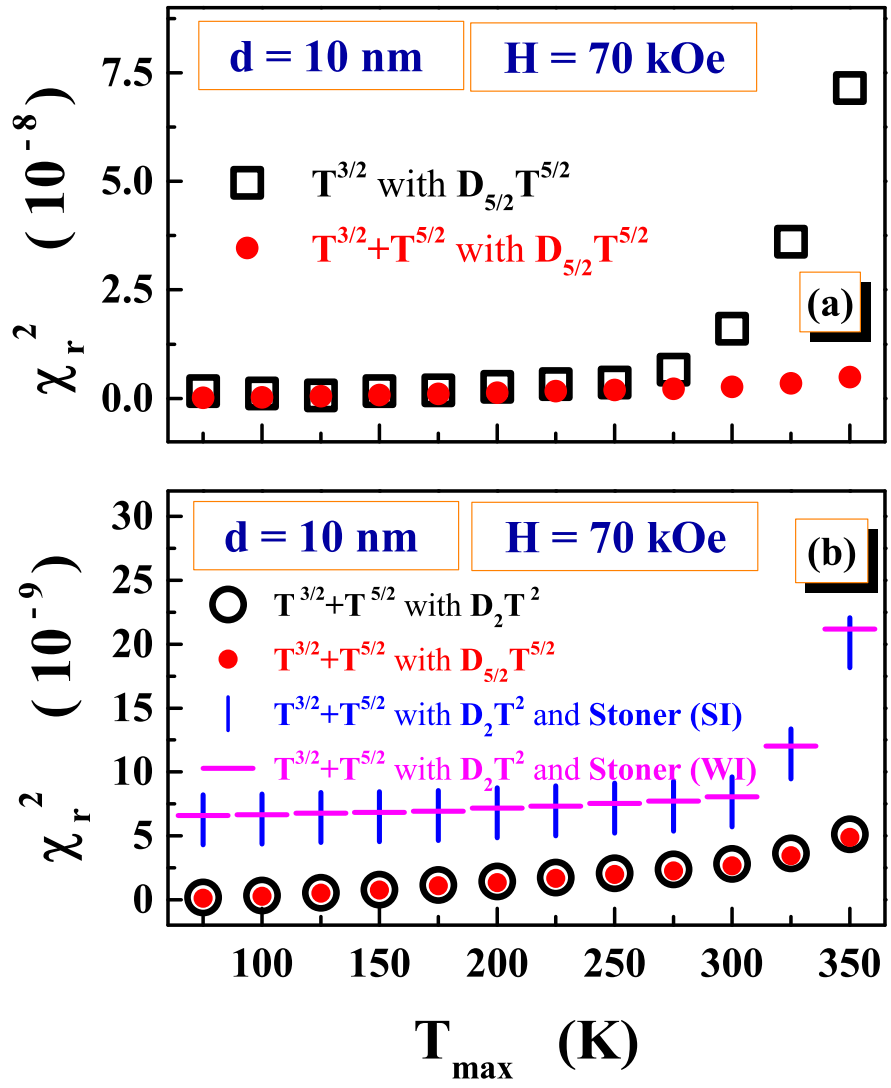

Figure 4.5: *χ_r^2 for the fits, based on equations (4.1) to (4.6), that cover the cases (i)-(iii) of the text, for the nanocrystalline Ni with an average crystallite size of 10 nm.*

(a) The spin-wave relation, Eq.(4.2), with the second term excluded, i.e., $\Delta m_{SW} \sim T^{3/2}$ and $D(T) \sim T^{5/2}$ (the case (i)) reproduces the observed $M_H(T)$ reasonably well for $T \leq 150$ K while the complete Eq.(4.2) with $D(T) \sim T^{5/2}$ (the case (ii)) describes the $M_H(T)$ data far better over an extended temperature range, i.e., up to $T = 350$ K (see Fig.4.5(a) for different nc-Ni samples with $d = 10$ nm, 20 nm, 40 nm);

(b) Inclusion of the Stoner single-particle (SP) contribution of either WI or SI type, in addition to both the SW terms, $T^{3/2} + T^{5/2}$, (the case (iii)) does not improve the quality of the SW-alone fits (see Fig.4.5(b) for different nc-Ni samples with $d = 10$ nm, 20 nm, 40 nm) in any temperature range so much so that the fits deteriorate for $T_{max} \geq 300$ K;

(c) Though a clear-cut distinction between the SW fits based on the expression $D(T) \sim T^{5/2}$ or $D(T) \sim T^2$ is not possible, the quality of the former fits is marginally better.

Consistent with the above findings, the fit parameters, $D(0)$, $D_{5/2}$ and β are *more robust* (see figure 4.6 for different nc-Ni samples with $d = 10$ nm, 15 nm, 20 nm, 25 nm, 40 nm) to the variation in T_{max} (particularly in the range 100 K $\leq T_{max} \leq$ 300 K) when the second-order SW term, $T^{5/2}$, is considered together with the first-order SW term, $T^{3/2}$, and in both the terms, the thermal renormalization of the spin-wave stiffness is due to magnon-magnon interactions, i.e., $D(T) = D(0)$ [1 - $D_{5/2}$ $T^{5/2}$]. The $T^{5/2}$ SW term starts becoming important when T_{max} increases beyond 75 K, as inferred from the non-zero value of 'β'. Note that these fit parameters remain essentially unaltered when the Stoner single-particle contribution of either weak itinerant or strong itinerant form is also included in the range-of-fit analysis.

To determine the widest possible temperature range (i.e., the highest value of T_{max}, T^*_{max}, with T_{min} fixed at 2 K for $d \geq 15$ nm and T^*_{min} for $d = 10$ nm) over which

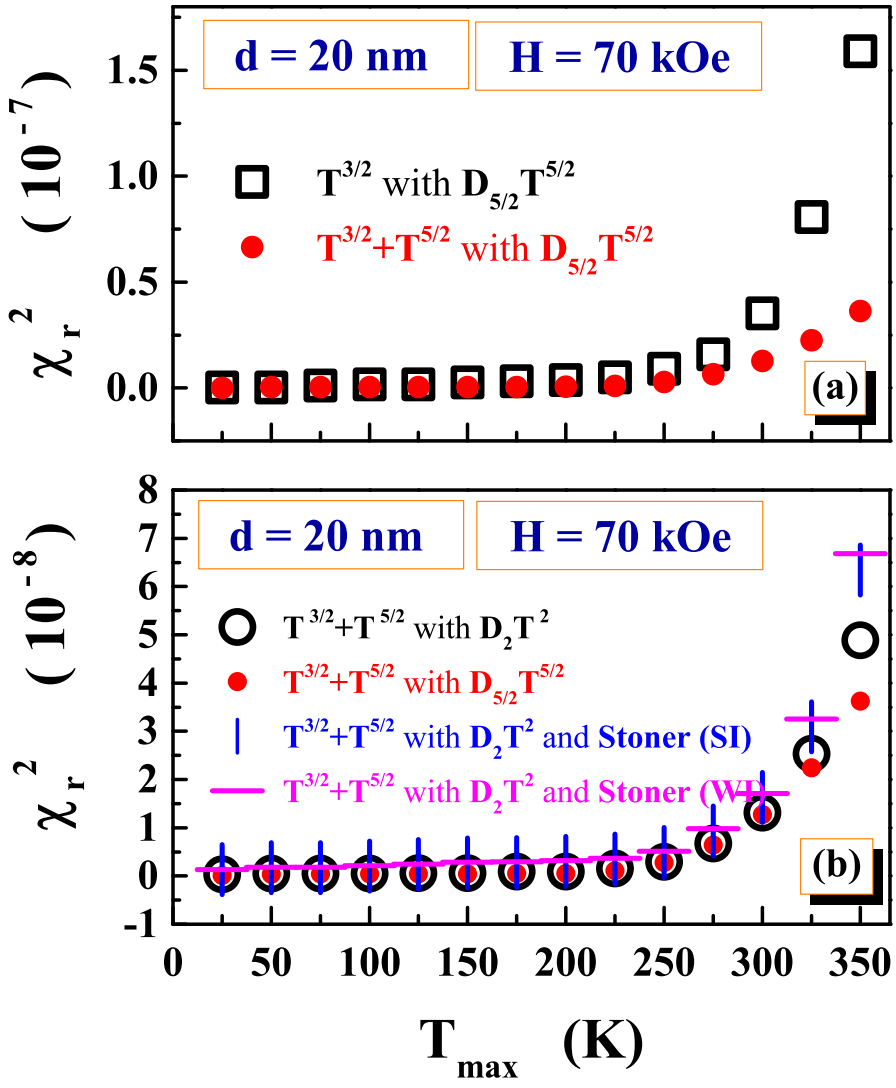

Figure 4.5 (Continued): *χ_r^2 for the fits, based on equations (4.1) to (4.6), that cover the cases (i)-(iii) of the text, for the nanocrystalline Ni with an average crystallite size of 20 nm.*

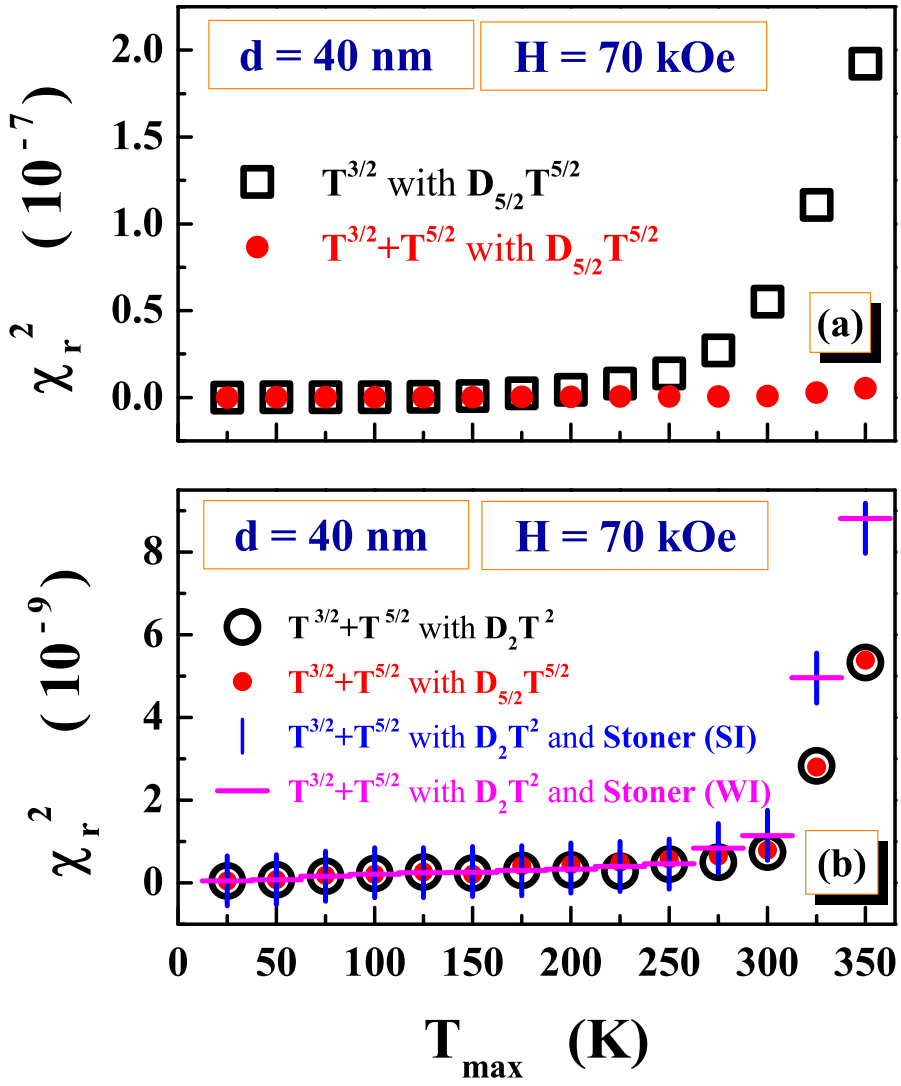

Figure 4.5 (Continued): *χ_r^2 for the fits, based on equations (4.1) to (4.6), that cover the cases (i)-(iii) of the text, for the nanocrystalline Ni with an average crystallite size of 40 nm.*

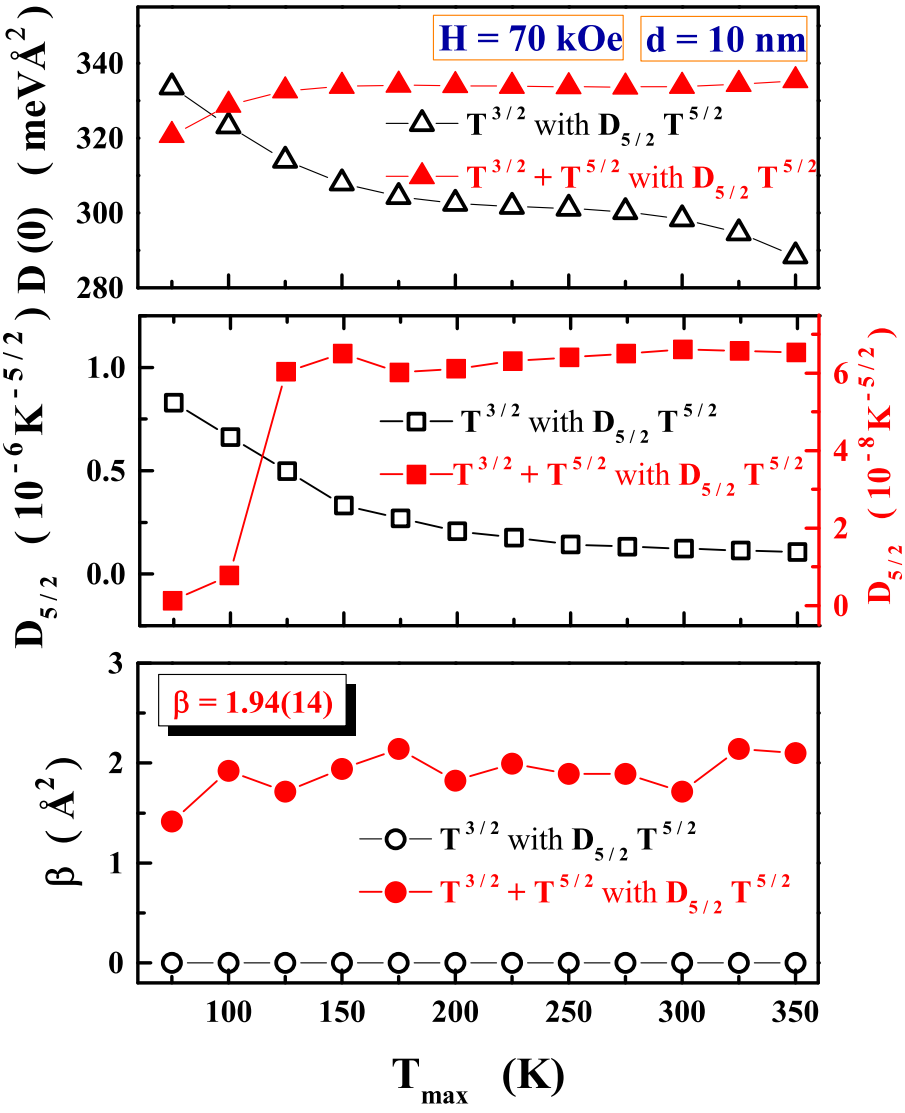

Figure 4.6: *Variations of the spin-wave parameters with the upper bound, T_{max}, of the fit temperature range, $T_{min} = 75\ K \leq T \leq T_{max}$ for the nanocrystalline Ni with $d = 10$ nm at a representative filed of $H = 70$ kOe.*

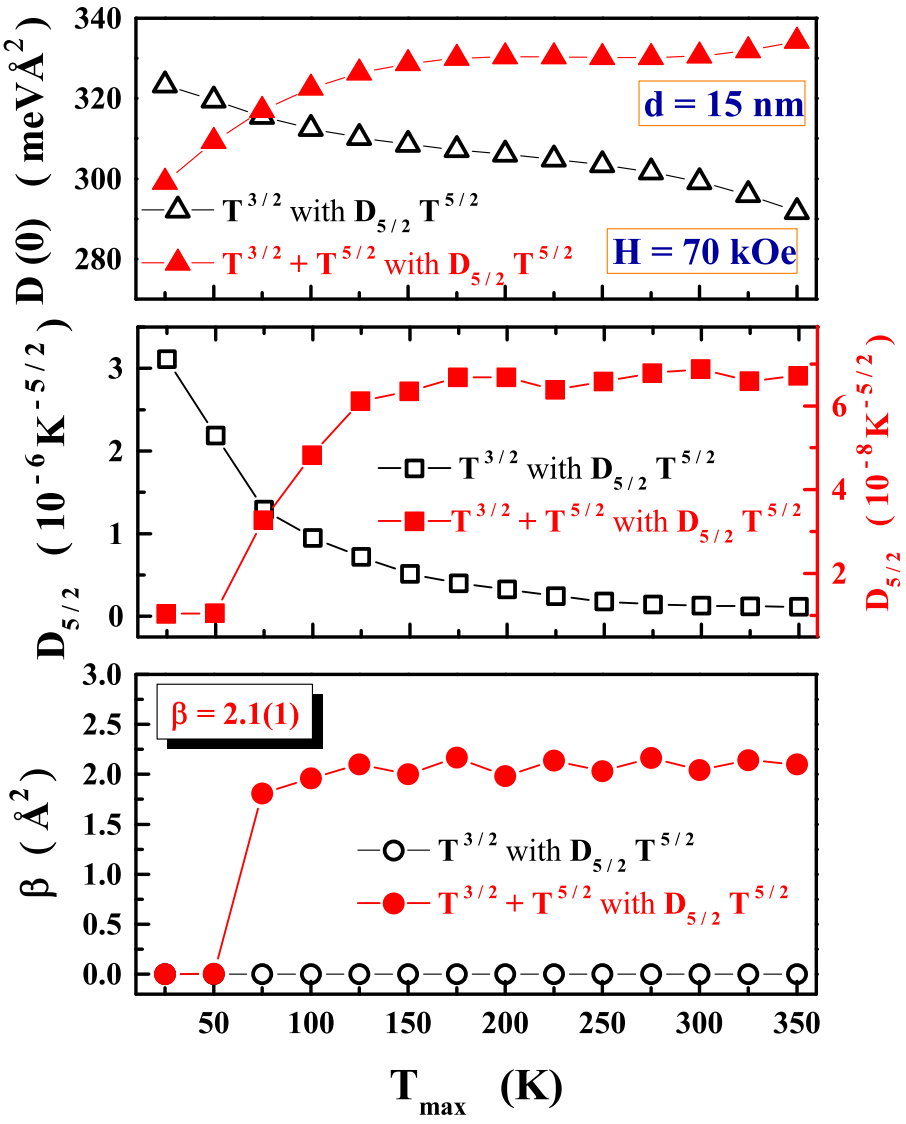

Figure 4.6 (Continued): *Variations of the spin-wave parameters with the upper bound, T_{max}, of the fit temperature range, $T_{min} = 2\ K \leq T \leq T_{max}$ for the nanocrystalline Ni with $d = 15\ nm$ at a representative filed of $H = 70\ kOe$.*

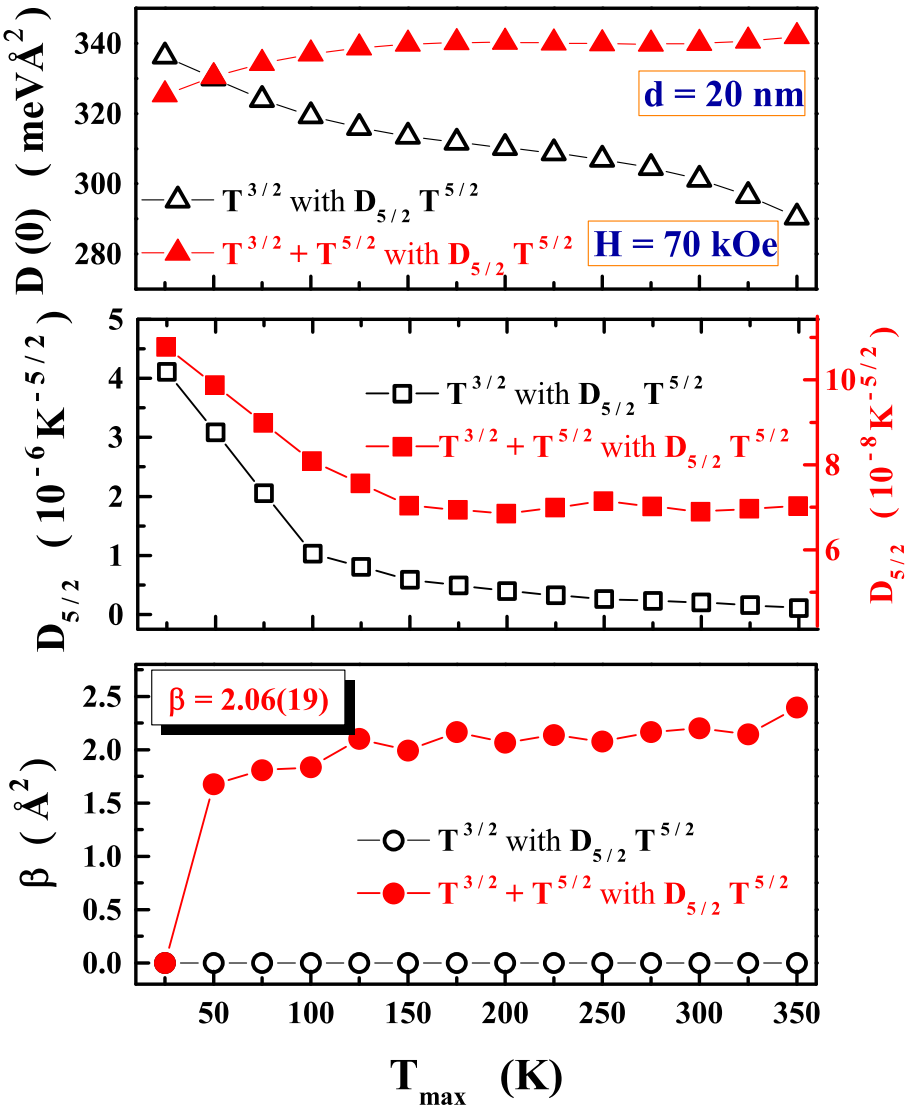

Figure 4.6 (Continued): *Variations of the spin-wave parameters with the upper bound, T_{max}, of the fit temperature range, $T_{min} = 2\ K \leq T \leq T_{max}$ for the nanocrystalline Ni with $d = 20\ nm$ at a representative filed of $H = 70\ kOe$.*

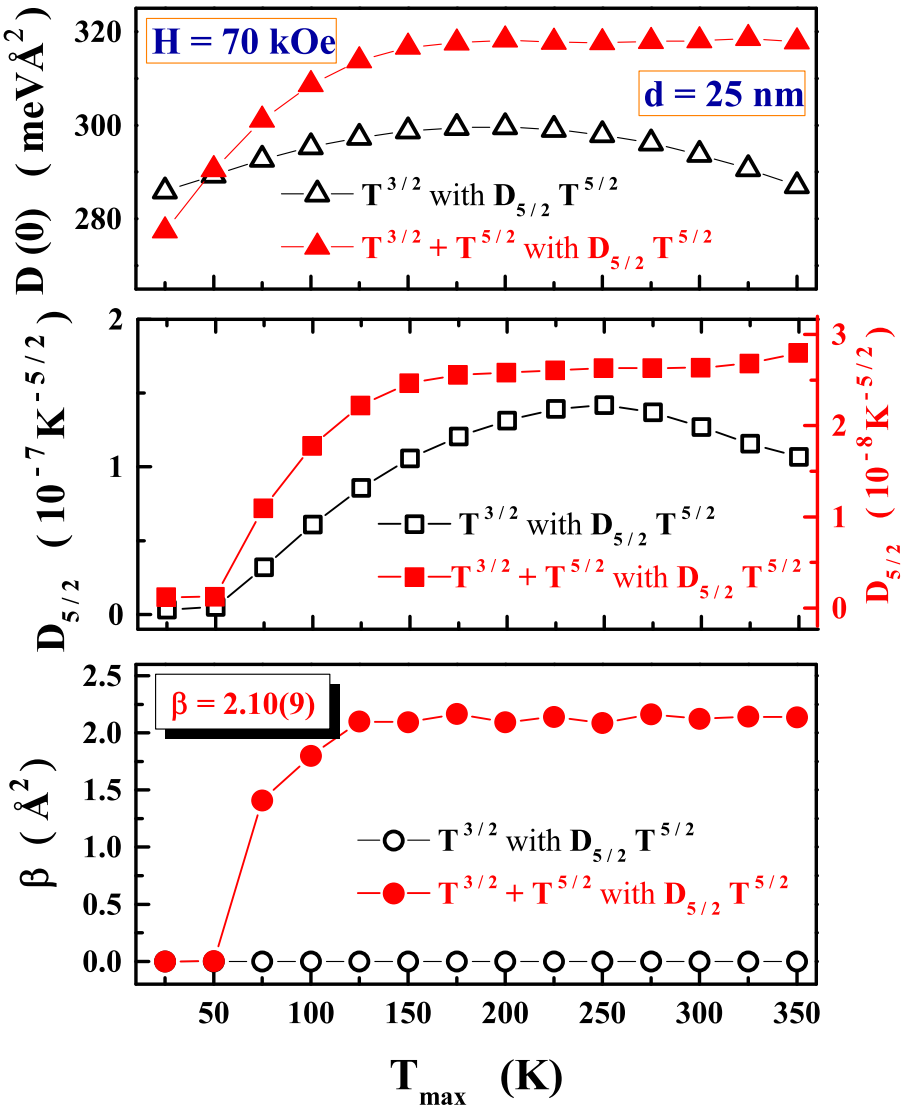

Figure 4.6 (Continued): *Variations of the spin-wave parameters with the upper bound, T_{max}, of the fit temperature range, $T_{min} = 2\ K \leq T \leq T_{max}$ for the nanocrystalline Ni with $d = 25$ nm at a representative filed of $H = 70$ kOe.*

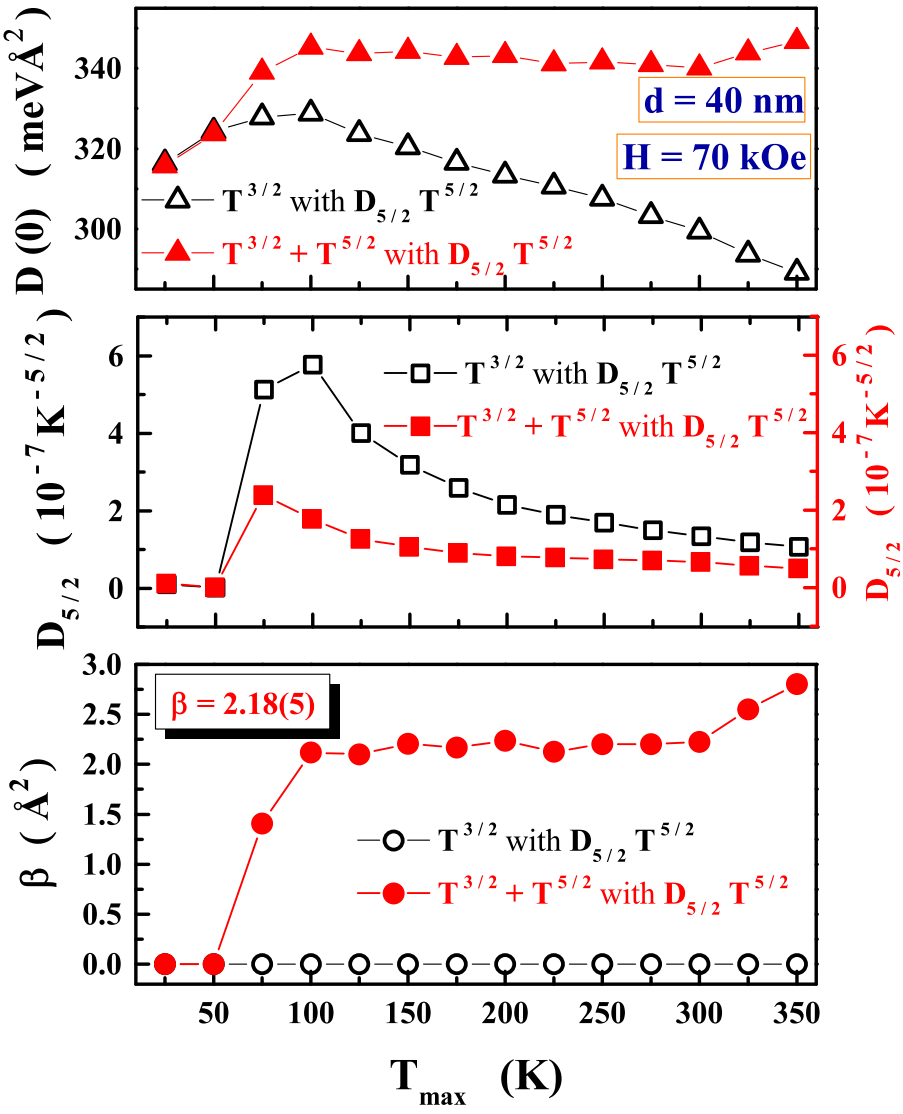

Figure 4.6 (Continued): *Variations of the spin-wave parameters with the upper bound, T_{max}, of the fit temperature range, $T_{min} = 2\ K \leq T \leq T_{max}$ for the nanocrystalline Ni with $d = 40$ nm at a representative filed of $H = 70$ kOe.*

Eq.(4.2) with $D(T) = D(0)$ [1 - $D_{5/2}\, T^{5/2}$] accurately reproduces the observed $M_H(T)$ at a given H, use is made of the percentage reduced deviation of the fit from the data, defined as $[(M_{expt}$ - $M_{fit})/M_{expt}] \times 100$, as illustrated in figure 4.7 for nanocrystalline Ni samples with different d. To demonstrate this, for the nanocrystalline Ni sample with $d = 40$ nm at $H = 70$ kOe, the deviations are statistically distributed around zero up to $T_{max} = 250$ K but become systematic when $T_{max} \geq 300$ K. Thus, in this specific case, the SW relation, Eq.(4.2), describes the functional form of $M_H(T)$ correctly in the temperature range 2 - 250 K. To find T_{max} for other Ni samples with different d in question, similar procedure is followed for the $M(T)$ data taken at different applied magnetic fields 10 kOe $\leq H \leq$ 70 kOe. It is observed that the T_{max} at a given field H decreases with average size (d). Now, with the widest fit range, so determined for each sample from $M_H(T)$ at H in the range 10 kOe - 70 kOe, the percentage reduced deviation is plotted against temperature for different fits, based on the cases (i) - (iii) stated above. A representative plot is shown in figure 4.8 for nanocrystalline Ni with $d = 40$ nm at $H = 70$ kOe. It is evident from the figure 4.8, that the statistical deviations have the least amplitude only for the case (ii), i.e., when the contribution due to Stoner SP excitations, if present, is completely swamped by the spin-wave contribution ($\Delta m_{SW} \sim T^{3/2} + T^{5/2}$) and the thermal renormalization of spin-wave stiffness is primarily due to the magnon-magnon interactions ($D(T) = D(0)$ [1 - $D_{5/2}\, T^{5/2}$]) and the same holds for other Ni samples at different applied magnetic fields under investigation.

The ROF analysis thus permits us to completely rule out a possible Stoner single-particle contribution to the thermal demagnetization up to 350 K and establish that spin-wave excitations alone suffice to account for the observed $M_H(T)$ over the temperature range 2 K $\leq T \leq T^*_{max}$ ($T_{min} \leq T \leq T^*_{max}$) for 15 nm $\leq d \leq$ 40 nm (for d = 10 nm). Furthermore, it is evident from the data presented in Fig. 4.6 that the higher-order $T^{5/2}$ SW term becomes important only for temperatures $T \geq$ 100 K, where the parameter β acquires the temperature-independent value, β = 2.1(2) Å^2, regardless of the values of d and H. These deductions hold true for the nanocrystalline Ni samples of all d.

The variations of T^*_{max} with H for different nanocrystalline Ni samples with 15 nm $\leq d \leq$ 40 nm, depicted in the figure 4.9, reveal that for a given sample, the temperature range over which the SW fits accurately describe the observed $M(T)$ increases with H and for a given field $H \geq$ 10 kOe, the SW fit range increases with average crystallite size, d.

The optimum SW fits (continuous curves) to the $M_H(T)$ data (symbols) at H = 70 kOe for the nanocrystalline Ni samples with d ranging from 15 nm to 40 nm is shown in figure 4.10. The optimum SW fits (continuous curves) to the $M_H(T)$ data (symbols) at different fields 10 kOe $\leq H \leq$ 70 kOe for nanocrystalline Ni samples with d = 15 nm, 20 nm, 25 nm and 40 nm are shown in figures 4.11(a)- 4.11(d), respectively.

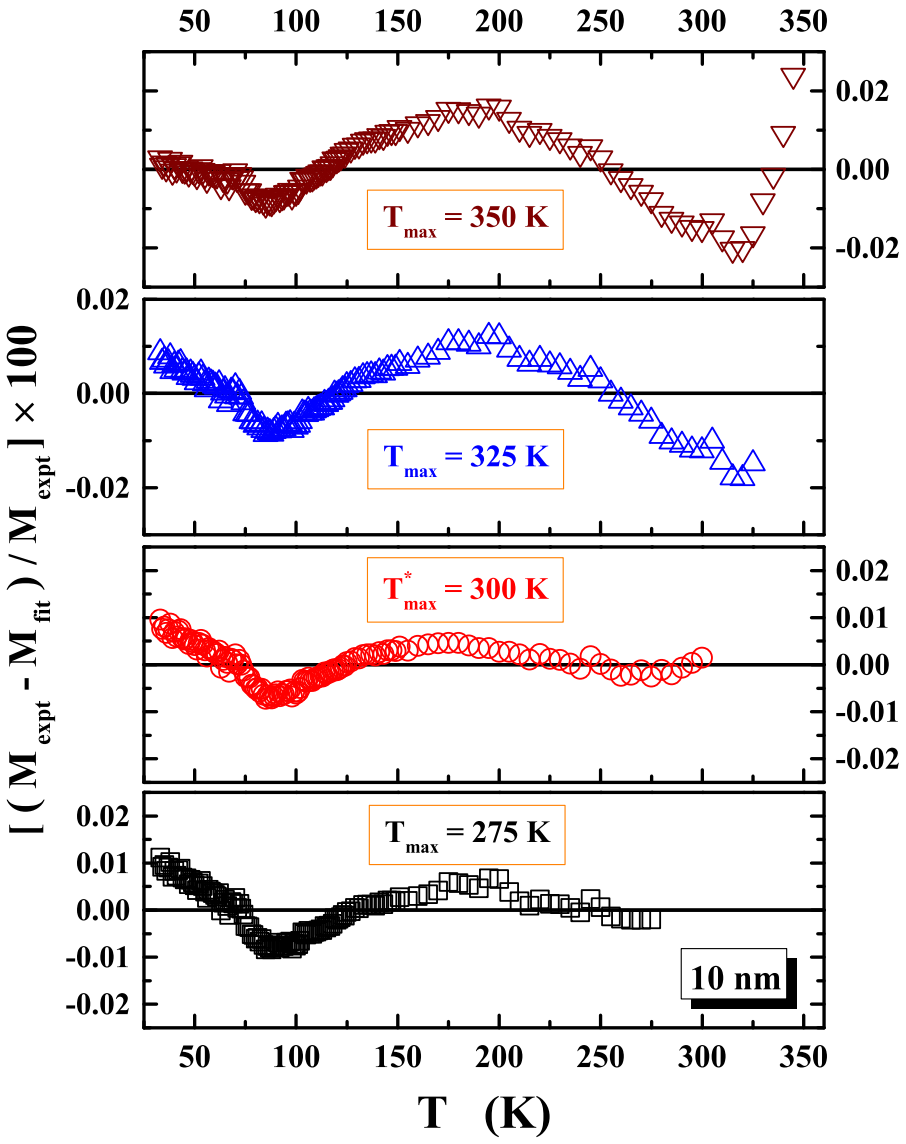

Figure 4.7: *Percentage deviations of the spin-wave fits (of type $T^{3/2}+T^{5/2}$ with $D_{5/2}T^{5/2}$) from the data in temperature ranges corresponding to a few representative values of T_{max} with T_{min} fixed at 2 K for $d = 10$ nm at $H = 70$ kOe.*

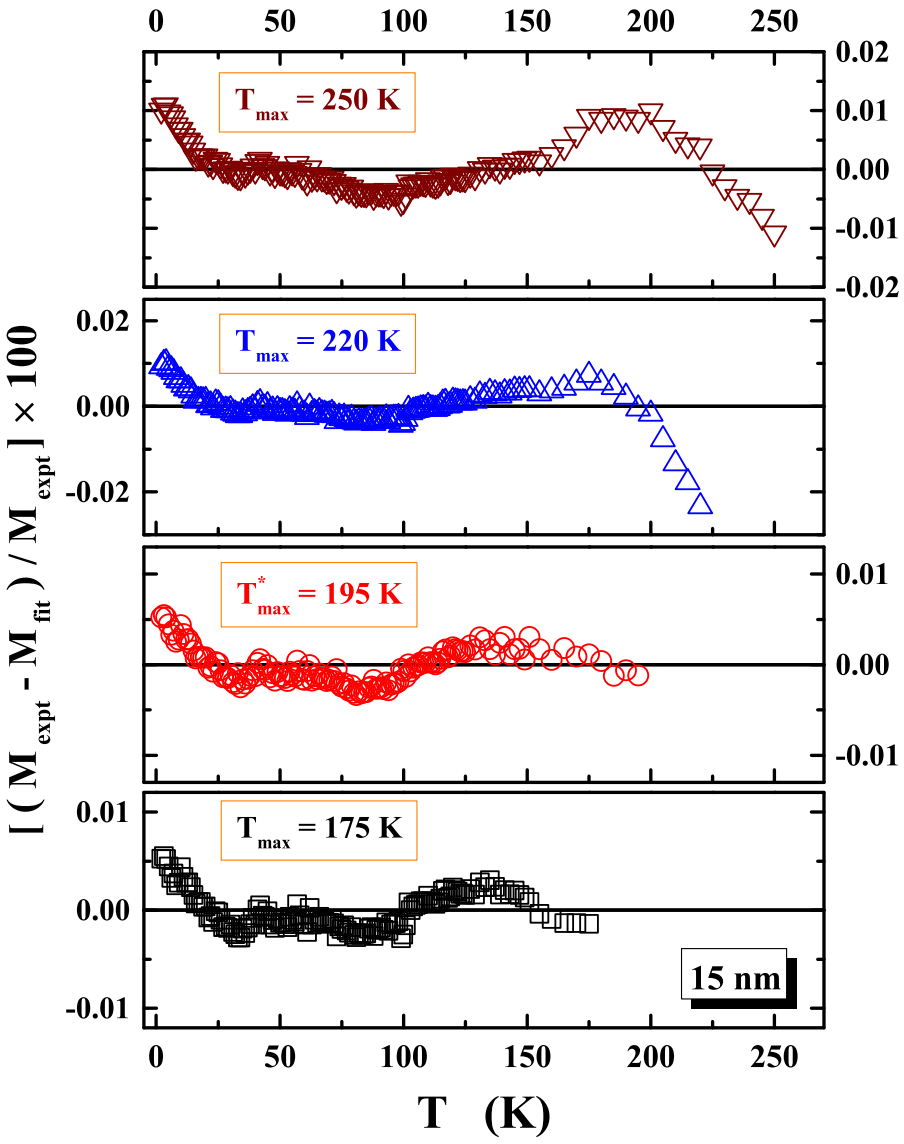

Figure 4.7 (Continued): *Percentage deviations of the spin-wave fits (of type $T^{3/2}+T^{5/2}$ with $D_{5/2}T^{5/2}$) from the data in temperature ranges corresponding to a few representative values of T_{max} with T_{min} fixed at 2 K for d = 15 nm at H = 70 kOe.*

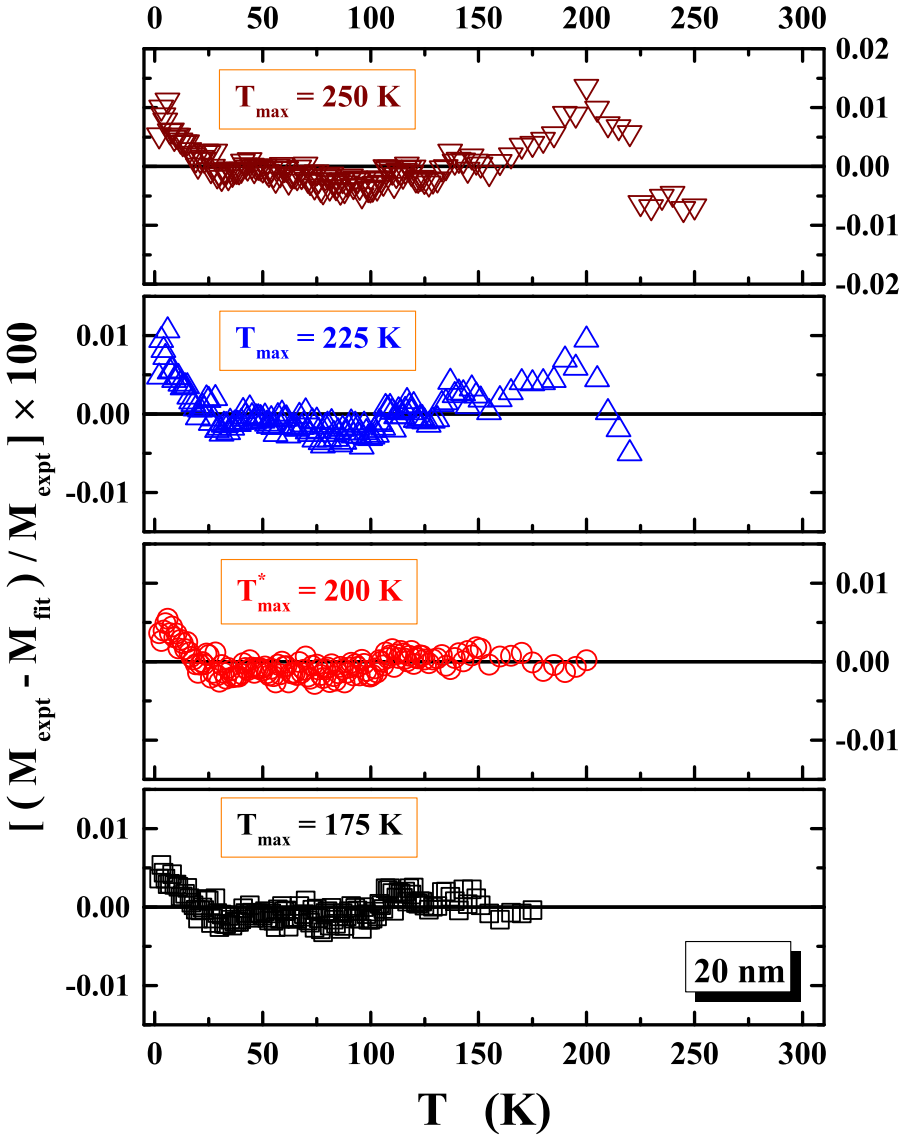

Figure 4.7 (Continued): *Percentage deviations of the spin-wave fits (of type $T^{3/2}+T^{5/2}$ with $D_{5/2}T^{5/2}$) from the data in temperature ranges corresponding to a few representative values of T_{max} with T_{min} fixed at 2 K for d = 20 nm at H = 70 kOe.*

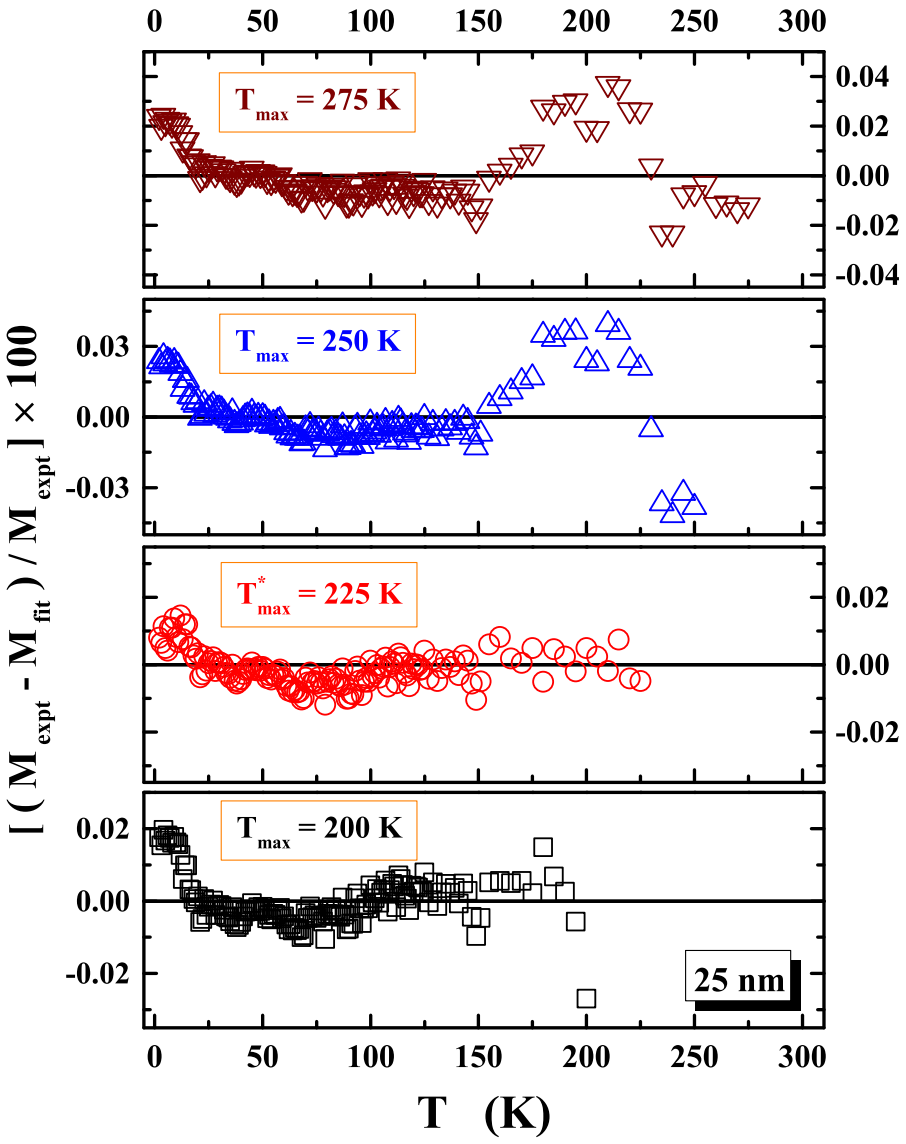

Figure 4.7 (Continued): *Percentage deviations of the spin-wave fits (of type $T^{3/2}+T^{5/2}$ with $D_{5/2}T^{5/2}$) from the data in temperature ranges corresponding to a few representative values of T_{max} with T_{min} fixed at 2 K for d = 25 nm at H = 70 kOe.*

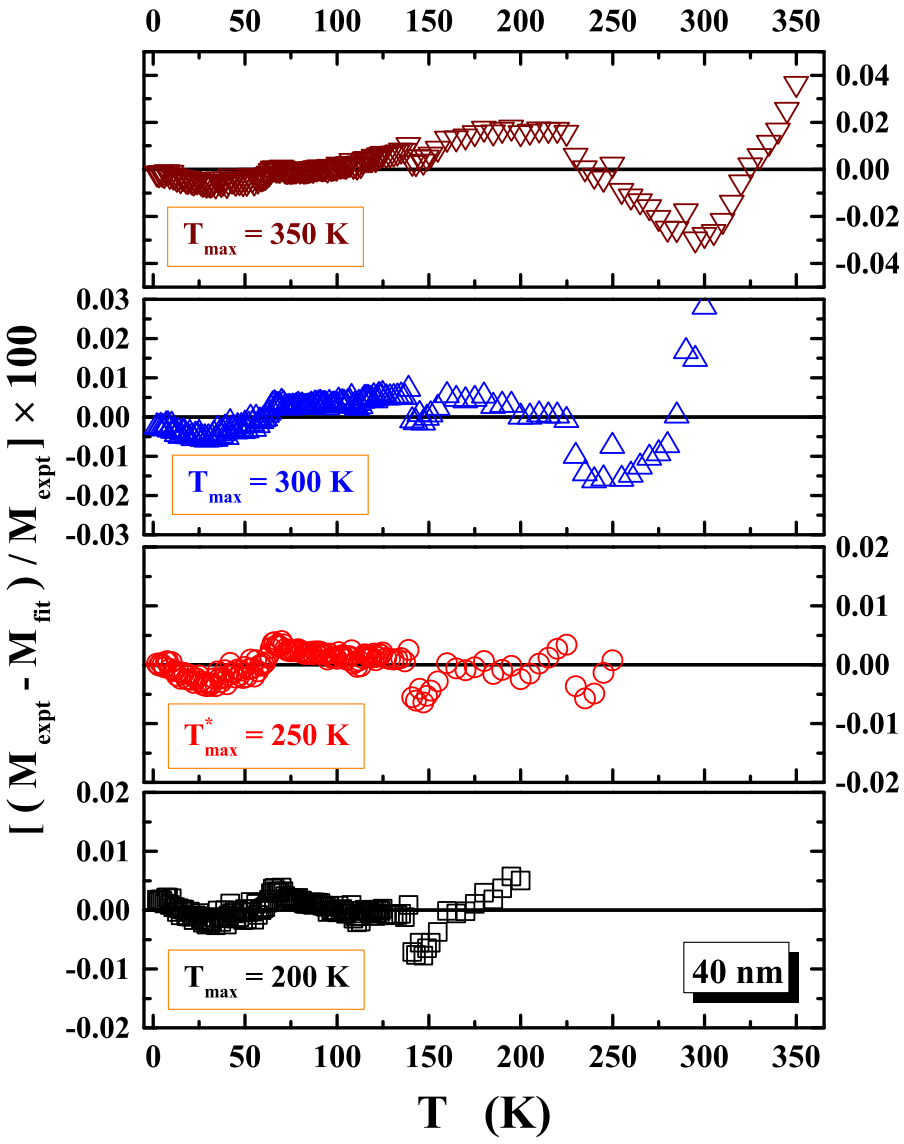

Figure 4.7 (Continued): *Percentage deviations of the spin-wave fits (of type $T^{3/2}+T^{5/2}$ with $D_{5/2}T^{5/2}$) from the data in temperature ranges corresponding to a few representative values of T_{max} with T_{min} fixed at 2 K for $d = 40$ nm at $H = 70$ kOe.*

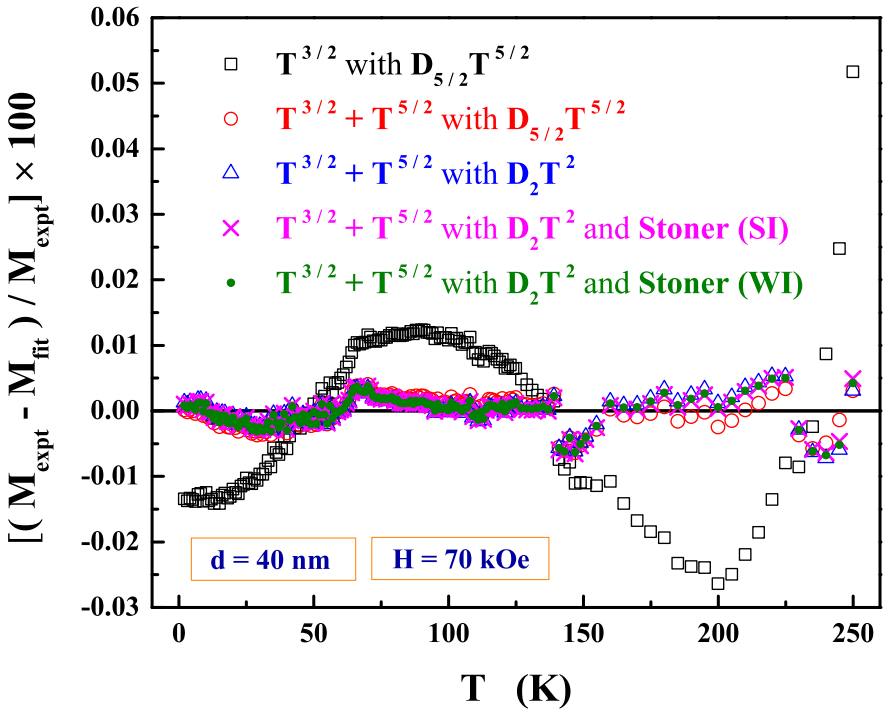

Figure 4.8: *Comparison of the percentage deviations of the different types of SW fits to the $M_H(T)$ data corresponding to different options based on equations (4.1) - (4.6) for nanocrystalline Ni with average crystallite size of 40 nm at $H = 70$ kOe.*

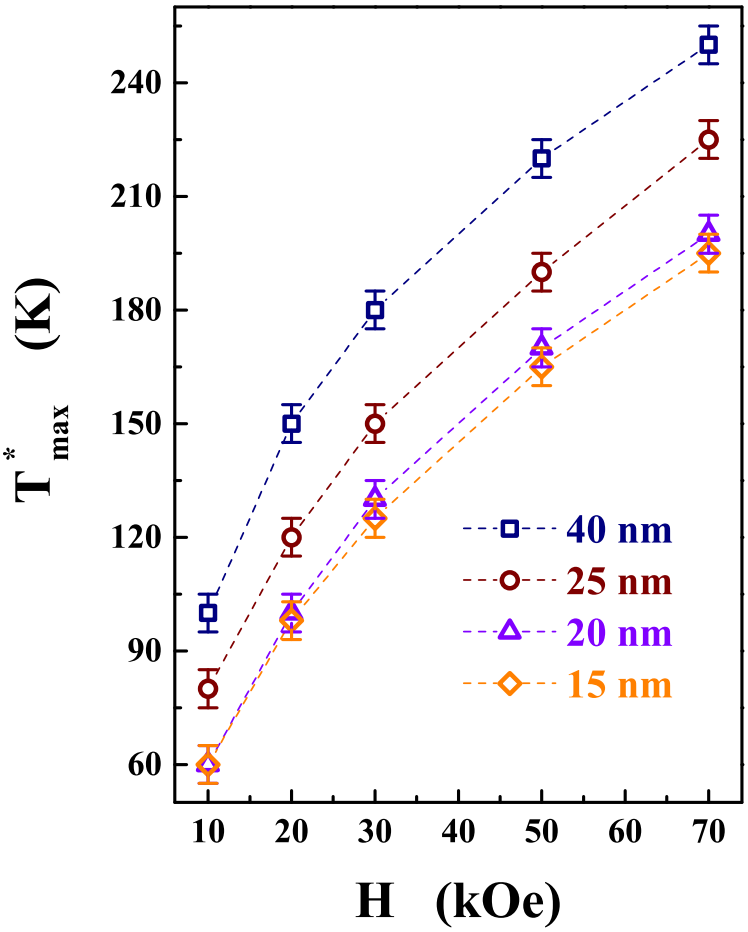

Figure 4.9: *The variation of T^*_{max} with applied magnetic field for the nanocrystalline Ni samples with $d \geq 15$ nm.*

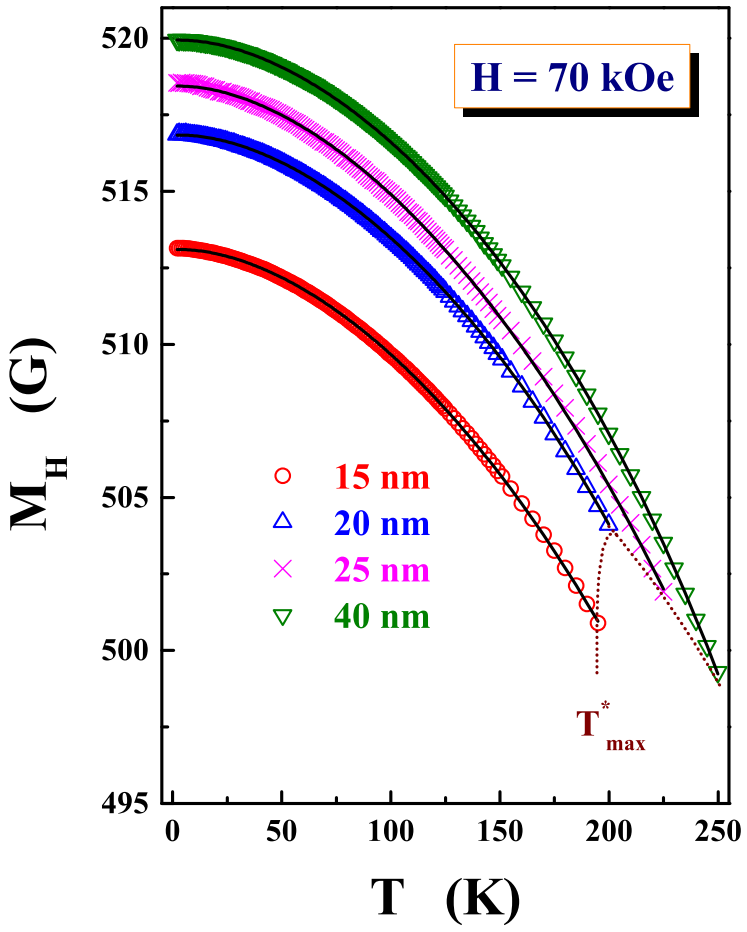

Figure 4.10: *SW-fits (continuous curves) to the $M_H(T)$ data (symbols) in the temperature range 2 $K \leq T \leq T_{max}$ at a field of 70 kOe for the nanocrystalline Ni samples with the average crystallite size, $d \geq 15$ nm.*

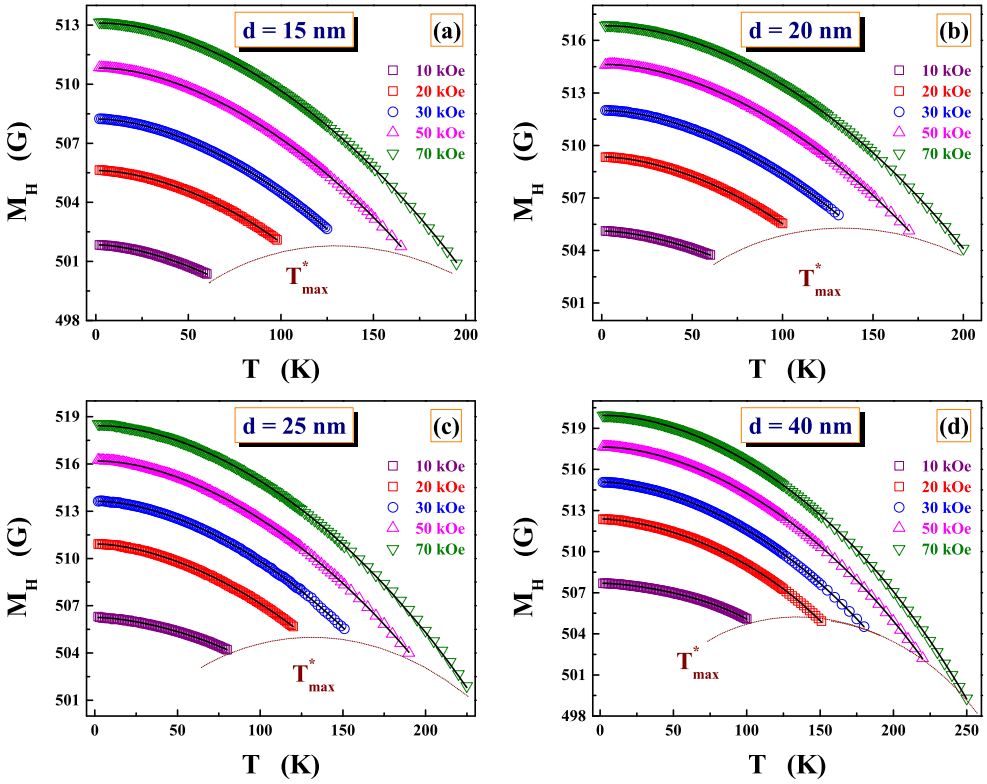

Figure 4.11: *SW-fits (continuous curves) to the $M_H(T)$ data (symbols) at fields 10 kOe $\leq H \leq$ 70 kOe in the temperature range 2 K $\leq T \leq T_{max}$ for the nanocrystalline Ni sample with $d \geq$ 15 nm. For the sake of clarity, the successive $M_H(T)$ data are given a constant downward shift of 2 G, starting from the field H = 50 kOe.*

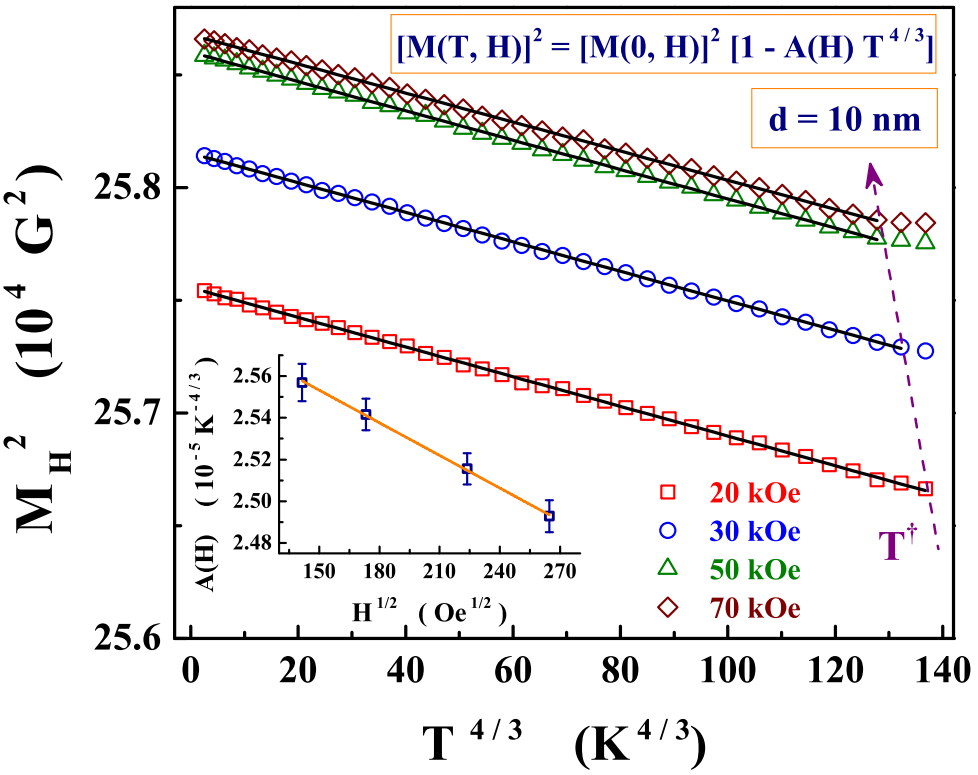

Figure 4.12: *Scaling of M^2 with $T^{4/3}$ for $T \leq T^{\dagger}$ at different fields in nanocrystalline Ni with $d = 10$ nm. Inset highlights the $H^{1/2}$ variation of the coefficient of the $T^{4/3}$ term in equation(4.7), i.e., $A(H)$.*

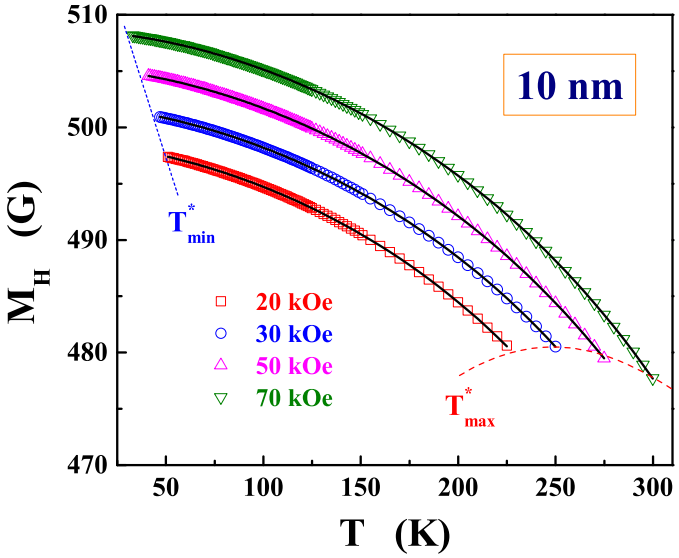

Figure 4.13: *Spin-wave (SW) fits (continuous curves) to the $M_H(T)$ data (symbols) in fields up to $H = 70$ kOe, based on equations (4.2) and (4.6) and corresponding to case (ii) of the text, for the nanocrystalline Ni sample with the average crystallite size $d = 10$ nm. For the sake of clarity, the successive $M_H(T)$ data, starting from $H = 50$ kOe, are given a constant downward shift of 3 G.*

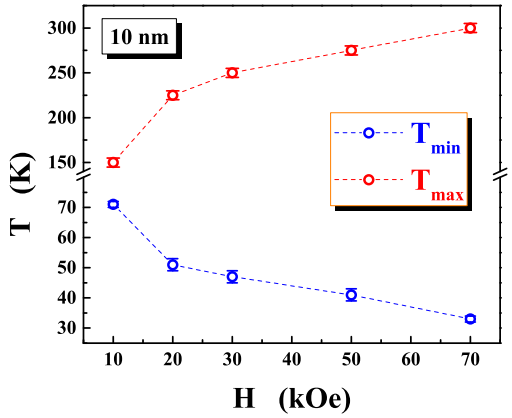

Figure 4.14: *Variations of the lower, T^*_{min}, and upper, T^*_{max}, bounds of the temperature ranges for the SW fits for the nanocrystalline Ni samples with the average crystallite size $d = 10$ nm. Note the break in the ordinate scale of the inset.*

As mentioned earlier, in nanocrystalline Ni with $d = 10$ nm, strong departures from the $T^{3/2} + T^{5/2}$ spin-wave behavior occur at low temperatures $T \leq T^{\dagger}(H)$ where $M_H(T)$, irrespective of H, follows the relation

$$[M_H(T)]^2 = [M_H(0)]^2 \, [1 - A(H) \, T^{4/3}] \tag{4.7}$$

with

$$A(H) = 1 - a \, H^{1/2} \tag{4.8}$$

(see, figure 4.12 and its inset), predicted by spin fluctuation theory [4, 5, 17] for the non-propagating spin fluctuations for temperatures close to T_C. $T^{\dagger}$ decreases from 40 K to 38 K as the field, H, increases from 10 kOe to 70 kOe. Considering that the surface area grows rapidly as crystallite size d falls to values as low as 10 nm, the surface magnetic anisotropy also increases drastically, more so at low temperatures. Strong departures from the SW behavior at low temperatures in $d =$ 10 nm nanocrystalline Ni sample could result from a severe damping of spin waves by the non-collinear arrangement of spins at the crystallite surface caused by a strong surface/interface magnetic anisotropy. A crossover from spin fluctuation to the SW behavior (of the type observed in samples with $d \geq 15$ nm) occurs at $T^*_{min}(H)$, as is evident from figure 4.13. The variations of T^*_{min} and T^*_{max} with H are shown in the Fig. 4.14. This figures brings out clearly that the temperature range over which spin waves completely account for $M_H(T)$ shrinks rapidly as $H \rightarrow 10$ kOe.

The spin-wave stiffness, D, at 0 K and finite field, $D(0, H)$, decreases with increasing H as $H^{1/2}$ in the field range 20 kOe $\leq H \leq$ 70 kOe (i.e., for fields, above the technical saturation, where magnetization has a tendency to saturate) for all the nc-samples with $d \geq 10$ nm, as shown in figure 4.15. The observed variation of D with H runs contrary to the normal theoretical expectation. In the case of a localized-spin ferromagnet, D should be *independent* of H because the energy gap

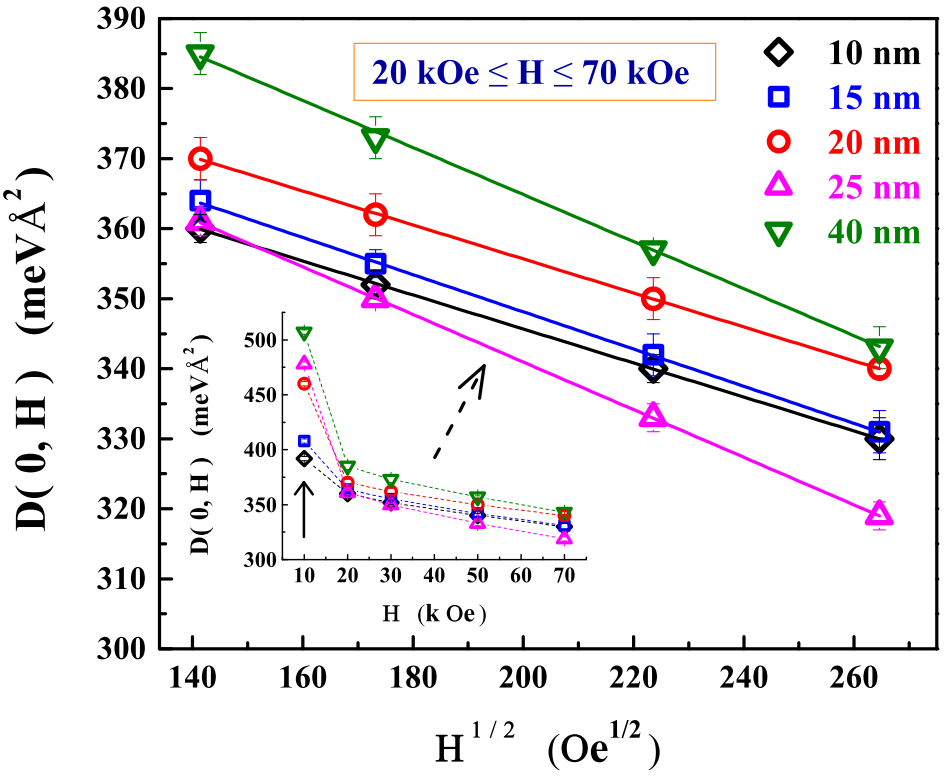

Figure 4.15: *$H^{1/2}$ variation of the spin-wave stiffness $D(0) \equiv D(T = 0, H)$ in nanocrystalline Ni samples regardless of the average crystallite size, d, in the range 10 nm $\leq d \leq$ 40 nm.*

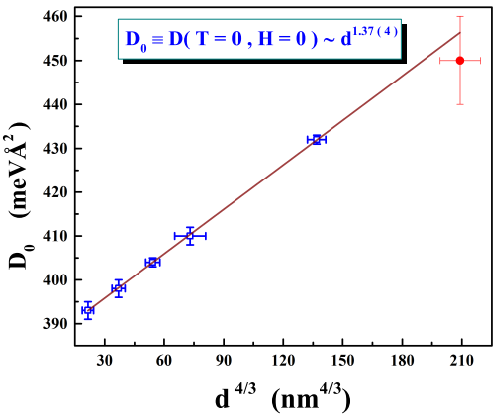

Figure 4.16: *$d^{4/3}$ power law variation of $D_0 \equiv D(T = 0, H = 0)$ with average particle size, d in nanocrystalline Ni. D_0 value obtained for nanocrystalline Ni with $d \simeq 55$ nm from the small angle neutron scattering (red triangle, reference [2]) is also shown for comparison.*

created in the SW spectrum by magnetic field is fully accounted for by the Bose-Einstein integral functions in Eq.(4.2). For itinerant-electron (band) ferromagnets, the theory predicts the relation [4, 5, 13–17] $D(T, H) = g\ \mu_B\ c_\perp\ M(T, H)$ (which holds for both $T = 0$ and $T \neq 0$), where $c_\perp$ determines the mode-mode coupling strength. According to this relation, $D(T, H) \propto M(T, H)$ and hence at any given temperature, like $M_T(H)$, D_T should increase steeply at low fields and tend to saturate at high enough fields. A possible explanation for the observed decrease in the spin-wave stiffness with increasing H could be provided as follows. By working against the strong surface/interface magnetic anisotropy, relatively high fields lower the energy cost for the thermal-excitation of spin waves by progressively improving the alignment of the spins at and across the surfaces/interfaces. This also explains as to why the temperature range, over which thermal demagnetization is solely due to spin waves, increases with H.

A linear extrapolation of the $D(0, H)$ versus $H^{1/2}$ straight line for a given d to $H =$

0 yields the value of D at 0 K and $H = 0$, D_0. Fig. 4.16 asserts that, for d in the range 10 nm $\leq d \leq$ 40 nm, D_0 follows the $d^{4/3}$ power law or more accurately, the relation $D_0(d) = D_0(d = 0) + c\ d^{1.37(4)}$ with $D_0(d = 0) = 386(2)$ meVÅ^2 and d in units of nm. The power law dependence of D_0 on d indicates that the average crystallite size is the relevant length scale for spin waves in nanocrystalline Ni. That average crystallite size, d sets a length scale for magnons in nanocrystalline Ni is a consequence of the effect of the crystallite size-dependent surface/interface magnetic anisotropy on spin waves, as elucidated earlier. In the limit $d \rightarrow 0$, nanocrystalline Ni should behave as amorphous Ni. Magnetic investigations [18, 19] on Ni-rich amorphous Ni-B alloys do indicate a similar value of D_0 for amorphous Ni. The value of the spin-wave stiffness at 5 K, $D(T = 5K, H = 0) = 450(10)$ meVÅ^2, reported [2] for the pulse electrodeposited nanocrystalline Ni sample with $d \simeq 55$ nm, giving proper weightage to the low-q SANS data [20, 21], is also included in the figure 4.16 for comparison. If the $d^{1.37(4)}$ power law behavior of $D_0(d)$ holds even for $d >$ 40 nm, the bulk values for the spin wave stiffness of Ni at 4.2 K, i.e., $D(4.2\text{ K}) = 550$ meVÅ^2 (when $\beta = 0$) and $D(4.2\text{ K}) = 593$ meVÅ^2 (when $\beta = 0.68$ Å^2), yielded previously by the inelastic neutron scattering (INS) experiments [22], are reached when $d \simeq 100$ nm and 120 nm, respectively.

The presently determined value of β, i.e., $\beta = 2.2(2)$ Å^2, is roughly three times larger than the INS estimate for bulk Ni. Larger β implies higher importance of the higher-order $T^{5/2}$ SW term and relatively long-range nature of exchange interactions, in the present case. A detailed analysis [23, 24] of earlier magnetization and hyperfine field data on crystalline Ni underscored the importance of Stoner single-particle (SP) excitations, besides magnons, for $T \lesssim 0.5\ T_C$. By contrast, in the same temperature range, SP excitations do not contribute significantly to $M_H(T)$ in nanaocrystalline Ni. The mean-square range of the exchange interaction, computed from the relation $\langle r^2 \rangle = 20\ \beta$ using the value $\beta = 2.2(2)$ Å^2, yields $\langle r^2 \rangle \simeq 7\ r_{nn}^2$ as against [25, 26]

16 r_{nn}^2 (where r_{nn} is the nearest-neighbor, nn, distance) for crystalline Ni. Inter-spin exchange interactions extending beyond 3 or 4 nn distance augurs well with the itinerant nature of magnetic moment bearing electrons in nanocrystalline Ni or bulk Ni.

4.4 Summary and Conclusion

Based on a systematic and detailed analysis of the observed thermal demagnetization, $M(T)$, data at external magnetic fields in the range, 10 kOe $\leq H \leq$ 70 kOe and temperatures $T \leq 350$ K, in nanocrystalline (nc-) Ni samples with average crystallite size, d, varying from 10 nm to 40 nm, we could draw the following conclusions.

- Stoner single-particle excitations do not make any significant contribution to the thermal demagnetization at external magnetic fields 10 kOe $\leq H \leq$ 70 kOe and temperatures $T \leq 350$ K.

- By contrast, spin-wave (SW) excitations alone account for the observed temperature dependence of magnetization at fixed magnetic fields, $M_H(T)$.

- The thermal renormalization of spin-wave stiffness is primarily due to the magnon-magnon interactions.

- $D_0 \equiv D(T = 0, H = 0)$ varies with d as $d^{1.37(4)}$. From this power-law dependence, we infer that the crystallite size is the relevant length scale for spin waves in magnetic nano-particulate systems.

- Strong departures from the spin-wave behavior (observed at low temperatures $T \leq T^{\dagger}(H)$ in nanocrystalline Ni with $d = 10$ nm and marked by the $T^{4/3}$ power law behavior of $[M_H(T)]^2$) have their origin in the damped spin waves,

which act as non-propagating spin fluctuations and get suppressed by magnetic field in accordance with the $H^{1/2}$ power law.

References

1. H.-E. Schaefer, H. Kisker, H. Kronmüller, and R. Würschum, *Nanostruct. Mater.* **1**, 523 (1992).

2. J. Weissmüller, A. Michels, J. G. Barker, A. Wiedenmann, U. Erb and R. D. Shull, *Phys. Rev. B* **63**, 214414 (2001).

3. S. N. Kaul, in *Handbook of Magnetism and Advanced Magnetic Materials*, edited by H. Kronmüller and S. Parkin, Vol.**1**, John Wiley, England, **p.305** (2007) and references cited therein.

4. S. N. Kaul, *J. Phys.: Condens. Matter* **11**, 7597 (1999).

5. S. N. Kaul, *J. Phys.: Condens. Matter* **17**, 5595 (2005).

6. T. Izuyama and R. Kubo, *J. Appl. Phys.* **35**, 1074 (1964).

7. E. D. Thompson, E. P. Wohlfarth and A. C. Bryan, *Proc. Phys. Soc.* (London) **83**, 59 (1964).

8. J. Mathon and E. P. Wohlfarth, *Proc. Roy. Soc.* (London) **A 302**, 409 (1968).

9. S. N. Kaul, *Phys. Rev. B* **27**, 5761 (1983).

10. S. N. Kaul, *Phys. Rev. B* **27**, 6923 (1983).

11. S. N. Kaul, *J. Phys.: Condens. Matter* **3**, 4027 (1991).

12. S. N. Kaul, V. Siruguri and G. Chandra, *Phys. Rev. B* **45**, 12343 (1992).

13. S. N. Kaul and P. D. Babu, *Phys. Rev. B* **50**, 9308 (1994).

14. S. N. Kaul and P. D. Babu, *Phys. Rev. B* **45**, 295 (1992).

15. S. N. Kaul and P. D. Babu, *J. Phys.: Condens. Matter* **10**, 1563 (1998).

16. S. N. Kaul and M. Rosenberg, *Phys. Rev. B* **27**, 5698 (1983).

17. A. Semwal and S. N. Kaul, *Phys. Rev. B* **60**, 12799 (1999).

18. S. N. Kaul and M. Rosenberg, *Phys. Rev. B* **25**, 5863 (1982).

19. S. N. Kaul and M. Rosenberg, *Phil. Mag. B* **44**, 357 (1981).

20. R. G. Calderón, L. F. Barquín, S. N. Kaul, J. C. Goméz Sal, P. Gorria and J. S. Pedersen, *Phys. Rev. B* **71**, 134413 (2005).

21. S. N. Kaul, *J. Appl. Phys.* **61**, 451 (1987).

22. J. W. Lynn and H. A. Mook, *Phys. Rev. B* **23**, 198 (1981).

23. A. T. Aldred, *Phys. Rev. B* **11**, 2597 (1975).

24. J. C. Ododo and M. W. Anyakoha, J. Phys. F: Met. Phys. **13**, 2335 (1983).

25. S. N. Kaul, *Phys. Rev. B* **24**, 6550 (1981).

26. S. N. Kaul, *Solid State Commun.* **52**, 1015 (1984).

Chapter 5

Electrical- and Magneto-transport

In this chapter, the results of an exhaustive study of 'zero-field' electrical resistivity, $\rho(T)$, and magnetoresistance, MR, (in magnetic fields up to 90 kOe) over the temperature range 1.8 K - 300 K in nanocrystalline (nc-) Ni with average crystallite size, d, ranging from 10 nm to 40 nm are presented. A quantitative comparison of these results with the predictions of the recent self-consistent calculations permits us to unambiguously identify the scattering mechanisms responsible for $\rho(T)$ and MR in different temperature ranges and accurately determine their relative magnitudes in nc-Ni samples of different d. Like in bulk 3d transition metal ferromagnets, ρ varies with temperature as T^2 at $T \lesssim 15$ K. Contrary to the widely-held view that the T^2 variation of ρ at low temperatures arises from the electron-magnon $(e-m)$ scattering, this contribution to $\rho(T)$ is shown to originate from the electron-electron (Baber) scattering. In the temperature range 15 K $\leq T \leq$ 300 K, the phonon-induced non-spin-flip (NSF) intraband (i.e., $s^{\uparrow\downarrow}-s^{\uparrow\downarrow}$, $d^{\uparrow\downarrow}-d^{\uparrow\downarrow}$ electron-phonon $(e-p)$) scattering and magnon-induced spin-flip (SF) interband (i.e., $s^{\uparrow\downarrow}$ - $d^{\downarrow\uparrow}$ $e-m$) scattering contributions completely account for the intrinsic resistivity. The former contribu-

This chapter is based on the following articles:
1. P. V. Prakash Madduri and S. N. Kaul, *Phys. Rev. B*, **95**, 184402 (2017).
2. P. V. Prakash Madduri and S. N. Kaul, *Physica B*, **448**, 147 (2014).

tion dominates over the latter at $T > T^{\star}$ whereas the reverse is true at temperatures 15 K $\leq T < T^{\star}$. $T^{\star}$, the temperature at which the SF interband $e-m$ and NSF intraband $e-p$ scattering contributions become equal, increases from $\sim$ 30 K for d = 10 nm to $\sim$ 65 K for bulk Ni. At $T > T^{\star}$, $\rho_{e-m}(T, H = 0)$ becomes comparable in magnitude to $\rho_{e-p}(T, H = 0)$ for $d \geq$ 25 nm. By contrast, the magnetoresistance in nc-Ni is entirely due to the $s^{\uparrow\downarrow}$ - $d^{\downarrow\uparrow}$ $e-m$ scattering. The present work clearly brings out the importance of the thermal renormalization of magnon mass (caused mainly by the magnon-magnon interactions) over the temperature range 15 K $\leq T \leq$ 300 K. Irrespective of the value of d (including the bulk, $d = \infty$), phonon-induced $s^{\uparrow\downarrow} - s^{\uparrow\downarrow}$, $d^{\uparrow\downarrow} - d^{\uparrow\downarrow}$ transitions are more frequent than the $e-p$ $s^{\uparrow\downarrow} - d^{\uparrow\downarrow}$ transitions over the entire temperature range 1.8 K $\leq T \leq$ 300 K. The saturation magnetization at 0 K, spin wave stiffness at 0 K, Debye temperature as well as the parameters that are a direct measure of the strength of $e-p$ coupling, $e-m$ coupling and level of suppression of $e-m$ scattering by external magnetic field, all exhibit power law variations with average crystallite size, d. The power law behavior asserts that the average crystallite size is the dominant length scale so far as the magnetism, electrical- and magneto-transport in nanocrystalline Ni are concerned.

5.1 Introduction

Traditionally, electrical resistivity, ρ, in crystalline $3d$ transition metal ferromagnets such as Fe, Co and Ni (and their alloys) has been understood within the framework of both localized-spin (scattering of conduction s-electrons from localized d-electrons [1–6]) and itinerant-electron [7–11] models. As the experimental evidence for the itinerant nature of d-electrons started mounting with time, it became increasingly clear that the itinerant-electron picture describes the magnetism and electrical transport in these systems far better than the localized-spin models, particularly

for temperatures below the Curie temperature, T_c. A major advancement in understanding transport phenomena occurred decades ago when the two-current conduction (TCC) model and its variants [12–23] provided a satisfactory explanation for a huge body of $\rho(T)$ and spontaneous resistivity anisotropy or anisotropic magnetoresistance (AMR) data, available on Fe-, Co- and Ni-based dilute alloys. TCC model rests on the basic assumption that spin $\uparrow$ and spin $\downarrow$ s-electrons, undergoing non-spin-flip scattering by mainly phonons, conduct in two *independent but parallel* channels while magnons mix the two channels by giving rise to the spin-flip scattering. Such models also brought out clearly that the spin-orbit coupling causes AMR. In the recent past, the basic idea of the TCC models that the spin $\uparrow$ and spin $\downarrow$ currents can be vastly different in the absence of the spin-mixing scattering, facilitated understanding of the giant magnetoresistance (GMR) effect in 3d transition metal (e.g., Fe, Cr) multilayer structures. This development, in turn, laid the basic foundation for the study of spin-polarized transport and spin-dependent scattering processes in nanostructured devices for spintronic applications.

The early versions of the itinerant-electron models [10, 21], referred to above, dealt exclusively with either the magnon-induced intraband spin-flip $s^{\uparrow\downarrow}$ - $s^{\downarrow\uparrow}$ and $d^{\uparrow\downarrow}$ - $d^{\downarrow\uparrow}$ scattering and/or the magnon-induced interband spin-flip $s^{\uparrow\downarrow}$ - $d^{\downarrow\uparrow}$ scattering processes. Raquet et al. [24] generalized this formalism to include the thermal renormalization of the spin-wave stiffness. All these models assumed *spherical* s and d energy bands. Photoemission experiments and electronic band structure calculations clearly demonstrate that the electron-gas approximation does not hold in *real* $3d$ transition metal systems. To get rid of this limitation of the earlier models, Kaul [25] has recently reported the results of a *self-consistent* calculation of the *propagating* transverse spin-fluctuation (spin-wave) and *non-propagating* longitudinal and transverse spin-fluctuation contributions to $\rho(T)$ at low temperatures, intermediate temperatures and for temperatures close to T_c in the absence and pres-

ence of an external magnetic field. These calculations are based on the two-band (s and d bands) model and the version of the spin-fluctuation theory for d-band that makes use of the Ginzburg-Landau formalism [26–28]. This model has enjoyed considerable success in explaining magnetic [29–32] and magneto-transport properties [33] of weak itinerant-electron ferromagnets with or without site disorder and/or compositional disorder primarily because it not only recognizes the importance of spin-wave excitations but also gives due consideration to the contributions made by the non-propagating spin fluctuations (which, like spin waves, are collective spin excitations) and Stoner single-particle excitations.

Modifications to the magnetic and electronic spin-dependent transport properties of a crystalline (bulk) ferromagnet brought about by a reduction in its physical dimensions to nanometer range ('finite-size effects') are of immense current interest because of the rich and novel physics they promise. Compared to the magnetic properties, electrical and galvanomagnetic transport in nanocrystalline ferromagnets remains largely unexplored. So far as the electrical resistivity is concerned, much of the effort has been devoted to the surface/interface and grain boundary scattering at very low temperatures in Ni nanowires [34, 35] and bulk nanocrystalline Ni [36–39]. No serious attempt (such as the one reported previously [40, 41] for amorphous ferromagnets or epitaxially-grown Fe, Co and Ni thin films [24]) has been made so far to unambiguously determine the magnetic contribution to $\rho(T)$ in nanocrystalline ferromagnets. Specifically, a quantitative estimation of non-spin-flip and spin-flip electronic scattering contributions to intrinsic resistivity in temperature ranges where the conduction electrons concomitantly scatter off phonons, collective spin excitations, s- or d-electrons, is lacking at present.

With a view to identify different scattering mechanisms: electron-electron ($e-e$) scattering, phonon-induced intraband and/or interband $s-s$ and $d-d$ scattering, magnon-induced interband and/or interband $s-d$ scattering and their relative

magnitudes that accounts to the electrical- and magnetoresistance in nanocrystalline itinerant-electron ferromagnets and also to ascertain the effect of finite size (nanometer scale) on various scattering contributions to the intrinsic resistivity and magnetotransport, an elaborate study of temperature dependent 'zero-field resistivity' and 'in-field resistivity' on bulk nanocrystalline Ni was undertaken.

5.2 Theoretical Considerations

5.2.1 'Zero-field' electrical resistivity

The electrical resistivity of a ferromagnetic metal is known to arise from the following sources.
(i) The temperature-independent part, called the residual or 'zero-temperature' resistivity, ρ_0, arising from the scattering of conduction electrons from the imperfections and impurities.
(ii) The scattering of conduction s-electrons from the itinerant d-electrons [48] gives a contribution (ρ_{e-e}) to ρ that is appreciable at very low temperatures only and varies with temperature as T^2.
(iii) Two main contributions to ρ, that progressively increase with temperature, have their origin in the scattering of conduction electrons by the lattice vibrations (phonons), ρ_{e-p}, and by spin waves (magnons), ρ_{e-m}. In the case of both phonons and magnons, the scattering could either occur within a single band (e.g., $s-s$ or $d-d$ scattering) or involve transitions from s-band to d-band, as elucidated below.

The expressions for the electron-phonon scattering contribution to $\rho(T)$ yielded by the Bloch-Grüneisen [49] and Bloch-Wilson [7–9] formalisms can be put into the generalized form as

$$\rho_{e-p}(T) = \rho_\Theta \left(\frac{T}{\Theta_D}\right)^n \int_0^{\Theta_D/T} \frac{x^n\, dx}{(e^x - 1)(1 - e^{-x})} \tag{5.1}$$

where ρ_Θ is a constant, which is characteristic of the metal and Θ_D is its Debye temperature. The above expression reduces to the usual Bloch-Grüneisen (BG) or Bloch-Wilson (BW) form when the exponent n, appearing in Eq.(5.1), equals 5 or 3. The Bloch-Grüneisen and Bloch-Wilson expressions respectively describe the phonon-induced non-spin-flip single-band ($s^{\uparrow\downarrow}-s^{\uparrow\downarrow}$, $d^{\uparrow\downarrow}-d^{\uparrow\downarrow}$) and two-band ($s^{\uparrow\downarrow}-d^{\uparrow\downarrow}$) scattering contributions to resistivity, $\rho(T)$. While the BG expression forms a correct description of the phonon contribution in non-magnetic alkali and noble metals, the BW expression is more appropriate for the $3d$ transition metals.

By contrast, besides the non-spin-flip ($s^{\uparrow\downarrow}-d^{\uparrow\downarrow}$) interband scattering, the electron-magnon scattering involves spin-flip $s^{\uparrow\downarrow}-s^{\downarrow\uparrow}$ and $d^{\uparrow\downarrow}-d^{\downarrow\uparrow}$ intraband, and $s^{\uparrow\downarrow}-d^{\downarrow\uparrow}$ interband transitions. The theoretical calculations, based on two-band models [10,24], of various electron-magnon scattering contributions to $\rho(T)$ in $3d$ transition metal ferromagnets (Fe, Co, Ni) have revealed the following. (I) At any given temperature well below the Curie temperature, T_c, magnon-induced non-spin-flip $s-d$ scattering contribution is two orders of magnitude smaller than that due to spin-flip $s-d$ scattering. (II) At temperatures as low as $\simeq$ 15 K, the spin-wave spin-flip $s-d$ scattering is negligible so that ρ_{e-m} is almost entirely due to spin-flip $s-s$ scattering and varies with temperature as T^2. (III) At temperatures $\gtrsim$ 15 K, the spin-flip $s-d$ scattering becomes increasingly important so much so that in the temperature range 50 K $\leq T \leq$ 300 K ($\approx T_c/2$), the spin-flip $s-d$ interband scattering contribution is atleast two orders of magnitude larger than that arising from the spin-flip $s-s$ intraband scattering. Thus, over the entire temperature range from 15 K to 300 K, the spin-flip $s-d$ scattering essentially determines ρ_{e-m}. According to the version of the spin fluctuation theory [25], that overcomes certain limitations of the earlier theories [10, 24] mentioned in the introduction, the magnon-induced spin-flip $s-d$

scattering contribution to $\rho(T)$ is given by

$$\rho_{e-m}(T, H = 0) = \left(\frac{\pi}{3}\right) \rho^{\star} \Gamma(3) \zeta(2) \left(\frac{g\mu_B M_s(0)}{\hbar}\right) \left(\frac{k_B T}{D(T)}\right)^2 \quad (5.2)$$

with

$$\rho^{\star} = \left(\frac{3}{4}\right) \left(\frac{m_s}{ne^2}\right) \Im_{s-d}^2 N(E_F^d) N(E_F^s) (k_F^s)^{-4} \quad (5.3)$$

and

$$D(T) = D_0 (1 - D_2 T^2 - D_{5/2} T^{5/2}) \quad (5.4)$$

where m_s and n are the mass and number density of s electrons,
$\Im_{s-d}$ is the $s-d$ exchange coupling constant,
$N(E_F^d)$ and $N(E_F^s)$ are the total density of states at the Fermi energy, E_F, for d and s electrons,
k_F^s is the Fermi wavevector for s electrons,
$M_s(0)$ is the spontaneous magnetization at zero temperature,
D is the spin wave stiffness, D_0 is the value of D at 0 K,
D_2 and $D_{5/2}$ account for the thermal renormalization of D due to Stoner single particle-magnon and magnon-magnon interactions.

5.2.2 'In-field' electrical resistivity and magnetoresistance

The contributions to resistivity arising from the scattering of conduction electrons from imperfections/impurities (residual resistivity), other electrons (Baber $s-d$ Coulomb $e^- - e^-$ scattering) and phonons (electron-phonon scattering) are insensitive to the externally applied magnetic field and hence these scattering mechanisms do not significantly contribute to magnetoresistance (MR). Thus, negative magnetoresistance originates solely from the suppression of magnons, and hence of the

electron-magnon scattering, by the magnetic field. As is the case for 'zero-field' resistivity, the spin-flip $s-d$ interband scattering contribution to magnetoresistance swamps all other magnon-induced spin-flip/non-spin-flip intraband/interband scattering contributions. The spin-flip $s-d$ electron-magnon scattering contribution to MR at low and intermediate fields ($h = g\mu_B H/k_B T < 0.693$) is given by the expression [25]

$$\left(\frac{\triangle\rho}{\rho}\right)_{mag} = \frac{\rho_{e-m}(T,H)}{\rho_{e-m}(T,H=0)} - 1$$
$$= [\Gamma(3)\ \zeta(2)]^{-1}\ \left[h\ ln(e^h-1) + 2\ \Sigma_{n=1}^{\infty}\frac{(-1)^n(e^h-1)^n}{n^2}\right] \quad (5.5)$$

In most cases, MR at moderate fields ($h < 1$) is of main interest and hence the above expression can be simplified further by approximating the $(e^h - 1)$ term by h and retaining only the first two (leading) terms in the sum over n, with the result that [25]

$$\left(\frac{\triangle\rho}{\rho}\right)_{mag} \cong 0.304\ \left[h\ lnh - 2h + \frac{h^2}{2}\right] \quad (5.6)$$

Alternatively,

$$\rho_{e-m}(T,H) = \rho_{e-m}(T,H=0)\ \left[1 + \left(\frac{\triangle\rho}{\rho}\right)_{mag}\right] \quad (5.7)$$

with $\rho_{e-m}(T,H=0)$ and $(\triangle\rho/\rho)_{mag}$ given by Eqs. (5.2) and (5.6), respectively.

5.3 Data Analysis, Results and Discussion

Rectangular strips of dimensions $10 \times 2.5 \times 0.3$ mm^3 were spark-cut from the pulse electrodeposited [46, 47] nanocrystalline (nc-) Ni sheets with different average crystallite sizes ranging from 10 nm to 40 nm with atomic density $\simeq$ 99.6(3) % of bulk

density. Electrical resistivity, $\rho(T)$ and transverse magnetoresistance (MR(T, H)) measurements were performed on the Quantum Design make Physical Property Measurement System using standard four-probe method. 32/34 SWG copper wire was used as current/ voltage leads. Very tiny drops of silver paste were sandwiched between the pressure-contacts and the sample to improve the electrical contact with the samples. Use of silver paste resulted in a huge reduction (by more than an order of magnitude) in the scatter in the $\rho_H(T)$ data compared to the preliminary results reported previously [46]. The four-probe arrangement was made using a rectangular sample holder made of 1 mm thick single side Copper clad PCB. The sample holder was fixed to the resistivity-puck provided by Quantum Design and compatible with PPMS transport option. To ensure a good thermal contact of the sample with the thermometers, a thin layer of Apiezon-N grease was applied to the resistivity-puck platform before mounting the sample on the puck. Since the puck platform is a conducting base, a thin mica sheet for complete electrical insulation and good thermal conduction is sandwiched between the sample with measuring leads and transport-puck platform. Typically, a dc current of 5 mA in the AC drive mode was used to measure the voltage drop across the sample. In the AC mode, the user bridge board applies a DC excitation to the sample and reads the potential drop across the sample. Then the user bridge board reverses the current and reads the potential drop again. The final voltage reading is the absolute value of the positive and negative voltage readings. The AC excitation, which is a square-wave excitation, is synchronized to the AC line frequency of 50 Hz in order to reject AC line noise. AC mode eliminates errors from DC offset voltages and produces the most accurate readings.

Electrical resistivity, ρ, was measured as a function of temperature at 1 K intervals in the range 2 K $\leq T \leq$ 50 K and at 2 K intervals in the range 50 K $\leq T \leq$ 300 K in 'zero-field' and at various fixed external magnetic fields (H) up to 90 kOe, with the direction of H perpendicular to the sample plane and the electrical current along the

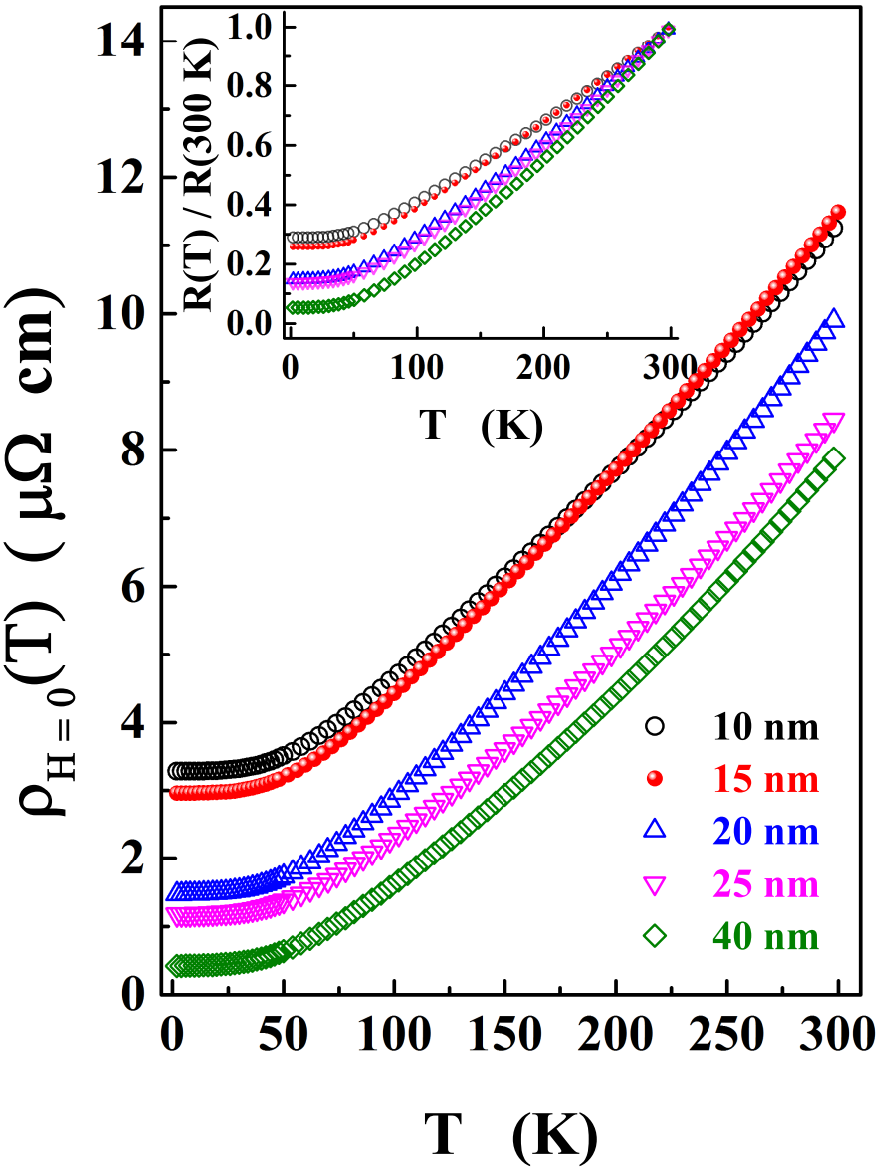

Figure 5.1: *The temperature variations of the 'zero-field' resistivity, $\rho(T, H = 0)$, for different nanocrystalline Ni samples. The inset shows $\rho(T, H = 0)$ normalized to its value at 300 K. For the sake of clarity, only alternate data points are shown in the main figure and one data point in four in the inset.*

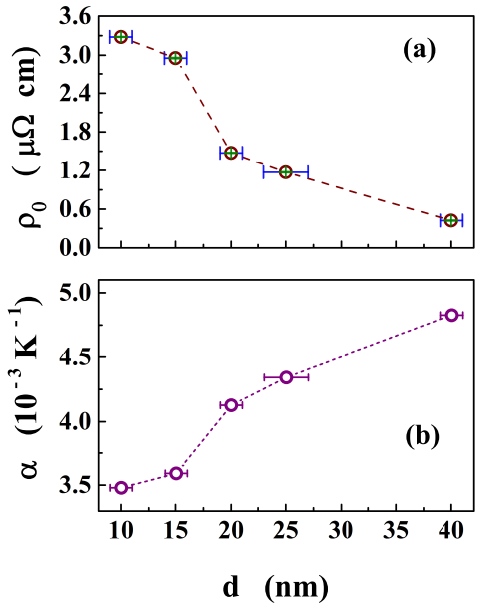

Figure 5.2: *Variations of the residual rsistivity, $\rho_0 \equiv \rho_{H=0}(T = 1.8\ K)$ (panel a) and the temperature coefficient of resistivity (α) near room temperature (panel b) with the average crystallite size, d in nanocrystalline Ni.*

length in the sample plane (Transverse magnetoresistance) on the nanocrystalline Ni samples under investigation. Magnetoresistance (MR) was measured as a function of external magnetic field from $H = 0$ to $H = 90$ kOe in 10 kOe intervals at fixed temperatures covering the range 1.8 K - 300 K.

Assuming the validity of the Mattheissen's rule that various scattering contributions to electrical resistivity of a metallic ferromagnet (enumerated in the previous section) are additive, $\rho(T, H = 0)$ can be expressed as

$$\rho(T, H = 0) = \rho_0 + \rho_{e-p}(T, H = 0) + \rho_{e-m}(T, H = 0) \tag{5.8}$$

In Eq.(5.8), $\rho_{e-p}(T, H = 0)$ is given by Eq.(5.1) with the exponent $n = 3$ ($n = 5$) for the Bloch-Wilson, BW, (Bloch-Grüneisen, BG) description, and $\rho_{e-m}(T, H = 0)$ by Eqs.(5.2) - (5.4). In the following, the electrical resistivity and magnetoresistance data are analysed in terms of Eqs.(5.1) - (5.8).

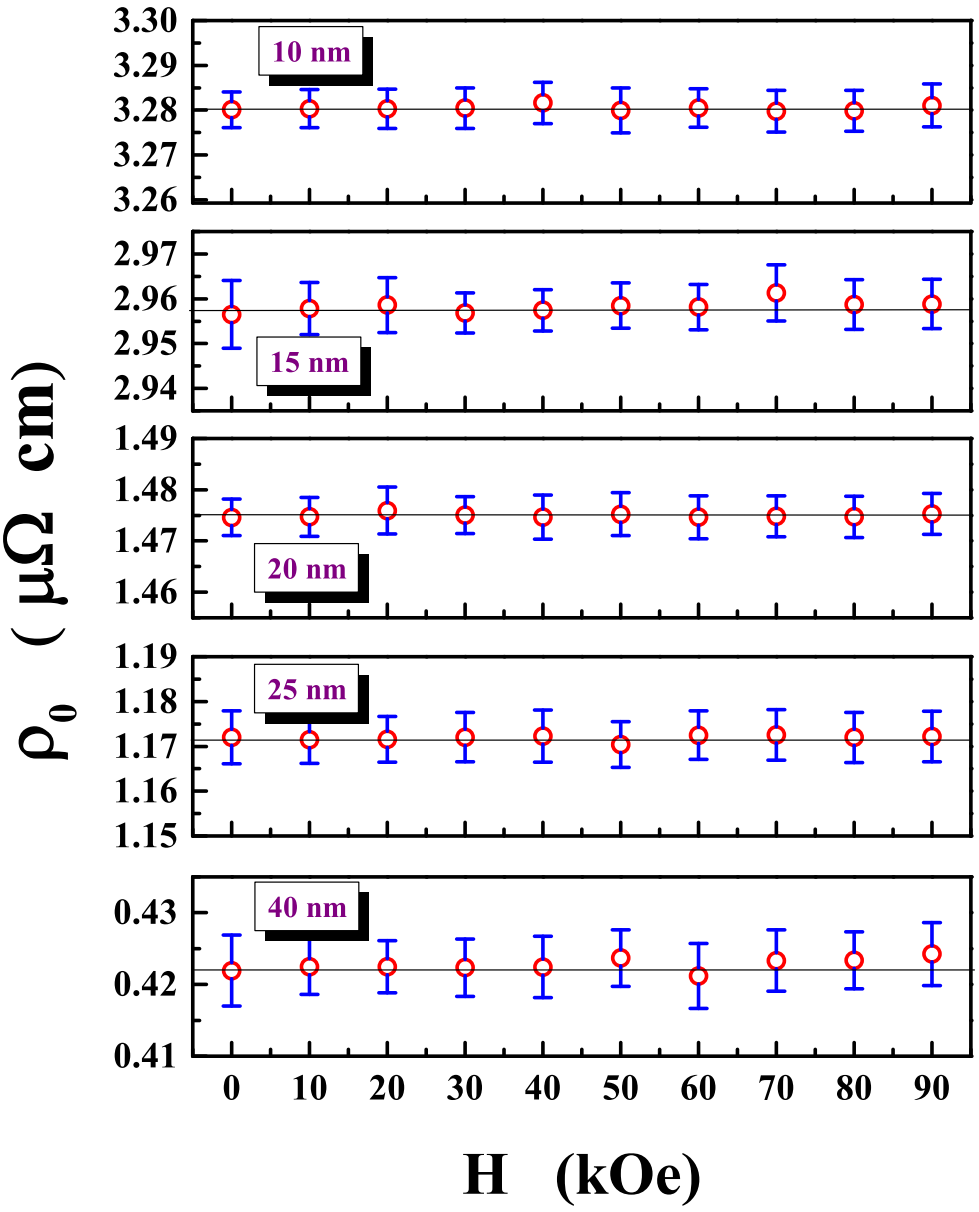

Figure 5.3: *Variation of the residual resistivity, $\rho_0 \equiv \rho$ (T = 1.8 K), with magnetic field, H, ranging from 0 to 90 kOe, in nanocrystalline Ni samples with different average crystallite size.*

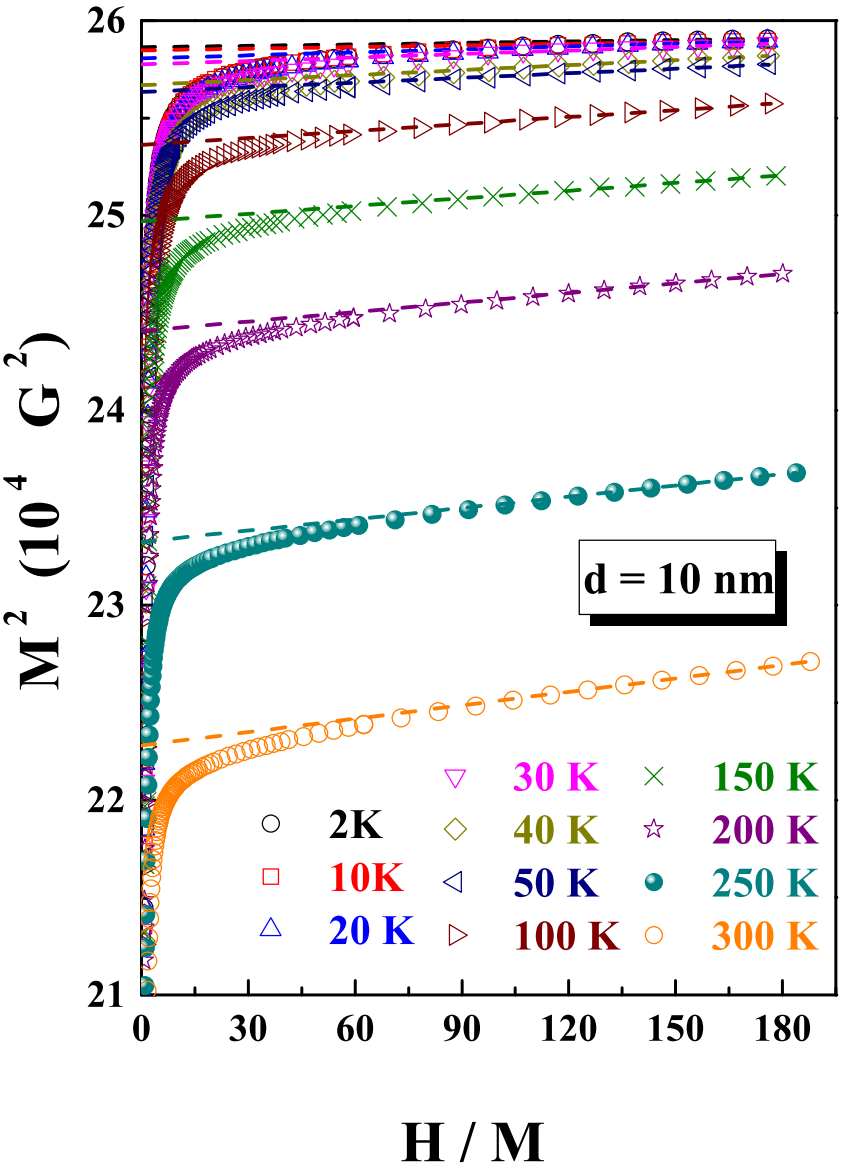

Figure 5.4: *Arrott (M^2 versus H/M) plot, constructed from the magnetization (M) versus magnetic field (H) isotherms taken at temperatures in the range 2 K - 300 K, for the nc-Ni sample with average crystallite size d = 10 nm.*

5.3.1 Residual resistivity and temperature coefficient of resistivity

Figure 5.1 displays the temperature variations of the 'zero-field' resistivity, $\rho(T, H = 0)$, for different nanocrystalline (nc-) Ni samples while the inset shows $\rho(T, H = 0)$ normalized to its value at 300 K. Evidently, with increasing average crystallite size, d, the resistivity at low temperatures reduces in magnitude while the slope of the $\rho(T)$ curve near 300 K increases. The value of resistivity (ρ) at the lowest temperature $T = 1.8$ K is taken to be the residual resistivity, ρ_0. Panel (a) of figure 5.2 displays the average crystallite size, d, dependence of ρ_0. A rapid increase in the ρ_0 as d falls below $\sim$ 20 nm basically reflects enhanced scattering of conduction electrons from atomic disorder/imperfections prevalent at surfaces/interfaces and grain-boundaries as the volume fraction of grain boundaries increases substantially with increasing surface area (or equivalently, with reducing crystallite size). Surface/interface/grain-boundary scattering contribution to residual resistivity has been extensively studied in Ni nanowires [34, 35] and bulk nc-Ni [36–39]. A new finding that the external magnetic field, H, has practically no effect on residual resistivity (ρ_0) in the bulk nc-Ni samples studied, is shown in figure 5.3. This is expected particularly when the field-dependent domain-wall scattering is absent in the present case due to nearly single-domain size of the nanocrystallites. The presently determined values of the temperature coefficient of resistivity (TCR), defined as, $\alpha = (1/\rho_{300K})[(\rho_{300K} - \rho_{270K})/(300\text{ K} - 270\text{ K})]$ (since the $\rho(T)$ curves are *approximately linear* in the temperature range 270 K - 300 K) compare favorably with those repoted previously for nc-Ni [36, 37]. The residual resistivity (ρ_0) and the temperature coefficient of resistivity (α) are plotted against average particle size (d) and shown in the (a) and (b) panels of Fig. 5.2, highlight that the increase in the residual resistivity, ρ_0 with the reduction in d is associated with the decrease in temperature coefficient of resistivity, α. Such a relation is expected since the disorder increases

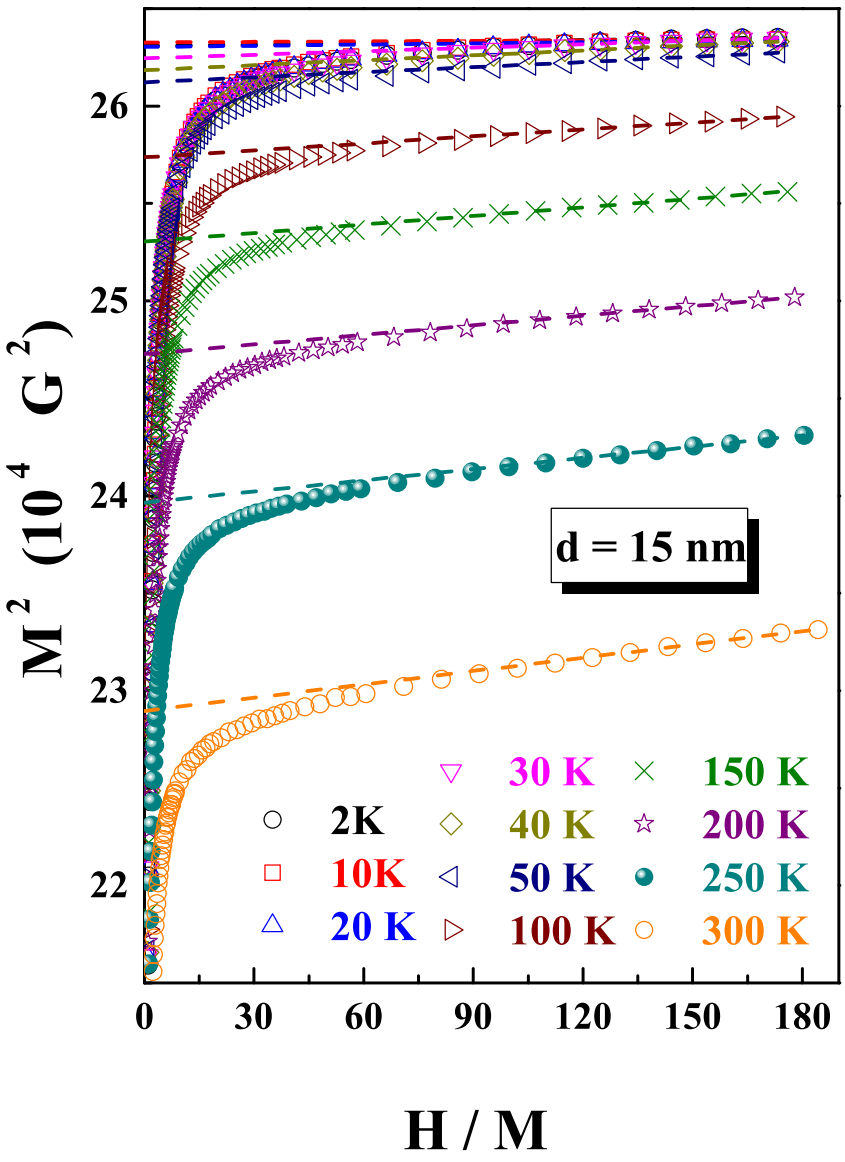

Figure 5.4 (Continued): *Arrott (M^2 versus H/M) plot, constructed from the magnetization (M) versus magnetic field (H) isotherms taken at temperatures in the range 2 K - 300 K, for the nc-Ni sample with average crystallite size d = 15 nm.*

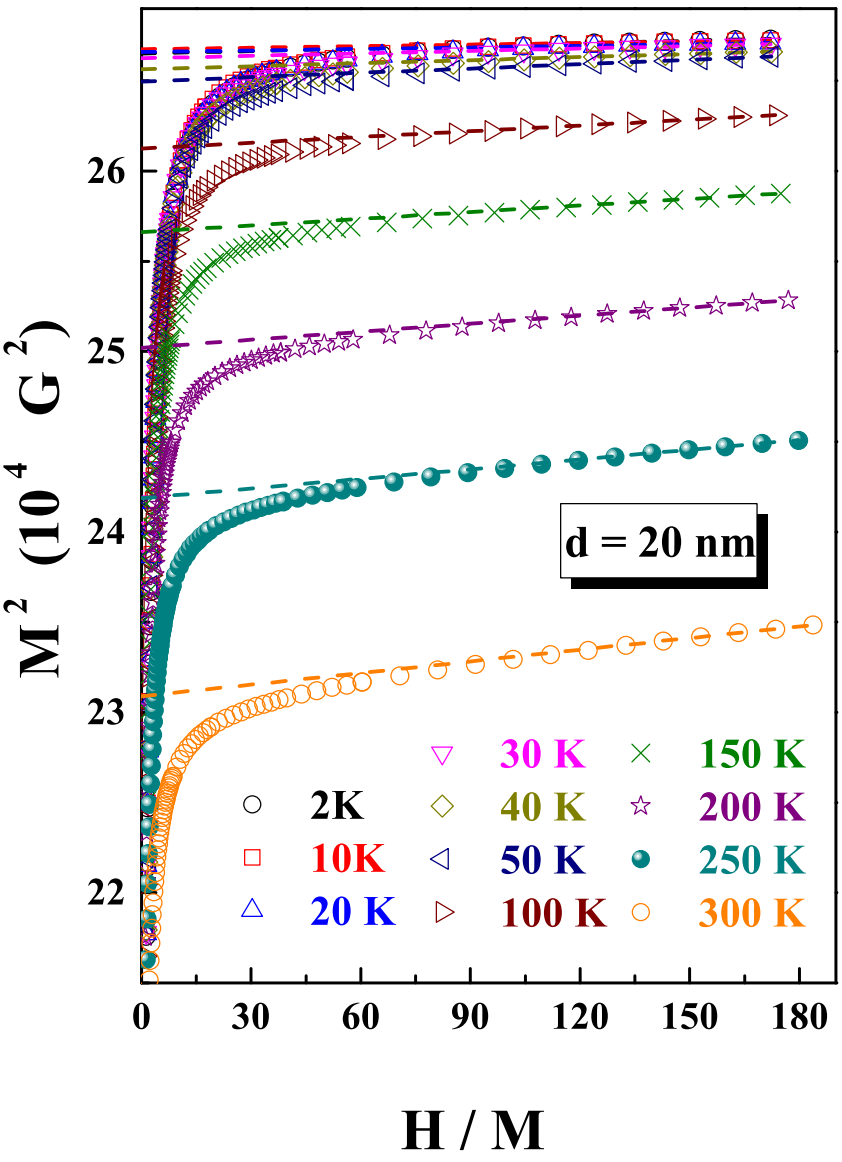

Figure 5.4 (Continued): *Arrott (M^2 versus H/M) plot, constructed from the magnetization (M) versus magnetic field (H) isotherms taken at temperatures in the range 2 K - 300 K, for the nc-Ni sample with average crystallite size d = 20 nm.*

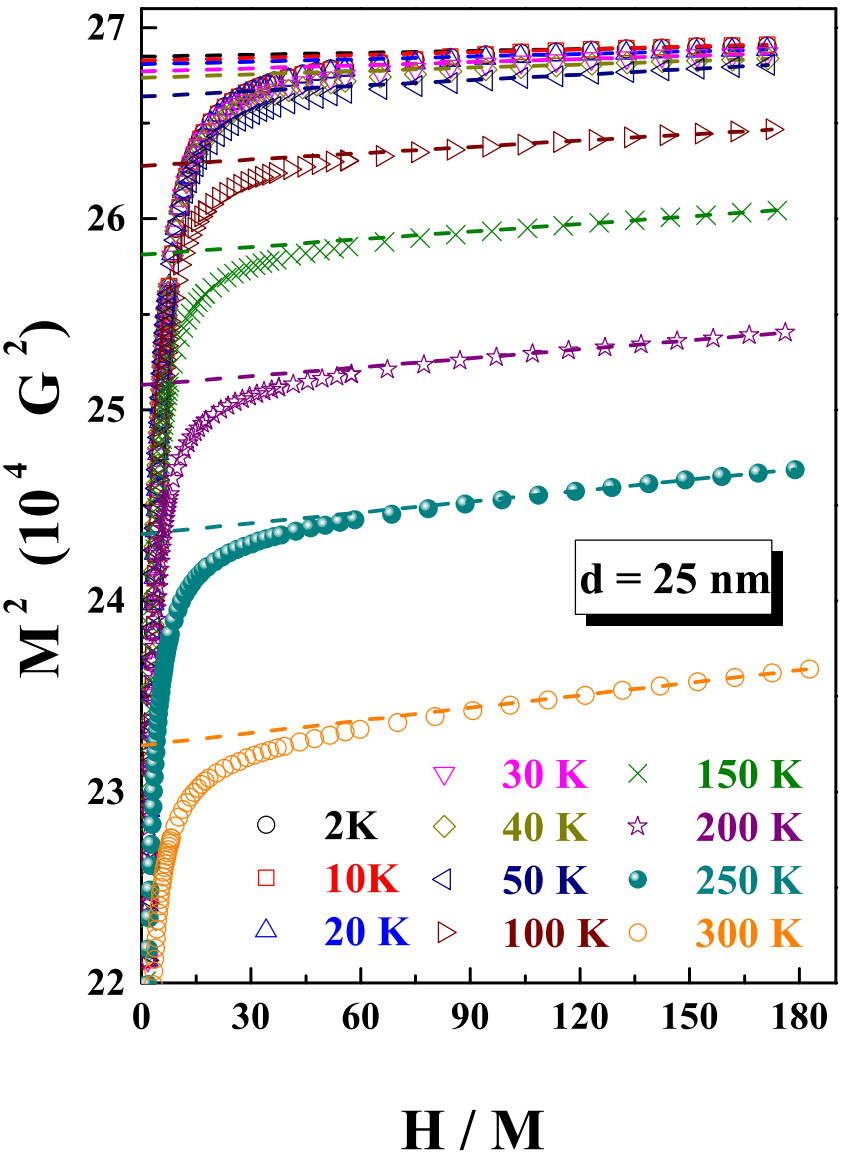

Figure 5.4 (Continued): *Arrott (M^2 versus H/M) plot, constructed from the magnetization (M) versus magnetic field (H) isotherms taken at temperatures in the range 2 K - 300 K, for the nc-Ni sample with average crystallite size d = 25 nm.*

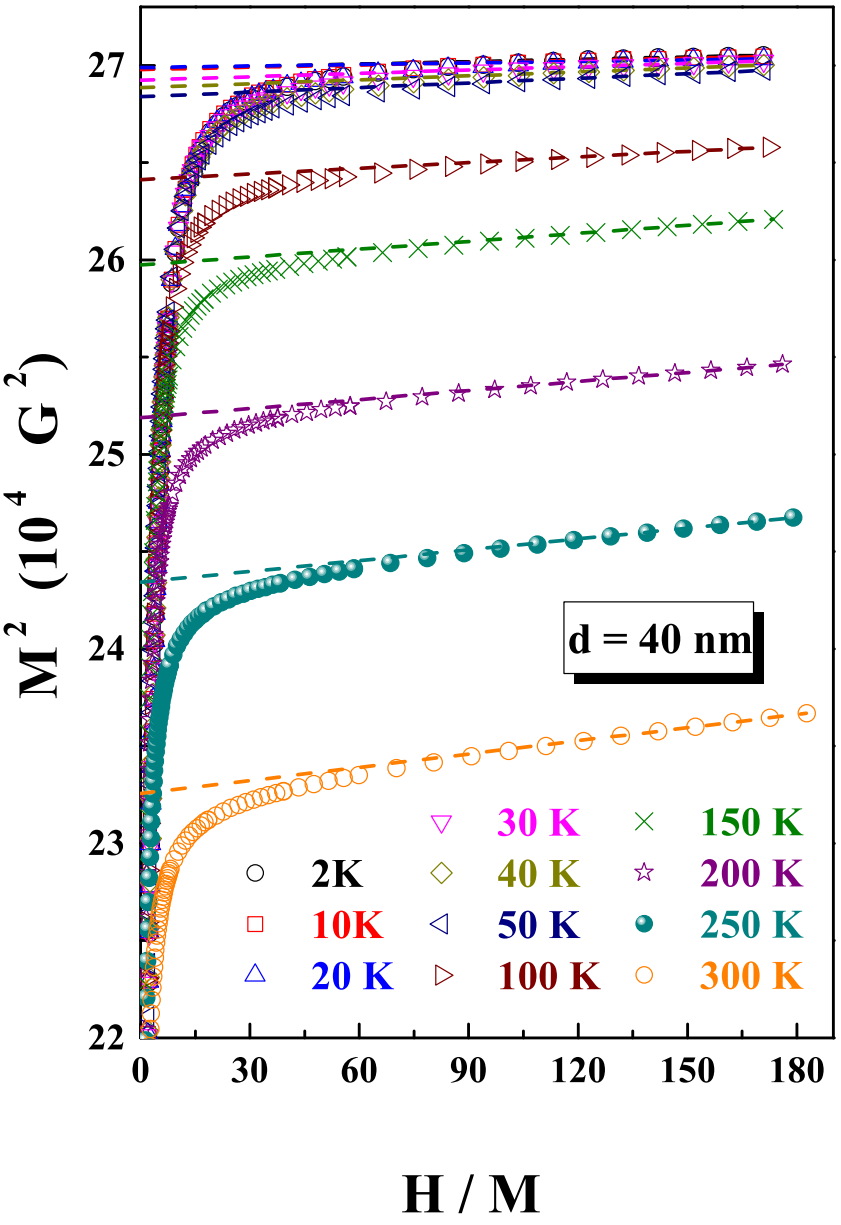

Figure 5.4 (Continued): *Arrott (M^2 versus H/M) plot, constructed from the magnetization (M) versus magnetic field (H) isotherms taken at temperatures in the range 2 K - 300 K, for the nc-Ni sample with average crystallite size d = 40 nm.*

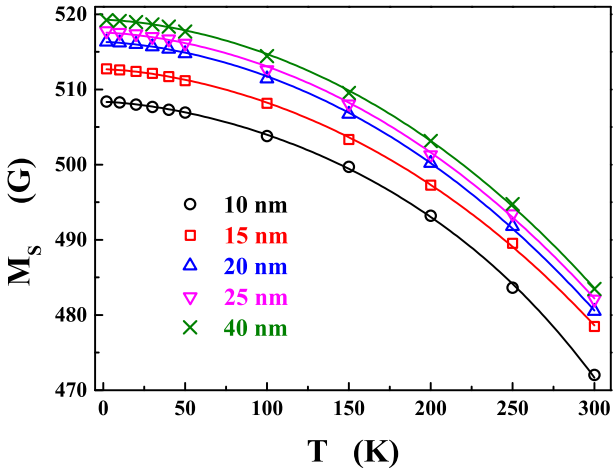

Figure 5.5: *Spontaneous magnetization (symbols) as a function of temperature, $M_s(T)$, for the nanocrystalline Ni samples of different d, extracted from the Arrott plots following the procedure descibed in the text. The continuous curves through the $M_s(T)$ data (symbols) represent the optimum spin-wave (SW) fits based on the spin-wave expression, i.e., Eq.(5.9) of the text.*

(temperature-independent) residual resistivity more than the temperature-dependent part of resistivity.

5.3.2 Spin wave stiffness and its thermal renormalization

To facilitate a quantitative comparison between theory (Eqs.(5.1) - (5.8)) and experiment (observed temperature variation of resistivity, $\rho(T)$ and magnetoresistance, MR) and to keep the number of free fitting parameters to a bare minimum, the values of spontaneous magnetization at 0 K, $M_s(0)$ and thermal renormalization of spin-wave stiffness, $D(T)$, needed in Eq.(5.2), are determined as follows. Instead of obtaining $D(T)$ directly from the neutron scattering experiments [50,51], both $M_s(0)$ and $D(T)$ are deduced from bulk magnetization, $M(T,H)$. The magnetization (M) versus magnetic field (H) isotherms taken on these nanocrystalline Ni samples [47]

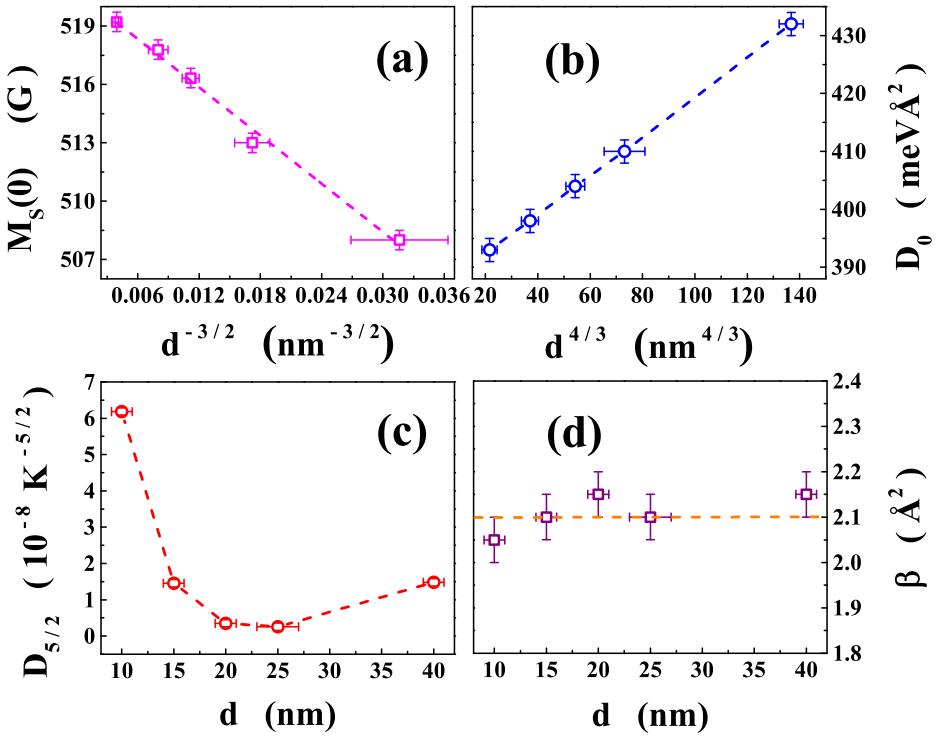

Figure 5.6: *(a) $d^{-3/2}$ variation of spontaneous magnetization at 0 K, $M_s(0)$. (b) $d^{4/3}$ variation of the spin-wave stiffness at 0 K, D_0. (c) and (d) depict the variations of the coefficients $D_{5/2}$ and β (appearing in Eqs.(5.4) and (5.9) of the text) with the average crystallite size, d.*

at various temperatures in the range 2 K - 300 K, are converted into the Arrott (M^2 versus H/M) plots. Arrott plots (AP) for nanocrystalline Ni samples with different crystallite sizes are shown in figure 5.4.

As illustrated in the figure, spontaneous magnetization at different temperatures, $M_s(T)$, is computed from the intercepts on the ordinate obtained when the linear high-field portions of the Arrott plot isotherms are extrapolated to $H = 0$. Spontaneous magnetization as a function of temperature, $M_s(T)$, for different samples, so obtained, is depicted in figure 5.5. The continuous curves through the spontaneous magnetization ($M_s(T)$) data (symbols) represent the optimum spin-wave (SW) fits based on the well-known spin-wave expression [26–28, 52–57]

$$M_s(T) = M_s(0) - g\ \mu_B \times \left[\zeta(3/2)\left(\frac{k_B T}{4\pi D(T)}\right)^{3/2} + 15\pi\ \beta\ \zeta(5/2)\left(\frac{k_B T}{4\pi D(T)}\right)^{5/2}\right] \quad (5.9)$$

with thermal renormalization of $D(T)$ given by Eq.(5.4) and the parameter $\beta = \langle r^2 \rangle/20$, where $\langle r^2 \rangle$ is the mean-square range of the exchange interaction. In Eq. (5.9), the parameters $M_s(0)$, D_0, D_2, $D_{5/2}$ (defined in the section 5.2.1) and β are varied so as to obtain the best spin-wave fits. Consistent with the results of our earlier work [57] on thermomagnetic data ($M_H(T)$), D_2 is negligible compared to $D_{5/2}$. The finding that $D_{5/2} \gg D_2$ implies that the thermal renormalization of the spin wave stiffness is primarily due to the magnon-magnon interactions while the Stoner single-particle excitations have essentially no role to play. The variations of the fit parameters $M_s(0)$, D_0, $D_{5/2}$ and β with the average crystallite size, d, are displayed in figure 5.6. The absolute values of spin-wave stiffness D_0 for nanocrystalline Ni samples with different average crystallite size, d, determined in this work, are in excellent agreement with those obtained earlier on bulk magnetization data [57]. Detailed analaysis of thermal demagnetization data ($M(T)$) at different external magnetic fields H using Eq.(5.9), yielded spin-wave stiffness, $D_0(H)$. By extrapolat-

ing the observed $H^{1/2}$ dependence of $D_0(H)$ to $H = 0$, spin-wave stiffness at $H = 0$ i.e., D_0 was obtained. Consequently, the previously observed [57] $D_0 \sim d^{4/3}$ power law behavior is preserved (Fig.5.6(b)). Moreover, like saturation magnetization [47], spontaneous magnetization at 0 K, $M_s(0) \sim d^{-3/2}$ (Fig.5.6(a)). In conformity with our earlier observation on thermal demagnetization data ($M_H(T)$) [57], regardless of the value of average crystallite size d, $\beta = 2.1(1)$ $\mathring{A}^2$ and hence the mean-square range of the exchange interaction, $\langle r^2 \rangle \simeq 7\ r_{nn}^2$, where r_{nn} is the nearest-neighbor distance.

5.3.3 Electrical resistivity below 15 K

At very low temperatures ($T \lesssim 15$ K), electrical resistivity is found to vary with temperature as T^2 in 3d transition metal ferromagnets Fe, Co, Ni and in a large number of alloys based on them [16, 42, 43]. In crystalline Ni, the values of the coefficient A of the T^2 term, $A = 1.6 \times 10^{-11}$ Ω cm K^{-2}, $1.55(5) \times 10^{-11}$ Ω cm K^{-2} and 1.4×10^{-11} Ω cm K^{-2} have been reported [42–45]. The same temperature dependence of electrical reistivity, ρ has been observed at $T \leq 15$ K in Ni nanowires [35] as well.

Against this backdrop, we attempted to fit the zero-field resistivity, $\rho(T, H = 0)$ data to Eq.(5.8), in which electron-phonon contribution to resistivity, $\rho_{e-p}(T, H = 0)$ has either the Bloch-Grüneisen (BG) or Bloch-Wilson (BW) form and electron-magnon contribution, $\rho_{e-m}(T, H = 0) = A\ T^2$, by treating ρ_0, ρ_Θ, Θ_D and A as free fitting parameters. The fits, based on Eq.(5.8), to the *intrinsic* resistivity, $\rho_{int} = \rho - \rho_0$ (open circles), so obtained, are depicted by the continuous curves in figure 5.7. We find that the Bloch-Grüneisen (BG) fits are far superior to the Bloch-Wilson (BW) counterparts and the coefficient A of the T^2 term has the value $A = 1.65(15) \times 10^{-11}$ Ω cm K^{-2} irrespective of average crystallite size, d. This value conforms well with those reported earlier for bulk Ni.

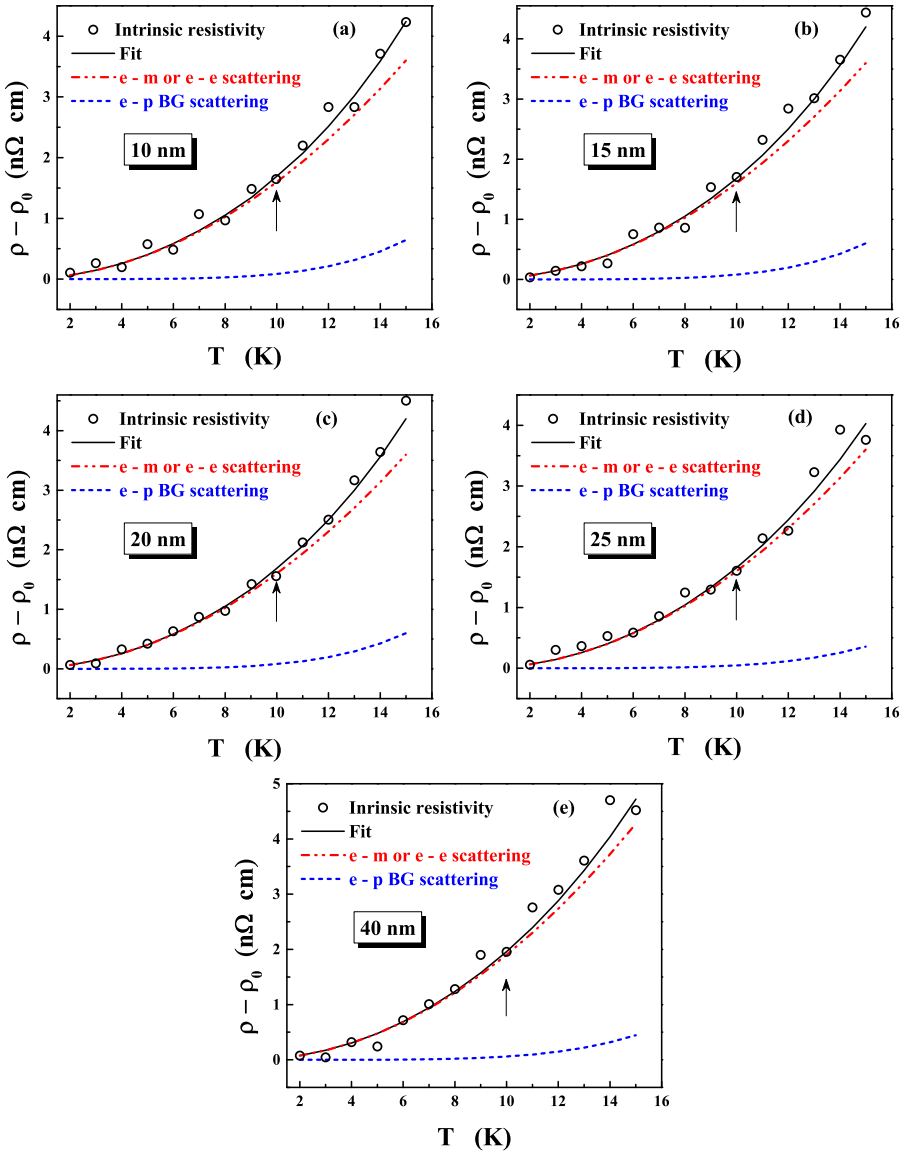

Figure 5.7: *Intrinsic resisitivity as a function of temperature, $\rho_{int}(T) \equiv \rho(T) - \rho_0$ (open circles) along with the theoretical fit (continuous curve), based on Eq.(5.8), for the different nanocrystalline Ni samples, in the temperature range $T \leq 15$ K. The temperature variations of the individual contributions to $\rho_{int}(T)$ arising from the electron-phonon, ρ_{e-p} (BG form), and electron-magnon, ρ_{e-m} $(= A\ T^2)$, or electron-electron, ρ_{e-e} $(= A^{\dagger}\ T^2)$ scattering, obtained as various components of the theoretical fit, are denoted by the dashed and dash-double-dot curves in the panels (a) - (e) for (a) $d = 10$ nm, (b) $d = 15$ nm, (c) $d = 20$ nm, (d) $d = 25$ nm, (e) $d = 40$ nm.*

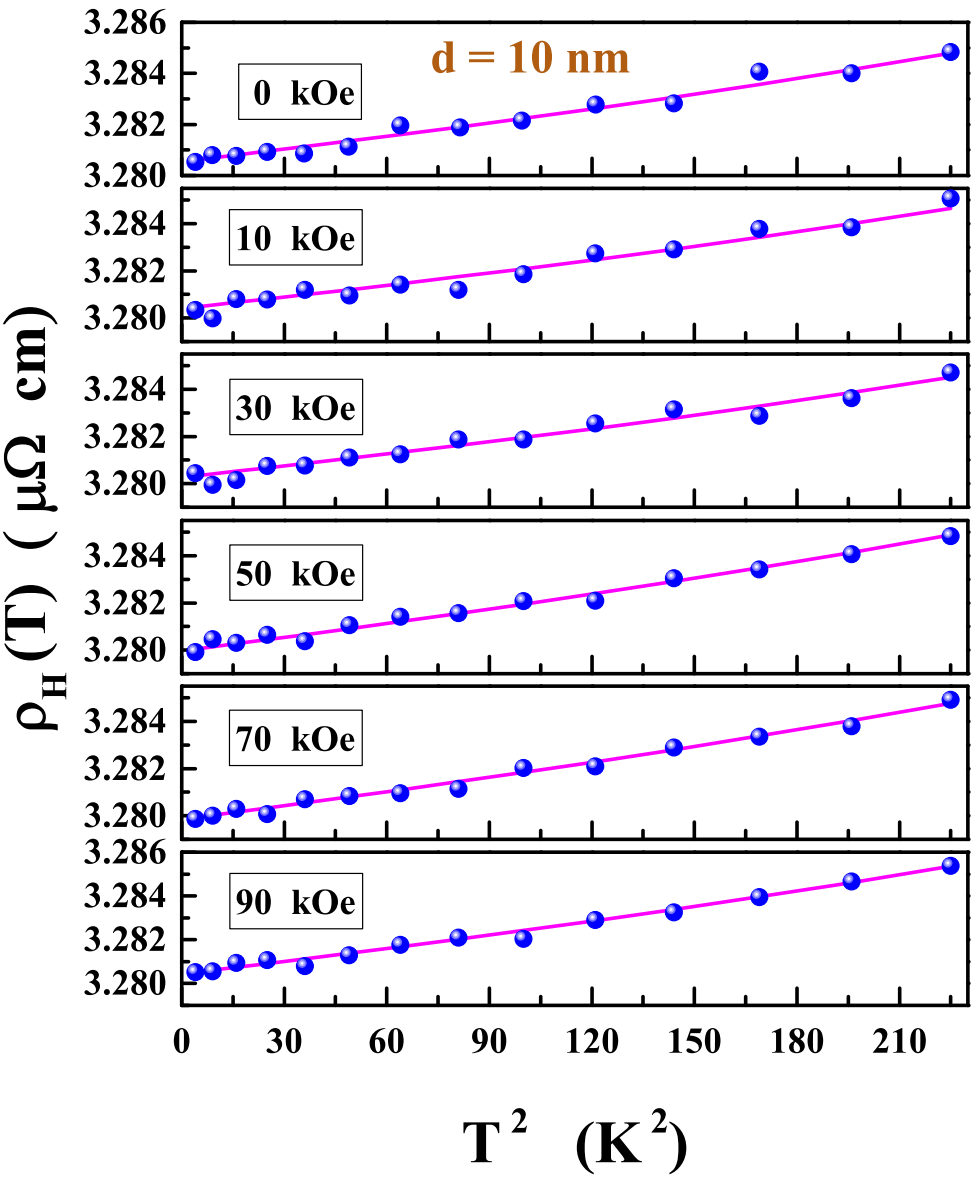

Figure 5.8: *'Zero-field' and 'in-field' resistivity, $\rho_H(T)$, of the nc-Ni sample with $d = 10$ nm, plotted against T^2, in the temperature range 1.8 K $\leq T \leq$ 15 K. Insensitivity of the slope of the linear $\rho_H - T^2$ plots to the magnetic field establishes the $e-e$ scattering as the sole mechanism for $\rho_H(T)$ at temperatures $T \leq 15$ K.*

In Fig. 5.7, the temperature variations of the ρ_{e-p} (BG form) and ρ_{e-m} ($= A\,T^2$) contributions to $\rho_{int}(T)$ are denoted by the dashed and dash-double-dot curves. Evidently, electron-magnon scattering contribution to resistivity, ρ_{e-m} completely accounts for the observed intrinsic resistivity, $\rho_{int}(T)$ at T $\lesssim$ 10 K whereas electron-phonon scattering contribution to resistivity, ρ_{e-p} starts picking up as the temperature increases beyond 10 K. The T^2 variation of resistivity, ρ is generally attributed to [35, 42, 43] the electron-magnon scattering (i.e., Eq.(5.2) with $D(T) \cong D_0$). However, the electron-electron (Baber) scattering contribution also varies as T^2 (i.e., $\rho_{e-e}(T, H = 0) = A^{\dagger}\,T^2$) at such low temperatures. The following considerations enable us to unambiguously distinguish between the electron-magnon $(e-m)$ and electron-electron $(e-e)$ scattering contributions. An external magnetic field H introduces a gap in the spin-wave spectrum and hence makes the thermal excitation of spin waves increasingly difficult particularly at low temperatures. Alternatively, the applied magnetic field, H suppresses magnons and so also the electron-magnon $(e-m)$ scattering. By contrast, the electron-electron $(e-e)$ Coulomb scattering is *insensitive* to applied magnetic field, H, i.e., H does not affect the $e-e$ scattering. ρ_H versus T^2 plots, displayed in figure 5.8, clearly demonstrate that the coefficient A (slope of the linear $\rho_H(T^2)$ plots) of the T^2 term retains (within the uncertainty limits) its 'zero-field' value even in fields as high as 90 kOe. This finding rules out completely the electon-magnon $(e-m)$ scattering as a possible origin for the T^2 term.

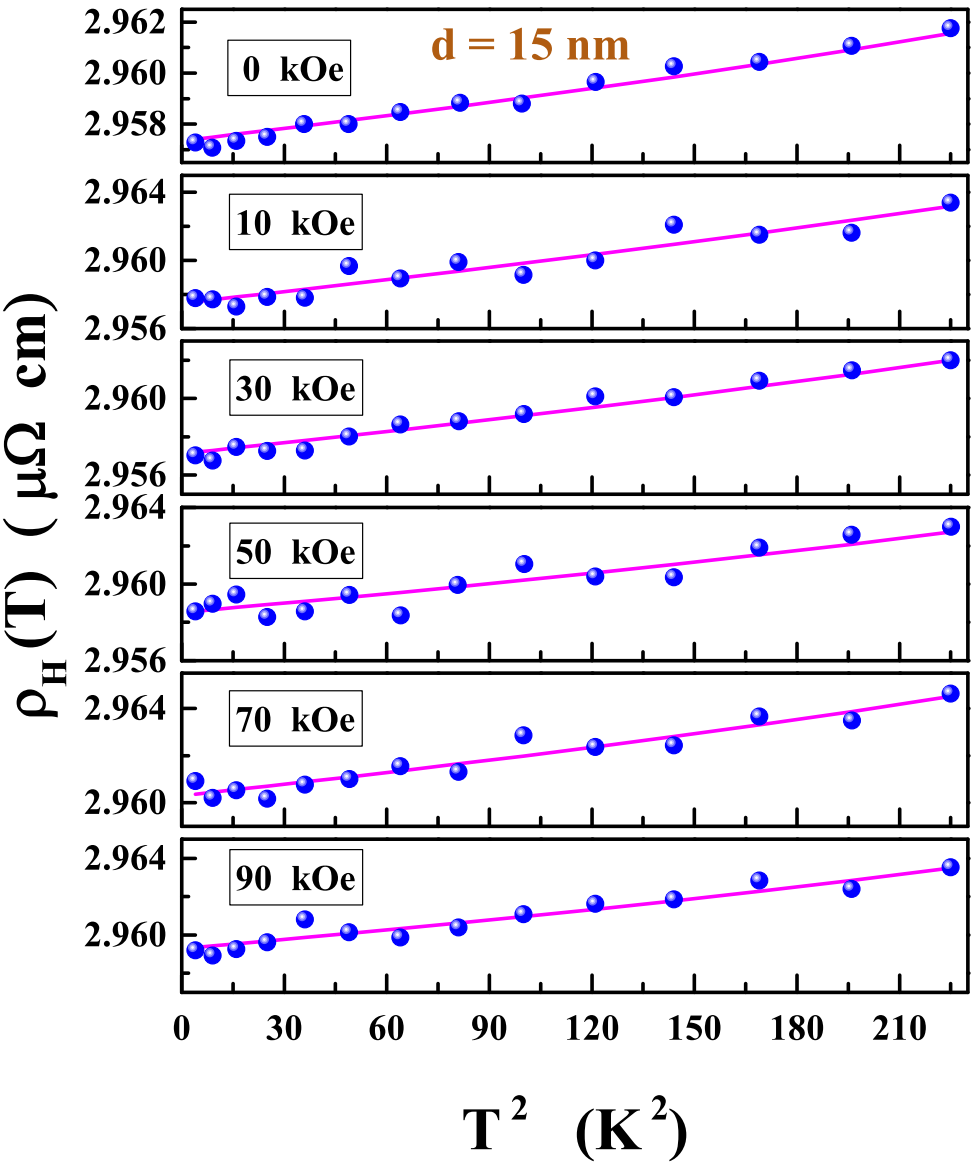

Figure 5.8 (Continued): *'Zero-field' and 'in-field' resistivity, $\rho_H(T)$, of the nc-Ni sample with $d = 15$ nm, plotted against T^2, in the temperature range 1.8 K $\leq T \leq$ 15 K. Insensitivity of the slope of the linear $\rho_H - T^2$ plots to the magnetic field establishes the $e - e$ scattering as the sole mechanism for $\rho_H(T)$ at temperatures $T \leq 15$ K.*

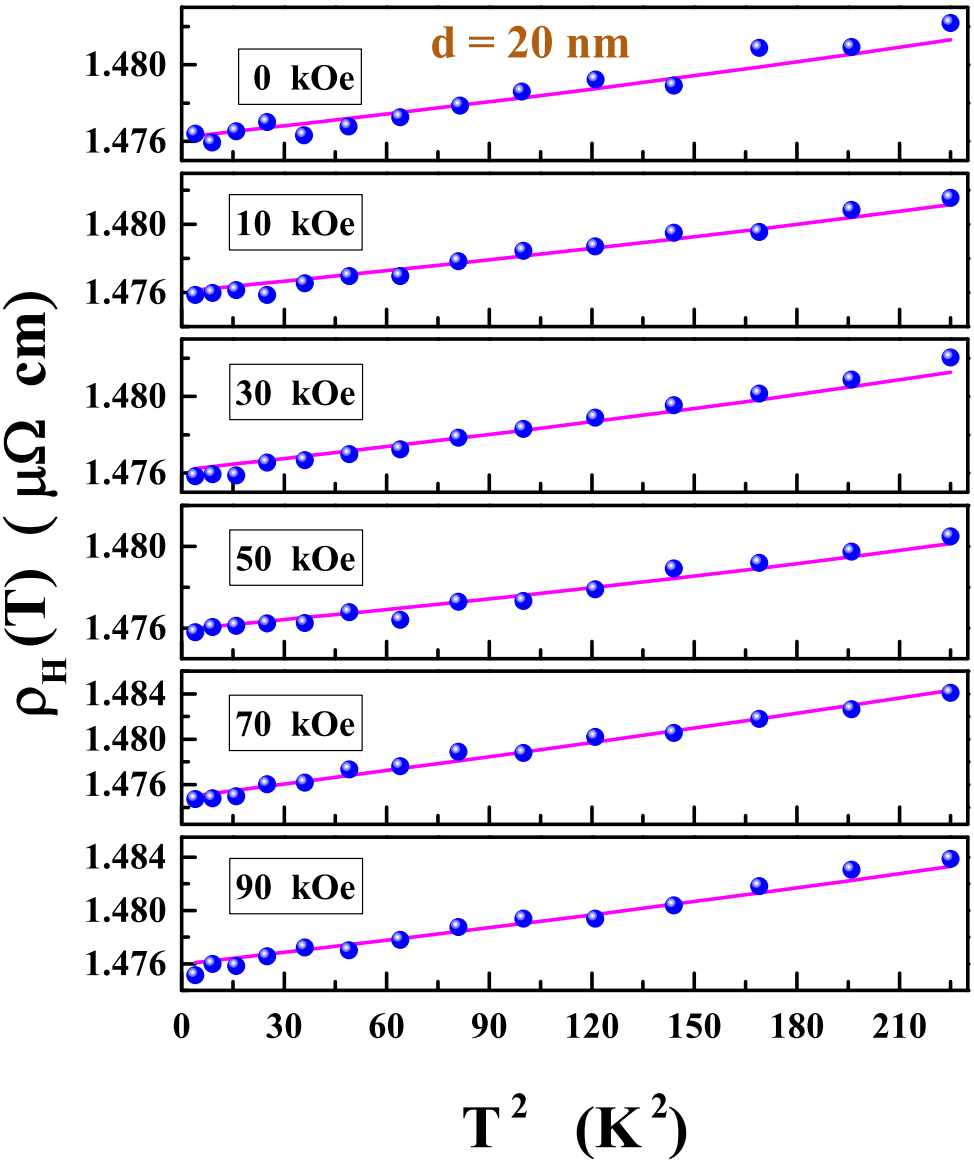

Figure 5.8 (Continued): *'Zero-field' and 'in-field' resistivity, $\rho_H(T)$, of the nc-Ni sample with $d = 20$ nm, plotted against T^2, in the temperature range 1.8 K $\leq T \leq$ 15 K. Insensitivity of the slope of the linear $\rho_H - T^2$ plots to the magnetic field establishes the $e-e$ scattering as the sole mechanism for $\rho_H(T)$ at temperatures $T \leq 15$ K.*

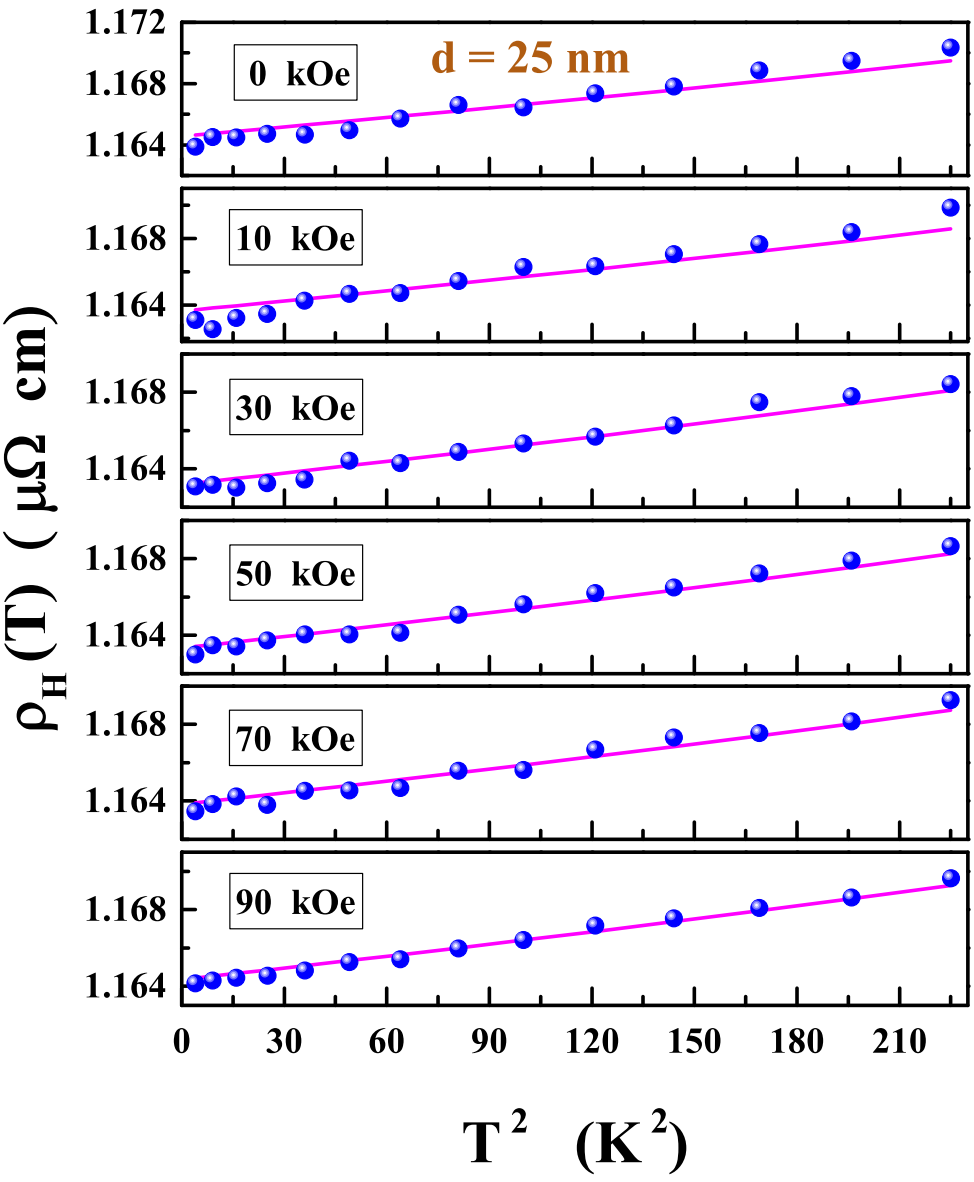

Figure 5.8 (Continued): *'Zero-field' and 'in-field' resistivity, $\rho_H(T)$, of the nc-Ni sample with $d = 25$ nm, plotted against T^2, in the temperature range 1.8 K $\leq T \leq$ 15 K. Insensitivity of the slope of the linear $\rho_H - T^2$ plots to the magnetic field establishes the $e-e$ scattering as the sole mechanism for $\rho_H(T)$ at temperatures $T \leq 15$ K.*

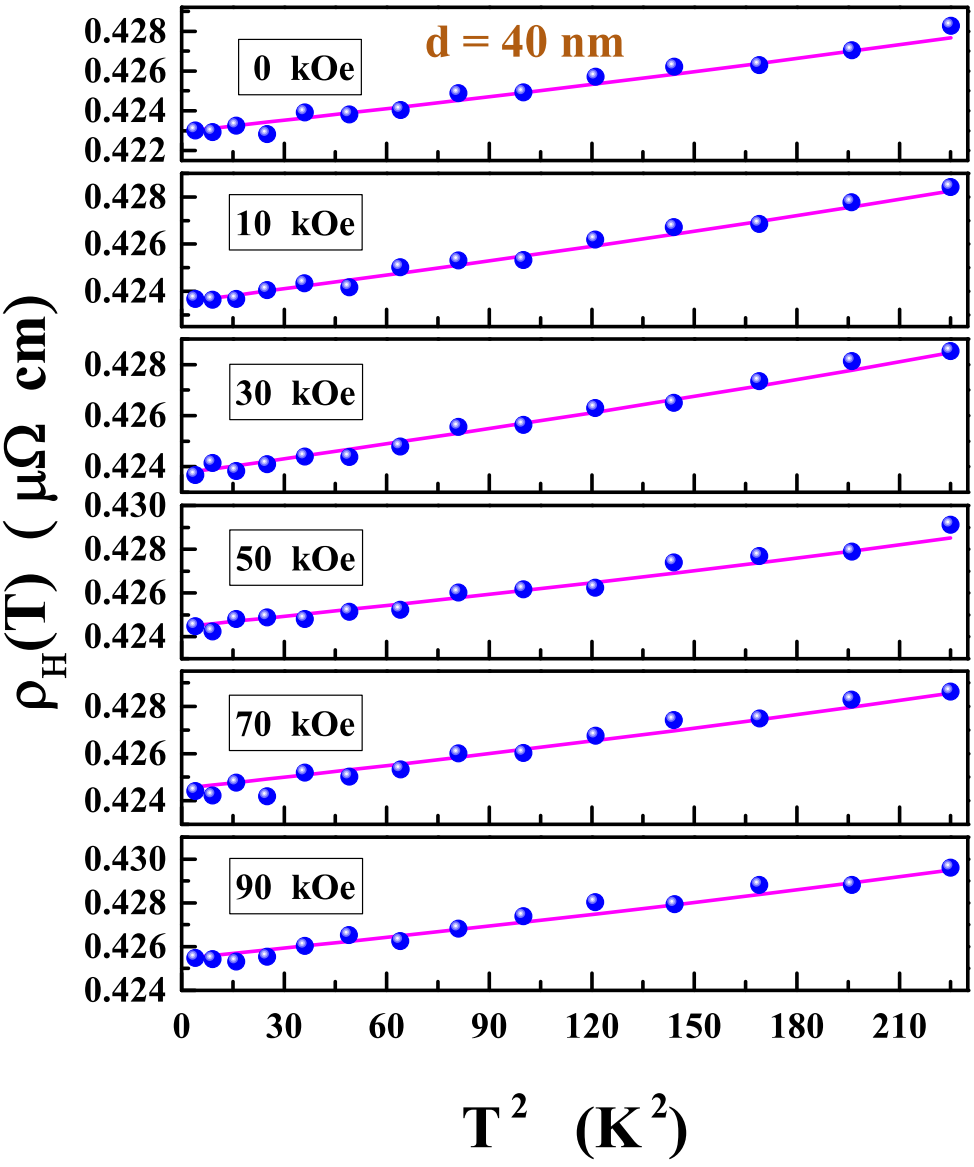

Figure 5.8 (Continued): *'Zero-field' and 'in-field' resistivity, $\rho_H(T)$, of the nc-Ni sample with $d = 40$ nm, plotted against T^2, in the temperature range 1.8 K $\leq T \leq$ 15 K. Insensitivity of the slope of the linear $\rho_H - T^2$ plots to the magnetic field establishes the $e-e$ scattering as the sole mechanism for $\rho_H(T)$ at temperatures $T \leq 15$ K.*

5.3.4 Electrical resistivity above 15 K

To unravel the scattering mechanisms responsible for $\rho(T)$ at $T \geq 15$ K, we adopt the following approach. At first, in the entire temperature range 1.8 K $\leq T \leq$ 300 K, fits to $\rho(T)$ are attempted based on the form of Eq.(5.8) which excludes the magnon term and considers the phonon term of either the Bloch-Grüneisen (BG) or Bloch-Wilson (BW) form. From the percentage reduced deviations of the fits from the data, defined as $[(\rho_{exp} - \rho_{fit})/\rho_{exp}] \times$ 100 and depicted in the figure 5.9, it is evident that both the Bloch-Grüneisen (BG) and Bloch-Wilson (BW) fits present *systematic* deviations but the amplitude is smaller in the latter case. When, besides the BG or BW phonon term in Eq.(5.8), the magnon contribution, represented by a T^2 term, is included, deviations are still systematic but now the amplitude of deviations for the BG + T^2 fits is an order of magnitude smaller (see Fig.5.10). From this result, it immediately follows that (i) the $e - p$ scattering alone cannot account for the observed $\rho(T)$ and the $e - m$ scattering has to be considered along side the phonon contribution, and (ii) Bloch-Grüneisen expression forms a much better description of the phonon term in Eq.(5.8) than the Bloch-Wilson version. This result runs contrary to the popular belief [35,42] that the Bloch-Wilson version is more appropriate particularly for 3d transition metal ferromagnets. The inference (ii) permits us to conclude that, irrespective of the value of d (including the bulk, $d = \infty$), *phonon-induced* $s^{\uparrow\downarrow} - s^{\uparrow\downarrow}$, $d^{\uparrow\downarrow} - d^{\uparrow\downarrow}$ transitions are more frequent than the $e - p$ $s^{\uparrow\downarrow} - d^{\uparrow\downarrow}$ transitions over the entire temperature range 1.8 K $\leq T \leq$ 300 K.

The data analysis same as that followed for the nanocrystalline Ni samples, has been carried out on the resistivity data for crystalline Ni taken from reference 42. The deviation plots, shown in figures 5.9 and 5.10 testify that all the above-stated observations also hold for bulk Ni.

In order to ascertain whether or not the thermal renormalization of the spin wave

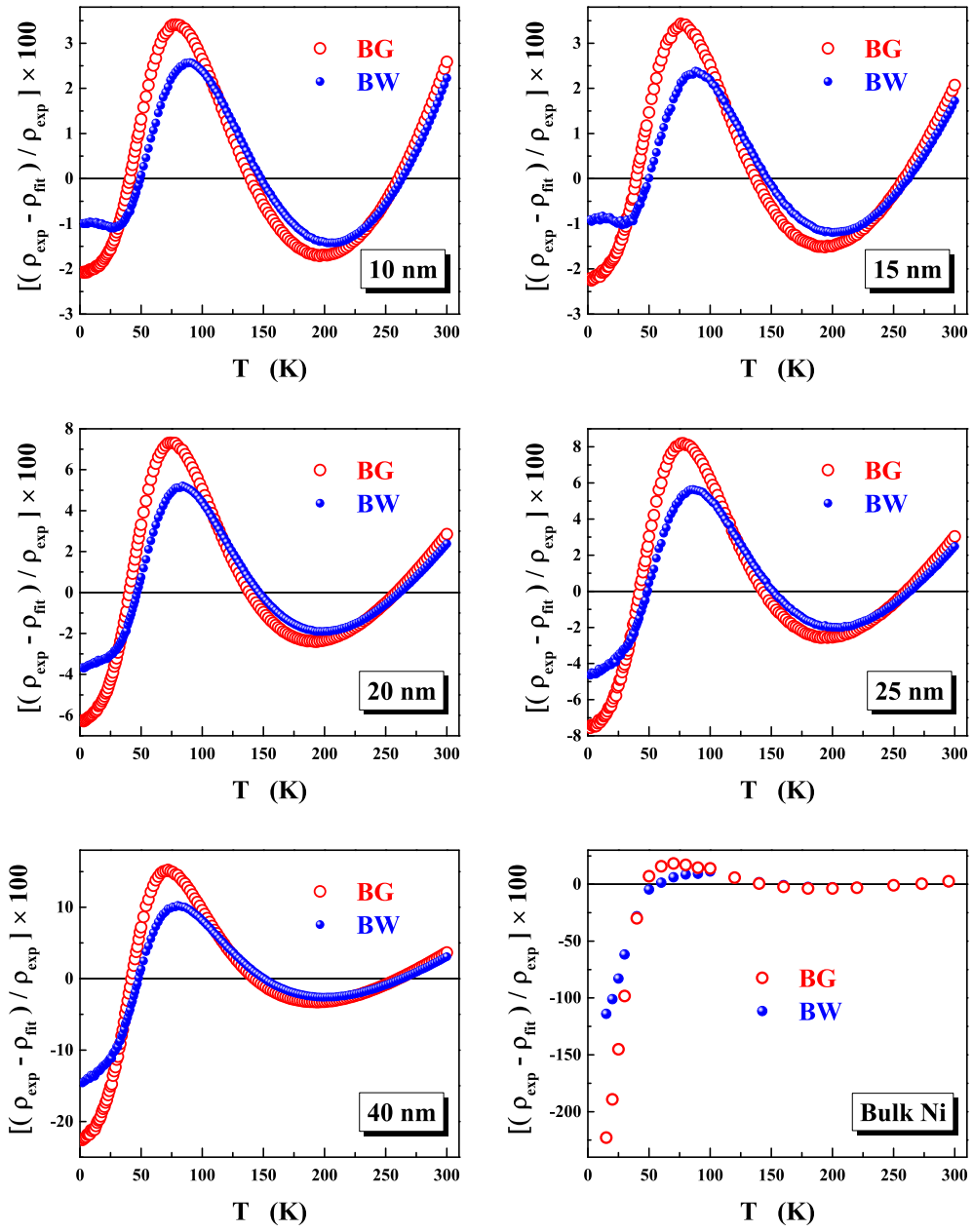

Figure 5.9: *The percentage deviations of the 'zero-field' resistivity data, $\rho_{exp}(T)$, from the BG and BW fits, $\rho_{fit}(T)$, for the nc-Ni samples and for bulk Ni (note that the resistivity data for crystalline Ni have been taken from reference 42); for details, refer to subsection 5.3.4.*

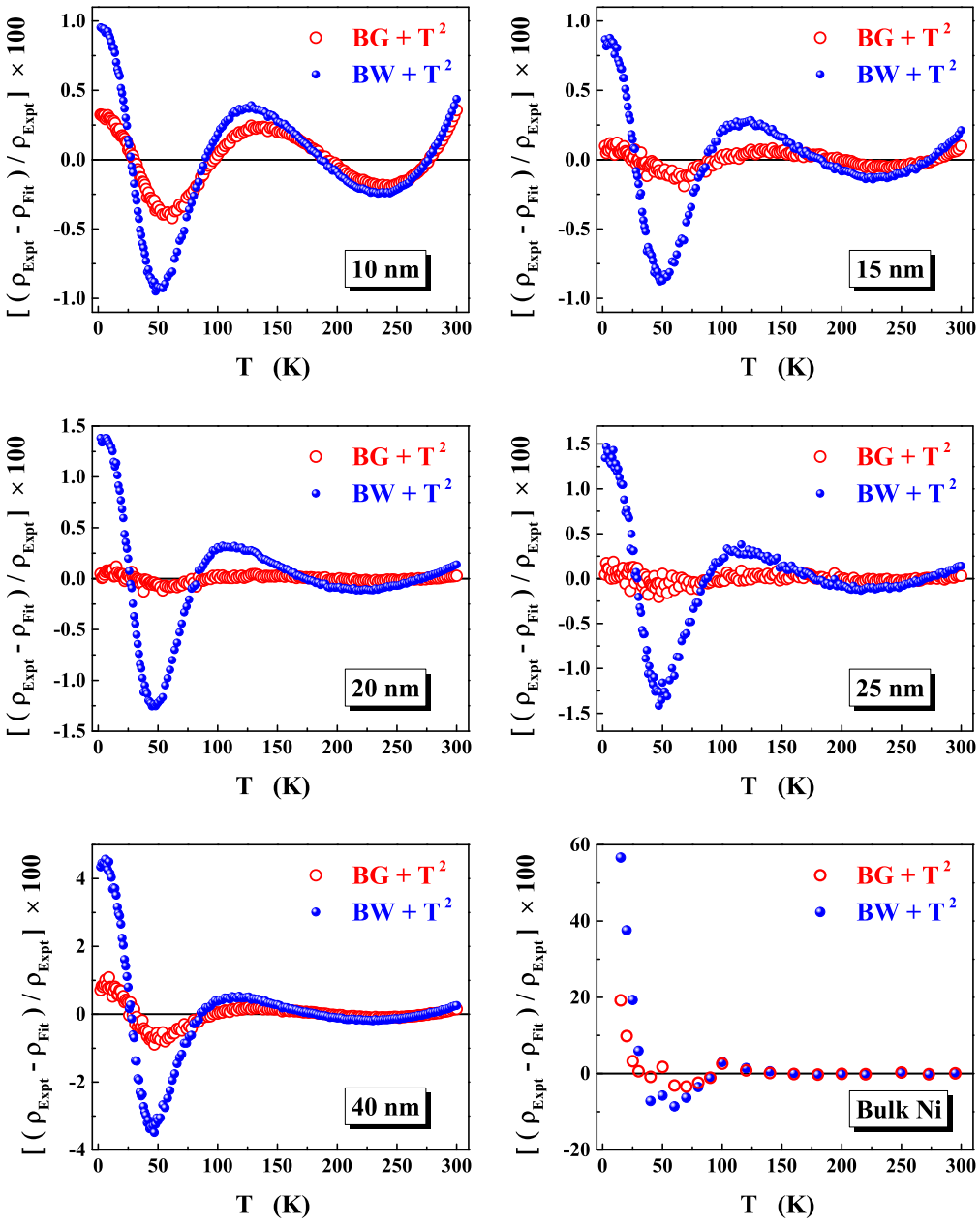

Figure 5.10: *The percentage deviations of the 'zero-field' resistivity data, $\rho_{exp}(T)$, from the $BG + T^2$ and $BW + T^2$ fits, $\rho_{fit}(T)$, for the nc-Ni samples and for bulk Ni (note that the resistivity data for crystalline Ni have been taken from reference 42); for details, refer to subsection 5.3.4.*

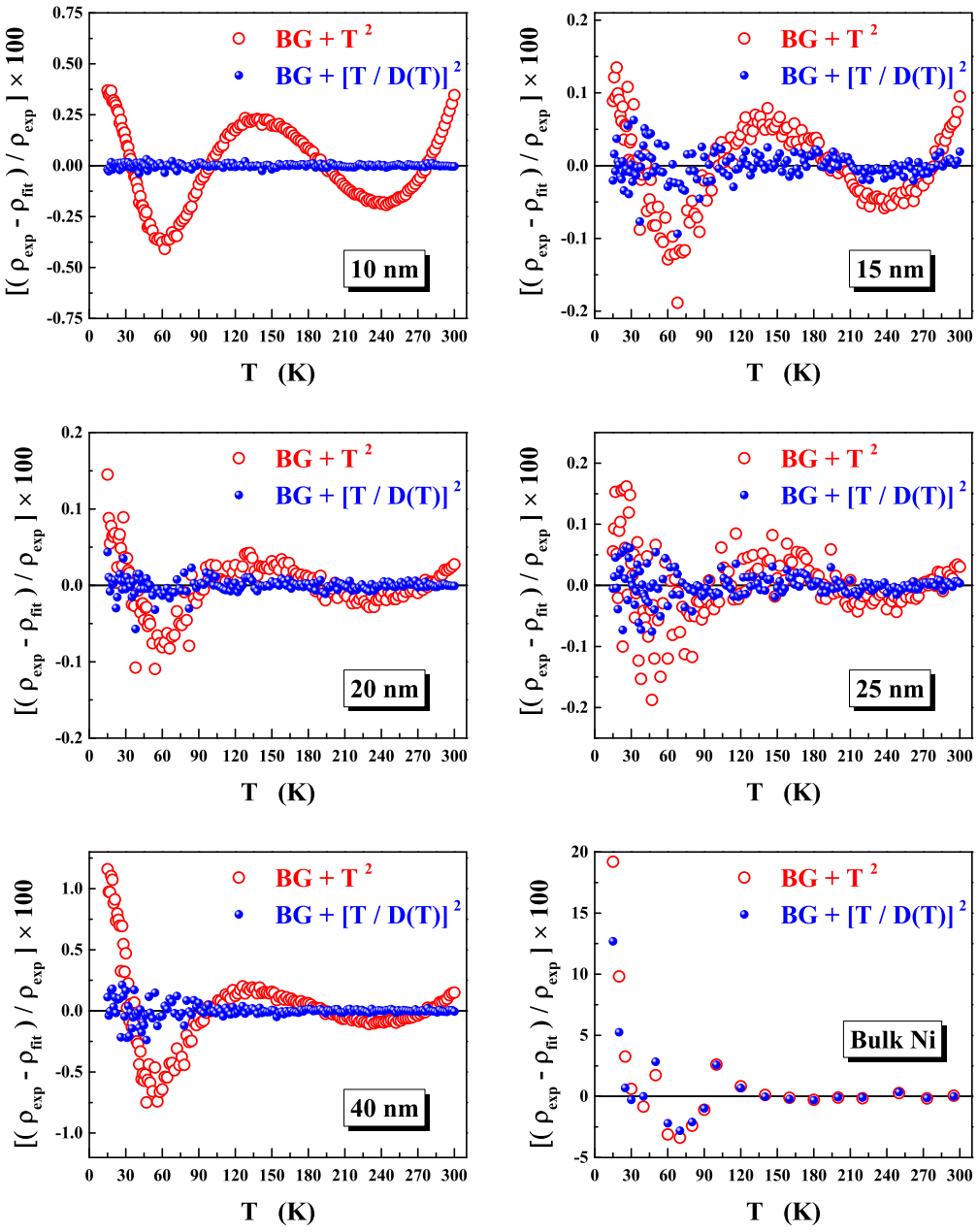

Figure 5.11: *The percentage deviations of the 'zero-field' resistivity data, $\rho_{exp}(T)$, from the $BG+T^2$ and $BG+[T/D(T)]^2$ fits, $\rho_{fit}(T)$, for the nc-Ni samples and for bulk Ni (note that the resistivity data for crystalline Ni have been taken from reference 42); for details, refer to subsection 5.3.4.*

stiffness, D (cf. Eq.(5.4)) is important, the fits to the $\rho(T)$ data are attempted based on the version of Eq.(5.8) in which the $\rho_{e-p}(T)$ has the BG form (i.e., Eq.(5.1) with $n = 5$) and $\rho_{e-m}(T)$ is either given by $A\ T^2$ (which completely ignores the thermal renormalization of D, i.e., sets $D(T) = D_0$ in Eq.(5.2)) or by Eq.(5.2), which includes the thermal renormalization of D. In the former fit, the Debye temperature, Θ_D, the prefactor ρ_Θ, in Eq.(5.1), and the coefficient A of the T^2 term in the expression for $\rho_{e-m}(T)$ are varied to achieve optimum agreement with the observed $\rho(T)$. On the other hand, in the latter fits involving $D(T)$, $M_s(0)$, in Eq.(5.2), along with D_0 and $D_{5/2}$, in Eq.(5.4), are kept fixed at their values extracted from the spontaneous magnetization data in section 5.3.2, and Θ_D, ρ_Θ and the prefactor $\rho^\star$, in Eq.(5.2), are optimized. The data analysis same as that followed for the nanocrystalline Ni samples, has been carried out on the resistivity data for crystalline Ni taken from reference [42] and the values $M_s(0) = 521$ G, $D_0 = 550\ meV\mathring{A}^2$, $D_{5/2} = 1.0 \times 10^{-8}\ K^{-5/2}$ taken from Ref. [57,58]. The percentage deviations for the $BG + T^2$ and $BG + [T/D(T)]^2$ fits are compared in Fig. 5.11. For bulk Ni and all the nanocrystalline Ni samples, the deviations for the fit that completely ignores the thermal renormalization of D are *systematic* whereas the deviations are *statistically distributed* around zero when the thermal renormalization of D is given due consideration. This result proves conclusively that the thermal renormalization of the spin wave stiffness (mainly due to magnon-magnon interactions) has to be taken into account for a correct description of the $e - m$ scattering process in nanocrystalline Ni as well as in bulk Ni. Figure 5.12 highlights the power law variations of the free-fitting parameters Θ_D, ρ_Θ and $\rho^\star$ (corresponding to the optimum $BG + [T/D(T)]^2$ fits) with the average crystallite size, d. The expressions $\Theta_D(d) = \Theta_D(d = \infty)$ - $c\ d^n$ with $\Theta_D(d = \infty) = 390(5)$ K, $c = 104(30)$ and $n = -0.25(5)$, $\rho_\Theta(d) = \rho_\Theta(d = 0)$ - $c'\ d^{n'}$, with $\rho_\Theta(d = 0) = 4.1(9) \times 10^{-5}\ \Omega\ cm$, $c' = 6.5(30) \times 10^{-6}$ and $n' = 0.33(16)$, and $\rho^\star(d) = \rho^\star(d = \infty)$ - $c''\ d^{n''}$ with $\rho^\star(d = \infty) = 43.3(5) \times 10^{-47}\ \Omega$ cm cm^4 sec, $c'' = 103(16)$ and $n'' = 0.52(6)$, closely reproduce the observed variations of Θ_D, ρ_Θ and $\rho^\star$ with average

crystallite size, d.

Returning to Fig. 5.12, while the Debye temperature, Θ_D and $\rho^\star$ (the prefactor in Eq.(5.2)) increase, ρ_Θ (the prefactor in the Debye integral of Bloch-Grüneisen expression) decreases with increasing average crystallite size, d. Increased disorder in the atomic locations at the surfaces/interfaces and grain boundaries due to considerable increase in the surface area for the samples with reduced crystallite (d) has two main consequences. First, it leads to an increase in the average atomic displacements at a given temperature (especially at surfaces/interfaces and grain boundaries) compared to that in the ordered (crystalline) system and hence results in the overall reduction in the Debye temperature. Second, it tends to smear out the sharp features in the total density of states (DOS) near the Fermi level, E_F, and thereby reduces the DOS at E_F, $N(E_F)$. In view of the relation [49] $\rho_\Theta \propto [N(E_F)]^{-1}$ and Eq.(5.3), decrease in $N(E_F)$ is responsible for both the enhancement in ρ_Θ as well as the decline in $\rho^\star$. The experimental value $\rho^\star = 4.33(5) \times 10^{-46}$ Ω cm cm^4 sec, yielded by the present analysis of the resistivity data for bulk Ni taken from reference 42, is in perfect agreement with the theoretical estimate of $\rho^\star = 4.29 \times 10^{-46}$ Ω cm cm^4 sec, computed for crystalline (bulk) Ni when the values [10,59] $\Im_{s-d} = 0.48$ eV, $E_F^s = \hbar^2\ (k_F^s)^2/2\ m_s = 3$ eV, $N(E_F^d) = 1.87$ atom^{-1} eV^{-1}, $N(E_F^s) = 0.21$ atom^{-1} eV^{-1} and standard values for s-electron mass, m_s, and number density of s electrons are inserted in Eq.(5.3).

The most optimum fits, based on Eq.(5.8), to the *intrinsic* resistivity, ρ_{int}, data (open circles) in the temperature range 15 K $\leq T \leq$ 300 K, are depicted by the continuous curves in figure (5.13). In this figure, the temperature variations of the ρ_{e-p} (Bloch-Grüneisen form) and ρ_{e-m} ($\propto [T/D(T)]^2$) contributions to $\rho_{int}(T)$ are denoted by the dashed and dash-dot curves. The main observations are as follows.

• The phonon-induced non-spin-flip intraband ($s-s$ and $d-d$ electron-phonon) scattering (of Bloch-Grüneisen form) and magnon-induced spin-flip inter-band

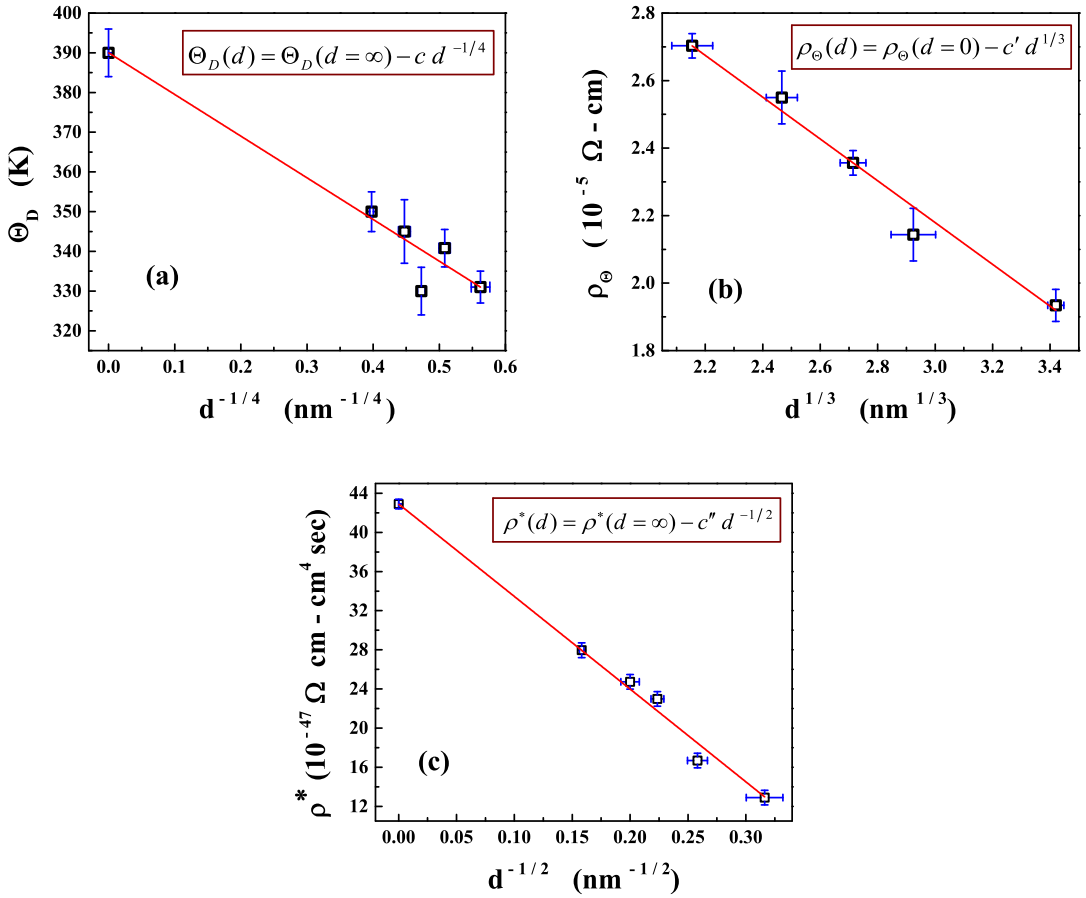

Figure 5.12: *The variations of (a) Debye temperature, Θ_D, (b) the prefactor ρ_Θ in Eq.(5.1) with $n = 5$, and (c) the prefactor $\rho^\star$ in Eq.(5.2), with the average crystallite size, d. These parameters are obtained from the theoretical fits to $\rho(T, H = 0)$, based on Eq.(5.8) with $\rho_{e-p}(T, H = 0)$ given by the BG form of Eq.(5.1) corresponding to $n = 5$ and $\rho_{e-m}(T, H = 0)$ given by Eq.(5.2).*

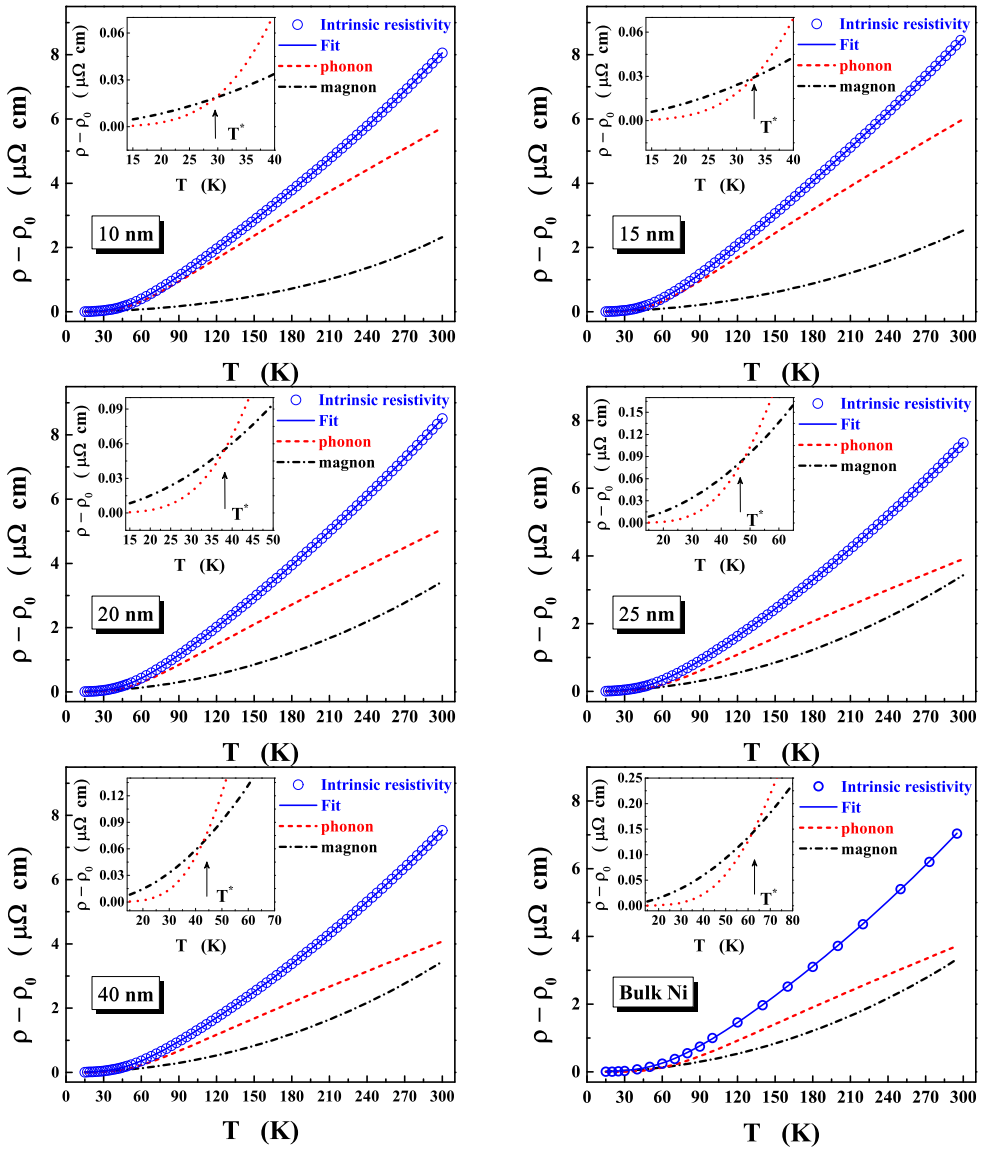

Figure 5.13: *The intrinsic resistivity, $\rho_{int}(T) \equiv \rho(T) - \rho_0$, (open circles) in the temperature range 15 K $\leq T \leq$ 300 K, along with the theoretical fits (continuous curves), based on Eq.(5.8) with $\rho_{e-p}(T)$ given by the BG ($n = 5$) version of Eq.(5.1) and $\rho_{e-m}(T)$ by Eqs.(5.2) - (5.4), for the nanocrystalline Ni samples with $d = 10$ nm to 40 nm and for bulk Ni [42]. The temperature variations of the individual contributions to $\rho_{int}(T)$ arising from the $e-p$ scattering, ρ_{e-p} (BG form), and from the $e-m$ scattering, ρ_{e-m} ($\propto [T/D(T)]^2$), obtained from the above-mentioned theoretical fits, are denoted by the dashed and dash-dot curves. Insets of all the panels serve to highlight the crossover, occuring at $T = T^\star$, between the phonon (short-dash curves) and magnon (dash-dot curves) contributions at low temperatures.*

($s-d$ electron-magnon) scattering contributions to the intrinsic resistivity are concomitantly present and both have sizable magnitudes.

• The insets of Fig. 5.13 clearly bear out that the phonon contribution dominates over that due to magnons at $T > T^{\star}$ whereas the reverse is true at temperatures 15 K $\leq T < T^{\star}$.

• $T^{\star}$, the temperature at which the electron-magnon and electron-phonon scattering contributions become equal, increases from $\sim$ 30 K for $d = 10$ nm to $\sim$ 65 K for bulk Ni.

• At any temperature above $T^{\star}$, electron-phonon contribution to resistivity, ρ_{e-p}, drops rapidly while electron-magnon contribution to resistivity, ρ_{e-m}, increases relatively slowly with the result that the difference in the magnitudes of the $e-p$ and $e-m$ scattering contributions reduces progressively as the average cystallite size increases. In view of the relation $\rho_{e-p} \sim \Theta_D^{-5}\ \rho_{\Theta}$ (Cf. Eq.(5.1) with $n = 5$), a large drop in ρ_{e-p} with the increase in average crystallite size (d) is more due to a slight increase in Debye temperature, Θ_D than the reduction in the prefactor ρ_{Θ} of Debye integral for Bloch-Grüneisen form (Fig. 5.12).

5.3.5 Magnetoresistance

To facilitate a direct comparison of the variation of magnetoresistance (MR) with temperature at a fixed magnetic field, H, or with H at a given temperature, yielded by the theory [25], with the experimentally measured $(\Delta\rho/\rho)_H(T)$ or $(\Delta\rho/\rho)_T(H)$, we proceed as follows. Eq.(5.8) is modified to give the temperature- and field-dependent

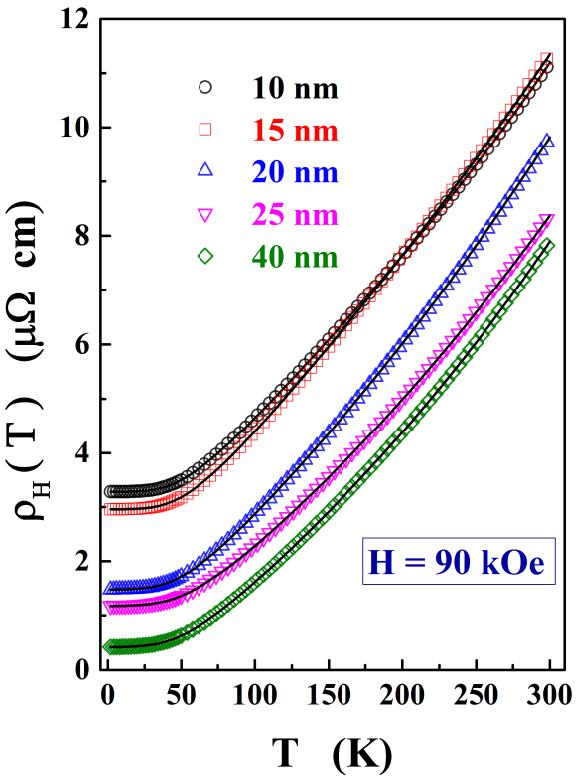

Figure 5.14: *The theoritical fits (continuous curves) to the $\rho(T, H = 90\ kOe)$ data (symbols), based on Eq.(5.10), for the present nc-Ni samples.*

electrical resistivity, $\rho(T, H)$, as

$$\rho(T, H) = \rho_0 + \rho_{e-p}(T, H = 0) + \rho_{e-m}(T, H) \tag{5.10}$$

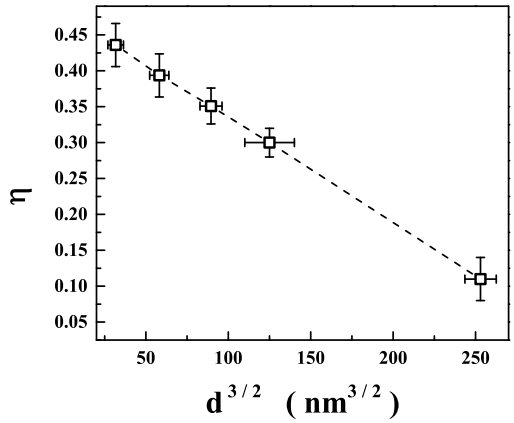

Figure 5.15: *$d^{3/2}$ variation of the parameter η (see text for details).*

The residual resistivity, ρ_0, and the electron-phonon contribution, $\rho_{e-p}(T,H)$, do not depend on H and hence retain their $H = 0$ values i.e., $\rho_{e-p}(T,H) = \rho_{e-p}(T,H=0)$. By contrast, $\rho_{e-m}(T,H)$, in Eq.(5.10), is given by Eq.(5.7) in conjunction with Eq.(5.6). In an attempt to theoretically fit the observed $\rho_H(T)$, we use the previously determined 'zero-field' values of ρ_0, $\rho_{e-p}(T,H=0)$ and $\rho_{e-m}(T,H=0)$, replace the fixed prefactor 0.304 in Eq.(5.6) by the parameter η, and allow it to vary from sample to sample so as to arrive at the most optimum fit. While attempting the single parameter (η) fit, it turns out that the first (leading) term in Eq.(5.6), i.e., $h\ lnh$, alone is needed to closely reproduce $\rho_H(T)$, or even $\rho_T(H)$, and, for a given nanocrystalline Ni sample, the parameter η depends only on the average nanocrystallite size, d, but not on temperature or field, as expected. The theoretical fits at H = 90 kOe for different samples, shown in figure (5.14), serves to illustrate this fitting procedure. Figure (5.15) highlights the $d^{3/2}$ variation of η. Having determined $\rho(T,H)$ this way and $\rho(T,H=0)$ previously, we use the standard definition for magnetoresistance, MR, i.e.,

$$\left(\frac{\triangle\rho}{\rho}\right) = \frac{\rho(T,H)}{\rho(T,H=0)} - 1 \tag{5.11}$$

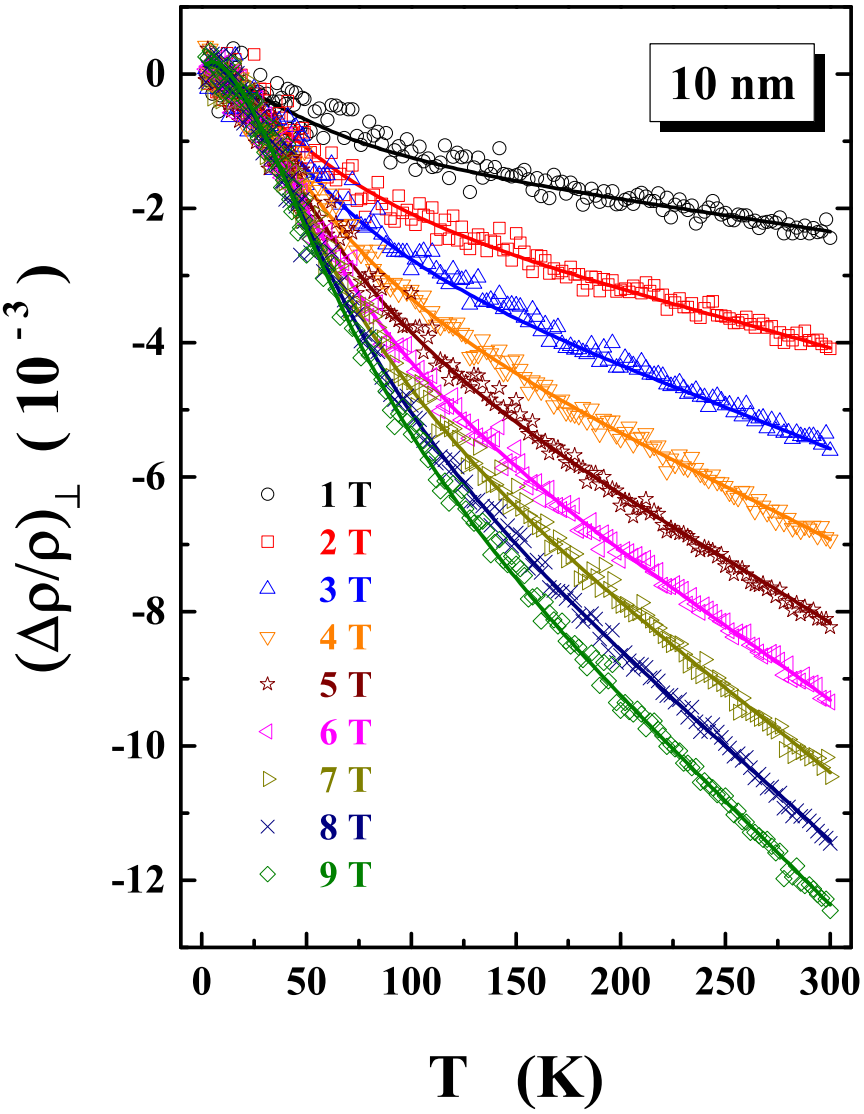

Figure 5.16: *Transverse magnetoresistance (symbols) as a function of temperature in the range 1.8 K $\leq T \leq$ 300 K, at fixed magnetic fields, H, up to 90 kOe, for the nc-Ni sample with d = 10 nm. The continuous curves denote the optimum theoretical fits to the magnetoresistance data (symbols) based on Eq.(5.11) combined with Eqs.(5.1)-(5.4), (5.6) - (5.8) and (5.10), of the text.*

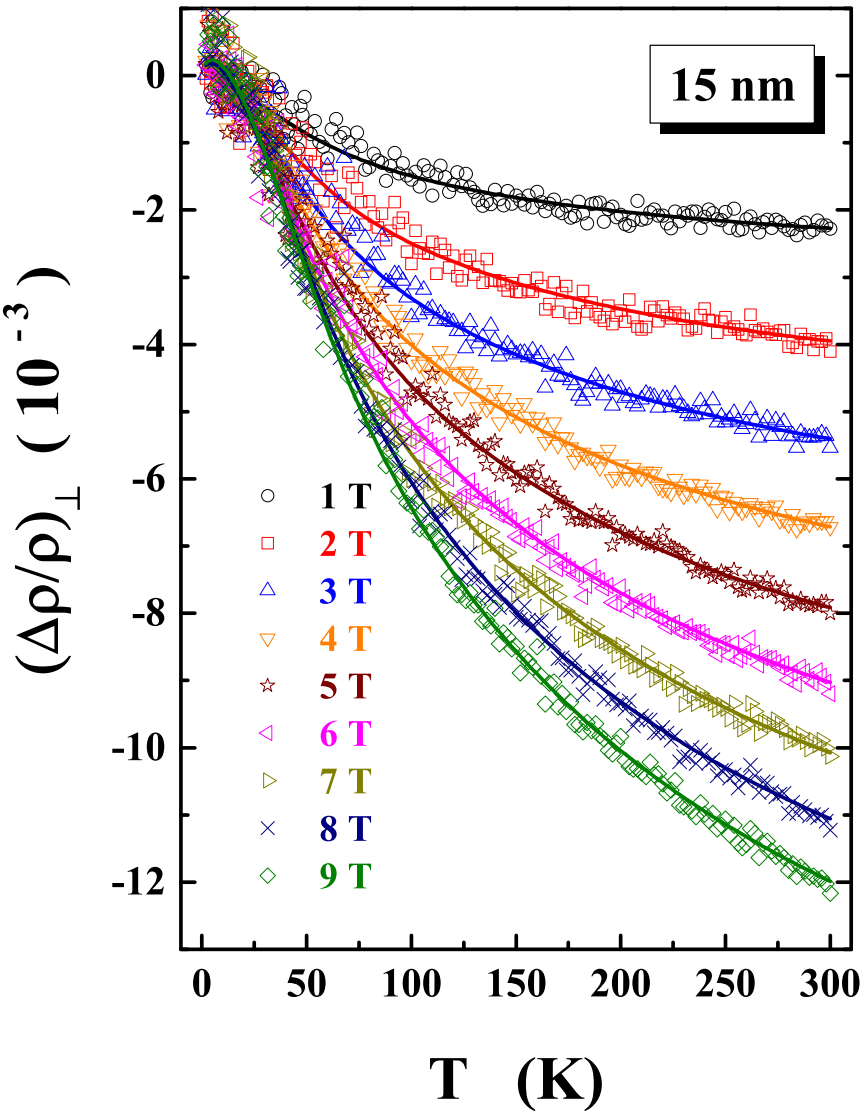

Figure 5.16 (Continued): *Transverse magnetoresistance (symbols) as a function of temperature in the range 1.8 K $\leq T \leq$ 300 K, at fixed magnetic fields, H, up to 90 kOe, for the nc-Ni sample with d = 15 nm. The continuous curves denote the optimum theoretical fits to the magnetoresistance data (symbols) based on Eq.(5.11) combined with Eqs.(5.1)-(5.4), (5.6) - (5.8) and (5.10), of the text.*

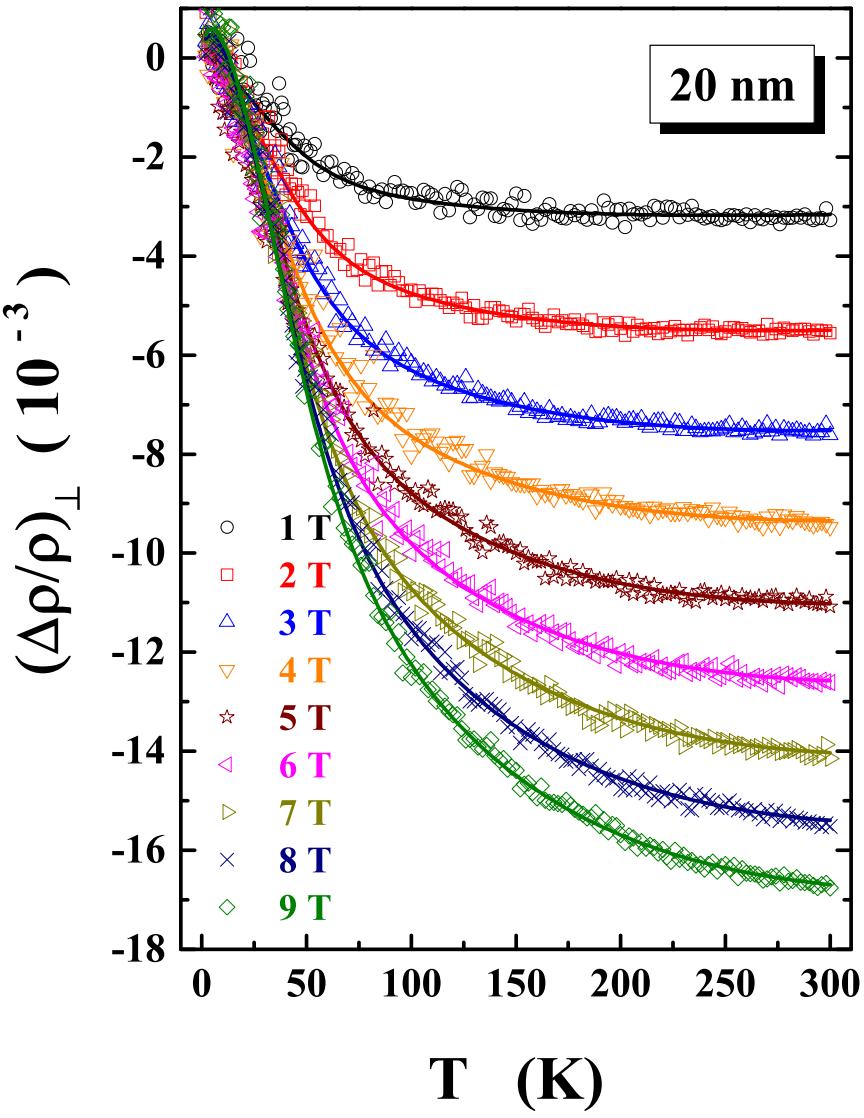

Figure 5.16 (Continued): *Transverse magnetoresistance (symbols) as a function of temperature in the range 1.8 K $\leq T \leq$ 300 K, at fixed magnetic fields, H, up to 90 kOe, for the nc-Ni sample with d = 20 nm. The continuous curves denote the optimum theoretical fits to the magnetoresistance data (symbols) based on Eq.(5.11) combined with Eqs.(5.1)-(5.4), (5.6) - (5.8) and (5.10), of the text.*

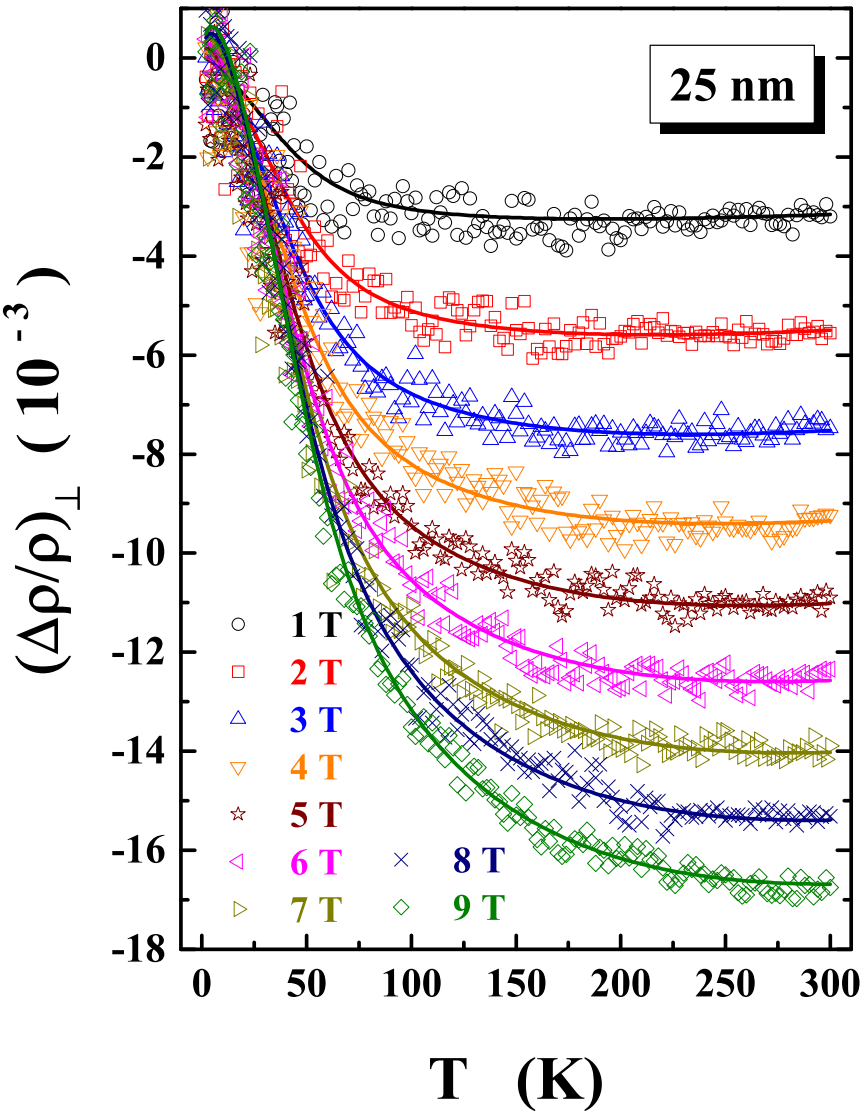

Figure 5.16 (Continued): *Transverse magnetoresistance (symbols) as a function of temperature in the range 1.8 K $\leq T \leq$ 300 K, at fixed magnetic fields, H, up to 90 kOe, for the nc-Ni sample with d = 25 nm. The continuous curves denote the optimum theoretical fits to the magnetoresistance data (symbols) based on Eq.(5.11) combined with Eqs.(5.1)-(5.4), (5.6) - (5.8) and (5.10), of the text.*

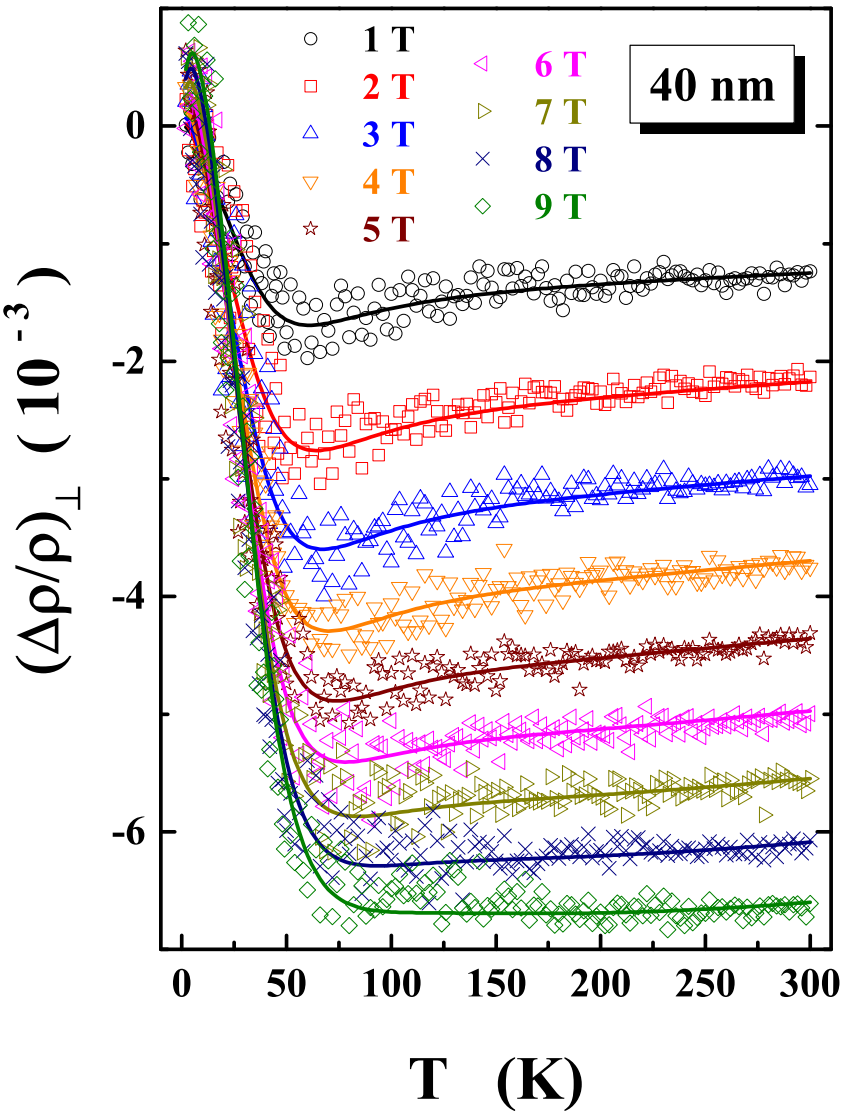

Figure 5.16 (Continued): *Transverse magnetoresistance (symbols) as a function of temperature in the range 1.8 K $\leq T \leq$ 300 K, at fixed magnetic fields, H, up to 90 kOe, for the nc-Ni sample with d = 40 nm. The continuous curves denote the optimum theoretical fits to the magnetoresistance data (symbols) based on Eq.(5.11) combined with Eqs.(5.1)-(5.4), (5.6) - (5.8) and (5.10), of the text.*

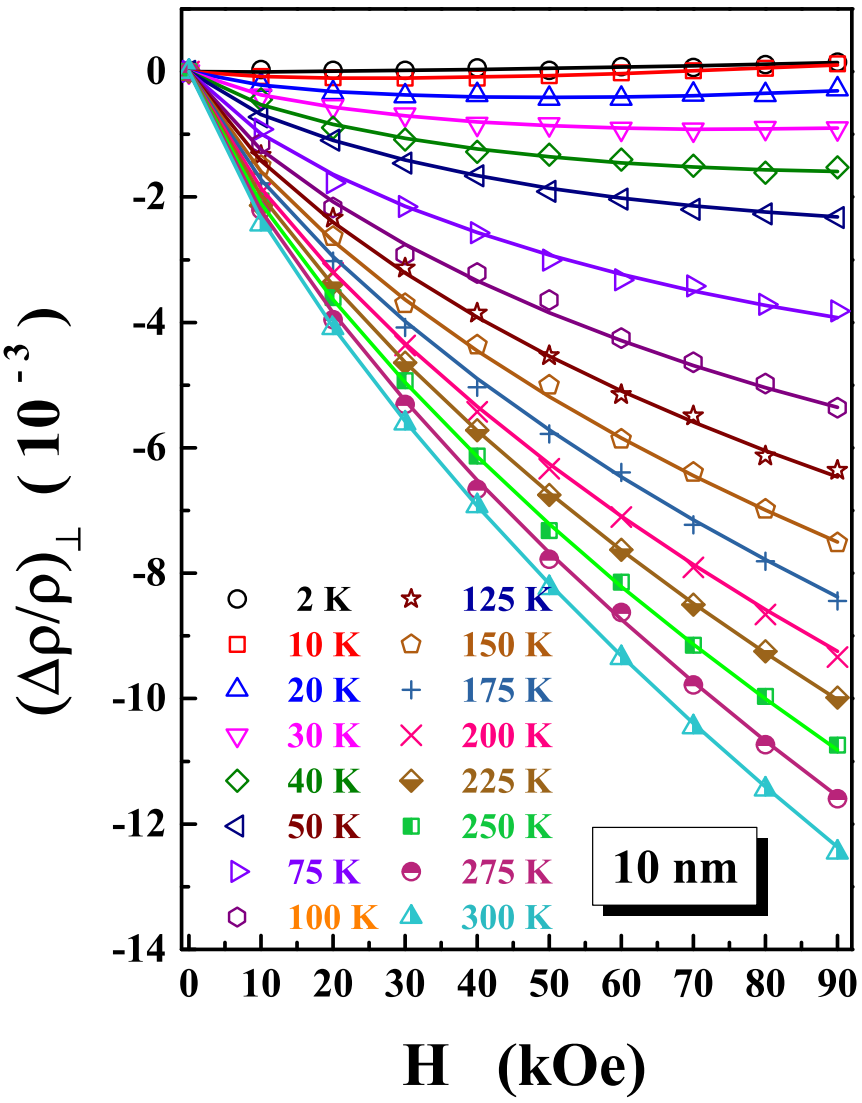

Figure 5.17: *Measured transverse magnetoresistance (symbols) versus magnetic field isotherms at temperatures ranging from 2K to 300K for the nc-Ni sample with d = 10 nm. The continuous curves denote the optimum theoretical fits to the magnetoresistance data (symbols) based on Eq.(5.11) combined with Eqs.(5.1)-(5.4), (5.6) - (5.8) and (5.10), of the text.*

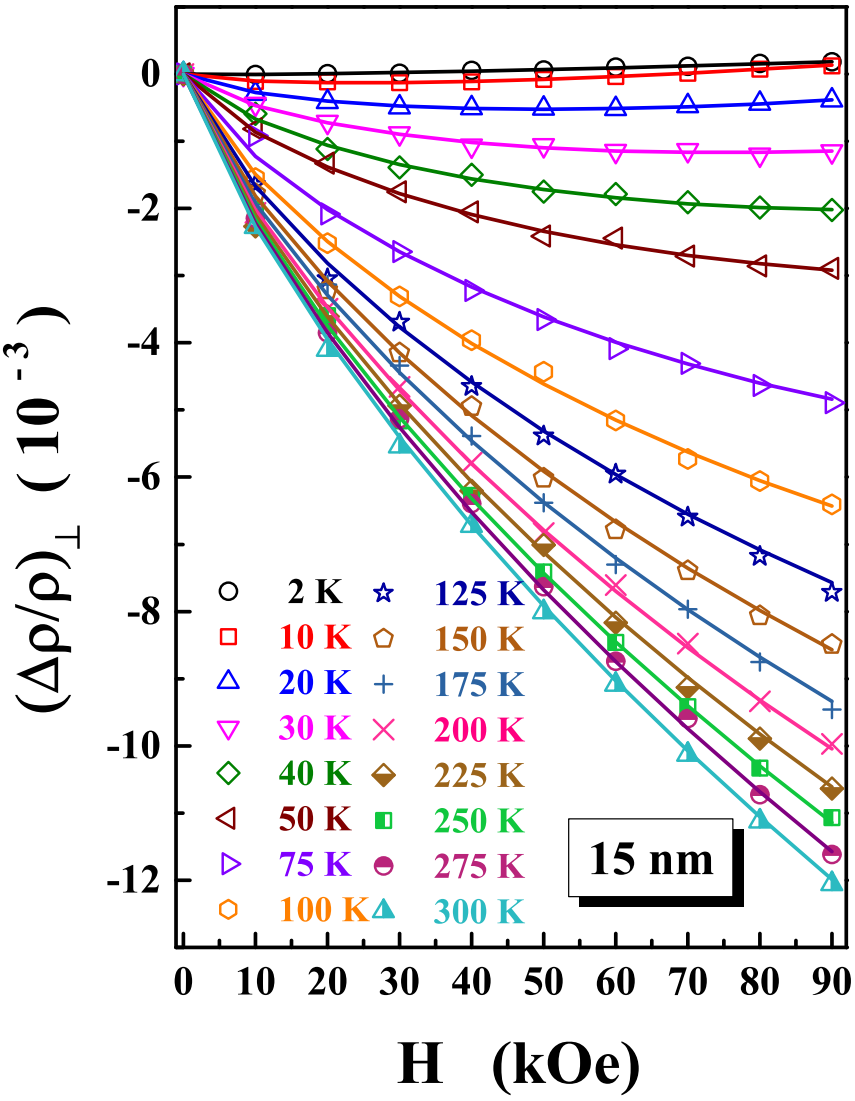

Figure 5.17 (Continued): *Measured transverse magnetoresistance (symbols) versus magnetic field isotherms at temperatures ranging from 2K to 300K for the nc-Ni sample with d = 15 nm. The continuous curves denote the optimum theoretical fits to the magnetoresistance data (symbols) based on Eq.(5.11) combined with Eqs.(5.1)-(5.4), (5.6) - (5.8) and (5.10), of the text.*

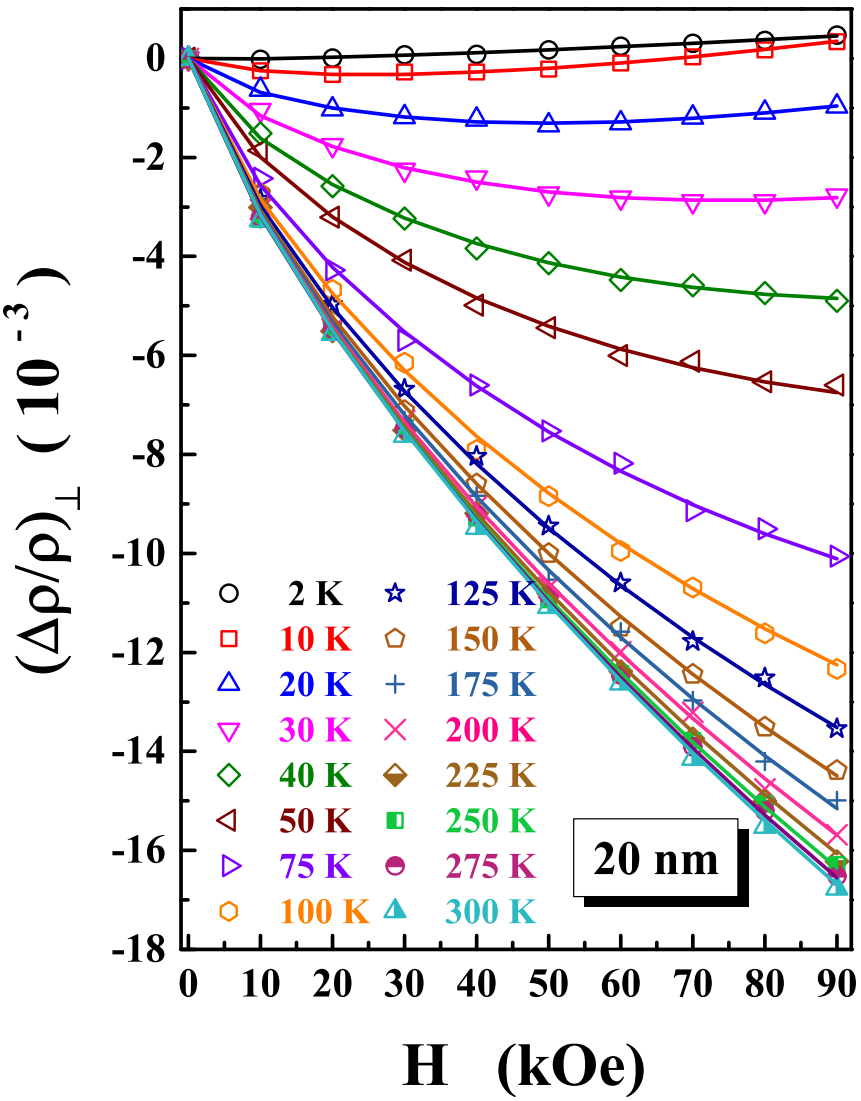

Figure 5.17 (Continued): *Measured transverse magnetoresistance (symbols) versus magnetic field isotherms at temperatures ranging from 2K to 300K for the nc-Ni sample with d = 20 nm. The continuous curves denote the optimum theoretical fits to the magnetoresistance data (symbols) based on Eq.(5.11) combined with Eqs.(5.1)-(5.4), (5.6) - (5.8) and (5.10), of the text.*

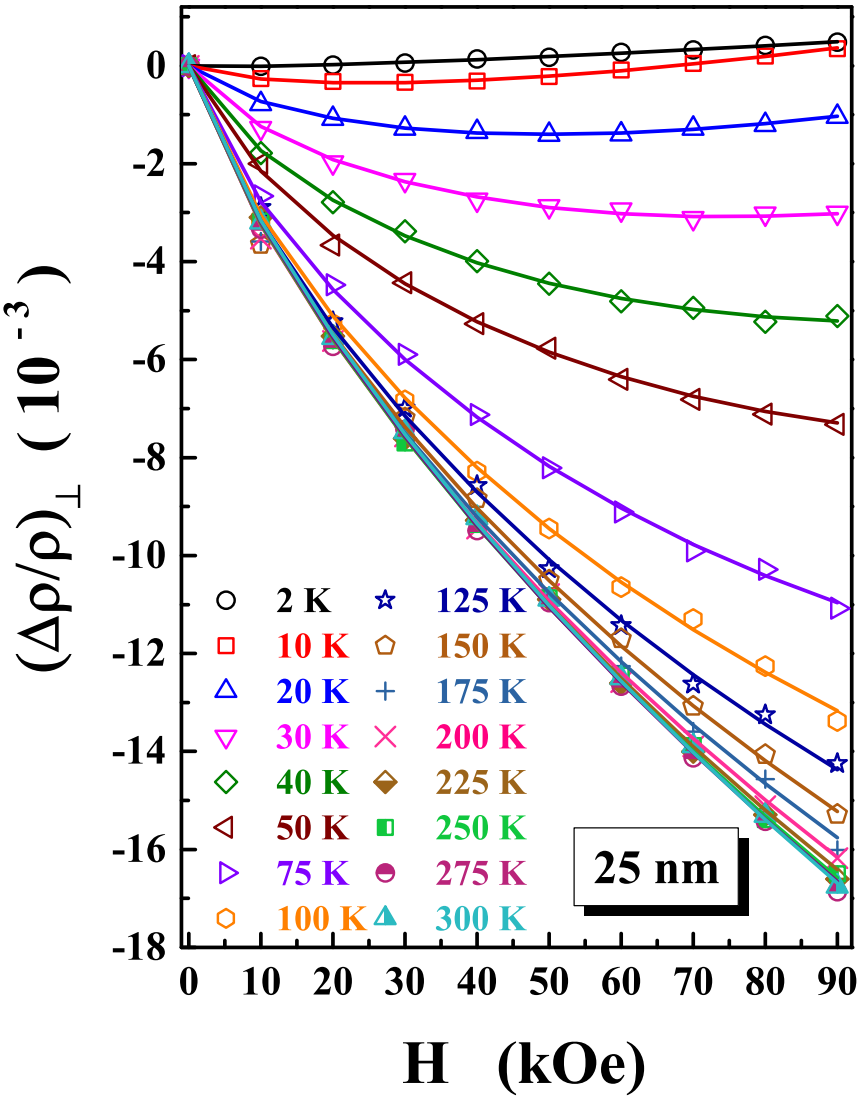

Figure 5.17 (Continued): *Measured transverse magnetoresistance (symbols) versus magnetic field isotherms at temperatures ranging from 2K to 300K for the nc-Ni sample with d = 25 nm. The continuous curves denote the optimum theoretical fits to the magnetoresistance data (symbols) based on Eq.(5.11) combined with Eqs.(5.1)-(5.4), (5.6) - (5.8) and (5.10), of the text.*

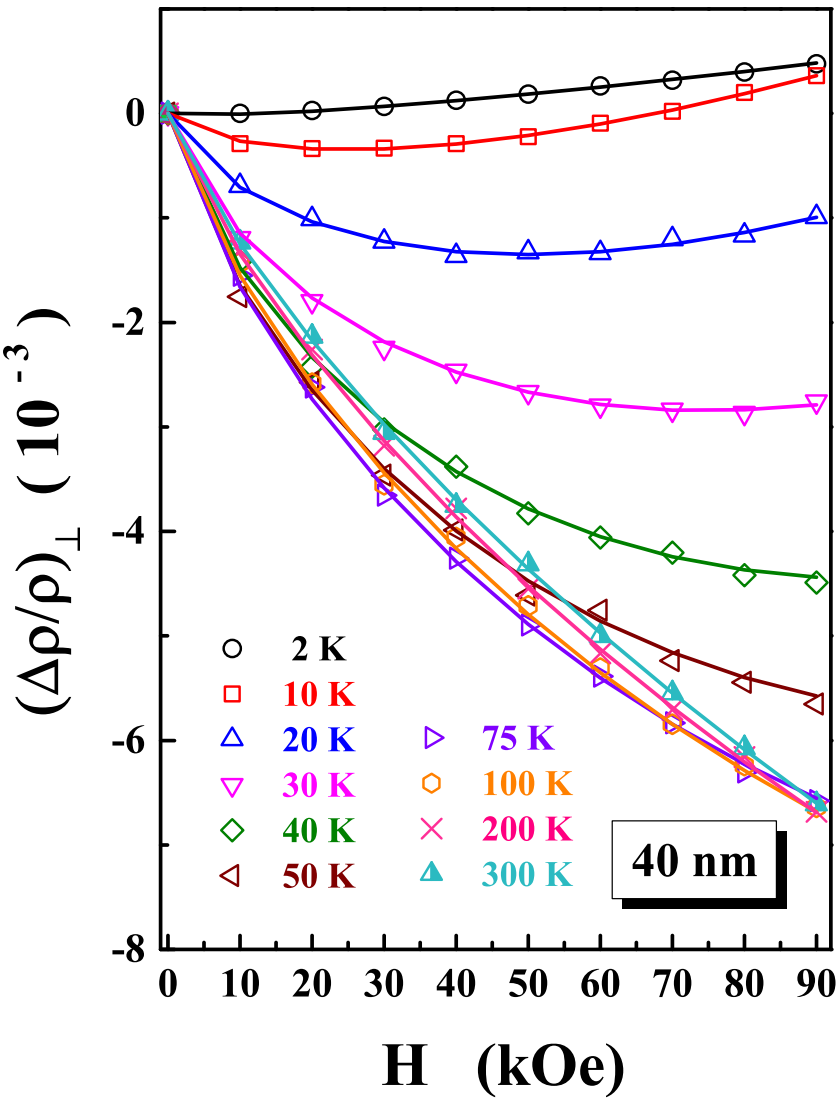

Figure 5.17 (Continued): *Measured transverse magnetoresistance (symbols) versus magnetic field isotherms at temperatures ranging from 2K to 300K for the nc-Ni sample with d = 40 nm. The continuous curves denote the optimum theoretical fits to the magnetoresistance data (symbols) based on Eq.(5.11) combined with Eqs.(5.1)-(5.4), (5.6) - (5.8) and (5.10), of the text.*

to compute MR. Making use of the expressions for $\rho(T, H = 0)$ (Eq.(5.8)) and $\rho(T, H)$ (Eq.(5.10)) and the above considerations, Eq.((5.11)) can be written in its explicit form as

$$\left(\frac{\triangle\rho}{\rho}\right) = \frac{\eta\ (h\ lnh)\ \rho_{e-m}(T, H = 0)}{\rho_0 + \rho_{e-p}(T, H = 0) + \rho_{e-m}(T, H = 0)} \tag{5.12}$$

A direct comparison between theoretically predicted and experimentally observed variations of magnetoresistance (MR) with temperature at fixed fields (10 kOe $\leq H \leq$ 90 kOe) is made for nanocrystalline Ni with different average crystallite sizes (10 nm $\leq d \leq$ 40 nm) is shown in figure 5.16. Similar comparison for magnetoresistance as a function of applied field at various but fixed temperatures (2 K $\leq T \leq$ 300 K) is made and shown in figure 5.17. Note that $(\Delta\rho/\rho)(T)$ at constant H is determined by the temperature variations of both $\rho_{e-m}(T, H = 0)$ in Eq.(5.7) and the leading term $h\ lnh$ in Eq.(5.6) whereas $(\Delta\rho/\rho)(H)$ at constant temperature (T) is governed by the term $h\ lnh$ alone. According to Eq.(5.12), η is a direct measure of MR at a given H and/or T. Thus, with decreasing d, the $d^{3/2}$ power law growth of η (Fig. 5.15) implies an increased suppression of the electron-magnon scattering at a given temperature by a magnetic field of given strength. More the number of thermally-excited spin waves at a certain temperature, more the suppression by externally applied magnetic field (H). Considering that the surface/interface and core magnetic anisotropies have opposite signs [47] in the nanocrystalline Ni samples in question, the effective magnetic anisotropy energy (which is the sum of surface/interface and core magnetic anisotropy energies) diminishes as the surface/interface magnetic anisotropy energy grows in magnitude with shrinking average crystallite size. Thus, the energy gap in the spin-wave spectrum, introduced by the effective magnetic anisotropy, decreases as crystallite size (d) reduces. Consequently, larger number of thermally-excited magnons are available at a fixed temperature in the samples with smaller crystallite size, d. It immediately follows that the magnitude of (negative) magnetorresistance increases with decreasing crystallite size (d).

5.4 Summary and Conclusion

'Zero-field' electrical resistivity, $\rho(T)$, and transverse magnetoresistance, $[\Delta\rho_{\perp}/\rho](T)$, (in magnetic fields up to 90 kOe) of pulse electrodeposited nanocrystalline Ni sheets (of thickness 300 μm) with average crystallite size, d, varying between 10 nm and 40 nm, have been measured over the temperature range 1.8 K to 300 K. A quantitative comparison of the observed $\rho(T)$ and $[\Delta\rho_{\perp}/\rho](T)$ with the predictions of the self-consistent calculations, based on the two-band (s and d bands) spin fluctuation model, permits an unambiguous identification of the scattering mechanisms responsible for $\rho(T)$ and $[\Delta\rho_{\perp}/\rho](T)$ in different temperature ranges as well as a first accurate determination of their relative magnitudes. The following conclusions can be drawn from such a comparison between experiment and theory.

(i) The T^2 variation of ρ, observed at low temperatures ($T \lesssim 15$ K), originates from the electron-electron (Baber) scattering but not from the electron-magnon scattering, as is believed to be the case in $3d$ crystalline ferromagnets [42] Fe, Co, Ni and in Ni nanowires [35].

(ii) In the temperature range 15 K $\leq T \leq$ 300 K, non-spin-flip intraband (i.e., $s^{\uparrow\downarrow} - s^{\uparrow\downarrow}$, $d^{\uparrow\downarrow} - d^{\uparrow\downarrow}$) electron-phonon ($e-p$) scattering, $\rho_{e-p}(T, H = 0)$, and spin-flip interband (i.e., $s^{\uparrow\downarrow}$ - $d^{\downarrow\uparrow}$) electron-magnon ($e-m$) scattering, $\rho_{e-m}(T, H = 0)$, contributions completely account for the intrinsic resistivity. The former contribution dominates over the latter at $T > T^{\star}$ whereas the reverse is true at temperatures 15 K $\leq T < T^{\star}$. $T^{\star}$, the temperature at which the $e-m$ and $e-p$ scattering contributions become equal, increases from $\sim$ 30 K for $d = 10$ nm to $\sim$ 65 K for bulk Ni. At $T > T^{\star}$, $\rho_{e-m}(T, H = 0)$ becomes comparable in magnitude to $\rho_{e-p}(T, H = 0)$ for $d \geq 25$ nm.

(iii) By contrast, the magnetoresistance in nanocrystalline Ni is entirely due to the spin-flip interband $s^{\uparrow\downarrow}$ - $d^{\downarrow\uparrow}$ electron-magnon scattering.

(iv) Irrespective of the average crystallite size (including the bulk, $d = \infty$), thermal renormalization of the spin-wave stiffness, caused mainly by the magnon-magnon interactions, is significant over the temperature range 15 K $\leq T \leq$ 300 K.

(v) Regardless of the value of d (including $d = \infty$), the *phonon-induced* non-spin-flip intraband $s^{\uparrow\downarrow} - s^{\uparrow\downarrow}$, $d^{\uparrow\downarrow} - d^{\uparrow\downarrow}$ transitions are more frequent than the $e - p$ interband $s^{\uparrow\downarrow} - d^{\uparrow\downarrow}$ transitions over the entire temperature range 1.8 K $\leq T \leq$ 300 K.

(vi) Increase in atomic disorder at the surfaces/interfaces and grain boundaries as the surface area increases due to the reduction in the average crystallite size, resulting in changes in the density of states at the Fermi level, explains the observed enhancement (reduction) in the electron-phonon (electron-magnon) scattering contribution to $\rho(T, H = 0)$.

(vii) The power law variations with d of saturation magnetization at 0 K, $M_s(0)$, in Fig. 5.5(a), spin wave stiffness at 0 K, D_0, in Fig. 5.5(b), Debye temperature, Θ_D, in Fig. 5.9(a) and the parameters ρ_Θ ($\rho^\star$) in Fig. 5.9(b) (Fig. 5.9(c)) and η in Fig. 5.12, measuring respectively the strength of $e - p$ ($e - m$) coupling and the degree of suppression of $e - m$ scattering by external magnetic field, assert that the average crystallite size is the dominant length scale so far as the magnetism, electrical- and magneto-transport in nanocrystalline Ni are concerned.

References

1. T. Kasuya, *Prog. Theor. Phys.* **16**, 58 (1956).
2. P. G. de Gennes and J. Friedel, *J. Phys. Chem. Solids* **4**, 71 (1958).
3. T. Kasuya, *Prog. Theor. Phys.* **22**, 227 (1959).
4. I. Mannari, *Prog. Theor. Phys.* **22**, 335 (1959).
5. F. C. Schwerer and L. J. Cuddy, *Phys. Rev.* B **2**, 1575 (1970).
6. S. N. Kaul, *Solid State Commun.* **15**, 1179 (1974).
7. N. F. Mott, *Proc. Roy. Soc.* A **153**, 699 (1936).
8. N. F. Mott, *Proc. Roy. Soc.* A **156**, 368 (1936).
9. A. H. Wilson, *Proc. Roy. Soc.* A **167**, 580 (1938).
10. D. A. Goodings, *Phys. Rev.* **132**, 542 (1963).
11. N. F. Mott, *Adv. Phys.* **13**, 325 (1964).
12. I. A. Campbell, A. Fert and A. R. Pomeroy, *Phil. Mag.* **15**, 977 (1967).
13. T. Farrel and D. Greig, *J. Phys. C: Solid State Phys.* **1**, 1359 (1968).
14. I. A. Campbell, *Phys. Rev. Lett.* **24**, 269 (1970).
15. F. C. Schwerer and J. W. Conroy, *J. Phys. F: Metal Phys.* **1**, 877 (1971).
16. D. C. Price and G. Williams, *J. Phys. F: Metal Phys.* **3**, 810 (1973).
17. T. R. McGuire and R. I. Potter, *IEEE Trans. Magn.* **11**, 1018 (1975) and the references cited therein.

18. A. Fert and I. A. Campbell, *J. Phys. F: Metal Phys.* **6**, 849 (1976).

19. S. N. Kaul, *J. Phys. F: Metal Phys.* **7**, 2091 (1977).

20. O. Jaoul, I. A. Campbell and A. Fert, *J. Magn. Magn. Mater.* **5**, 23 (1977).

21. I. A. Campbell and A. Fert, *Ferromagnetic Materials* Vol.**3** Edited by E. P. Wohlfarth (North-Holland, Amsterdam, 1982) p. 747, and the references cited therein.

22. S. N. Kaul and M. Rosenberg, *Phys. Rev.* B **27**, 5698 (1983).

23. S. N. Kaul, *Phys. Stat. Sol.* (b) **116**, K99 (1983).

24. B. Raquet, M. Viret, E. Sondergard, O. Cespedes and R. Mamy, *Phys. Rev.* B **66**, 024433 (2002).

25. S. N. Kaul, *J. Phys.: Condens. Matter* **17**, 5595 (2005).

26. S. N. Kaul, *J. Phys.: Condens. Matter* **11**, 7597 (1999).

27. A. Semwal and S. N. Kaul, *Phys. Rev.* B **60**, 12799 (1999).

28. S. N. Kaul and A. Semwal, *Phys. Lett.* A **254**, 101 (1999).

29. A. Semwal and S. N. Kaul, *J. Phys.: Condens. Matter* **16**, 8675 (2004).

30. S. N. Kaul and A. Semwal, *J. Phys.: Condens. Matter* **16**, 8695 (2004).

31. S. N. Kaul, A. Semwal and H. -E. Schaefer, *Phys. Rev.* B **62**, 13892 (2000).

32. A. C. Abhyankar, A. Semwal and S. N. Kaul, *J. Phys.: Condens. Matter* **20**, 445228 (2008).

33. A. C. Abhyankar and S. N. Kaul, *J. Phys.: Condens. Matter* **20**, 445227 (2008).

34. M. N. Ou, S. R. Harutyunyan, S. J. Lai, C. D. Chen, T. J. Yang and Y. Y. Chen, *Phys. Stat. Sol.* (b) **244**, 4512 (2007).

35. M. Venkata Kamalakar and A. K. Raychaudhuri, *Phys. Rev.* B **79**, 205417 (2009).

36. I. Bakonyi, E. Toth-Kadar, J. Toth, A. Cziraki and B. Fogarassy, *Nanophase Materials* NATO ASI Series E, Vol. 260, p.423 (1994, Kluwer Academic, Netherlands), Edited by G. C. Hadjipanayis and R. W. Siegel.

37. M. J. Aus, B. Szpunar, U. Erb, A. M. El-Sherik, G. Palumbo and K. T. Aust, *J. Appl. Phys.* **75**, 3632 (1994).

38. S. Wang, I. Brooks, J. McCrea, G. Palumbo, G. Cingara and U. Erb, *Adv. Mater. Res.* **409**, 561 (2012).

39. J. E. Darnbrough, B. Roebuck and P. E. J. Flewitt, *J. Appl. Phys.* **118**, 184302 (2015).

40. S. N. Kaul, W. Kettler and M. Rosenberg, *Phys. Rev.* B **33**, 4987 (1986).

41. S. N. Kaul, W. Kettler and M. Rosenberg, *Phys. Rev.* B **35**, 7153 (1987).

42. G. K. White and S. B. Woods, *Phil. Trans. Roy. Soc.* A **251**, 273 (1959).

43. D. Greig and J. P. Harrison, *Phil. Mag.* **12**, 71 (1965).

44. F. C. Schwerer and J. Silcox, *Phys. Rev. Lett.* **20**, 101 (1968).

45. S. N. Kaul, *Solid State Commun.* **15**, 1821 (1974).

46. P. V. Prakash Madduri and S. N. Kaul, *Physica* B **448**, 147 (2014).

47. P. V. Prakash Madduri and S. N. Kaul, *J. Alloy. Comp.* **689**, 533 (2016).

48. W. G. Baber, *Proc. Roy. Soc.* A **158**, 383 (1937).

49. J. M. Ziman, *Electrons and Phonons* (Oxford University Press, New York, 1960), p. 364.

50. J. Weissmüller, A. Michels, J. G. Barker, A. Wiedenmann, U. Erb and R. D. Shull, *Phys. Rev.* B **63**, 214414 (2001).

51. R. G. Calderón, L. Fernandéz Barquín, S. N. Kaul, J. C. Goméz Sal, P. Gorria and J. S. Pedersen, *Phys. Rev.* B **71**, 134413 (2005).

52. S. N. Kaul, *Phys. Rev.* B **27**, 5761 (1983).

53. S. N. Kaul, *Phys. Rev.* B **27**, 6923 (1983).

54. S. N. Kaul, *J. Phys.: Condens. Matter* **3**, 4027 (1991).

55. S. N. Kaul and P. D. Babu, *Phys. Rev.* B **50**, 9308 (1994).

56. S. N. Kaul and P. D. Babu, *J. Phys.: Condens. Matter* **10**, 1563 (1998).

57. P. V. Prakash Madduri and S. N. Kaul, *J. Magn. Magn. Mater.* **418**, 143 (2016).

58. A. T. Aldred, *Phys. Rev.* B **11**, 2597 (1975).

59. J. Callaway and C. S. Wang, *Physica* B **91**, 337 (1977).

Chapter 6

Ferromagnetic resonance (FMR)

This chapter presents the results of the lineshape analysis of the ferromagnetic resonance (FMR) spectra taken on pulse electrodeposited nanocrystalline Ni sheets with the average crystallite size, d, varying from 10 nm to 40 nm, at temperatures ranging from 113 K to 325 K. An elaborate lineshape analysis yielded accurate values for saturation magnetization, $M_s(T)$, Landé splitting factor, g, anisotropy field, $H_K(T)$, and FMR linewidth, $\Delta H_{pp}(T)$. Thermally-excited spin waves completely account for $M_s(T)$ and the spin-wave description of saturation magnetization gives the values for the saturation magnetization and spin-wave stiffness at absolute zero of temperature, i.e., $M_s(0)$ and D_0, for nanocrystalline Ni samples of different average crystallite size, d, that are in excellent agreement with the corresponding values deduced previously from a thorough spin wave analysis of the bulk magnetization data (Chapter 4). While $M_s(0)$ varies with d as $M_s(0) \sim d^{-3/2}$, D_0 follows the power law $D_0 \sim d^{4/3}$. In the 'in-plane' as well as 'out-of-plane' sample configurations (i.e., when the static magnetic field lies within or normal to the sample plane), the main contribution to $H_K(T)$ comes from the cubic magnetocrystalline anisotropy and 'in-plane' uniaxial anisotropy. The exchange-conductivity mechanism describes the observed thermal de-

A manuscript is under preparation based on the results presented in this chapter.

cline of ΔH_{pp} reasonably well but fails to explain the very large magnitude of ΔH_{pp} at any given temperature. By comparison, the Landau-Lifshitz-Gilbert (LLG) damping gives a much greater contribution to ΔH_{pp} but the LLG contribution is relatively insensitive to temperature.

6.1 Introduction

Ferromagnetic resonance (FMR) is an extremely sensitive experimental tool to study magnetization dynamics, magnetic excitations and relaxation phenomena. This technique has the added advantage of enabling an unambiguous distinction between different types of magnetic anisotropies (e.g., shape, magnetocrystalline, magnetoelastic and surface anisotropies) through their characteristic angular variations of the resonance field. Thus, FMR technique has been extensively used to extract information about any of these physical phenomena in thin films, ultrathin films, multilayers, superlattices [1–5], superparamagnetic nanoclusters/nanoparticles [4–7], nanowire arrays [8], circular dot arrays [9] and ferromagnetic (FM) nanoparticles embedded in an amorphous FM matrix [10, 11]. Continued interest in studying magnetic nanomaterials stems from the complex physical phenomena that come into play when the particle size (a few nanometers) becomes comparable to the characteristic magnetic lengths such as the critical single-domain size (D_{cr}), domain wall width (δ_0) and exchange correlation length (L_{ex}). A complete knowledge of how the different types of magnetic anisotropies compete to produce the resultant anisotropy is of paramount interest both from the basic and technological points of view. In the latter case, particularly in applications such as magnetic data storage devices, magnetic logic devices, spintronic devices and magnetic field sensors.

So far as nanocrystalline (nc-) 3d transition metal ferromagnets Fe, Co, Ni and their alloys are concerned, FMR technique has hitherto been used to study the su-

perparamagnetic behavior [4–7] in an assembly of 'non-interacting' nanoparticles. In this work, we have undertaken an exhaustive study of low-lying magnetic excitations, magnetic anisotropy and FMR relaxation mechanisms in pulse electrodeposited Ni sheets [12], in which nanocrystalline particles of nearly single-domain size strongly interact with one another via direct short-range exchange (across grain boundaries) and indirect long-range dipole-dipole interactions.

6.2 Theoretical Considerations

The resonant absorption of (external) microwave radiation in ferromagnetic materials constitutes the ferromagnetic resonance phenomenon. When a magnetic dipole, associated with the spin angular momentum of an electron, is placed in an external static magnetic field of uniform strength, H, it precesses around the direction of the magnetic field with the frequency (the Larmor precession frequency)

$$\omega_L = \gamma H \tag{6.1}$$

where $\gamma = g\mu_B/\hbar$ is the magneto-mechanical (gyromagnetic) ratio of the electron. As illustrated in Fig. 6.1, resonant absorption of energy can occur when the precessing magnetic dipole is exposed to an external electromagnetic microwave radiation of frequency $\omega = \omega_L$, applied in a plane perpendicular to the direction of H. The resonance condition ($\omega = \omega_L$) can be written in an alternative form as

$$\hbar\omega = g\mu_B H \tag{6.2}$$

This phenomenon is the well-known electron spin resonance (ESR) which occurs in substances with unpaired electron spins and in which the magnetic moments do not interact with one another. By contrast, in ferromagnetic substances, unpaired electron spins interact strongly with another through direct exchange or indirect

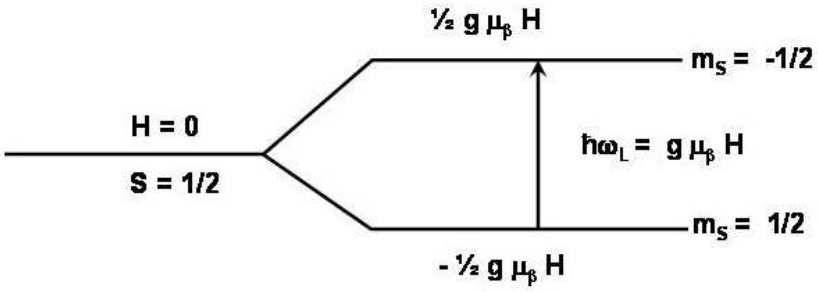

Figure 6.1: *Principle of the ESR experiment.*

interactions. The phenomenon of ferromagnetic resonance (FMR), first discovered by Griffiths [13], is the resonant microwave absorption in a system of strongly interacting spins. A strong short-range exchange interaction leads to a spontaneous parallel alignment of spins in the ground state. The parallel spin alignment, in turn, gives rise to a large spontaneous magnetization or a large internal exchange field. A given spin within a ferromagnetic material thus not only experiences the external magnetic field, H, but also the internal (exchange) field due to the remaining spins in the system. Consequently, the resonance condition, Eq.(6.2), needs to be modified in that the external field H has to be replaced by an effective field H_{eff}, which, besides H, takes into account the internal fields as well as the anisotropy fields present in ferromagnetic materials.

Landau and Lifshitz (LL) [14] proposed the first phenomenological equation of motion for magnetization in a ferromagnet in the presence of an external magnetic field H of the form,

$$\frac{d\vec{M}}{dt} = \gamma\left(\vec{M}\times\vec{H}_{eff}\right) - \frac{\lambda}{M_s^2}\left(\vec{M}\times\vec{M}\times\vec{H}_{eff}\right) \tag{6.3}$$

The first term on the right-hand-side represents the torque experienced by the magnetization vector, $\vec{M}$, in an effective magnetic field, $\vec{H}_{eff} = \vec{H}+\vec{h}(t)-\vec{H}_{dem}+\vec{H}_k+\vec{H}_{ex}$. Here $\vec{H}$ is the applied static magnetic field, $\vec{h}(t)$ is a weak microwave magnetic field, $\vec{H}_{dem}$ is the demagnetizing field and $\vec{H}_k$ is the magnetocrystalline anisotropy field,

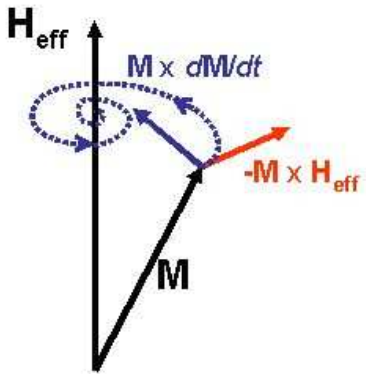

Figure 6.2: *Schematic representation of precession and damping of magnetization.*

$\vec{H}_{ex} = (2A/M_s^2)(\bigtriangledown^2\vec{M})$ is the exchange field, with 'A' as the exchange stiffness constant. $\gamma = ge/2mc$ is the magneto-mechanical ratio, g is the spectroscopic Landé splitting factor and M_s is the saturation magnetization. The second term in Eq.(6.3) is the LL damping torque which governs the relaxation towards equilibrium and the parameter 'λ' characterizes the relaxation rate. As this equation is not entirely correct at low frequencies, Gilbert (G) [15] suggested a modified equation of motion, i.e.,

$$\frac{d\vec{M}}{dt} = \gamma\left(\vec{M} \times \vec{H}_{eff}\right) - \frac{\lambda}{\gamma M_s^2}\left(\vec{M} \times \frac{d\vec{M}}{dt}\right) \tag{6.4}$$

In the small damping limit, the Landau-Lifshitz and Gilbert damping forms are equivalent and hence the equation of motion for magnetization, Eq.(6.4), is known as the LLG equation and λ as the LLG damping parameter.

Two approaches have been adopted to determine the resonance frequency or equivalently, resonance field, from Eq.(6.4). In the first approach, coupled differential equations for the time-dependent magnetization components are solved to yield the microwave power absorption in the ferromagnetic resonance process, FMR lineshape and resonance linewidth. The second approach neglects the dynamical aspects of FMR to arrive at the resonance frequency or field. Both the approaches have certain

advantages and limitations, as brought out clearly below by the model calculations based on them. The evaluation of magnetization under precession and damping are schematically represented in figure 6.2.

6.2.1 Lineshape calculations

Consider an ellipsoidal isotropic ferromagnetic sample which is subjected to a homogeneous external static magnetic field $\vec{H}$ directed along the z-axis and to a weak alternating magnetic field, $\vec{h}(t) = \vec{h}\ e^{i\omega t}$ ($|\vec{h}(t)| << |\vec{H}|$) acting in the xy plane. As a result of the combined action of these fields, the magnetization comprises a steady and an alternating component, i.e., $\vec{M} = \vec{M}_s + \vec{m}(t)$ with $\vec{m}(t) = \vec{m}\ e^{i\omega t}$ and $|\vec{m}(t)| << |\vec{M}_s|$. Assuming that the steady field is intense enough to saturate the ferromagnetic sample so that $\vec{M}_s$ and $\vec{H}$ point in the same direction, the Gilbert form of equation of motion for magnetization (hereafter referred to as the LLG equation) is given by Eq.(6.4) where $\vec{H}_{eff} = \vec{H} + \vec{h}(t) + \vec{H}_{dem} + \vec{H}_A$, $\vec{H}_{dem} = -D \cdot \vec{M}$ is the demagnetizing field, $\vec{H}_A$ is the magnetic anisotropy field arising from magnetocrystalline anisotropy, which for illustration prupose, is to be taken of uniaxial type; $\vec{H}_K = -\vec{D}_K \cdot \vec{M}$ is the uniaxial anisotropy field with easy axis along $\vec{H}$; $\vec{D}$ and $\vec{D}_k$ are diagonal tensors, $\gamma = ge/2mc$ is the gyromagnetic ratio, M is the saturation magnetization and λ is the Gilbert damping parameter. Since the exchange stifness (A) is of the order of 10^{-11} J/m, to simplify the calculations, A is set to 0. Substitution for $\vec{M}$ and $\vec{H}_{eff}$ in Eq.(6.4) yields [17, 49]

$$\begin{aligned}\frac{d\vec{m}(t)}{dt} =& \gamma\Bigg[\vec{M}_s \times \vec{h}(t) + \vec{m}(t) \times \vec{H} - \vec{M} \times (\vec{D} \cdot \vec{M}) - \vec{M} \times (\vec{D}_k \cdot \vec{M}) \\ & - \frac{\lambda}{\gamma M^2}\left([\vec{M}_s + \vec{m}(t)] \times \frac{d}{dt}[\vec{M}_s + \vec{m}(t)]\right)\Bigg] \end{aligned} \tag{6.5}$$

where use has been made of the relation $d\vec{M}_s/dt = 0 = \gamma(\vec{M}_s \times \vec{H})$ and the term $\gamma[\vec{m}(t) \times \vec{h}(t)]$ has been dropped because of its small magnitude. Using the above-

mentioned exponential form for $\vec{m}(t)$ and neglecting the second order terms, the Cartesian components of Eq.(6.5) can finally be written in the form [17, 49]

$$(i\omega/\gamma)m_x + [H + (D_y + D_{ky} - D_z - D_{kz})M_s + i\Gamma]\, m_y = M_s h_y \tag{6.6}$$

$$-[H + (D_x + D_{kx} - D_z - D_{kz})M_s + i\Gamma]\, m_x + (i\omega/\gamma)m_y = -M_s h_x \tag{6.7}$$

and

$$m_z = 0 \tag{6.8}$$

where the FMR LLG linewidth $\Gamma = \lambda\omega/\gamma^2 M_s$. Elimination of m_y from Eqs.(6.6) and (6.7) gives

$$m_x = \chi_{xx} h_x + \chi_{xy} h_y \tag{6.9}$$

with

$$\chi_{xx} = \left[H + (D_y + D_{ky} - D_z - D_{kz})M_s + i\Gamma\right] M_s \eta^{-1} \tag{6.10}$$

$$\chi_{xy} = (i\omega/\gamma) M_s \eta^{-1} \tag{6.11}$$

and

$$\begin{aligned}\eta =& [H + (D_x + D_{kx} - D_z - D_{kz})M_s]\,[H + (D_y + D_{ky} - D_z - D_{kz})M_s] \\ & - \Gamma^2 - (\omega/\gamma)^2 + i\Gamma\,[2H + (D_x + D_y + D_{kx} + D_{ky} - 2D_z - 2D_{kz})M_s]\end{aligned} \tag{6.12}$$

Elimination of m_x instead of m_y from Eqs.(6.6) and (6.7) would have resulted in

$$m_y = \chi_{yx} h_x + \chi_{yy} h_y \tag{6.13}$$

where $\chi_{xx} = \chi_{yy} = \chi$ is the dynamic susceptibility and $\chi_{xy} = -\chi_{yx} = iG$, $\vec{G}$ is the gyration vector. Recalling that both the dynamic susceptibility and dynamic permeability μ are complex, i.e., $\chi = \chi' - i\chi''$ and $\mu = \mu' - i\mu''$, and using the relation $\mu = 1 + 4\pi\chi$, the real and imaginary parts of the (complex) dynamic permeability are given by [17, 49]

$$\mu' = \frac{\alpha\{[H+(D_y+D_{ky}-D_z-D_{kz})M_x][B+(D_x+D_{kx}-D_z-D_{kz})]-\Gamma^2 \\ -(\omega/\gamma)^2\}+\beta\Gamma[(B+H)+(D_x+D_y+D_{kx}+D_{ky}-2D_z-2D_{kz})M_s]}{(\alpha^2+\beta^2)} \tag{6.14}$$

$$\mu'' = \frac{\{-\alpha\Gamma[(B+H_k)-(H+H_k)]+\beta[(B+H_k)-(H+H_k)] \\ \times[H+(D_y+D_{ky}-D_z-D_{kz})M_s]\}}{(\alpha^2+\beta^2)} \tag{6.15}$$

with

$$\alpha = [H+(D_x+D_{kx}-D_z-D_{kz})M_s][H+(D_y+D_{ky}-D_z-D_{kz})M_s] \\ -\Gamma^2-(\omega/\gamma)^2 \tag{6.16}$$

$$\beta = \Gamma[2H+(D_x+D_y+D_{kx}+D_{ky}-2D_z-2D_{kz})M_s] \tag{6.17}$$

and

$$B = H+4\pi M_s \tag{6.18}$$

For a flat circular disc (the sample shape used in the present experiments), with H applied along the symmetry axis (z axis) so far as the uniaxial anisotropy is concerned and lying in the sample plane (parallel geometry or configuration), $D_x = D_z = 0$, $D_y = 4\pi$ (x-axis is taken to coincide with the polar axis), $D_{kx}M_s = D_{ky}M_s = H_k$ and $D_{kz} = 0$. Substituting these values of components of $\vec{D}$ and $\vec{D}_k$, Eqs.(6.14)-(6.17) are simplified to yield [17, 49]

$$\mu' = \frac{[(H+H_k)(B+H_k)-\Gamma^2-(\omega/\gamma)^2][(B+H_k)^2-\Gamma^2-(\omega/\gamma)^2] \\ +2\Gamma^2(B+H_k)(B+H+2H_k)}{[(H+H_k)(B+H_k)-\Gamma^2-(\omega/\gamma)^2]^2+\Gamma^2(B+H+2H_k)^2} \tag{6.19}$$

and

$$\mu'' = \frac{\begin{array}{c}-2\Gamma(B+H_k)[(H+H_k)(B+H_k)-\Gamma^2-(\omega/\gamma)^2] \\ +\Gamma(B+H+2H_k)[(B+H_k)^2-\Gamma^2-(\omega/\gamma)^2]\end{array}}{[(H+H_k)(B+H_k)-\Gamma^2-(\omega/\gamma)^2]^2+\Gamma^2(B+H+2H_k)^2} \tag{6.20}$$

The power absorbed by the sample, which is proportional to the surface impedance, in the parallel geometry, is given by

$$P_{\parallel} \propto [(\mu'^2+\mu''^2)^{1/2}+\mu'']^{1/2} \tag{6.21}$$

The theoretical variation of the Power absorption derivative, $dP_{\parallel}/dH$, can, therefore, be computed by combining equations (6.19)-(6.21) and taking the field derivative of the resulting expression. From Eqs.(6.6) and (6.7), the resonance frequency $\omega = \omega_{res}$ is calculated by the condition that m_x and m_y have non-trivial solutions only when $h_x = h_y = 0$. In other words, this implies that

$$\begin{vmatrix} i\omega_{res}/\gamma & \left\{-[H_{res}+(D_y+D_{ky} \right. \\ & \left. -D_z-D_{kz})M_s+i\Gamma]\right\} \\ \left\{-[H_{res}+(D_x+D_{kx} \right. & \\ \left. -D_z-D_{kz})M_s+i\Gamma]\right\} & i\omega_{res}/\gamma \end{vmatrix} = 0 \tag{6.22}$$

where H_{res} is the (steady) resonance field corresponding to ω_{res}. After a few simplifying steps, the following relation is arrived at [17, 49]

$$[(\omega/\gamma)^2+\Gamma^2] = [H_{res}+(D_y+D_{ky}-D_z-D_{kz})M_s][H_{res}+(D_x+D_{kx}-D_z-D_{kz})M_s] \tag{6.23}$$

The subscript for ω_{res} is dropped because in experiments the microwave-field frequency, ω, is kept constant while the steady field, H, is swept through the resonance.

6.2.2 Resonance field: Angular variation

With the choice of the coordinate system shown in figure 6.3, different contributions to the free-energy density, F, for a film with cubic magnetocrystalline anisotropy and

an in-plane uniaxial anisotropy, are given as follows. The direction cosines of magnetization vector, $\vec{M}$, with reference to x, y, z axes are $\alpha_1 = \sin\theta_M \cos\phi_M \quad ; \quad \alpha_2 = \sin\theta_M \sin\phi_M$ and $\alpha_3 = \cos\theta_M$ so that the contribution of cubic magnetocrystalline anisotropy (MCA) to F is

$$\begin{aligned} F_{K_C} &= K_1(\alpha_1^2\alpha_2^2 + \alpha_2^2\alpha_3^2 + \alpha_3^2\alpha_1^2) + K_2\alpha_1^2\alpha_2^2\alpha_3^2 \\ &= \sin^2\theta_M[K_1\cos^2\theta_M + (K_1 + K_2\cos^2\theta_M)\sin^2\theta_M \sin^2\phi_M \cos^2\phi_M] \end{aligned}$$

The easy axis for the uniaxial anisotropy lies along a direction ($\vec{H}_K$) which makes an angle ϕ_K with x-axis (Fig. 6.3) with the result that the contribution to F due to uniaxial anisotropy is given by $F_{K_u} = K_u \sin^2\theta'$; where θ' is the angle between M and H_k. Recognizing that $\theta' = \cos^{-1}[\sin\theta_M \cos(\phi_M - \phi_K)]$,

$$F_{K_u} = K_u(1 - \cos^2\theta') = K_u[1 - \sin^2\theta_M \cos^2(\phi_M - \phi_K)]$$

Including the Zeeman, F_Z, and shape anisotropy, F_S, contributions, the total free-energy density becomes

$$\begin{aligned} F &= F_Z + F_S + F_{K_c} + F_{K_u} \\ &= -MH(\sin\theta_M \sin\theta_H \cos(\phi_M - \phi_H) + \cos\theta_M \cos\theta_H) + 2\pi M^2 \cos^2\theta_M \\ &\quad + K_1 \sin^2\theta_M(\cos^2\theta_M + \sin^2\theta_M \sin^2\phi_M \cos^2\phi_M) \\ &\quad + K_2 \cos^2\theta_M \sin^4\theta_M \sin^2\phi_M \cos^2\phi_M + K_u[1 - \sin^2\theta_M \cos^2(\phi_M - \phi_K)] \end{aligned} \quad (6.24)$$

The equilibrium conditions for magnetization are $\partial F/\partial\theta_M = 0$ and
$\partial F/\partial\phi_M = 0$ and the resonance condition is [18]

$$\left(\frac{\omega}{\gamma}\right)^2 = \frac{1}{M^2 \sin^2\theta_M}\left[\left(\frac{\partial^2 F}{\partial\theta_M^2} \cdot \frac{\partial^2 F}{\partial\phi_M^2}\right)^2 - \left(\frac{\partial^2 F}{\partial\theta_M \partial\phi_M}\right)\right]$$

Using the first and second order derivatives of F with respect to θ_M and ϕ_M, the final expression for resonance condition is

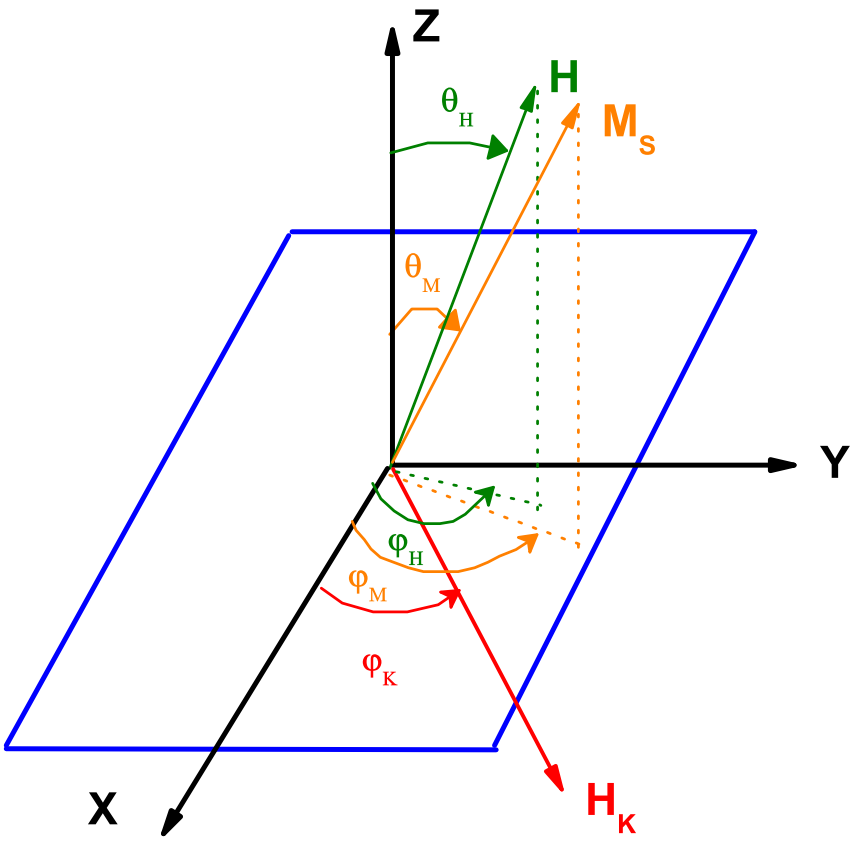

Figure 6.3: *Coordinate system showing various angles used in the computation of angular variation of resonance field for the 'in-plane' (IP) and 'out-of-plane' (OP) cases.*

$$\left(\frac{\omega}{\gamma}\right)^2 = \Big[H_r(\sin\theta_M \sin\theta_H \cos(\phi_H - \phi_M) + \cos\theta_M \cos\theta_H)$$
$$- \cos 2\theta_M[4\pi M + H_{K_u}\cos^2(\phi_M - \phi_K)] + H_{K_1}(\cos 4\theta_M$$
$$+ \frac{1}{4}\sin^2 2\theta_M \sin^2 2\phi_M + \frac{1}{2}\sin^2\theta_M \cos 2\theta_M \sin^2 2\phi_M) - H_{K_2}[\sin^4\theta_M \cos 2\theta_M$$
$$+ \frac{1}{4}\sin 2\theta_M(2\sin 2\theta_M - \sin 4\theta_M - \frac{3}{2}(\cos^3\theta_M(\cos\theta_M - \cos 3\theta_M)$$
$$+ \frac{3}{2}(\sin^3\theta_M(\sin\theta_M + \sin 3\theta_M)]\frac{1}{4}\sin^2 2\phi_M\Big]$$
$$\times \Big[H_r(\sin\theta_M \sin\theta_H \cos(\phi_H - \phi_M) + \cos\theta_M \cos\theta_H)$$
$$- \cos^2\theta_M[4\pi M + H_{K_u}\cos^2(\phi_M - \phi_K)] + H_{K_u}\cos 2(\phi_M - \phi_K)$$
$$+ H_{K_1}(\sin^2\theta_M \cos 4\phi_M + \cos^2\theta_M \cos 2\theta_M + \frac{1}{8}\sin^2 2\theta_M \sin^2 2\phi_M)$$
$$+ H_{K_2}[\sin^2\theta_M \cos^2\theta_M \cos 4\phi_M - \frac{1}{16}\sin^2\theta_M \sin^2 2\theta_M \sin^2 2\phi_M$$
$$+ \frac{1}{8}\cos^2\theta_M \sin^2 2\theta_M \sin^2 2\phi_M]\Big] - \Big[\frac{1}{4}(H_{K_1} + H_{K_2})\sin^2\theta_M \cos\theta_M \sin 4\phi_M$$
$$- \frac{5}{4}H_{K_2}\cos\theta_M \sin^4\theta_M \sin 4\phi_M + \frac{1}{2}H_{K_u}\cos\theta_M \sin 2\phi\Big]^2 \qquad (6.25)$$

The first equilibrium condition for magnetization, $\partial \mathrm{F}/\partial\theta_M = 0$, yields the result

$$H_r(\sin\theta_M \cos\theta_H - \cos\theta_M \sin\theta_H \cos(\phi_M - \phi_H)) = 2\pi M \sin 2\theta_M$$
$$- \frac{K_1}{2M}[\sin 4\theta_M + 4\sin^2\theta_M \sin 2\theta_M \sin^2\phi_M \cos^2\phi_M]$$
$$+ \frac{K_2}{4M}[\frac{1}{2}\sin 2\theta_M(\cos 4\theta_M - 4\cos 2\theta_M + 3)$$
$$- (3\sin\theta_M - \sin 3\theta_M)(3\cos\theta_M + \cos 3\theta_M)]\sin^2\phi_M \cos^2\phi_M$$
$$+ \frac{H_{K_u}}{2}\sin 2\theta_M \cos^2(\phi_M - \phi_K) \qquad (6.26)$$

the second equilibrium condition for magnetization, $\partial F/\partial\phi_M = 0$, gives,

$$H_r \sin\theta_H \sin(\phi_H - \phi_M) = \frac{1}{2M}\sin^3\theta_M \sin 4\phi_M(K_1 + K_2\cos^2\theta_M)$$
$$+ \frac{H_{K_u}}{2}\sin\theta_M \sin 2(\phi_M - \phi_K) \qquad (6.27)$$

where $H_{K_u} = 2K_u/M$, $H_{K_1} = 2K_1/M$ and $H_{K_2} = 2K_2/M$.

'In-plane' case

In the 'in-plane' case, applied magnetic field (H) is confined to the sample plane (xy-plane), i.e., $\theta_H = \frac{\pi}{2}$. Since the easy axis of magnetization, M, makes an angle $\theta_M = cos^{-1}(1/\sqrt{3})$ and the angles ϕ_M, ϕ_H and ϕ_K are measured with respect to the x-axis in the sample plane, i.e., $\phi_M = \phi$, $\phi_H = \psi$ and $\phi_K = \xi$. The resonance and equilibrium conditions in this case are obtained from Eqs.(6.25) and (6.27) as

Resonance condition

$$\begin{aligned}\left(\frac{\omega}{\gamma}\right)^2 &= \left[H_r^{\parallel}(\sqrt{2/3})\cos(\psi-\phi) + \frac{1}{3}(4\pi M + H_{K_u}\cos^2(\phi-\xi))\right.\\ &\quad \left. + \frac{H_{K_1}}{9}(\sin^2 2\phi - 7) - H_{K_2}(0.186 \times \sin^2 2\phi)\right]\\ &\quad \times \left[H_r^{\parallel}(\sqrt{2/3})\cos(\psi-\phi) - \frac{1}{3}(4\pi M + H_{K_u}\cos^2(\phi-\xi))\right.\\ &\quad \left. + H_{K_u}\cos 2(\phi-\xi) + \frac{H_{K_1}}{18}(\cos 4\phi - 1) + \frac{H_{K_1}}{9}(2\cos 4\phi)\right]\\ &\quad - \left[\frac{1}{2\sqrt{3}}(H_{K_1}+H_{K_2})\sin 4\phi - \frac{5}{9\sqrt{3}}H_{K_2}\sin 4\phi + \frac{1}{2\sqrt{3}}H_{K_u}\sin 2\phi\right]^2 \end{aligned} \quad (6.28)$$

Equilibrium condition for magnetization

$$H_r^{\parallel} = \left[0.544\left(H_{K_1} + \frac{H_{K_2}}{3}\right)(\cos^2\phi) + 0.817\ H_{K_u}\right]\left[\frac{\sin\psi}{\sin\phi} - \frac{\cos\psi}{\cos\phi}\right]^{-1} \quad (6.29)$$

'Out-of-plane' case

In the 'out-of-plane' case, H, M and H_{K_u} are confined to the xz-plane with H_{K_u} pointing along x-axis, so that $\phi_H = \phi_M = \phi_K = 0$ and the angles θ_H and θ_M are measured with respect to the z-axis (normal to the sample plane). The resonance and equilibrium conditions in this case are derived from Eqs.(6.25) and (6.26).

Resonance condition

$$\left(\frac{\omega}{\gamma}\right)^2 = \left[H_r^{\perp}\cos(\alpha-\theta) - (4\pi M + H_{K_u})\cos 2\theta + H_{K_1}\cos 4\theta\right] \times \left[H_r^{\perp}\cos(\alpha-\theta) - 4\pi M\cos^2\theta + H_{K_u}\sin^2\theta + H_{K_1}(\sin^2\theta + \cos^2\theta\cos 2\theta) + H_{K_2}\sin^2\theta\cos^2\theta\right] \quad (6.30)$$

where $\theta_H = \alpha$ and $\theta_M = \theta$.

Equilibrium condition for magnetization

$$H_r^{\perp} = [4\pi M + H_{K_u} - H_{K_1}\cos 2\theta]\left[\frac{\cos\alpha}{\cos\theta} - \frac{\sin\alpha}{\sin\theta}\right]^{-1} \quad (6.31)$$

6.2.3 Linewidth

The 'peak-to-peak' ferromagnetic resonance linewidth, ΔH_{pp}, is a measure of the rate at which magnetization relaxes back to equilibrium once the static magnetic field is switched off. The measured FMR linewidth, ΔH_{pp}, is caused by two mechanisms: the intrinsic damping of magnetization, and the magnetic inhomogeneity of the ferromagnetic sample, and is given by

$$\Delta H_{pp} = \Delta H_{inhom} + 1.16\frac{\lambda}{\gamma^2 M(T,H)}\,\omega \quad (6.32)$$

Here, ΔH_{inhom} describes the frequency-independent (inhomogeneous) FMR line-broadening that originates either from two-magnon or multi-magnon scattering from spatially localized magnetic inhomogeneities [19] such as (a) the variation in the crystallographic directions from one nanocrystal to the other, (b) randomly distributed defects, which is a predominant effect in nanocrystalline materials, (c) the distribution in the internal fields, etc. or from a distribution in the demagnetizing fields [20]

or from the exchange-conductivity mechanism [21–24]. ΔH_{inhom} is particularly large when the uniform mode resonance (k = 0) couples to the spin waves with k $\neq$ 0 [25]. Magnetic inhomogeneity is reflected in FMR spectra as a distribution of local resonance fields.

The frequency-dependent intrinsic damping (ΔH_{hom}), described by the second term on the right-hand side of the Eq.(6.4) (Gilbert damping term, ΔH_{LLG}), reflects the viscous damping of the magnetization precession (and low-energy spin waves) excited in the FMR process. ΔH_{LLG}, resulting from the LLG relaxation mechanism [17, 21, 26, 27, 49], is a measure of microscopic mechanism by means of which the absorbed microwave energy is dissipated from the spin system to the lattice resulting in the generation of phonons. λ depends on temperature [28], the wavevector $\overrightarrow{K}$, and may exhibit anisotropy [27, 29].

6.2.4 Linewidth: Angular variation

The LLG contribution to ΔH_{pp} depends on the polar, θ, and azimuthal, ϕ, angles of magnetization [30], and can be calculated from the expression

$$\Delta H_{hom}(\theta,\phi) = \frac{2}{\sqrt{3}} \frac{1}{|\frac{\partial\omega}{\partial H_{res}}|} \frac{\lambda}{M^2} \left(\frac{\partial^2 F}{\partial\theta^2} + \frac{1}{sin^2\theta} \frac{\partial^2 F}{\partial\phi^2} \right) \tag{6.33}$$

ΔH_{hom} goes through a minimum at the principal magnetic directions and it has a maximum where the magnetization direction varies strongly. The magnetization precessing around easy axis is more viscously damped, since it has to move into an unfavorable hard direction. For the magnetic field along the hard axis, $\overrightarrow{M}$ precess towards the easy direction and is less damped. The viscous damping mechanism has its microscopic origin in the spin-orbit interaction, which couples the spin to the lattice.

As a result of the magnetic inhomogeneities prevalent in nanocrystalline materi-

als, anisotropy paprameters K_i that appear in Eqs.(6.28) and (6.30) get distributed. This yields an *angular-dependent* inhomogeneous linewidth. With reference to the coordinate system specified in Fig. 6.3, $\Delta \mathrm{H}_{inhom}$ has been approximated as [31]

$$\Delta H_{inhom} = \Delta H_{int} + \Delta H_{pp}(\psi) + \Delta H_{pp}(\alpha) \tag{6.34}$$

While ΔH_{int} represents broadening in linewidth due to internal field inhomogeneities, $\Delta H_{pp}(\psi)$ ($\Delta H_{pp}(\alpha)$) results from angular spread in crystallographic axis in the in-plane (out-of-plane) configurations.

6.2.5 Exchange Conductivity

In ferromagnetic materials, apart from the damping term, there is also a contribution to the line-broadening due to the exchange-conductivity mechanism. It is well-known that in highly conducting metallic specimens, microwave field penetrates only a thin surface layer of the sample of thickness $50nm$ and as a result, the dynamic magnetization (exchange-coupled set of spins) becomes inhomogeneous. The spatial variations in magnetization exert a torque on $\vec{M}$ which is expressed as $(2A\gamma/M^2)(\vec{M} \times \nabla^2 \vec{M})$, where A is a phenomenological exchange stiffness parameter. Thus, this exchange-conductivity term should be included in the equation of motion of the magnetization, Eq.(6.4), and then the resulting equation solved in conjunction with the Maxwell's equations to obtain a correct solution for the observed lineshape. The exchange term leads to a shift in the resonance field and also contributes to the broadening of the resonance line. This term would become unimportant if the conductivity is low or if the exchange stiffness is small.

6.3 Microwave Power Absorption Derivative (PAD) curves, FMR Lineshape analysis and Discussion

The microwave power absorption derivative with respect to the static field H, i.e., $dP_{\|}/dH$ versus H, curves were recorded on disk-shaped (5 mm in diameter) nc-Ni samples with different average crystallite sizes, 'd' = 10(1) nm, 15(1) nm, 20(1) nm, 25(2) nm and 40(1) nm, at fixed microwave field frequency of 9.23 GHz and fixed temperatures in the range 110 K $\lesssim T \lesssim$ 325 K in the parallel ($\|$) sample configuration (i.e., when the applied static field lies within the sample plane). $dP_{\|}/dH$ versus H curves, recorded at room temperature (open symbols) for the nanocrystalline Ni samples with d ranging from 10 nm to 40 nm, are shown in Fig. 6.4. This figure is the representative of the PAD curves at other temperatures in the range 110 K $\lesssim T \lesssim$ 325 K. The $dP_{\|}/dH \equiv dP_{IP}/dH$ versus H (dP_{OP}/dH versus H) curves, at a few selected temperatures in the range 127 K $\leq T \leq$ 321 K, were also recorded as a function of the angle 'Ψ' ('α'). The angles 'Ψ' and 'α' subtended by the static magnetic field in the 'in-plane', IP, and 'out-of-plane', OP, sample configurations are defined as shown in figure 6.3. The observed (open circles) field variations of the power absorption derivative, dP/dH, in the IP sample configuration, along with the optimum theoretical fits (continuous curves) yielded by an elaborate lineshape analysis [32–34] using the Landau-Lifshitz-Gilbert (LLG) equation of motion for dynamic magnetization, i.e., Eq.(6.4), is depicted in Fig. 6.4. In arriving at these optimum fits, the lineshape analysis treats g, M_s, H_k and the 'peak-to-peak' linewidth, ΔH_{pp} (defined as the field difference between the extrema of the dP/dH versus H curve, refer to the top panel of Fig. 6.4), as free-fitting parameters. The lineshape analysis reveals that g has the *temperature-independent* and *crystallite size-independent* value of $g = 2.21(3)$ (the same as that in bulk Ni [35, 36]) whereas M_s, H_k and ΔH_{pp} vary

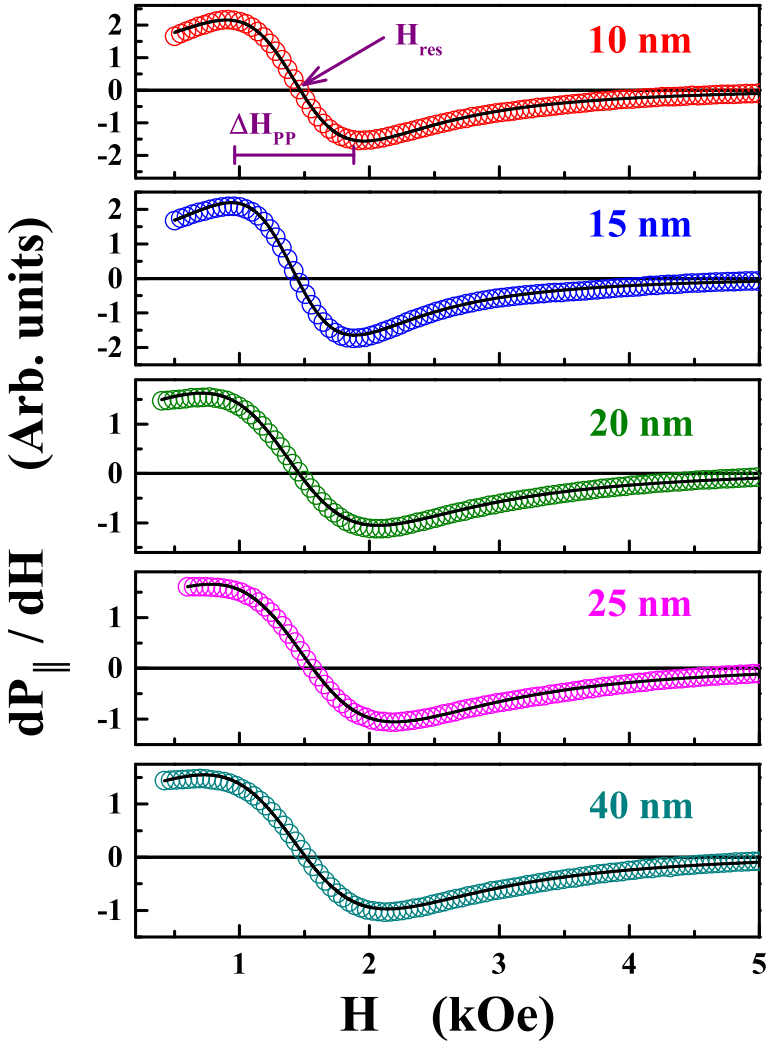

Figure 6.4: *Field dependence of the microwave power absorption derivative, taken at room temperature (open symbols) in the 'in-plane' (∥) sample configuration, along with the optimum lineshape fits (continuous curves) for the nanocrystalline Ni samples with the average crystallite size ranging from 10 nm to 40 nm.*

with temperature. The temperature variations of these quantities are presented in the following sections.

6.3.1 Magnetization: Temperature dependence

Figure 6.5 shows the functional dependence of magnetization on temperature, M(T) (open circles), yielded by the lineshape analysis. The continuous curves through the $M_s(T)$ data (symbols) in Fig. 6.5 represent the optimum spin-wave (SW) fits based on the well-known spin-wave expression [37–45]

$$M_s(T) = M_s(0) - g\ \mu_B \left[\zeta(3/2)\left(\frac{k_B T}{4\pi D(T)}\right)^{3/2} + 15\pi\ \beta\ \zeta(5/2)\left(\frac{k_B T}{4\pi D(T)}\right)^{5/2}\right] \quad (6.35)$$

where $M_s(0)$ is the saturation magnetization at zero temperature, $D(T) = D_0\ (1 - D_2T^2 - D_{5/2}T^{5/2})$, D_0 is the value of spin-wave stiffness, D, at 0 K, D_2 and $D_{5/2}$ account for the thermal renormalization of D due to Stoner single particle-magnon and magnon-magnon interactions, $\beta = \langle r^2\rangle/20$, where $\langle r^2\rangle$ is the mean-square range of the exchange interaction. Now that the parameters $M_s(0)$, D_0, D_2, $D_{5/2}$ and β in Eq.(6.35) cannot be determined, all at once, in the absence of $M_s(T)$ data at low temperatures, we set [45] $D_2 = 0$ and $\beta = 2.2\ \mathring{A}^{\,2}$ and vary $M_s(0)$, D_0 and $D_{5/2}$ so as to optimize agreement with the observed $M_s(T)$. The optimum fits (continuous curves) to the $M_s(T)$ data (open symbols), based on Eq.(6.35), are shown in figure 6.5. The variations of $M_s(0)$, D_0 and $D_{5/2}$ with the average crystallite size, d, are displayed in the figure 6.6, figure 6.7(a) and Fig 6.7(b), respectively. The absolute values of D_0 and $M_s(0)$ for different d, determined in this work, are in close agreement (within the uncertainty limits) with those obtained earlier [45] from the bulk magnetization data. Consequently, the previously observed [45] power law behavior $M_s(0) \sim d^{-3/2}$ (Fig 6.6) and $D_0 \sim d^{4/3}$ (Fig 6.7a) is preserved. In the limit $d \longrightarrow \infty$, the linear

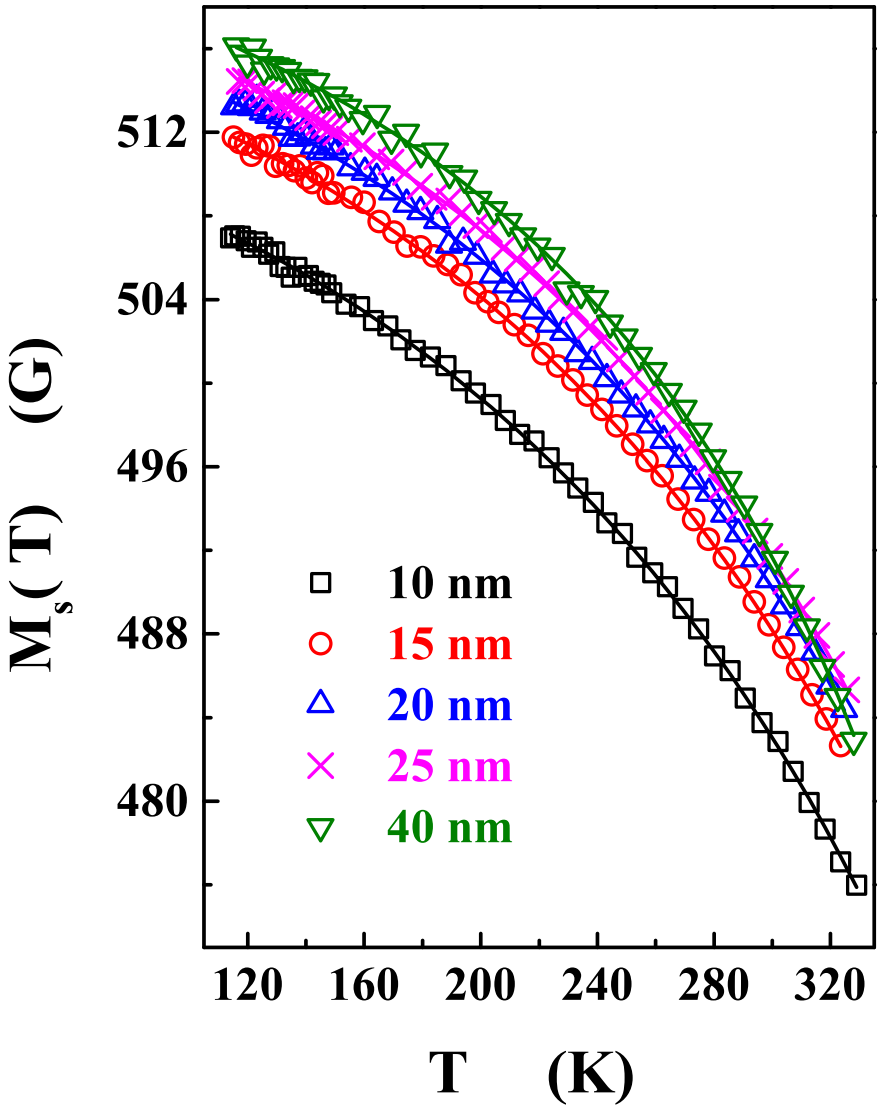

Figure 6.5: *Theoretical fits (continuous curves), based on the spin wave relation (Eq.(6.35)), to the $M_s(T)$ data (symbols), obtained using the lineshape analysis, for the nc-Ni samples with the average crystallite size, d = 10 nm, 15 nm, 20 nm, 25 nm and 40 nm.*

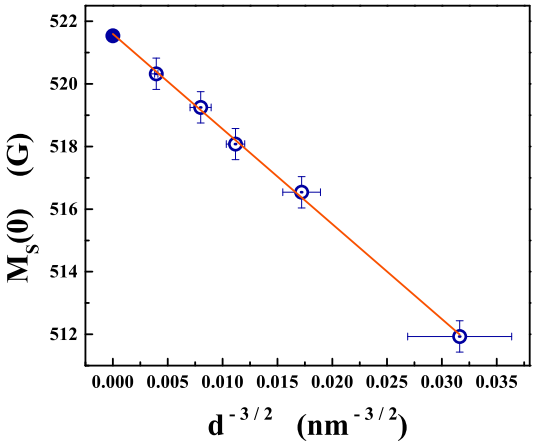

Figure 6.6: *Scaling of the saturation magnetization at 0 K, $M_s(0)$, with $d^{-3/2}$.*

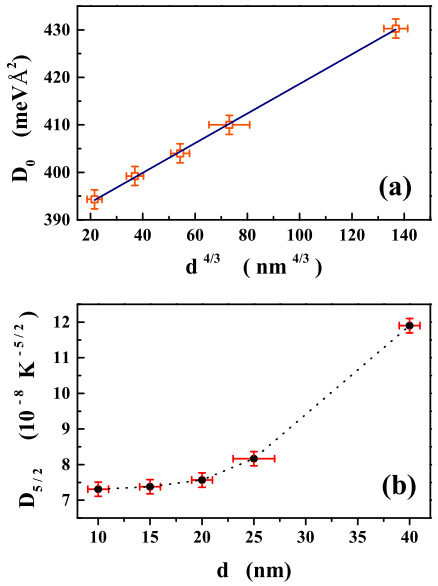

Figure 6.7: *Panel (a) demonstrates the $d^{4/3}$ power law variation of spin-wave stiffness at zero temperature $D_0 \equiv D(T = 0)$ while the panel (b) shows the variation of $D_{5/2}$ (which is a measure of the strength of the thermal renormalization of the spin-wave stiffness due to magnon-magnon interactions) with d.*

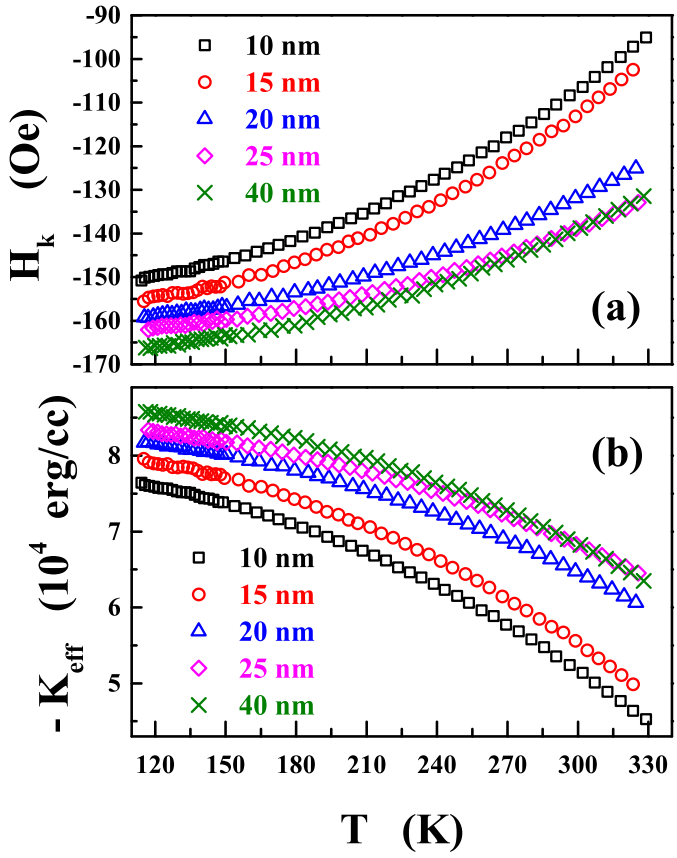

Figure 6.8: *Temperature variations of the (a) anisotropy field (H_K) and (b) effective magnetic anisotropy constant (K_{eff}), deduced from the detailed FMR lineshape analysis.*

relation between $M_s(0)$ and $d^{-3/2}$ gives the value $M_s(0) = 521.59$ (11) G, which conforms well with $M_s(0) = 521.27(3)$ G, reported earlier for Ni single crystal [46]. Moreover, the $D_0 \sim d^{4/3}$ variation, when extrapolated to $d = 55$ nm ($d = 0$), yields the value $D_0 = 452$ meV$\mathring{A}^{\ 2}$ ($D_0(d = 0) = 387(4)$ meV$\mathring{A}^{\ 2}$), which matches the corresponding value obtained previously for pulse electro-deposited nc-Ni with $d = 55$ nm from the small-angle neutron scattering data [47–49] (from the magnetization data [50, 51] taken on Ni-rich amorphous Ni-B alloys).

6.3.2 'In-plane' magnetic anisotropy: Temperature dependence

Panel (a) of figure 6.8 highlights that the anisotropy field H_k is *negative* throughout the temperature range of the present investigation. In view of the relation $H_k \propto K_{eff}/M_s$ (where K_{eff} is the effective magnetic anisotropy constant), negative H_k implies that $K_{eff} < 0$. Consequently, like in bulk Ni, the set of $< 111 >$ directions are the easy directions of magnetization whereas the cube edges are the hard directions. The panel (b) displays the temperature variations of $K_{eff} \equiv H_k \times M_s$ for different nc-Ni samples arrived at by using the presently determined $M_s(T)$ and $H_k(T)$ shown in Fig. 6.5 and Fig. 6.8(a). Consistent with our earlier observation, based on $K_{eff}(T)$ deduced from the law of 'approach-to-saturation' in magnetization [12], at any given temperature, K_{eff} is negative and its *magnitude* increases with d. However, the present values of K_{eff} are an order of magnitude smaller than those reported earlier [12] for the nc-Ni samples same as the present ones.

6.3.3 FMR linewidth: Temperature dependence

Fig. 6.9 displays the relative 'peak-to- peak' ferromagnetic resonance linewidth ($\Delta H_{PP}(T)/\Delta H_{PP}(T_{max})$) (symbols) with temperature in nanocrystalline Ni sam-

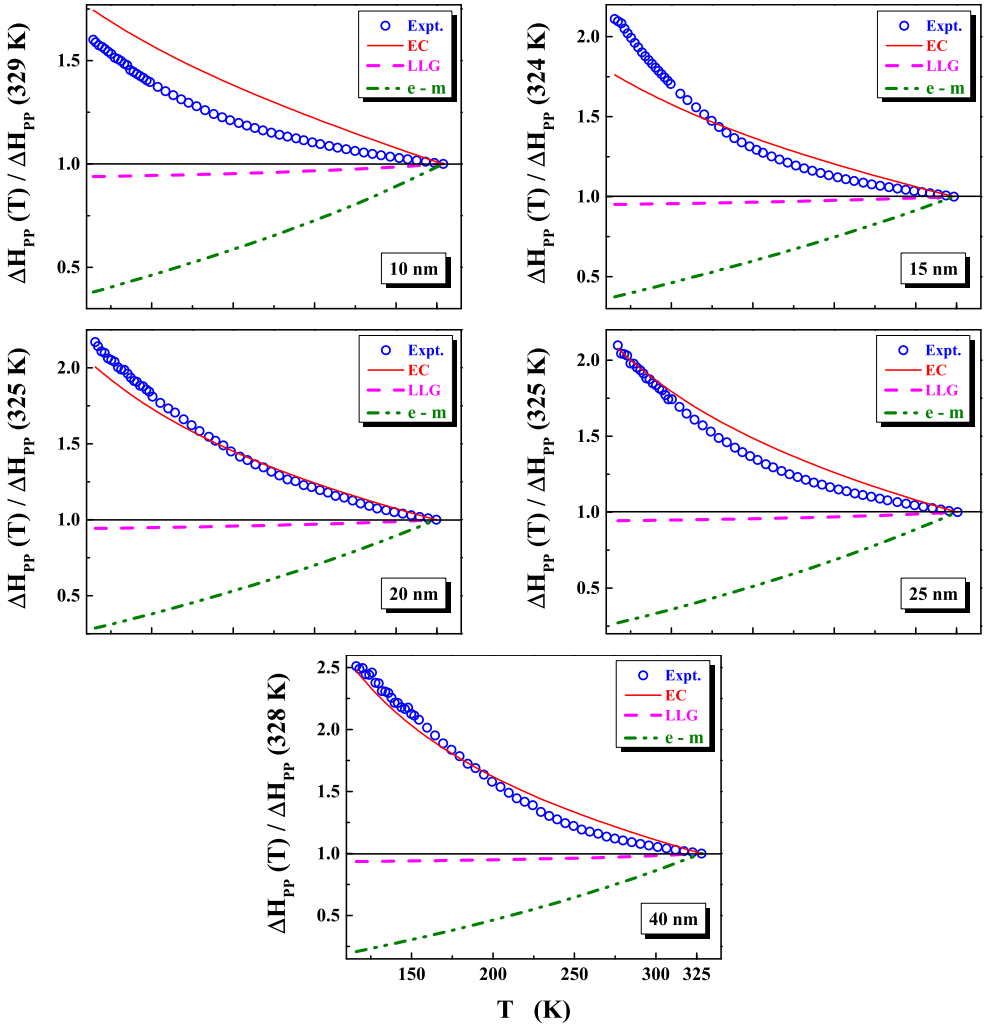

Figure 6.9: *Variation of relative linewidth ($\Delta H_{PP}(T)/\Delta H_{PP}(T_{max})$) (symbols) with temperature in nanocrystalline Ni samples under study. The relative magnitudes of various contributions to the linewidth (normalized to their value at $T = T_{max}$), (a) exchange-conductivity (solid line), (b) Landau-Lifshitz damping (dashed-line), (c) s-d exchange interaction (dash-double dot line), are also indicated in the figures for comparison.*

Table 6.1: *Observed and computed linewidths in different nanocrystalline Ni samples*

Linewidth	d = 10 nm		d = 15 nm		d = 20 nm		d = 25 nm		d = 40 nm	
(Oe)	114 K	329 K	115 K	323 K	115 K	325 K	117 K	326 K	116 K	328 K
Experiment	1604.8	1002.3	1798.7	872.0	2779.2	1281.4	2813.3	1340.8	3335.1	1328.3
EC	49.9	28.6	51.4	29.2	62.5	31.2	69.8	33.6	83.0	33.6
LLG	88.5	94.2	87.7	92.9	87.4	92.6	87.2	92.4	86.9	92.9

ples under study, obtained from the lineshape analysis. The decline in ΔH_{pp} with increasing temperature (Fig. 6.9) for the nanocrystalline Ni samples is reminiscent of $\Delta H_{pp}(T)$ observed previously [36] in bulk Ni. Bhagat and Hirst [36] attribute the broadening of FMR linewidth as the temperature falls below room temperature in crystalline Ni to the exchange conductivity mechanism and pinning of surface spins by surface anisotropy. In an attempt to find out if this inference also holds for the nanocrystalline counterparts, we consider several possible additive contributions to the FMR linewidth, e.g.,

$$\Delta H_{pp}(T) \quad = \quad \Delta H(0) \; + \; \Delta H_{EC}(T) \; + \; \Delta H_{LLG}(T) \; + \; \Delta H_{e-m}(T) \quad (6.36)$$

where $\Delta H(0)$ is the temperature-independent and frequency-independent contribution to linewidth arising from magnetic inhomogeneities, $\Delta H_{EC}(T) = (16\pi/3)\ [(A(T)\ \omega_{res}/\rho(T))^{1/2}/c]$ (with exchange stiffness constant $A(T) = D(T)\ M_s(T)/2g\mu_B$, electrical resistivity ρ, $\omega_{res} = 2\pi\nu_{res}$, microwave resonant frequency ν_{res} and the velocity of light c) is the exchange-conductivity (EC) contribution [52] when $H_{res} \ll 4\pi M_s$, $\Delta H_{LLG}(T) = (2/3^{1/2})\ (\omega/\gamma)\ (\lambda/\gamma M_s(T))$ is the LLG damping contribution [1–5], and $\Delta H_{e-m}(T) \sim [\rho(T)/M_s(T)]$ is the contribution due to the interaction of conduction electron spin with the resonance-excited magnons [35]. The EC and LLG contributions to the FMR linewidth are calculated at different temperatures by making use of $D(T) = D_0(1 - D_{5/2}T^{5/2})$, $M_s(T)$, $g = 2.21$, determined in this work, $\lambda = 2.3 \times 10^8$ sec^{-1}, the same as that in bulk Ni [36], and $\rho(T)$ reported elsewhere [53]. The values of ΔH_{EC} and ΔH_{LLG} at $\simeq$ 115 K

and $\simeq$ 325 K, so obtained, are compared with the corresponding values of the observed FMR linewidth in Table 6.1. Figure 6.9 compares the observed $\Delta H_{pp}(T)$ with $\Delta H_{EC}(T)$ and $\Delta H_{LLG}(T)$, all normalized to their respective highest temperature values. $\Delta H_{e-m}(T)$ is also included in Fig. 6.9 for comparison. It is evident that the exchange-conductivity mechanism, at best, explains the thermal narrowing of the observed linewidth but not the large magnitude of ΔH_{pp} at any given temperature. By contrast, the Landau-Lifshitz-Gilbert damping gives a larger contribution to ΔH_{pp} but, instead of decreasing with increasing temperature, exhibits a slight increasing trend in the temperature range covered in the present measurements. A much steeper rise in ΔH_{e-m} with temperature clearly rules out the conduction electron spin-resonance-excited magnon contribution to ΔH_{pp}. This inference is consistent with the earlier observation that the conduction electron-magnon interactions are of no consequence when it comes to the thermal renormalization of the spin wave stiffness (i.e., $D_2 \simeq 0$).

6.4 Angular dependence of FMR spectra: 'In-plane' and 'out-of-plane' sample configurations

6.4.1 Angular variation of the Resonance field

The PAD curves were recorded at various fixed temperatures from 127 K to 321 K as a function of the angle ψ between the static magnetic field, $\overrightarrow{H}$, and the easy-direction within the sample plane in the 'in-plane' (IP) configuration, and as a function of the angle α that $\overrightarrow{H}$ makes with the normal to the sample plane in the 'out-of-plane' (OP) configuration. The angular variations of the PAD curves with the angles ψ and α in the IP and OP samples configurations for nanocrystalline nickel with $d = 10$ nm are displayed in figures 6.10 and 6.11. These PAD curves are also representative

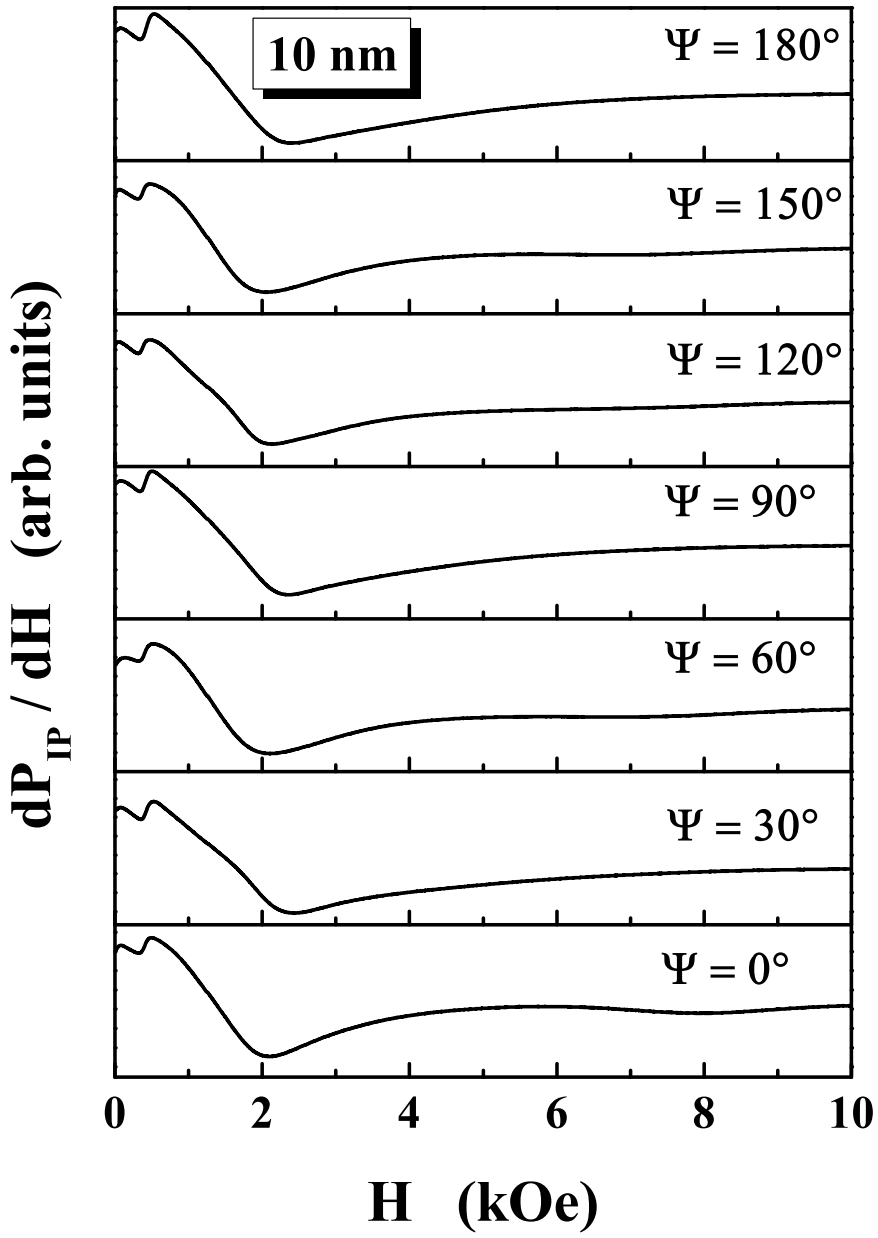

Figure 6.10: *The 'in-plane' angular (Ψ) variations of the PAD curves taken at a representative temperature of 321 K for the nanocrystalline Ni samples with the average crystallite size 10 nm.*

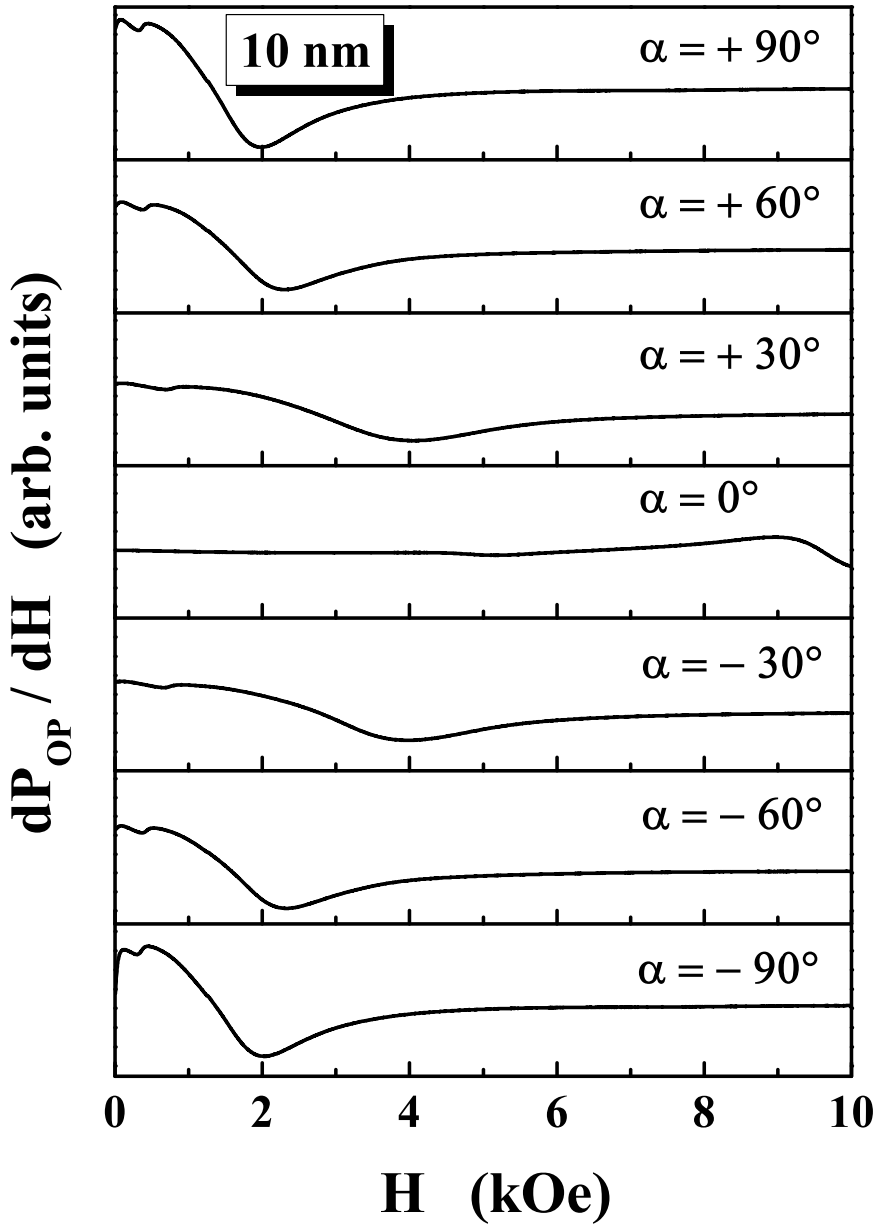

Figure 6.11: *The 'out-of-plane' angular (α) variations of the PAD curves taken at a representative temperature of 321 K for the nanocrystalline Ni samples with the average crystallite size 10 nm.*

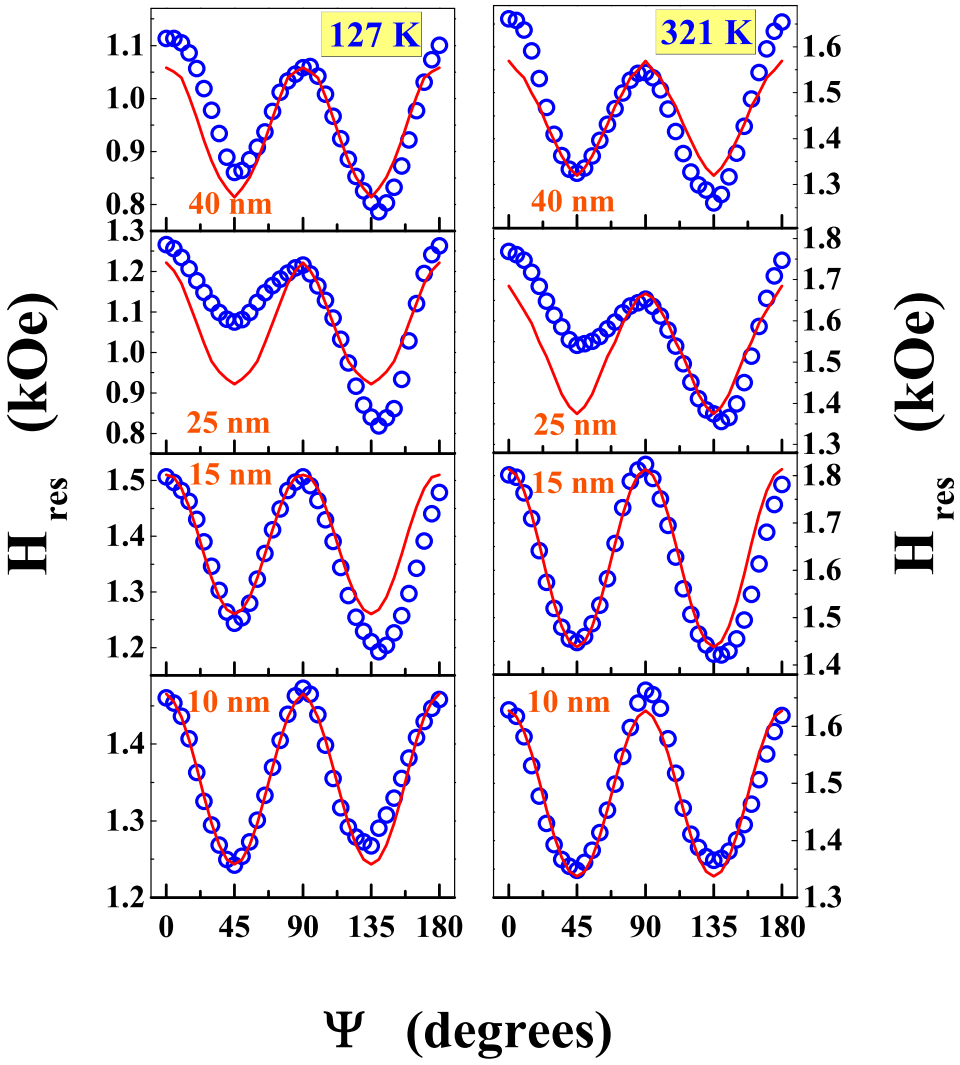

Figure 6.12: *The angular (Ψ) variations of the resonance field, H_{res} in the 'in-plane' sample configuration, at fixed temperatures T = 127 K and 321 K, for the nanocrystalline Ni samples with the average crystallite size ranging from 10 nm to 40 nm.*

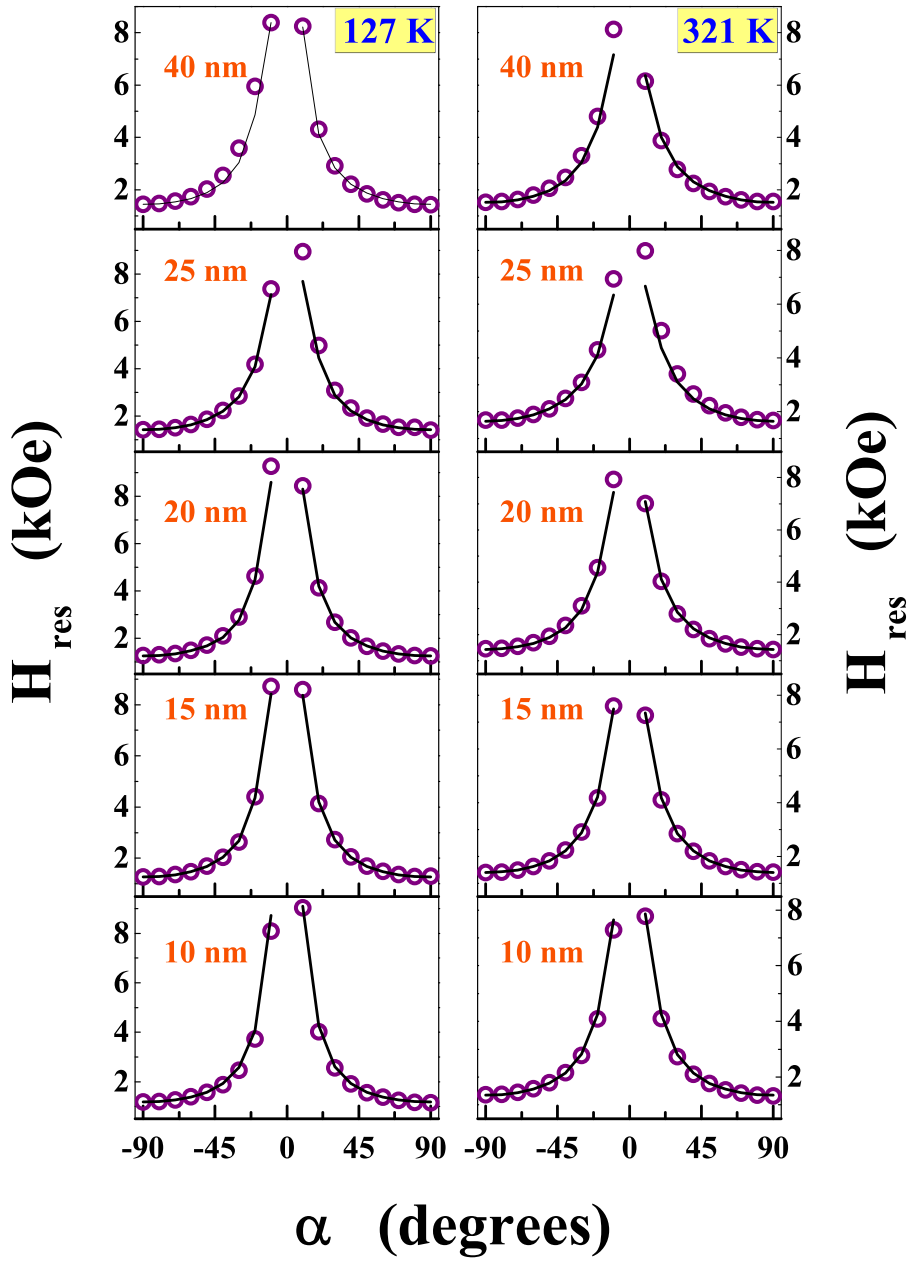

Figure 6.13: *The angular (α) variations of the resonance field, H_{res} in the 'out-of-plane' sample configuration, at fixed temperatures T = 127 K and 321 K, for the nanocrystalline Ni samples with the average crystallite size ranging from 10 nm to 40 nm.*

of other nanocrystalline Ni samples under study. The functional dependencies of the resonance field, H_{res}, and the 'peak-to-peak' linewidth, ΔH_{pp}, on the angles ψ and α for the two sample geometries, deduced from the observed dP/dH versus H curves (Fig. 6.10 and Fig. 6.11), are depicted in figures 6.12 and 6.13 for H_{res}, and in figures 6.14 and 6.15 for ΔH_{pp}.

It is evident from Fig. 6.12 that $H_{res}(\Psi)$ goes through two minima at $\Psi = 45^0$ and 135^0 and three maxima at $\Psi = 0^0$, 90^0, 180^0. H_{res} is maximum along the hard directions of magnetization (e.g., for the ab sample plane, $\Psi = 0^0$, 90^0, 180^0 correspond to $< 100 >$, $< 010 >$, $< \bar{1}00 >$ directions) since the large anisotropy field along the easy axis (e.g., $< 111 >$) shifts H_{res} to lower fields. $H_{res}(\Psi)$ thus establishes the presence of cubic magnetocrystalline anisotropy (MCA). However, the $H_{res}(\Psi)$ plots in Fig. 6.12 clearly demonstrate that H_{res} has the same value (within the uncertainty limits) at $\Psi = 0^o$ and 180^o but has a lower value at 90^o than at $\Psi = 0^o$ or 180^o in all the nanocrystalline Ni samples except for the one with d = 10 nm. This discrepancy between the value of Ψ at 90^o and that at $\Psi = 0^o$ or 180^o, apparent in the samples with d = 25 nm and 40 nm, indicates the presence of 'in-plane' uniaxial magnetic anisotropy, in addition to cubic magnetocrystalline anisotropy, and that the uniaxial anisotropy has a tendency to grow with average crystallite size, d. Consistent with this expectation, the concomitant presence of cubic MCA and 'in-plane' uniaxial anisotropy is established by the detailed analysis of $H_{res}(\Psi)$, as elucidated in the following text. Another important observation is that the peaks in resonance curve are asymmetric, presumably due to strong $< 200 >$ texture prevalent [12] particularly in the nanocrystalline Ni samples with d = 25 nm and 40 nm.

By contrast, in the OP case, $H_{res}(\alpha)$ has nearly the same values for the angles α = - 90^o and + 90^o but H_{res} exceeds 11 kOe (the upper instrumental limit on the static magnetic field) as $\alpha = 0^o$ is approached either from below or from above

(see, Fig. 6.13). This angular dependence of H_{res} on α is also consistent with the simultaneous presence of both cubic and uniaxial magnetic anisotropies but the latter contribution is dominant. The variations in H_{res} with the angle Ψ or α yielded by the resonance and equilibrium conditions [11] for a spin system in which the cubic and uniaxial magnetic anisotropies are simultaneously present [Refer Eqs.(6.28) and (6.29) or Eqs.(6.30) and (6.31)].

In figures 6.12 and 6.13, the continuous curves through the data points (symbols) denote the variations in H_{res} with the angle ψ or α yielded by the resonance and equilibrium magnetization conditions in the IP or OP case, i.e., equations (6.28) and (6.29) or (6.30) and (6.31), when the self-consistent procedure, illustrated below, is followed. For a given direction of $\overrightarrow{H}$ represented by a certain value of the angle ψ (α) in the IP (OP) case, the corresponding *equilibrium value* of the magnetization angle ϕ (θ) and the values of H_{K_1} and H_{K_u} for each sample are self-consistently calculated from equations (6.28) and (6.29) (equations (6.30) and (6.31)) using the experimentally observed value of $H_{res}(\psi)$ ($H_{res}(\alpha)$). To elucidate this procedure further, we treat the IP case as an illustrative example (as the same procedure is adopted to arrive at $\theta(\alpha)$ in the OP case). For a given field angle ψ, the magnetization angle ϕ is calculated from Eq.(6.29) using the H_{res} observed at that angle ψ, magnetization M given by the lineshape analysis and rough values for the anisotropy constants K_1 and K_u so as to arrive at the initial values of $H_{K_1} = 2K_1/M$ and $H_{K_u} = 2K_u/M$. H_{res} at this value of ψ, calculated from Eq.(6.28) and employing ϕ computed from Eq.(6.29), and the same values of M, H_{K_1} and H_{K_u} as those used in Eq.(6.29), is compared with the observed value of H_{res} in a non-linear least-squares fit computer program which optimizes agreement between the experiment and theory by treating K_1 and K_u as free-fitting parameters. The above procedure is repeated with the new values of K_1 and K_u till the values of K_1, K_u and ϕ computed from Eq.(6.29), when used in Eq.(6.28), yield the value of H_{res} at a given ψ that conforms well with the

corresponding observed value of H_{res}.

6.4.2 Angular variation of the Linewidth

Figures 6.14 and 6.15 respectively depict the variations of the FMR linewidth, ΔH_{pp}, with the static magnetic field angles ψ and α in the 'in-plane' and 'out-of-plane' sample configurations. $\Delta H_{pp}(\psi)$ and $\Delta H_{pp}(\alpha)$ almost mimic the corresponding angular variations of H_{res}. Such angular variations of ΔH_{pp} are generally attributed to the sum of the contributions [31] ΔH_0, $\Delta H_{int} = \Delta H_i \ (\partial H_{res}/\partial H_i)$ and $\Delta H_\psi = \Delta\psi \ (\partial H_{res}/\partial\psi)$ in the IP case or $\Delta H_\alpha = \Delta\alpha \ (\partial H_{res}/\partial\alpha)$ in the OP case. While the intrinsic linewidth contribution, ΔH_0, arises from the EC and LLG mechanisms in the present case, ΔH_{int} and ΔH_ψ (ΔH_α) are due to the internal field inhomogeneity and the angular spread of a-axis (c-axis), respectively. The analysis of the angular dependence of ΔH_{pp} is complicated by the fact that an unambiguous separation of the various contributions to ΔH_{pp} is not possible. For this reason, we have not made any attempt to quantify the angular variations of ΔH_{pp} observed in the IP and OP sample configurations.

6.5 Summary and Conclusion

The following conclusions have been drawn from the results of a detailed lineshape analysis of the ferromagnetic resonance (FMR) spectra taken on pulse electrodeposited nanocrystalline Ni sheets (with the average crystallite size, d, varying from 10 nm to 40 nm) at temperatures ranging from 113 K to 325 K.

- Thermally-excited spin waves are solely responsible for the observed thermal decline of magnetization, $M_s(T)$.
- The spin-wave description of $M_s(T)$ yields the values for the magnetization and

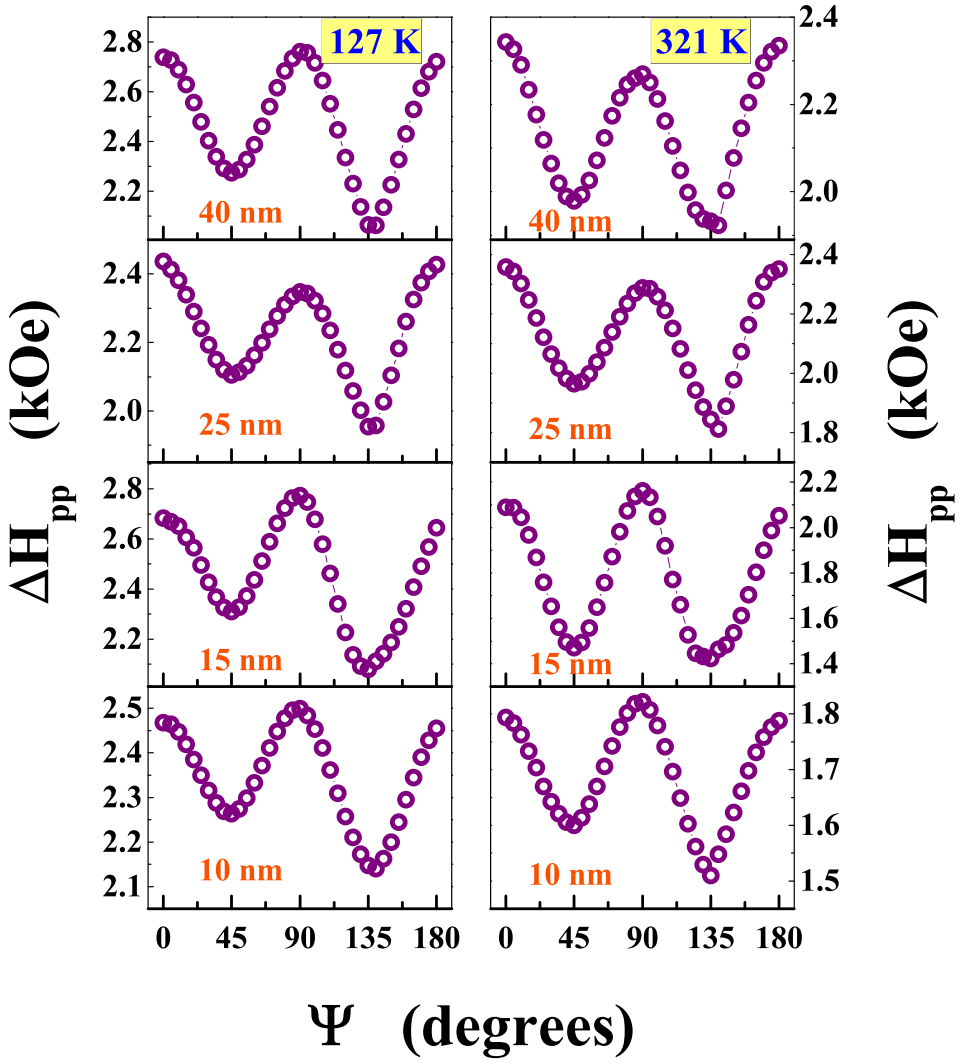

Figure 6.14: *The angular (Ψ) variations of the FMR linewidth, ΔH_{pp}, in the 'in-plane' sample configuration, at fixed temperatures T = 127 K and 321 K, for the nanocrystalline Ni samples with the average crystallite size ranging from 10 nm to 40 nm.*

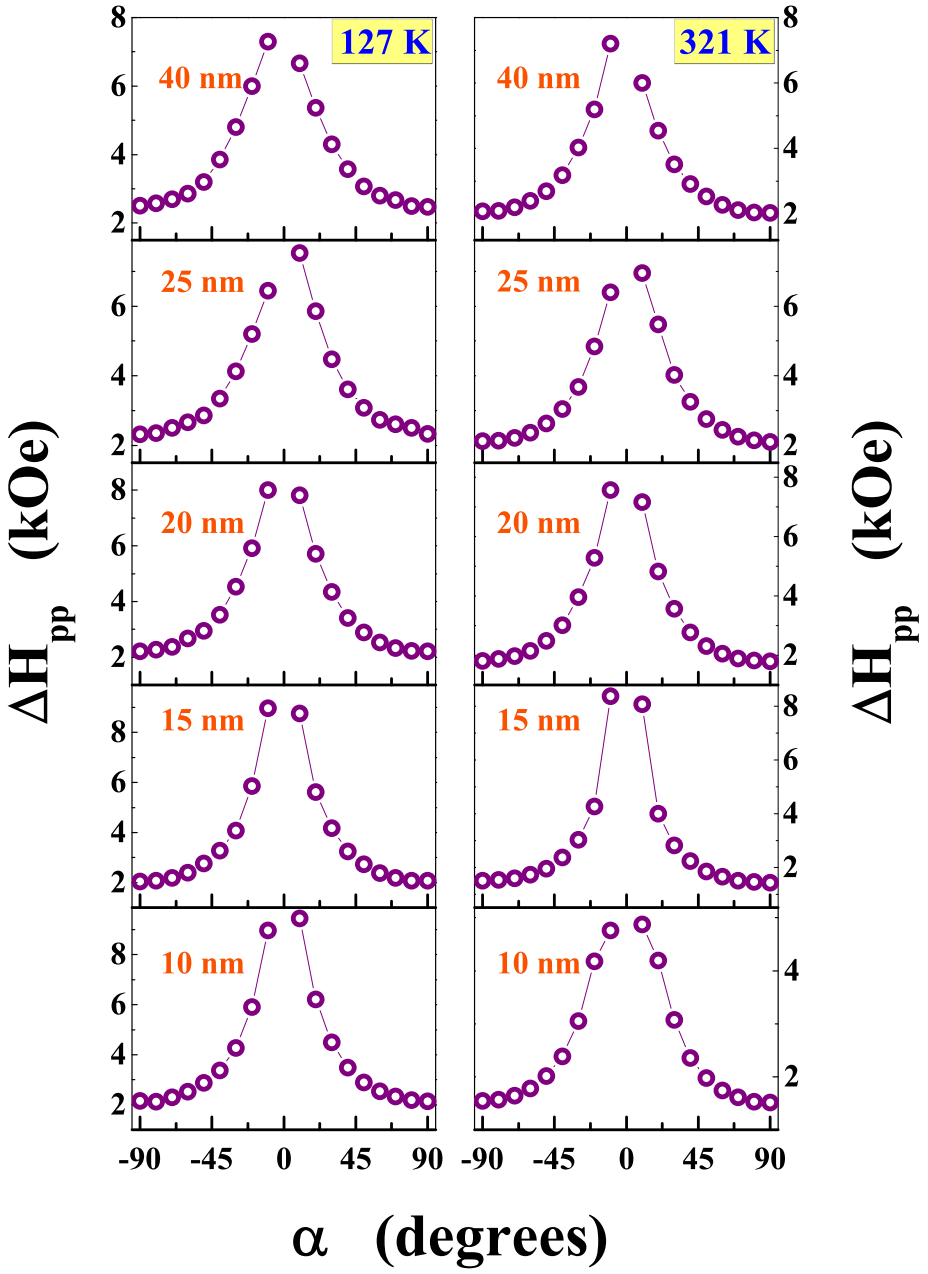

Figure 6.15: *The angular (α) variations of the FMR linewidth, ΔH_{pp}, in the 'out-of-plane' sample configuration, at fixed temperatures T = 127 K and 321 K, for the nanocrystalline Ni samples with the average crystallite size ranging from 10 nm to 40 nm.*

spin-wave stiffness at absolute zero of temperature, i.e., $M_s(0)$ and D_0, for nc-Ni samples of different d that are in excellent agreement with the corresponding values deduced previously from an elaborate spin wave analysis of the bulk magnetization data in chapter 4.

- While the magnetization at 0 K, $M_s(0)$, varies with average crystallite size, d, as $M_s(0) \sim d^{-3/2}$, the spin-wave stiffness at 0 K, D_0, follows the power law $D_0 \sim d^{4/3}$.

- Like in bulk Ni, Landé splitting factor, g, has the temperature-independent and crystallite size-independent value of $g = 2.21(3)$ over the temperature range covered in the present FMR experiments.

- In the 'in-plane' sample configuration (static magnetic field within the sample plane), major contribution to the anisotropy field, $H_K(T)$, comes from the cubic magnetocrystalline anisotropy. The values of H_K at different temperatures deduced from the calculations of the angular variations of the resonance field in the 'in-plane' and 'out-of-plane' sample configurations, conform very well with the corresponding values obtained from the lineshape analysis.

- The exchange-conductivity mechanism, at best, accounts for the observed thermal narrowing of the FMR linewidth, ΔH_{pp}, but fails to explain the very large magnitude of ΔH_{pp} at any given temperature. By comparison, the Landau-Lifshitz-Gilbert (LLG) damping makes a much greater contribution to the intrinsic FMR linewidth but the LLG contribution is weakly temperature-dependent. An overwhelmingly large contribution to ΔH_{pp} seems to arise from magnetic inhomogeneity and the spread in the angle subtended by the external magnetic field with the crystallographic axes, which vary in orientation from one crystallite to the other in nanocrystalline Ni samples studied.

References

1. M. Farle, *Rep. Prog. Phys.* **61**, 755 (1998) and references cited therein.

2. B. Heinrich, G. Woltersdorf, R. Urban and E. Simanek, *J. Appl. Phys.* **93**, 7545 (2003).

3. B. Heinrich, *Ultrathin Magnetic Structures III* (2005) (Springer, New York) and references cited therein.

4. J. Lindner, U. Wiedwald, K. Baberschke and M. Farle, *J. Vac. Sci. Technol.* **A 23**, 796 (2005).

5. Kh. Zakeri, Th. Kebe, J. Lindner, C. Antoniak, M. Farle, K. Lenz, T. Tolinski and K. Baberschke, *Phase Transitions* **79**, 793 (2006) and references cited therein.

6. Y. Zhai, Y. X. Xu, J. G. Long, Y. B. Xu, M. Lu, Z. H. Lu, H. R. Zhai and J. A. C. Bland, *J. Appl. Phys.* **89**, 7290 (2001).

7. V. K. Sharma and A. Baiker, *J. Chem. Phys.* **75**, 5596 (1981).

8. U. Ebels, J. -L. Duvail, P. E. Wigen, L. Piraux, L. D. Buda and K. Ounadjela, *Phys. Rev. B* **64**, 144421 (2001).

9. G. N. Kakazei, P. E. Wigen, K. Yu. Guslienko, R. W. Chantrell, N. A. Lesnik, V. Metlushko, H. Shima, K. Fukamichi, Y. Otani and V. Novosad, *J. Appl. Phys.* **93**, 8418 (2003).

10. G. A. Basheed, S. N. Kaul and A. Michels, *Appl. Phys. Lett.* **91**, 033105 (2007).

11. G. A. Basheed, S. N. Kaul and M. Vázquez, *J. Appl. Phys.* **109**, 07A321 (2011).

12. P. V. Prakash Madduri and S. N. Kaul, *J. Alloys. Comp.* **689**, 533 (2016).

13. J. H. E. Griffiths, *Nature* **158**, 670 (1946).

14. L. Landau and E. Lifshitz, *Phys. Z. Sowjetunion* **8**, 153 (1935).

15. T.L. Gilbert, *Phys. Rev.* **100**, 1243 (1955).

16. S. N. Kaul and V. Siruguri, *J. Phys. F* **17**, L255 (1987).

17. S. N. Kaul and V. Siruguri, *J. Phys.: Condens. Matter* **4**, 505 (1992).

18. J. Smit and H.G. Beljers, *Philips Res. Rep.* **10**, 113 (1955); H. Suhl, Phys. Rev. **97**, 555 (1955).

19. M. L. Spano and S. M. Bhagat, J. Magn. Magn. Mater., **24**, 143 (1981).

20. S. M. Bhagat, S. Harldson and O. Beckman *J. Phys. Chem. Solids* **38**, 593 (1977).

21. D. S. Rodbell, *Phys. Rev. Lett.* **13**, 471 (1964).

22. D. S. Rodbell, *Physica* **1**, 279 (1965).

23. S. M. Bhagat and H. O. Stevens, *J. Appl. Phys.* **39**, 1067 (1968).

24. S. Haradlson and L. Petterson, *J. Phys. Chem. Solids* **42**, 681 (1981).

25. S. V. Vonsovskii *Ferromagnetic resonance*, (Pergamon Press, London 1966).

26. Y. Li and K. Baberschke, *J. Magn. Magn. Mater.* **93**, 345 (1991); Y. Li, M. Farle and K. Baberschke, Phys. Rev. B **41**, 9596 (1990).

27. W. Platow, A. N. Anisimov, G. L. Dunifer, M. Farle and K. Baberschke *Phys. Rev. B* **58**, 5611 (1998).

28. Z. Frait, D. Fraitova, *Spin-wave resonance in metals: Spin Waves and Magnetic Excitations*, **2** ed. A. S. Borovik-Romanov and S. K. Schiha (Amsterdam: Elsevier).

29. F. Schreiber, J. Pflaum, Z. Frait, Th. Mühge and J. Pelzl, *Solid. State. Commum.* **93**, 965 (1995).

30. H. Suhl, *Phys. Rev.* **97**, 55 (1955).

31. C. Chappert, K. Le Dang, P. Beauvillain, H. Hurdequint and D. Renard, *Phys. Rev. B* **34**, 3192 (1986).

32. S. N. Kaul and V. Siruguri, *J. Phys.: Condens. Matter* **4**, 505 (1992).

33. S. N. Kaul and P. D. Babu, *Phys. Rev. B* **45**, 295 (1992).

34. V. Siruguri and S. N. Kaul, *J. Phys.: Condens. Matter* **8**, 4545 (1996); V. Siruguri and S. N. Kaul, *J. Phys.: Condens. Matter* **8**, 4567 (1996).

35. D. S. Rodbell, *Phys. Rev. Lett.* **13**, 471 (1964).

36. S. M. Bhagat and L. L. Hirst, *Phys. Rev.* **151**, 401 (1966).

37. S. N. Kaul, *Phys. Rev. B* **27**, 5761 (1983);

    S. N. Kaul, *Phys. Rev. B* **27**, 6923 (1983).

38. S. N. Kaul, *J. Phys.: Condens. Matter* **3**, 4027 (1991).

39. S. N. Kaul, *J. Phys.: Condens. Matter* **11**, 7597 (1999).

40. S. N. Kaul, *J. Phys.: Condens. Matter* **17**, 5595 (2005).

41. S. N. Kaul and P. D. Babu, *Phys. Rev. B* **50**, 9308 (1994).

42. S. N. Kaul and P. D. Babu, *J. Phys.: Condens. Matter* **10**, 1563 (1998).

43. S. N. Kaul and M. Rosenberg, *Phys. Rev. B* **27**, 5698 (1983).

44. A. Semwal and S. N. Kaul, *Phys. Rev. B* **60**, 12799 (1999).

45. P. V. Prakash Madduri and S. N. Kaul, *J. Magn. Magn. Mater.* **418**, 143 (2016).

46. A. T. Aldred, *Phys. Rev. B* **11**, 2597 (1975).

47. J. Weissmüller, A. Michels, J. G. Barker, A. Wiedenmann, U. Erb and R. D. Shull, *Phys. Rev. B* **63**, 214414 (2001).

48. R. G. Calderón, L. F. Barquín, S. N. Kaul, J. C. Goméz Sal, P. Gorria and J. S. Pedersen, *Phys. Rev. B* **71**, 134413 (2005).

49. S. N. Kaul, *J. Appl. Phys.* **61**, 451 (1987).

50. S. N. Kaul and M. Rosenberg, *Phys. Rev. B* **25**, 5863 (1982).

51. S. N. Kaul and M. Rosenberg, *Phil. Mag. B* **44**, 357 (1981).

52. E. A. Turov, in *Ferromagnetic Resonance* edited by S. V. Vonsovskii, Pergamon Press, New York (1966) p.206.

53. P. V. Prakash Madduri and S. N. Kaul, *Phys. Rev. B* **95**, 184402 (2017).

Publications

1. Magnon-induced interband spin-flip scattering contribution to resistivity and magnetoresistance in a nanocrystalline itinerant-electron ferromagnet: effect of crystallite size
   P. V. Prakash Madduri and S. N. Kaul
   Phys. Rev. B **95**, 184402 (2017).

2. Core and surface/interface magnetic anisotropies in nanocrystalline nickel
   P. V. Prakash Madduri and S. N. Kaul
   J. Alloys Compd. **689**, 533 (2016).

3. Thermal demagnetization due to spin waves in nanocrystalline Ni
   P. V. Prakash Madduri and S. N. Kaul
   J. Magn. Magn. Mater. **418**, 143 (2016).

4. Magnetic irreversibility and magnetocrystalline anisotropy in nanocrystalline nickel
   P. V. Prakash Madduri, S. Srinath and S. N. Kaul
   AIP Conf. Proc. **1665**, 130049 (2015).

5. Diorder-induced non-Fermi liquid behavior of electrical resisitivity in nanocrystalline Ni
   P. V. Prakash Madduri and S. N. Kaul
   Physica B **448**, 147 (2014).

6. Low-lying magnetic excitations, magnetic irreversibility and approach-to-saturation in nanocrystalline Ni
   P. V. Prakash Madduri, S. P. Mathew and S. N. Kaul
   AIP Conf. Proc. **1536**, 89 (2013).

Manuscripts Under Preparation

1. Ferromagnetic resonance in nanocrystalline nickel

Papers Presentad at National and International Conferences

1. *Ferromagnetic resonance in nanocrystalline nickel*
   P. V. Prakash Madduri, S. P. Mathew and S. N. Kaul
   International Conference on Magnetism and Magnetic Materials (ICMAGMA-2017), Hyderabad, India, February 2017.

2. *Thermal demagnetization due to spin waves in nanocrystalline Ni*
   P. V. Prakash Madduri and S. N. Kaul
   International Conference on Magnetism and Magnetic Materials (ICMAGMA-2015), Vellore, India, December 2015.

3. *Magnetic irreversibility and magnetocrystalline anisotropy in nanocrystalline nickel*
   P. V. Prakash Madduri, S. Srinath and S. N. Kaul
   59^{th} DAE-Solid State Symposium, VIT University, Vellore, India, December 2014.

4. *Spin Waves and Magnetic Anisotropy in Nanocrystalline Ni*
   P. V. Prakash Madduri, S. Srinath and S. N. Kaul
   Frontiers in Physics (FIP-2014) conference, School of Physics, University of Hyderabad, India, October 2014.

5. *Diorder-induced non-Fermi liquid behavior of electrical resisitivity in nanocrystalline Ni*

   P. V. Prakash Madduri and S. N. Kaul

   International Conference on Magnetism and Magnetic Materials (ICMAGMA-2013), Indian Institute of Technology, Guwahati, India, December 2013.

6. *Magnetic excitations, anisotropy and magneto-transport in nanocrystalline Ni*

   P. V. Prakash Madduri and S. N. Kaul

   Frontiers in Physics (FIP-2013) conference, School of Physics, University of Hyderabad, India, September 2014.

7. *Low-lying Magnetic Excitations, Magnetic Irreversibility and Approach-to-saturation in Nanocrystalline Ni*

   P. V. Prakash Madduri, S. P. Mathew and S. N. Kaul

   Recent trends in Applied Physics and Material Science conference (RAM)-2013, Govt. College of Engineering and Technology, Bikaner, India, February 2013.

This is to certify that the thesis entitled, ***"Low-lying magnetic excitations, magnetic anisotropy, electrical transport, magnetotransport and resonant microwave absorption in nanocrystalline Ni"****, submitted by my student Pavan Venu Prakash Madduri (Regn No: 10PHPH20), has been screened by the Turnitin software at the Indira Gandhi memorial library(IGML)-University of Hyderabad. This software shows 47 % similarity index out of which, 28 % came from the candidate's research articles (where he is the first author) directly related to this thesis.*

From the detailed similarity index report, it is obvious that the remaining 19 % of similarity index, is due to the similarity caused by the frequent use of the well-known standard terms such as temperature, magnetization, magnetic susceptibility, magnetic field, magnetic anisotropy, spin waves, exchange interaction, exchange correlation length, critical domain size, resistivity, magnetoresistance, ferromagnetic resonance, linewidth, nanocrystalline materials, grain size, small-angle neutron scattering (SANS), to name a few. Use of such terms is rampant in the literature and hence it is not surprising that the similarity index is artificially inflated. It should be noted that the use of such standard terms cannot be avoided.

Prof. S. N. Kaul
Thesis Supervisor
School of Physics
University of Hyderabad.